Single-Shot Spectroscopy of Solid-State Photoinduced Dynamics far from Equilibrium

by

Johanna Wendlandt Wolfson

B.S., University of Wisconsin—Madison, 2006

Submitted to the Department of Chemistry
in Partial Fulfillment of the Requirements for the Degree of

Doctor of Philosophy

at the

MASSACHUSETTS INSTITUTE OF TECHNOLOGY

June 2013

Author .....
Department of Chemistry
May 10, 2013

Certified by .....
Keith A. Nelson
Professor of Chemistry
Thesis Supervisor

Accepted by .....
Robert W. Field
Chairman, Departmental Committee on Graduate Students

This doctoral thesis has been examined by a Committee of the Department of Chemistry as follows:

Thesis Committee Chair .....

Andrei Tokmakoff
Professor of Chemistry

Thesis Supervisor .....

Keith A. Nelson
Professor of Chemistry

Thesis Committee Member.....

Robert W. Field
Professor of Chemistry

Single-Shot Spectroscopy of Solid-State Photoinduced Dynamics far from Equilibrium

by

Johanna Wendlandt Wolfson

Submitted to the Department of Chemistry
on May 24, 2013 in Partial Fulfillment of the
Requirements for the Degree of
Doctor of Philosophy in Physical Chemistry

Abstract

Ultrafast single-shot spectroscopy was developed and improved as a method to observe photoinduced dynamics far from equilibrium. The method was then employed to illuminate material dynamics in platinum-halide quasi-one-dimensional chain compounds (PtI) and in the semimetal bismuth. Both material systems exhibit strongly coupled energetic modes; as a result, their study under laser pulse excitation offers the opportunity to explore the same processes that underlie their unique properties. Our measurements have pushed the photoinduced study of these materials to new extremes toward a better understanding of material response and control far from equilibrium.

In this thesis, the single-shot method is introduced and analyzed, and measurements on PtI and bismuth are presented and discussed. Collectively, the measurements offer a view into how materials with strong electron-phonon coupling respond to photoexcitation across dimension, timescale, and excitation density. Dimensionality is explored qualitatively between the PtI chain sample and bismuth samples of varying thickness. The time evolution upon laser excitation is monitored from the instantaneous response out to several hundred picoseconds. The photoexcitation itself is varied from weak (corresponding to most published literature on both materials) to very strong (exceeding the thresholds for visualizing dynamics with conventional methods). We describe our results in the context of material dynamics on the microscale and propose future directions.

New dynamics were observed in PtI chains that suggest long-lived structural and electronic states under high irradiation. The possibility of collective structural rearrangement with a long lifetime is proposed. In bismuth, high photoexcitation measurements traversed the material's potential energy surface along the coordinate of structural distortion. We report control of the excitation-dependent photoinduced phase by dimensional constraint, as well as ballistic transport effects that govern this interplay.

This research enables future advancements on two fronts. The instrumental developments enable visualization of irreversible events for a wider range of materials. The physical insights gained for the materials studied here characterize key processes pertinent to technological applications and off insights that may govern behavior far from equilibrium for broader classes of materials.

Thesis Supervisor: Keith Nelson
Title: Professor of Chemistry

For my teachers: from Edison Elementary to MIT,
and everywhere in between.

Thank you for teaching me how to ask questions,
seek answers, and learn for the sake of learning.

Acknowledgements

Many wonderful people have made it possible for me to do the work presented here, and I am deeply grateful to them all. They prepared me for graduate school, supported me through it, and helped me look ahead. Some taught me about science and how to be a scientist. Others provided much-needed perspectives outside the scientific realm. Mentors, teachers, friends, colleagues, and family—collectively, they have provided me with a support network second to none. Thank you to all the wonderful people who have been involved in my life and in this process.

I am thankful to my advisor, Keith Nelson, for being a terrific and brilliant example to learn from. He is relentlessly optimistic about the science we do and excited about its possibilities. His incredibly vast knowledge base is rivaled only by his desire to understand, learn, and discover more. He is supportive and respects his students. In turn, this has cultivated a positive dynamic in the research group, making the Nelson group a wonderful place to do science, make friends, work, and learn. I have also been very fortunate to have Andrei Tokmakoff as chair of my thesis committee. A few key conversations with Andrei went a long way in encouraging my pursuits. My meetings with him also provided fresh perspectives on my experimental work, causing me to reevaluate my approaches and modify them for the better.

Several people have worked with me on these and other single-shot projects, and the work is better for it. Taeho Shin is responsible for turning the single-shot instrument into its current more robust and reliable form. He was also a great friend to me, a supportive mentor, and possesses a remarkable amount of patience. Maria Kandyla worked with us both on several early-stage measurements, and I am grateful for her contributions, as well as her continued encouragement even long after she left the group. Ikufumi Katayama and Taro Kawano joined the single-shot lab for a summer of collaboration which initiated our work on Platinum-iodide. I am thankful to them, as well as to Jun Takeda, for the collaboration, which brought a fundamentally interesting physical chemistry problem to the single-shot doorstep, their strong scientific perspective, their positive presence in the lab, and our continued conversation as we move the work forward. I could not have completed the work presented here without the strong contributions of Sam Teitelbaum, who joined the single-shot lab more recently. Sam was eager to learn, explore, and contribute from the start. This enthusiasm fostered several improvements in the lab by way of productive brainstorming and fruitful discussions. I'm very glad Sam joined the project he did and I look forward to seeing where he takes it in the future. In addition to those directly involved, several members of the Nelson group past and present have provided valuable insight and expertise: Kit Werley, Sharly Fleischer, Brad Perkins, Harold Hwang, Alex Maznev, and Darius Torchinsky have all contributed to this work over the years.

I have always appreciated the collegial and fun work atmosphere that coexists in the Nelson group alongside the tough scientific problems we tackle together. Thanks to Harold Hwang, Jeremy Johnson, and Kit Werley, I was part of an incoming cohort of classmates that provided ongoing support—from the problem sets of first year to writing my dissertation. Special thanks to Harold for helping me weather the daily ups

and downs of graduate school the whole way through. I'm glad to have overlapped with some terrific senior group members at the time I joined, especially Darius Torchinsky, Kathy Stone, and Ka-Lo Yeh, who provided great advice and friendship from the start. Kara Manke, Pat Wen, Dylan Arias and Nate Brandt arrived in the group in the two years following me, and I consider them to be my adopted classmates. I've been lucky to share lab space over the years with Eric Statz, Kit Werley, Steph Teo, Ben Ofori-Okai, and Prasahnt Sivarajah in addition to single-shot folks. Sharing the space with them has meant daily contact with smart people providing fresh perspectives and help with experimental problems, as well as the great conversation and occasional diversions needed to withstand the long days in lab. I will greatly miss spending time with them. Finally, two post-doctoral scientists who joined the group in the last few years have been especially supportive. Sharly Fleischer has been a great friend—always willing to brainstorm, help, listen, and provide comic relief. Brad Perkins spent a great deal of time helping me reevaluate the single-shot experiment and implement key improvements. He became my closest friend in the group and provided me with daily support, helping to navigate challenges ranging from detection schemes and manuscript preparation to my job search and graduation timeline. I feel very lucky to have had his help throughout this period. For all my coworkers in the group—past and present—I look forward to seeing the great things they do next.

All my incoming p-chem classmates made the first year of graduate school better. Krupa Ramasesha and my now-husband Misha journeyed with me from Wisconsin to MIT for graduate school. I remember walking with them into Building 7 on a rainy day before the semester's start and realizing how grateful I was to have them with me. But new friendships waited too: Brian Walker, Harold Hwang, Kit Werley, Lee-Ping Wang, Barratt Park, and Tony Colombo all became close friends as we battled our way through problem sets late into the evenings and stayed in touch throughout grad school across different research groups.

Outside the chemistry department, I have gotten to know many amazing people at MIT. Retsina Meyer, Whitney Bernstein, and Rachel Alonso are incredible women who continue to inspire me. Retsina has been my thesis-writing partner, and I have been lucky to have such a positive, fun, and brilliant friend with whom to go through this final process, and with whom to launch off into the next phase. Whitney is my partner in crime for generating big world-changing ideas, which is a pretty incredible type of friend to have. Rachel and I became fast friends after meeting at a leadership seminar and spontaneously formed a two-woman support network just when I needed it the most. Our weekly chats kept me going during challenging times. A big part of my experience and education at MIT has been through the Science Policy Initiative, an organization engaging scientists with policymakers and the public. Through this organization, I have met countless brilliant emerging scientists who are dedicated to making a difference in the world. This wonderful and inspiring community taught me about my own goals and professional purpose, and it continues to do the same for other students at MIT while also serving science and society at large. I am especially grateful to those I've had the opportunity to work with directly: Bridget Dolan, Megan Brewster, Scott Carlson, Noah Spies, Mike Henninger, Dan Chavas, Jenny Rood, Nicole Casasnovas, Nathaniel Schafheimer, Nat Twarog, Sam Brinton, and Kat Saad.
I have also been blessed with wonderful mentors at MIT outside my scientific field, including Bill Bonvillian, Claude Canizares, Lita Nelsen, and Jon Spaner. They have

each played an important role in helping me define and explore my interests and goals as well as my strengths and weaknesses, and I continue to be amazed by their generosity of time and helpfulness.

I could never have made it through what I affectionately call 23rd grade without many amazing teachers, and I have dedicated my thesis to them. It is only because of the great education I received that I have myself been able to contribute new knowledge. I list here those teachers who made an especially strong impression on me: Beth Tobler, Marlene Angevine, David Erickson, Jan Thompson, Terry Gorges, Greg Lee, Robert Hillestad, Bernie Edmonds, Mark Ropella, Cindy Fahrenkrug, and Carol Sanderfoot.

At the University of Wisconsin, Shannon Stahl taught the organic chemistry class that caused this history major to add on a chemistry major mid-way through college. Shannon also accepted me into his research group under Michelle Rogers, whose tutelage and kindness I greatly appreciated. Alas, synthesis was not for me. Yet in a gesture I will always appreciate, Shannon took the effort to find a project more to my liking; I rounded out my research experience at Wisconsin under Brian Popp, from whom I learned a great deal. I am also grateful to Anders Nilsson at SLAC for taking me in as a summer student, and to Dennis Nordlund and the rest of the Nilsson group for welcoming me and allowing me to take a crack at a fundamentally fascinating problem. I credit my growing interest in physical chemistry to two terrific professors: Frank Weinhold and Qiang Cui. Frank Weinhold's challenging course made me think that Thermodynamics was one of the most exciting topics I'd encountered. As I now realize having taught it myself at MIT, this was no easy feat. And Qiang Cui's class in Quantum Chemistry introduced me to the fascinating and strange world of quantum mechanics in a way that was accessible, challenging, and engaging all at once. It also happened to be the class in which I met my husband.

Misha has been my strongest supporter, my best friend, and all-around the greatest husband on the planet. He helps me in countless ways each day through his kindness, generosity, and love, which I have come to understand are as natural to him as breathing. We graduated from college together, entered graduate school together, integrated with our incoming class together, studied together, and taught together. Going through these experiences side by side was not without its challenges, but it also meant we could support each other in a way that was truly unique. Best of all, we now look ahead to the next stage with twice the excitement and sense of accomplishment. I wouldn't have wanted to do this, nor anything else, without Misha by my side.

Finally, I would like to thank those who have supported me from afar. Laura Behm, Andrea Bufford, and Caitlin Kiley, respectively my closest friends from elementary school, middle school, and college, were always just a phone call away. My second family, the Wolfsons, have always believed in me and I am thankful for their support. And I am deeply thankful to my parents, my brothers John, Matt, and Dan, and my sisters-in-law Nancy and Lori for their endless support, encouragement, and love over the years.

To all who have been involved—in big ways and small—thank you. I couldn't have done it without you.

Contents

Chapter 1 Introduction and Background 25

1.1 Toward Material Design 26

1.2 Light-Matter Interactions 27

1.2.1 Dielectric Function: Bound electrons and lattice vibrations 29
1.2.2 Dielectric Function: Free electrons 30
1.2.3 Observing the Complex Dielectric Function 31
1.2.4 Relating Observables to Microscopic Events 33

1.3 Ultrafast material dynamics 35

1.3.1 Electronic Excitation, Scattering, and Recombination 37
1.3.2 Coherent Phonon Generation via ISRS and DECP 41

1.4 Watching Dynamics Unfold: Experimental Techniques 45

1.4.1 Pump-probe Spectroscopy 45
1.4.2 Single-shot Spectroscopy 47

1.5 Photo-induced Phase Transitions 48

1.5.1 Energetics and Timescales of Photoinduced Phase Transitions 49
1.5.2 Theory of Photoinduced Phase Transitions 51

1.6 Summary and scope of work 57

Chapter 2 Femtosecond Single-shot Spectroscopy 59

2.1 Light Source Generation 59

2.1.1 Laser system 59
2.1.2 Pulse optimization and characterization 64
2.1.3 Tunable-wavelength pulses 65

2.2 Single-shot Optical Instrument 68

2.2.1 Measurement via spatio-temporal mapping 68
2.2.2 Optical layout 71

2.3 Single-shot Instrument Operation 80

2.3.1 Alignment 80
2.3.2 Electronics and Timing 82
2.3.3 Image Collection and Analysis 85

2.4 Summary 91

Chapter 3 Analysis of Single-shot Detection 93

3.1 Digital Signal Detection and Noise Level Calibrations 94

3.2 Pixel variation and averaging 98
3.3 Modeling the Spatio-Temporal Probe Array 103
3.3.1 Beam Power and Intensity Profile 103
3.3.2 Spatio-Temporal Interactions Among Probe Pulses 104
3.3.3 Probe Beam Array Interactions under Photoinduced Change 118
Chapter 4 Photo-induced Structural Change in Platinum-Iodide 121
4.1 Metal-halide chain crystals 122
4.2 Excitations and Phase Transitions 125
4.2.1 Fundamental excitations in Metal-halide chains 125
4.2.2 Structural Transitions 127
4.2.3 Key Questions for Single-shot Study 130
4.3 Measurement and Analysis 131
4.3.1 Experimental Details 131
4.3.2 Data Analysis 132
4.4 Experimental Results 136
4.4.1 Conventional Pump-Probe Measurements: the reversible photoexcitation regime 136
4.4.2 Single-Shot One-Pump Measurements: the irreversible photoexcitation regime 144
4.4.3 Single-Shot Two-Pump Measurements: measuring dynamics on the highly photo-excited state 151
4.5 Discussion of Results 156
4.5.1 Excitation Dependence of Electronic and Lattice Dynamics in Photo-excited PtI(en) 156
4.5.2 Cooperative Effects in Structural Change 161
4.5.3 Dynamics of the Highly Photo-excited State 167
4.6 Conclusions and Future Work 171
Chapter 5 High-excitation Photoinduced Dynamics in Bismuth 173
5.1 Material and Literature Overview 174
Structural properties and photoinduced response 174
5.2 Experimental Results 180
5.2.1 Instantaneous Response to Strong Photo-excitation 182
5.2.2 Long-time Response to Strong Photo-excitation 194
5.2.3 One-pump Thin Film Measurements: Key Results 198
5.2.4 Spectroscopy of Photoexcited Bismuth: Two-pump Measurements 200
5.3 Modeling of Nonequilibrium and Equilibrium Dynamics 210
5.3.1 Carrier Population Estimates 211
5.3.2 The Two-temperature Model 213
5.3.3 Modifications to the two-temperature model 219

5.4 Discussion: Relating Measurements and Modeling 232
5.5 Conclusions and Future Work 242

References 245

List of Tables and Figures

Figure 1-1: *Real (left) and imaginary (right) parts of the dielectric function for a generic charged-atom pair harmonic oscillator. For comparison, the same functions for silicon are inset.*[21]. 30
Figure 1-2: *Real and imaginary parts of the conductivity for unbound carriers. For comparison, the same functions for weakly-doped silicon are inset.*[22] 31
Figure 1-3: *Reflectance of silicon as a function of frequency (energy) measured at normal incidence and at room temperature.*[21] *Compare to the inset in Figure 1-1.* 33
Figure 1-4: *Sourced from Kuzmany, 1998.*[19] *A generalized plot of absorption coefficient for low (left) to high (right) excitation energies in solids.* 34
Table 1-1: *Coupling between radiation and materials and the relevant timescales and processes.* [25] 36
Figure 1-5: *Excitations and relaxation processes after photoexcitation in GaAs (simplified band structure of GaAs from the Ioffe Physico-Technical Institute electronic archives). After photo-excitation, electrons lose energy via electron-electron scattering (e-e), electron-phonon scattering (e-ph), electron-hole recombination (e-h), or relaxation to defect states (D). The blue shaded regions indicate thermalized populations; processes enclosed in the dashed region are only transiently measureable.* 39
Figure 1-6: *From Mero et al., 2005.*[27] *Electron energy distribution post-excitation at different timepoints, as calculated using the Boltzmann distribution and Keldysh rate equations. The 5 fs instance is modulated at the photon frequency due to multiphoton processes and polarization; these modulations are quickly averaged out.* 40
Figure 1-7: *Examples of possible microscopic dynamics leading to a typical time-domain reflectivity signal in a crystalline band-gap material with a Raman active phonon mode. Electron-electron interaction occurs on the 100 fs timescale; electron-hole recombination on the several ps timescale, and electron-phonon interactions on intermediate timescales.* 41
Figure 1-8: *Adapted from Ishioka, 2012.*[35] *Depictions of generation mechanisms and example nuclear trajectories for coherent phonon generation via ISRS (top) and DECP (bottom). The greyed portions beneath the time-dependent traces represent the driving force—a delta function for ISRS (similar to striking the pendulum ball) and a step function for DECP, (analogous to translating the pendulum string). The ISRS mechanism maintains nuclei equilibrium positions generating sine function oscillations about those positions, while the DECP mechanism displaces nuclei equilibrium positions generating cosine function about the new positions when the wavepacket is launched.* 42
Figure 1-9: *In a conventional pump-probe time-domain measurement, an intense pump pulse induces a change in the sample via light absorption and a probe pulse reports on the resulting measurable change in optical or electronic properties. This pump-probe sequence is repeated while varying the inter-pulse time delay, and a time-dependent response is reconstructed* 46
Figure 1-10: *In a single-shot spectroscopy measurement, an intense pump pulse induces a change in the sample. Because either the recovery timescale or the strength of response renders the event irreversible on the femtosecond timescale, a temporal stream of probe pulses is used to monitor the material response in real-time. One full time-sequence is constructed from one laser shot* 48
Figure 1-11: *Adapted from Nasu, 2001.* [54] *The system can be taken from the initial ground state $|i\rangle$ to state $|h\rangle$ on the same potential energy surface via thermal heating. Photoexcitation from state $|i\rangle$ to state $|t\rangle$ allows relaxation to the metastable photoinduced state $|p\rangle$ which can be structurally distinct. Relaxation proceeds to either $|i\rangle$ or $|h\rangle$.* 50
Figure 1-12: *Adapted from Nasu et al., 2001.*[54] *Representation of phase change between CDW (**N**) and SDW (**I**) states in TTF-CA. Lattice displacement q_1 is the site-specific displacement parameter; sites ι are labeled for reference in the equations. Black and white circles represent TTF and CA ions, respectively.* 54
Figure 1-13: *Adapted from Nasu et al, 2001.*[54] ***Top:*** *Calculated energies per site from the Hartree-Fock method for the phases depicted in Figure 1-12. Phase I (SDW; blue dashed) is shown to be the true ground state; both phases are locally stable. Photoexcitation is indicated from the ground state to the Phase N energy surface (CDW; red dotted); the green arrow describes the relaxation along the excited surface.* ***Bottom:*** *Cross-sections of ground (blue dashed) and first excited (red dotted) potential energy surfaces as a function of domain size. After photoexcitation, the system relaxes to a metastable N phase on the excited surface and to the ground-state N phase after exciton relaxation. The three-dimensional valley around the cross-section is indicated for visualization; the functional form for displacement as a function of amplitude and unit cell site is sketched, inset.* 56
Figure 2-1: *Key elements of the laser system used for single-shot spectroscopy measurements. Pulse properties (or their pertinent changes) are summarized between each block diagram element. Not to scale, arrowheads schematically represent wavelength by color, repetition rate by spacing, pulse duration by length, and pulse energy by base width.* 60

Figure 2-2: [A] *Chirped pulse amplification (CPA): an ultrafast pulse is stretched in time, amplified, and then compressed in time to near its original pulse duration.* [B]: *Kerr lens mode-locking (KLM): the optical Kerr effect and an aperture are employed in the oscillator to produce a train of ultrafast pulses.* [C] *Stretcher: group velocity dispersion (GVD) is introduced by varying the path lengths of separated frequencies with a grating, mirror, and curved mirror.* [D] *Amplification: within the amplifier cavity, the 800 nm seed pulse makes many round trips while the crystal is pumped with a single high-energy nanosecond pulse.* [E] *Compressor: GVD is reduced via multiple passes between a grating and retro-reflectors.* 61
Figure 2-3: *Mechanism of a regenerative amplifier in a simplified cavity. A pulse is rejected from (or trapped inside) the cavity by switching off (on) the left-most Pockels cell, rendering the polarization changed (unchanged) after two passes and consequently reflected (transmitted) by the polarizer while the right-most Pockels cell remains off. Multiple round-trips are made, and the right-most Pockels cell is switched on to change the polarization after two passes and dump the amplified pulse from the cavity.* 63
Figure 2-4: *Energy-level picture of second-order optical processes for new frequency generation. Green shading indicates incident photons; yellow shading indicates emitted photons.* [A]: *SHG of 800 nm light to 400 nm, a special case of SFG.* [B]: *In parametric amplification, one DFG mechanism is favored, and we amplify a chosen seed frequency* ω_2. 66
Figure 2-5: *Concept of the dual-echelon single-shot measurement. A beam is passed through a thin echelon with 15μm steps running down and a thick echelon with 300μm steps running across, imparting relative time delays of 22.7 and 453 fs, respectively, and a total time window of 9.1 ps across 400 pulses. The beam array is eventually imaged onto a CCD camera, as shown on right.* 69
Figure 2-6: *Experimental implementation of the dual-echelon time-dependent probe concept. The probe pulse is expanded and the center is collimated before echelon grid formation. The spatio-temporal grid of pulses is formed and focused onto the sample by a lens. The sample experiences a stream of pulses at the same location, and the pulse grid is then reconstructed onto a CCD detector. A strong pump pulse is indicated preceding the probe pulse train.* 70
Figure 2-7: *Schematic illustration of the single-shot instrument after pulse generation and compression. The pulse energy is split along pump and probe paths of varying relative path lengths. The probe beam is expanded and separated into a spatio-temporal grid via crossed echelons. A reference grid is split off from the probe, and both grids are imaged onto a CCD detector. The layout is shown in the reflection geometry; Figure 2-9 shows both reflection and transmission options.* 71
Figure 2-8: *Two-pump setup. An 800 nm pump is split into two pumps using a series of beam-splitters and retro-reflectors. The path of pump 1, which retains most of the incoming power, is shown in red; the path of pump 2, which acts as a weak perturbation, is shown in purple. Both pulses are 800 nm; color is for clarity. A single pass through a half-wave plate (pump 1) and a double-pass through a quarter-wave plate (pump 2), when paired with a polarizer, provides independent power attenuation.* 73
Figure 2-9: *Optical layout after generation of the echelon array. The reference path is shaded in purple. The signal grid travels in either the reflection (shaded in green) or transmission geometry (shaded in yellow) depending on the measurement details. A flip mirror activated for reflection mode enables easy switching. The CCD camera sits at the imaging plane for all three imaging systems shown. Focal lengths are not drawn to scale.* 76
Figure 2-10: *Centermost part of pump's focused Gaussian intensity (with a focused beam radius at* $1/e^2$ *intensity of 500μm). The open black square shows the focused probe region. At this pump size and for near-perfect overlap, each probe pulse sees up to a 2% variation in pump intensity.* 77
Figure 2-11: *ORCA-ER spectral response curve shows the camera's quantum efficiency under high light conditions. From Hamamatsu Corporation. Available online: http://www.spectracore.com/cameras/pdf/QECurves.pdf* 79
Figure 2-12: *Connectivity diagram for the laser system and single-shot instrument. Curved black lines show physical connections. Dotted blue lines indicated synchronized processes in the laser system described in §2.1.1. Dashed red arrows indicate the sending of TTL pulses that facilitate the single-shot measurement. Numerals indicate an approximate time-ordering of signals; this time-ordering is set by the delay generators and the LabView acquisition code.* 83
Figure 2-13: *Pulse ordering for a single-shot measurement. Shaded in yellow is the first iteration without pump for a background image; shaded in green is the second iteration with pump for a data image. Circled are the two trigger pulses that launch the process. The exposure window is shown as a red rectangle, its width set by the computer program. The 10 Hz pulse train and the admitted single pulses for measurement are shown as photodiode traces on an oscilloscope; detected laser pulses are shown as photodiode traces downstream of the shutters.* 84
Figure 2-14: *Pair of images with (data) and without (background) pump pulse, each containing a signal and reference array that derive from the same laser pulse. Blue arrows mark key difference between the grid arrays that are exploited in image analysis.* 86

Figure 2-15: *Top: the result of dividing the data image by the background image (after discarding values under threshold). The pump arrival is visible in the 3rd echelon column of the signal image. Bottom: a coarse view along the columns of the thick echelon show the material response in 453 fs steps.* 88
Figure 2-16: *Image processing steps. After obtaining the divided image, the signal and reference arrays are separately processed. Pixel-averaging yields 20x20 matrices from the signal and reference arrays. Their quotient minus unity gives the time-dependent material response when unfolded into one dimension.* 89
Figure 2-17: *$\sqrt{N}$ improvement in baseline noise is observed when the number of measurements N is increased. Acquiring 10 single–shot measurements allows significant improvement of the noise level while still preserving the integrity of real-time near-threshold dynamics measurements.* 90
Table 3-1: *Sample response pixel detection for full and half dynamic range (DR)* 94
Figure 3-1: *Illustration of orders of magnitude in signal detection.* [A] *Sample signal, exhibiting a 0.7% differential reflectivity change.* [B] *The result of averaging each grid point of the divided image (signal/background) illustrates the baseline and signal locations on the grid.* [C] *The data image signal matrix yields a difference of 29 counts, adjusted to 27 when corrected by the difference between data and background images* [D]. 95
Figure 3-2: *The pixel-by-pixel standard deviation across 20 images taken at a rate of about 1 Hz. The experimental acquisition rate is 0.8 Hz.* 98
Figure 3-3: [A] *Signal obtained by averaging over increasingly large fraction of pixels per square, from 10% (top) to near 100% (bottom).* [B] *Standard deviation of last 2 picoseconds of data as a function of the number of averaged pixels per square* 99
Figure 3-4: *The reported average over randomly selected pixel squares is shown as a function of pixel area averaged. The instance seen to change most appreciably as the number of averaged pixels increases beyond ~300 is [10,4], which corresponds to 1.6 ps—in this data, the time of a strong pump response* 100
Figure 3-5: *The signal side of a divided image (data image / background image) shows strong variations in each grid square during the time of the electronic rise in the data (1.3 to 1.6 ps), and moderate but distinct variations after 1.6 ps.* 101
Figure 3-6: *Unfolded traces of the image in Figure 3-5 derived from the average of pixel values in each grid point (top) and the standard deviation of pixel values in each grid point (bottom). The dashed line is a guide to the eye placed on the rising edge of both time traces* 102
Figure 3-7: *Power of input Gaussian beam of radius 3.35 cm (inset) permitted by an aperture of varying size, determined by integrating under the Gaussian intensity surface (inset). After expansion, the single-shot probe encounters a 1'' diameter aperture (12.7 mm radius) that permits 25% of the power.* 103
Figure 3-8: *Intensity profile of the probe beam across the echelon grid before being focused onto the sample. The beam is ~1 cm across, and its intensity varies up to 6% from the beam center to the corners.* 104
Figure 3-9: *Far-field diffraction patterns from* [A] *a single rectangular aperture,* [B] *3 apertures, one above and one below the original, and* [C] *5 apertures, with 4 placed symmetrically about the original. The values used for center-to-center distances between apertures were equal to the aperture dimensions* 106
Figure 3-10: [A] *Angular phase factors relative to center result from varying path lengths traveled by individual probe beams.* [B] *Transmissive phase factors relative to the first timepoint result from varying thickness of glass in individual probe beam paths. Calculated for 800 nm.* [C] *The sum of the two phase factors defines each beam's phase delay relative to the others. The slight asymmetry present in the angular phase factor distribution is due to numerical rounding from an even number of echelon columns and rows* 107
Figure 3-11: *Time overlap matrices for the grid square [10,10], where each element is formed by the dot products of two Gaussian intensity profiles in time. Left: an input pulse of 100 fs confines the time overlap to a single column of pulses. Right: an input pulse of 400 fs induces very strong overlap over a single column and moderate overlap with the preceding and following columns.* 110
Figure 3-12: *Representative examples of calculated interacting fields $E_{I_{j,i}}$ along the grid array diagonal. Variation in background intensity is observed, as well as structure both in the fringes and the central region.* 111
Figure 3-13: *Examples of calculated grid squares on the camera, the result of taking the inverse Fourier transform of the square of interacting fields at the focus. Examples from the central area are shown along with examples from each corner. The [2,19] square, representative of squares along the corners and edges that have internal structure, is magnified. The area covered by the inner dimension is 50% that of the outer* 112
Figure 3-14: *5×5 echelon grid square detail of a CCD image, showing the first five columns of the last five rows. The section was taken from a signal image in the absence of a pump.* 113
Figure 3-15: *Demonstration of normalization procedure used.* [A] *The isolated field amplitudes were calculated according to Eq. 3-20. Their largest values were computed, and all 400 fields were scaled so that the largest amplitude of any one field was unity.* [B] *Interacting fields, calculated according to Eq. 3-21, result in higher amplitudes due to constructive adding in the time domain.* 114

Figure 3-16: *Calculated average intensities from probe array beam interactions. Each value is the two-dimensional mean of the inverse Fourier transform of the square of the corresponding interacting field—i.e.,* $\mathcal{F}^{-1}\left(|E_{I_{j,i}}(X,Y)|^2\right)$*, examples of which are shown in Figure 3-13. The calculation parameters are specified in each case, separately varying the initial intensity distribution, the pulse duration, and the wavelength.* 115
Figure 3-17: *Calculated intensity standard deviations from probe array beam interactions. Each value is the two-dimensional standard deviation of the inverse Fourier transform of the square of the corresponding interacting field—i.e.,* $\mathcal{F}^{-1}\left(|E_{I_{j,i}}(X,Y)|^2\right)$*, examples of which are shown in Figure 3-13. The calculation parameters are specified in each case, separately varying the initial intensity distribution, the pulse duration, and the wavelength.* 116
Figure 3-18: *[A]: The pixel-averaged reference matrix computed as described in 2.3.3. The large-scale intensity variations are due to the probe intensity profile.* [B]: *The difference of two pixel-averaged reference matrices from separate laser shots shows the variation underneath the probe beam intensity profile. While not ordinarily used in processing, this averaged matrix provides a rough calibration for scaling the averaged values calculated in the probe array simulations.* 117
Figure 3-19: [A]*: A step change in refractive index was introduced for the timepoints shown to simulate a material response to a pump pulse.* [B]*: The largest isolated field amplitude, calculated without beam interactions, demonstrates the effect of a refractive index change confined to specified grid points.* [C]*: Average intensity per grid point under a simulated pump pulse.* [D]*: Standard deviation per grid point under a simulated pump pulse.* 119
Figure 3-20: [A]: *The effect of a simulated pump response on the averages measured at the camera. Shown is the difference of the matrices shown in Figure 3-19 {C}* and *Figure 3-16 {A}.* [B]: *The effect of a simulated pump response on the standard deviations measured at the camera. Shown is the difference of the matrices shown in Figure 3-19 {D} and Figure 3-17 {A}.* [C]: *Unfolded traces of both difference matrices, with time points specifying the first {40} and last {92} perceptible changes, as well as the temporal region of changed refractive index {58-82}.* 120
Figure 4-1: *Structural and electronic configurations typical of mixed-valence metal-halide ground-state chain configurations when coulombic interactions* U *yield the symmetric ground state (top, Mott-Hubbard state, e.g. Ni-Br chains) and when electron-phonon interactions* S *yield the distorted ground state (bottom, Charge Density Wave state, e.g. Pt-Br chains.)* 123
Figure 4-2: *PtI(en) lattice structure with a symmetry-breaking, energy-lowering Peierls distortion of alternating valences and bond lengths. Perchlorate counterions neutralize the overall charge and minimize steric effects while linking parallel chains; ethylenediamine (en) ligands occupy the metal binding sites.* 124
Figure 4-3: *Structure and electronic distribution in the highly localized extreme for the ground state, charge-transfer exciton state, and self-trapped exciton state. (Sourced from [118]).* 126
Figure 4-4: *Spectrogram showing the power spectrum as a function of time and frequency, for the data collected at the lowest pump fluence in Figure 4-6. A time window of 1.95 ps was used. Intensity is centered at the breathing mode frequency near 3.5 THz, with the strongest contribution in the first few picoseconds of measurement time.* ..134
Figure 4-5: *Two representative spectrograms constructed from the same data trace (lowest pump fluence in Figure 4-6, 0.2 mJ/cm²). On the left a time window of 0.9 ps was used; on the right a time window of 5 ps was used. While the frequency resolution from the wider time window is excellent, in our case the loss of time resolution is costly because the frequency is expected to change perceptibly within a few vibration cycles.* 135
Figure 4-6: *Reflectivity response of PtI(en) versus time for pump fluences between 0.20 and 1.6 mJ/cm². Fourier spectra are inset, showing a time-averaged 3.6 THz frequency for the launched mode.* 137
Figure 4-7: *The electronic amplitudes resulting from exponential decay fits to the data in Figure 4-6 are shown as functions of pump fluence. A single exponential fit was found to be sufficient for pump fluences below 0.6 mJ/cm²; above this fluence a biexponential fit was used. Increasingly negative amplitudes are observed for both fit parameters, with the second amplitude decreasing only slightly within error.* 138
Figure 4-8: *The decay times resulting from exponential decay fits to the data in Figure 4-6 are shown as functions of pump fluence. A single exponential fit was found to be sufficient for pump fluences below 0.6 mJ/cm²; above this fluence a biexponential fit was used. The first decay time is near constant with fluence, while the second increases.* 139
Figure 4-9: *Signal amplitudes based on exponential fit scaled by pump fluence, exhibiting a maximum in multi-exciton effects at 0.31 mJ/cm². Reflectivity traces from Figure 4-6 and scaled by incident pump fluence are also displayed.* 140
Figure 4-10: [A]: *Oscillatory components extracted by subtracting exponential fits from the raw data.* [B]: *Normalized Fourier peaks at the main STE lattice frequency.* [C]: *Full non-normalized spectrum with experimental frequency steps of 0.2 THz.* 141
Figure 4-11: *Low-frequency mode observed from conventional pump-probe measurements (color axis is normalized for each plot so that the color codes ranges from 0 (blue) to 1 (red) across 2D plots). The time and frequency axes are identical in all 2D plots. A mode at 1.7 THz is present at the lowest fluence, blue-shifting slightly (to 1.8 THz) for slightly increased fluence but losing its distinct shape upon further increasing fluence. At the highest fluences*

shown here, a low-frequency band is observed that peaks at 1.9 THz. Non-normalized early-time cross-sections (lower left-hand plots) suggest two modes are present. 142
Figure 4-12: *'Instantaneous' (earliest measureable STFT time) breathing mode frequency in PtI(en) extracted from conventional pump-probe measurements (time window = 1.95 ps)* 143
Figure 4-13: *[A]: Reflectivity response of PtI(en) versus time for pump fluences between 1.6 and 9.4 mJ/cm². [B]: Reflectivity response of PtI(en) versus time for 1.6 mJ/cm² pump fluence. In each case, the measurement was taken on the sample region that was previously irradiated with the indicated fluence. The bottom curve, from 1.6 mJ/cm² on a fresh sample spot, is re-plotted from Figure 4-6 for reference.* 144
Figure 4-14: *Single-shot differential reflectivity of PtI(en) versus time, showing fast dephasing at higher pump fluences. The data are offset for ease of comparison.* 145
Figure 4-15: *The electronic amplitudes resulting from biexponential decay fits to the data in Figure 4-14 are shown as functions of pump fluence. The first amplitude increases until 2.5 mJ/cm² and then decreases; the second increases with fluence.* 146
Figure 4-16: *The short-lived electronic component decay time resulting from biexponential decay fits to the data in Figure 4-14 is shown as a function of pump fluence. The decay, of <1 ps, is relatively constant with fluence within error.* 147
Figure 4-17: *Single-shot differential reflectivity of PtI(en) versus time, with the y-axis scaled by incident number of photons (fluence). Scaled signals increase with increasing fluence until 4.5 mJ/cm², and the scaled signal drops off sharply for the highest fluence, 12 mJ/cm².* 147
Figure 4-18: [A]: *Oscillatory components of single-shot data shown in Figure 4-14 obtained by subtraction of biexponential fits to the electronic background.* [B]: *The normalized STE lattice mode peaks from the single-shot data through 2.5 mJ/cm²* 148
Figure 4-19: *'Instantaneous' (earliest measureable STFT time) breathing mode frequency in PtI(en) extracted from single-shot measurements (time window = 1.7 ps). Significant red-shifting is observed as fluence increases, and the peak is broadened, indicating faster dephasing or a broader range of frequencies.* 149
Figure 4-20: *Summary of single-shot one-pump results in the regime of high excitation density. Top: Relative phonon amplitude (oscillatory amplitude relative to electronic amplitude). Middle: STE phonon frequency. Bottom: Phonon frequency dephasing time. No oscillation is reported for the 12 mJ/cm² data, but a dotted line is shown to emphasize the trend.* 150
Figure 4-21: *Reflectivity versus probe window time for time delays Δt (4 ps through infinity) after a 1.4 mJ/cm² pump pulse* 152
Figure 4-22: *Reflectivity versus probe window time for time delays Δt (3 ps through infinity) after a 4.5 mJ/cm² pump pulse* 153
Figure 4-23: *Reflectivity versus probe window time for time delays Δt (3 ps through infinity) after a 12 mJ/cm² pump pulse* 153
Figure 4-24: *Instantaneous frequencies from two-pump data of varying initial pump fluences and interpump time delays. A time window of 1.7 ps was used, which corresponds to the first 1.7 ps of the probe window following excitation. At higher initial fluences, the frequency is significantly red-shifted after Δt ~ 3.5 ps after the initial pump pulse, and the recovery to ground-state levels is on the order of hundreds of picoseconds. In addition, the mode is broad and exhibits lower-frequency structure at the earliest interpump delay times.* 154
Figure 4-25: *Single-shot two-pump results. Amplitudes, phonon frequencies, and phonon dephasing times versus Δt for each of the above three pump fluences. The amplitudes of oscillations launched by a fixed pump fluence are directly comparable to one another.* 155
Figure 4-26: *Charged kink defect, projected to have a frequency roughly 56% below the ground-state Raman stretching mode.* 158
Figure 4-27: *Absolute value of initial reflectivity change versus calculated absorbed photons per Platinum atom (magenta). The same data are scaled by incident fluence to emphasize regions deviating from linear behavior (blue). Both dashed lines indicate the behavior that is expected for isolated, non-interacting excitations yielding signal in the linear regime. Each point on a given line is derived from the initial t=0 rise of the conventional pump-probe and the single-shot data.* 164
Figure 4-28: *Added initial signal per additional absorbed photon. The initial signal responses are plotted cumulatively. The dashed line indicates approximate expected linear behavior in the non-interacting regime.* 165
Figure 4-29: *Added initial signal versus the distance to the next-nearest excitation along a single chain, estimated by experimental conditions and PtI(en) lattice parameters. The initial signal responses are plotted cumulatively.* 166
Figure 5-1: *The bismuth lattice unit cell has a distorted face-centered cubic structure due to a symmetry-breaking energy-lowering Peierls distortion. From Murray et al., 2005:[159] The potential energy surface of bismuth, calculated via density functional theory, exhibits a double-well in the ground state. When a sizeable fraction of valence*

electrons (~3%) are excited, the calculated surface exhibits a double well corresponding to the structurally symmetric state. 175
Figure 5-2: *From Murray et al., 2005.[159] Frequency versus fraction of valence electrons excited, calculated by the frozen phonon method. The harmonic frequency is highlighted by the red dashed curve, and is calculated from the potential energy surface in Figure 5-1 from the same reference.* 176
Figure 5-3: *From Fritz et al., 2007.[40] Left: Bismuth potential energy surface contour superimposed with results from x-ray diffraction measurements (red circles) that report on the fractional lattice spacing and indicate a harmonic potential up to 2% carrier density. Right: optical phonon measurements, conducted simultaneously with the x-ray diffraction measurements, enable a mapping between frequency and carrier density.* 177
Figure 5-4: *From Sciaini, et al., 2009.[62] Laser-induced melting of a 30 nm bismuth film was demonstrated via electron diffraction measurements, at high excitation and with 200 fs laser pulses, and reported to occur in less than the time of a vibrational period.* 178
Figure 5-5: *Adapted from Melnikov, et al.[178] Key symmetry points in the bismuth electronic band diagram. Optical transitions near the Γ point create carriers that collect near the T symmetry point (highlighted in red). This electronic population is thought to couple strongly with the A_{1g} lattice mode. The indirect band overlap is highlighted in blue, and occurs between the L conduction band minimum and the T valence band maximum. Thermal transitions cause the buildup of carriers near the L point, which is expected to have minimal coupling with the optical phonon mode.* 180
Figure 5-6: *Single-shot reflectivity response of bulk bismuth at 800 nm for a pump fluence range of 1.5 to 35.5 mJ/cm^2. The red dashed line indicates pump arrival at 0 ps. The blue dashed line is a guide to the eye to emphasize the perceptible frequency down-shift upon increasing fluence.* 183
Figure 5-7: *Short-time (<10 ps) electronic component* A *extracted by fitting the bulk data in Figure 5-6 to Eq. 5-1. The amplitude is shown in green, and the amplitude scaled by incident fluence is shown in purple, also inset. The positive short-time electronic amplitude per incident photon decreases up to ~20 mJ/cm^2, and then plateaus.* 184
Figure 5-8: *Long-time (>10 ps) electronic component* B *extracted by fitting the bulk data in Figure 5-6 to Eq. 5-1. The amplitude is shown in green, and the amplitude scaled by incident fluence is shown in purple, also inset. The long-time electronic amplitude per incident photon increases near-linearly for all fluences measured.* 185
Figure 5-9: *Single-shot reflectivity response of 300 nm bismuth film for a pump fluence range of 0.566 to 48.6 mJ/cm^2. The red dashed line indicates pump arrival at 0 ps. The blue dashed line is a guide to the eye to emphasize the perceptible frequency down-shift upon increasing fluence.* 186
Figure 5-10: *Response of the 500 nm film to the highest fluence employed in our single-shot measurements: 57 mJ/cm^2. The reflectivity drops below the pre-pump level after a few picoseconds and does not recover within the probe time window. No oscillations are visible.* 187
Figure 5-11: *Short-time (<10 ps) electronic component* A *extracted by fitting the 300 nm data in Figure 5-9 to Eq. 5-1. The amplitude is shown in green, and the amplitude scaled by incident fluence is shown in purple, also inset. The positive short-time electronic amplitude per incident photon decreases up to ~10 mJ/cm^2, and then plateaus.* 187
Figure 5-12: *Long-time (> 10 ps) electronic component* B *extracted by fitting the 300 nm data in Figure 5-9 to Eq. 5-1. The amplitude is shown in green, and the amplitude scaled by incident fluence is shown in purple, also inset. The long-time electronic amplitude per incident photon increases, then plateaus above 20 mJ/cm^2.* 188
Figure 5-13: *Measured phonon frequency for a range of pump fluences in 300 nm bismuth films. We observe decreasing frequency with a sharp drop above 30 mJ/cm^2. No phonon signal was resolvable in the highest fluence measurement (57 mJ/cm^2), the data for which is shown in Figure 5-10.* 189
Figure 5-14: *Single-shot reflectivity response of 50 nm bismuth film for a pump fluence range of 2.6 to 9.4 mJ/cm^2. The red dashed line indicates pump arrival at 0 ps. The blue dashed line is a guide to the eye to emphasize the perceptible frequency down-shift upon increasing fluence.* 190
Figure 5-15: *Short-time (<10 ps) electronic component* A *extracted by fitting the 50 nm data in Figure 5-14 to Eq. 5-1. The amplitude is shown in green, and the amplitude scaled by incident fluence is shown in purple, also inset. The positive short-time electronic amplitude per incident photon increases up to ~5 mJ/cm^2, and then plateaus.* 191
Figure 5-16: *Long-time (>10 ps) electronic component* B *extracted by fitting the 50 nm data in Figure 5-14 to Eq. 5-1. The amplitude is shown in green, and the amplitude scaled by incident fluence is shown in purple, also inset. The long-time electronic amplitude per incident photon increases, then plateaus above 8 mJ/cm^2.* 192
Figure 5-17: *Measured phonon frequency for a range of pump fluences in 50 nm bismuth films. We observe decreasing frequency with a sharp drop above 5 mJ/cm^2. The highest fluence measurement yields a frequency below or 2 THz. The measurement at 8.5 mJ/cm^2 fluence is the highest fluence which yields a well-resolved frequency.* 193
Figure 5-18: *The absolute value of the instantaneous reflectivity response for pump arrival is shown for each sample. The value is defined as the maximum (bulk and 300 nm) or minimum (50 nm) $\Delta R/R$ value reached relative to the pre-pump baseline in the first 1 ps.* 194

Figure 5-19: *Composite time trace derived from multiple single-shot measurements on 300 nm bismuth film after varying time delays following excitation by a 26 mJ/cm^2 fluence pump pulse. Variations over individual 9.5 ps snapshots are due to variation over the echelon profiles, and do not bear physical meaning in interpreting the signal.* 195
Figure 5-20: *Composite time traces collected from multiple single-shot measurements of varying time delays on the 300 nm sample. The ~10 ps response increases with fluence beyond the level visible by our 9.5 ps probe pulse, and recovers by 25-50 ps for most fluences measured. Colors for a given composite time trace indicate consecutive measurements.* 196
Figure 5-21: *Emphasis on the 100-800 ps reflectivity evolution of 300 nm bismuth data shown in Figure 5-23, with instrumental error of 0.001%.* 197
Figure 5-22: *Composite time traces collected from multiple single-shot measurements of varying time delays on the 50 nm sample. The response increases toward the pre-pump level for 10-15 ps and remains relatively unchanged through 100 ps except for the acoustic strain pulse. Colors for a given composite time trace indicate consecutive measurements.* 198
Figure 5-23: *Summary of timescales of interest in bismuth single-shot measurements for two samples: a 300 nm film (top), which approximates a three-dimensional environment, and a 50 nm film (bottom), which approximates a two-dimensional environment. The 300 nm traces were collected out to 800 ps, and are displayed on a log time scale in the main figure (linear scale: inset). Both samples exhibit an instantaneous response on the order of 500 fs (red), an early-time recovery on the order of 10-15 ps (orange), and long-time dynamics past 20-50 ps (blue). We observe an intermediate relaxation stage in the 300 nm sample onset at 10 ps with a ~15 ps time constant (green).* 199
Figure 5-24: *Representative two-pump measurements on 300 nm bismuth film across different excitation fluences and measurement time delays. Left: the photoexcited state is probed 3 ps after excitation by the fluence indicated. Qualitatively, we observe the familiar lattice response below 20 mJ/cm^2 excitation. Above this excitation, the measurement does not identify lattice vibrations 3 ps after photoexcitation. Right: the highly photoexcited state is probed at varying time delays. We see oscillations after 3 ps, and the response resembles the ground-state excitation response after ~400 ps.* 202
Figure 5-25: *Electronic amplitudes extracted from two-pump measurements on 300 nm bismuth at varying time delays and degrees of photoexcitation. The first 100 ps are shown.* 203
Figure 5-26: *Electronic amplitudes extracted from two-pump measurements on 300 nm bismuth at varying time delays and degrees of photoexcitation. The full 800 ps are shown.* 204
Figure 5-27: *Phonon frequency extracted from two-pump measurements on 300 nm bismuth at varying time delays and after varying degrees of photoexcitation. The first 100 ps are shown.* 205
Figure 5-28: *Phonon frequency extracted from two-pump measurements on 300 nm bismuth at varying time delays and after varying degrees of photoexcitation. The full 800 ps are shown.* 205
Figure 5-29: *Representative two-pump measurements on 50 nm bismuth film across different excitation fluences and measurement time delays. Left: the photoexcited state is probed from 3 to 100 ps after excitation by a moderate fluence, 4.5 mJ/cm^2. Right: the photoexcited state is probed from 3 to 100 ps following excitation at a high fluence, 9.5 mJ/cm^2.* 206
Figure 5-30: *Electronic amplitudes extracted from two-pump measurements on 50 nm bismuth at varying time delays (0-100 ps) and after varying degrees of photoexcitation.* 207
Figure 5-31: *Phonon frequency extracted from two-pump measurements on 50 nm bismuth at varying time delays (0-100 ps) and after varying degrees of photoexcitation.* 208
Figure 5-32: *Comparison of the effects of similar incident fluence on the photoexcited state lattice response in 300 nm and 50 nm bismuth films. The thinner film exhibits a more dramatic frequency reduction, and recovers more slowly, than does the thicker film for comparable incident pulse fluences.* 209
Figure 5-33: *Comparison of lattice frequency after the highest photoexcitation fluence (as determined by the disappearance of phonon oscillations in one-pump measurements). The initial 300 nm film lattice recovery time appears to be less then 20 ps, while that of the 50 nm film appears to be ~20 ps. The long-time reflectivity responses are inset for each sample-fluence pair for comparison of timescales.* 210
Figure 5-34: *Carrier densities are interpolated based on the frequency of each measurement. The dashed curved line is the calculated frequency as a function of carrier density from Figure 5-2. Horizontal lines among the low-frequency data connect the two resulting estimates from one single-shot measurement.* 212
Figure 5-35: *The solutions to coupled differential equations of the two-temperature model with diffusion and electron-phonon coupling for the first 100 picoseconds (y-axis) in a 300 nm (x-axis) bismuth film under 8 mJ/cm^2 excitation. Initial electron density is given by the laser source with temporal and spatial profiles determined experimentally. The color indicates the value of the relevant property as a function of time and depth: electron density (top), electron temperature (middle), and lattice temperature (bottom).* 216

Figure 5-36: *The solution to the simple two temperature model for the lattice temperature in a 300 nm bismuth film under 8 mJ/cm^2 excitation is shown out to 200 ps. The solution calculates an extended heating time that is not consistent with our experimental data.....217*
Figure 5-37: *Composite long-time traces of 300 nm film under 7.9 mJ/cm^2 excitation suggest that the calculation shown in Figure 5-36 overestimates the lattice heating time. Near full recovery is observed by 100 ps, with very slowly varying reflecitivity modulation past 100 ps. 218*
Figure 5-38: *Demonstration of integrating calculated surfaces for lattice temperature into the sample depth to simulate the effect of an optical probe pulse reporting on material dynamics. Here, the difference in reported lattice temperature using the two methods is about 400 K. 219*
Figure 5-39: *Solutions to the coupled differential equations modified to include electron-hole recombination, with multiple recombination times displayed. The input parameters were for a 300 nm bismuth film under 8 mJ/cm^2 excitation.....221*
Figure 5-40: *Calculated relation from Arnaud, et al.[191] giving the electron-phonon coupling constant as a function of electron temperature. The quantity is predicted to rise significantly with electron temperature. Red markers indicate correspondence to the electron diffraction results that reported sub-picosecond melting in bismuth.[62] The correspondence was established numerically by relating the electron-phonon coupling constant in the calculation to Debye-Waller factors extracted from the diffraction peaks in the experiment.....222*
Figure 5-41: *Demonstration of the effect of varying the electron phonon coupling constant g in the 300 nm film calculations at low fluence. The lattice heating time, the maximum temperature reached, and the rate of electronic relaxation are all dependent on the order of magnitude of g. In the calculations presented below, we use the temperature-dependent g(T_e) presented by Arnaud, et al.[191] The room temperature value is ~10^{-27} J/(ps nm^3 K) (yielding the green curve). 223*
Figure 5-42: *Demonstration of the effect of varying the electron phonon coupling constant g in the 300 nm film calculations at high fluence. The lattice heating time, the maximum temperature reached, and the rate of electronic relaxation are all dependent on the order of magnitude of g. In the calculations presented below, we use the temperature-dependent g(T_e) presented by Arnaud, et al.[191] The room temperature value is ~10^{-27} J/(ps nm^3 K) (yielding the green curve). 224*
Figure 5-43: *The interpolated carrier density from measured frequency (green) in 50 nm film measurements is compared to expected carrier densities resulting from varying carrier diffusivities. A value of ~7-8 cm^2/s is expected by extrapolation of the results by Sheu, et al. A diffusitivity of 7 cm^2/s is chosen by comparison of its slope with the measured quantity. 225*
Figure 5-44: *The interpolated carrier density from measured frequency (green) in 300 nm film measurements is compared to expected carrier densities resulting from varying carrier diffusivities. Diffusivities up to ten times the literature value fail to describe the measured phonon frequency 500 fs post-pulse, suggesting the contribution of ballistic transport to the carrier density at 500 fs.....226*
Figure 5-45: *The interpolated carrier density from measured frequency (green) in 300 nm film measurements is compared to expected carrier densities resulting from sub-picosecond ballistic transport. The ballistic population is allowed to propagate for 100, 200, and 300 fs before diffusion is onset. The result with no ballistic transport and a diffusivity value of 24 cm/^{2} is also shown.....228*
Figure 5-46: *The solutions to the coupled differential equations for a 300 nm bismuth film under varying degrees of excitation, with all modifications proposed in this section, for carrier density (left), and electron temperature change (right).....229*
Figure 5-47: *The lattice temperature solution to the coupled differential equations for a 300 nm bismuth film under varying degrees of excitation, with all modifications proposed in this section. Left: first 100 ps of evolution. Right: first 5 ns of evolution. 230*
Figure 5-48: *The solutions to the coupled differential equations for a 50 nm bismuth film under varying degrees of excitation, with all modifications proposed in this section, for carrier density (left), electron temperature change (middle), and lattice temperature change (right).....231*
Figure 5-49*: Left: Calculated short-time decay component amplitude (corresponding to <10 ps) of the carrier density for the 50 nm film (top) and the 300 nm film (bottom). Right: The measured short-time decay component amplitude of the reflectivity for both samples. The displayed calculated quantity may be a dominant contributor to the measured quantity. 234*
Figure 5-50: *Calculated maximum lattice temperature change scaled by fluence (left) for the 50 nm film (top) and the 300 nm film (bottom) as calculated from Figure 5-47 Figure 5-48 (green) and with consideration of the enthalpy of melting on the temperature change (blue). At right is the measured >10 ps electronic component amplitude scaled by fluence for each sample. This comparison suggests melting in the 50 nm case, but not in the 300 nm case.....235*
Figure 5-51*: Response of 300 nm bismuth film to strong initial excitation (top) and subsequent weak perturbation (bottom) at 0, 3, 5, and 10 ps. Blue-shifting of the measured frequency is observable within the first few picoseconds,*

indicating a rapid reduction in the carrier density that may prevent measurement of a transient symmetric crystalline phase. With ballistic transport, the carrier population is estimated to be reduced from 5.9% to 2.2% within 100 fs. 238
***Figure 5-52**: Early-time response to a second pump pulse after strong excitation in 50 nm (magenta) and 300 nm (black) bismuth thin films. A conservative indication of the instrumental noise, 0.002, is shown relative to the height of one oscillation. Oscillations in the 300 nm film are visible at all delays; oscillations in the 50 nm film are not visible until after 20 ps.* 240
***Figure 5-53:** For the 50 nm film, the percent latent heat per volume element provided by the laser pulse (past the melting temperature) is shown (blue, left axis). The approximate lattice displacement for the upper fluence range is also shown, and nears the 10% Lindemann melting criterion at the highest employed fluence (purple, right axis).* 241

Chapter 1

Introduction and Background

Light-matter interactions underlie key processes of our everyday life, from photosynthesis and vision to fiber optics and diode devices. The former examples occur in nature, and our quests to understand and reproduce these amazing phenomena have deepened our understanding of the complex processes at work. The latter have evolved jointly out of advanced understanding of light-matter interactions and the drive for innovative solutions to society's changing needs. For these processes and countless others, even where the fundamental physics is understood, questions and challenges abound—limiting our ability to push technologies further and to describe complexity better.[1-5] In this thesis, we examine fundamental questions about light-matter interactions on a small subset of materials, toward a new regime, via development of a unique experimental technique. This chapter first motivates our focus on solid-state materials and then provides a primer on fundamental light-matter interactions and ultrafast dynamics within materials. We then introduce our experimental technique in the context of standard measurements. Finally, the reader is introduced to phase changes in materials brought about by light with a brief discussion of events far from equilibrium that have motivated this study. The summary and scope of the thesis work are briefly described.

1.1 Toward Material Design

This thesis provides one window into the varied, vast, and promising realm of materials research. The study of materials is inter-disciplinary and far-reaching for good reason. Not only does their study help elucidate and refine core mathematical and physical principles that describe our world, but the potential to engineer materials to fine specification may hold the key to meeting some of our greatest challenges. Peruse compilations of recent top innovations in popular science magazines,[6] or survey the grand challenges set forth by the US Office of Science.[7] Material advances have been fundamental in improvements to computing speed, lightweight transport, medical capabilities, and much more. And by every indication, continued advances in the use of materials will be critical for our needs in defense, computing, healthcare, development, and energy for many decades to come.

Our ability to design and control materials to perform optimally lags behind what we reasonably believe to be possible. To take one example, many low-carbon energy solutions—such as thermoelectrics and photovoltaics—rely on a precisely coordinated energy exchange among light energy, electrons, and lattice vibrations at ultrafast timescales, nanometer length scales, and along quantized energy levels. Our ability to control and tune this exchange more precisely, efficiently, and reliably than is currently possible may well be a crucial difference between affordable, widespread low-carbon energy and promising technologies that never achieve their potentials. [6-10]

Overcoming these gaps will depend on several key parameters, but central among them is a thorough, sophisticated understanding of how materials behave and why, including how energy moves through them. Only with an understanding of the chemistry and physics governing their nature can new materials be engineered for specific properties from the bottom-up. This understanding goes beyond macroscopic measures of material properties (conductivity, strength, density, etc.) and asks about the underlying chemistry and physics of the system. What makes certain chemical bonds form in a given material environment? How do electrons and nuclei interact to yield complex observable properties? How do atoms respond individually and collectively to various stimuli? Do models exist to describe what we measure, and if not, can we build them? How can light or other stimuli be used to control material behavior? How do the

answers to these questions change far from equilibrium, where much physics of interest takes place? This level of questioning is at the heart of this thesis, and the emerging answers are central to the long-term goal of material control.[11]

1.2 Light-Matter Interactions

The tool used here for probing materials at the scale of electrons and nuclei is femtosecond spectroscopy. The principles of electromagnetism and quantum mechanics provide a framework for understanding how electromagnetic radiation and matter interact. Experimentally, femtosecond (10^{-15} seconds) spectroscopy can measure the movement of nuclei and electrons on the timescale that these complex interactions occur within materials. Many fascinating questions exist on this timescale which femtosecond spectroscopy has begun to address. To name just a few, water solvation,[12] bond-making and –breaking with laser pulses,[13] visualization of transition states,[14] and the mechanism of biological proteins[15] are areas that have been explored and advanced with femtosecond science. Still, many opportunities remain, especially with the advent of new experimental capabilities in the X-ray and terahertz (THz) spectral regimes.[16,17]

Spectroscopy is an exploration of the inner workings of materials using light. Because every material absorbs energy differently and measurably, depositing energy into a material is a way to get to know it better. When energy in the form of electromagnetic radiation interacts with materials, we observe characteristic spectra (the response of interest as a function of wavelength or frequency) that inform us about the material's structure, behavior, and core properties. The study of these interactions is the foundation of the field of spectroscopy.

Most natural materials and their alloys have been characterized fully in this manner. Things get more interesting when we can study not only the ground state of a material, but the material's structure, behavior, and core properties under dynamic perturbation. Depositing energy into a material over *a few femtoseconds* with *coherent light* to perturb the system, and measuring an output of the light-matter interaction on the timescale of that interaction, is *ultrafast laser spectroscopy*. By exciting the system, we are moving a material from one state to another. By measuring the system after excitation, we are learning about its structure, behavior, and properties after excitation as a function of time.

When light and matter interact, the material's polarization P scales to first order with the electromagnetic field E as

$$P = \chi \epsilon_0 E \qquad \textit{Eq. 1-1}$$

where χ is the electric susceptibility of the medium and ϵ_0 is the permittivity of free space. In dielectric materials, the electromagnetic field interaction with free charges induces an electric dipole moment characterized as a displacement field D:

$$D = \epsilon_0 E + P \qquad \textit{Eq. 1-2}$$

Since P is a macroscopic property characteristic of materials, it is convenient to define a material-specific permittivity from Eq. 1-2:

$$D = \epsilon_0 \epsilon_r E = \epsilon(\omega) E \qquad \textit{Eq. 1-3}$$

The dielectric permittivity $\epsilon(\omega)$ relates an induced internal electric displacement field to the incident electromagnetic field, effectively characterizing the unique energetic properties of a material system. For the optical frequencies discussed in this thesis, Eq. 1-3 holds for metals as well as dielectric materials.[18] The above equations combine to yield a useful relation:

$$\epsilon_r = 1 + \chi \qquad \textit{Eq. 1-4}$$

Because the dielectric function $\epsilon(\omega)$ offers a full description of the first-order material responce to electromagnetic radiation, measuring optical properties allows insight into material physics. Relating measureable optical changes directly to microscopic phenomena in the time domain is a complex endeavor, and will be a recurring focus of this thesis. We will measure components of the dielectric function, a complex representation of all possible excitations within a solid for a given frequency range, and interpret the excitations being observed. The dielectric function is influenced by such factors as polarization within the crystal, lattice vibrations, carrier absorption and relaxation, exciton generation, and other inter-band transitions. Making changes to the radiation (tuning the laser pulse or other light source) allows an opportunity to access those excitations in different ways. Tuning the material presents the opportunity to investigate different sets of excitations.

In optical spectroscopy experiments, we typically measure changes to the dielectric function via reflectance or absorption. Because of the complexity relating real microscopic phenomena to the dielectric function, various models have been developed to describe the primary sources of induced fields in solid materials. While detailed derivations may be found elsewhere,[19,20] a brief summary of these models is included here to provide context for understanding results presented in subsequent chapters.

1.2.1 Dielectric Function: Bound electrons and lattice vibrations

Fields resulting from bound electrons (electronic excitations) and from charged atom-pair vibrations (lattice excitations) can be modeled by building the dielectric function of a harmonic oscillator. The one-dimensional equation of motion that characterizes an oscillator's response to an external field $E(t)$ in one dimension is

$$m\ddot{x} + m\gamma\dot{x} + m\omega_0^2 x = qEe^{-i\omega t} \qquad \textit{Eq. 1-5}$$

with mass m, damping γ, eigenfrequency ω_0, and electrical charge q. Substituting as a solution $x = x_0 e^{-i\omega t}$ we find

$$x = \frac{e}{m}\frac{Ee^{-i\omega t}}{\omega_0^2 - \omega^2 - i\omega\gamma} \qquad \textit{Eq. 1-6}$$

For each displaced electron, there is a time-varying dipole moment $p(t) = -ex$, and accounting for n oscillators per unit volume (n is the carrier density) yields an overall polarization $P = nex$. Substituting into Eq. 1-1 along with Eq. 1-6, we find the dielectric function for a harmonic oscillator:

$$\epsilon_{osc}(\omega) = 1 + \frac{ne^2}{m\epsilon_0(\omega_0^2 - \omega^2 - i\omega\gamma)} \qquad \textit{Eq. 1-7}$$

The real and imaginary parts of the harmonic oscillator dielectric function are plotted in Figure 1-1 using typical molecular spectroscopy values. For very precise calculations of the dielectric function, and especially when frequencies of interest are far above resonance, it is necessary to account for the polarization from deformed ion cores as derived elsewhere.[19] Inset are the real and imaginary parts of the dielectric function for silicon.[21]

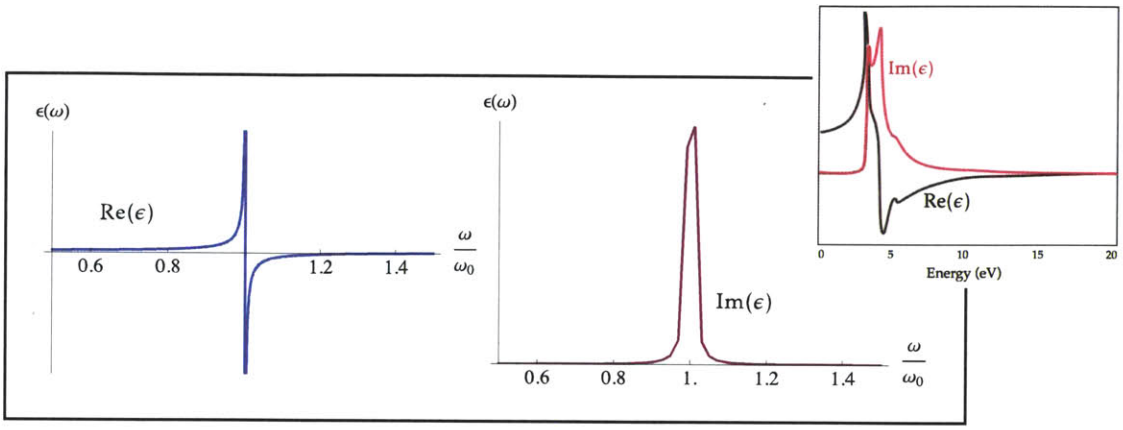

Figure 1-1: Real (left) and imaginary (right) parts of the dielectric function for a generic charged-atom pair harmonic oscillator. For comparison, the same functions for silicon are inset.[21].

1.2.2 Dielectric Function: Free electrons

To evaluate the dielectric function for free electrons and holes, which experience no restoring force when displaced, we can make conceptually straightforward modifications to Eq. 1-5. With no oscillating dipole, $\omega_0 = 0$. Further, $\dot{x}$ can be replaced with a characteristic velocity v, and the damping constant γ with an inverse collision time $1/\tau$. Here the relevant response function is current density per volume:

$$j(t) = ne\dot{x}(t) \qquad \textit{Eq. 1-8}$$

From Eq. 1-1,

$$j = \frac{\delta P}{\delta t} = \chi\epsilon_0\frac{\delta E}{\delta t} = -\chi\epsilon_0 i\omega E \qquad \textit{Eq. 1-9}$$

Using the relation $J = \sigma E$, the complex conductivity is related to the permittivity by

$$\sigma(\omega) = -i\omega\epsilon_0\chi(\omega) \qquad \textit{Eq. 1-10}$$

and using Eq. 1-4, the dielectric function can be expressed as

$$\epsilon(\omega) = 1 + \frac{i\sigma(\omega)}{\epsilon_0\omega} \qquad \textit{Eq. 1-11}$$

Evaluating the current density using the same solution for Eq. 1-9 shown in Eq. 1-6, the dielectric function for free carriers can be evaluated:

$$\epsilon_{carrier}(\omega) = 1 - \frac{ne^2}{\epsilon_0 m(\omega^2 + i\omega/\tau)} \qquad \textit{Eq. 1-12}$$

This relation, when expressed in terms of conductivity, yields the Drude model of conductivity of a free electron gas: (plotted in Figure 1-2, with experimentally verified calculations for Si inset.[22])

$$\sigma(\omega) = \frac{ne^2\tau}{m(1 - i\omega\tau)} \qquad \textit{Eq. 1-13}$$

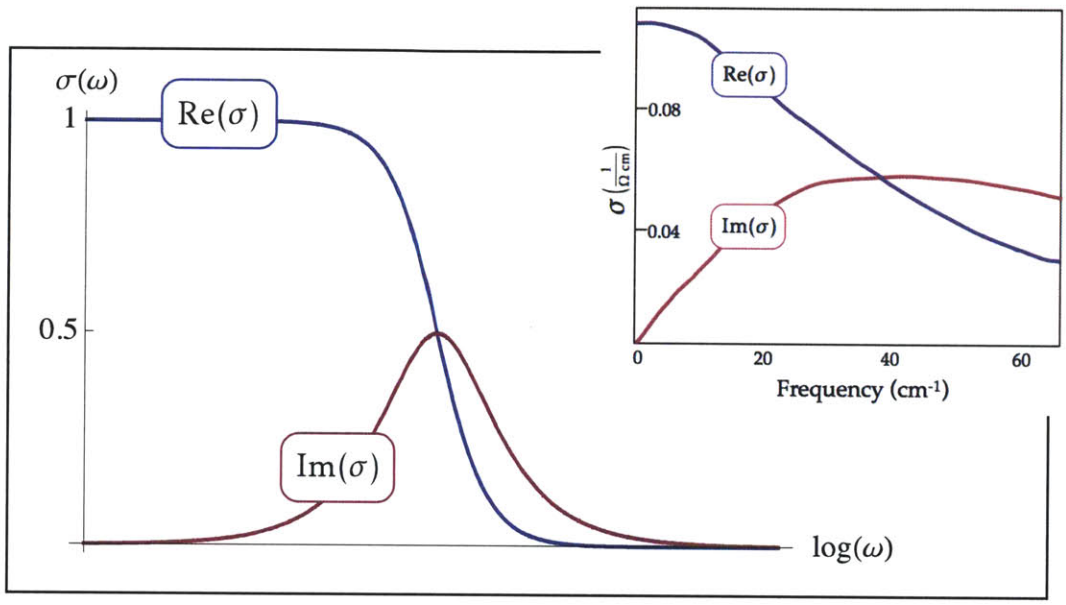

Figure 1-2: Real and imaginary parts of the conductivity for unbound carriers. For comparison, the same functions for weakly-doped silicon are inset.[22]

1.2.3 Observing the Complex Dielectric Function

In order to relate the complex dielectric function and the complex conductivity to observables that we can measure in the lab, we define the complex index of refraction $N(\omega)$ in terms of the index of refraction η and extinction coefficient κ

$$N = \eta + i\kappa \qquad \textit{Eq. 1-14}$$

such that

$$\epsilon = \epsilon_r + i\epsilon_i = (\eta + i\kappa)^2 \qquad \textit{Eq. 1-15}$$

For a given wavelength of light λ, the extinction coefficient is related to the absorption coefficient via

$$\alpha = \frac{4\pi\kappa}{\lambda} \qquad \textit{Eq. 1-16}$$

When a wave is incident on a surface, Maxwell's equation

$$\nabla \times \bar{E} = -\frac{1}{c}\frac{\partial \bar{B}}{\partial t} \qquad \textit{Eq. 1-17}$$

combined with the plane wave solution $\bar{E} = E_0 e^{i(\bar{K}\cdot\bar{r}-\omega t)}$, $K_0 = \omega\sqrt{\epsilon\mu}/c$ and requirement for continuity at the surface interface for the $\bar{B}$ field yields the normal-incidence reflectivity coefficient $\mathcal{R}$ which we measure as the percent of incident power that is reflected from the surface:

$$\mathcal{R} = \left|\frac{1-N}{1+N}\right|^2 = \frac{(1-\eta)^2+\kappa^2}{(1+\eta)^2+\kappa^2} \qquad \textit{Eq. 1-18}$$

Additionally, energy conservation yields the simple relation $\mathcal{R} + \mathcal{A} + \mathcal{T} = 1$, where the LHS terms indicate the fraction of incident power that is reflected, absorbed, and transmitted, respectively.

We have related the optical constants, and thus the dielectric function, to the observable material reflectivity. In order to obtain the optical constants from reflectivity measurements, two independent measurements are taken (e.g. at different incident angles). Alternatively, the optical constants η and κ can be calculated from normal incidence if the entire frequency range is scanned, because the two quantities are related by the Kramers-Kronig relation. For a more in-depth discussion of these methods, see Yu and Cardona, 2010.[21] In a qualitative sense, one can typically observe the features inherent to both the reflectance and, especially, ϵ_i. A reflectance measurement for silicon at room temperature is shown in Figure 1-3.

For semiconductors like silicon, the reflectivity rises substantially at the frequency of the fundamental absorption edge, a characteristic electronic transition of semiconductors discussed below. At higher energies (frequencies), the structure is determined by the contributions of many other transitions. At lower energies, the reflectance is smoother, and is dominated by the contribution of free carriers. This can be described as classical conductivity, and is easily seen by noting the inverse dependence of σ on ω in Eq. 1-13 and likewise the form of Eq. 1-12, which describes the carrier contribution to the dielectric function. At low frequencies, carrier absorption dominates the dielectric function; at higher frequencies, electronic transitions dominate

the dielectric function instead. The frequency at which the character changes is called the plasma frequency ω_p, and is formally defined as the frequency at which $\epsilon_r = 0$. From this framework, we can measure reflectance (or another optical property) at a specific wavelength in the time domain under perturbation, and know what processes are expected to be contributing to the observed changes as a function of time.

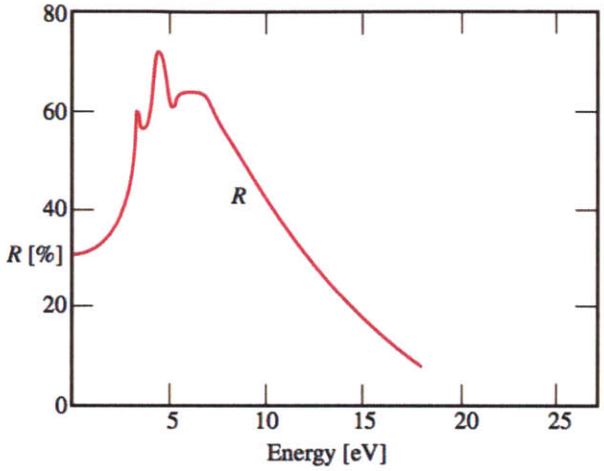

Figure 1-3: Reflectance of silicon as a function of frequency (energy) measured at normal incidence and at room temperature.[21] Compare to the inset in Figure 1-1.

1.2.4 Relating Observables to Microscopic Events

So far we have considered optical properties of solids using classical electromagnetism. But to relate the complex dielectric function and complex conductivity to microscopic events, we turn to quantum mechanics. To illustrate the above assertion that the dielectric function contains information about all excitations within a system, a schematic of the absorption coefficient versus excitation energy for solids in general is shown in Figure 1-4. In the work presented here, we will be concerned with excitations in the optical regime (~ 1.5 – 2.5 eV), inducing transitions among free carriers and fundamental excitations. These induced excitations can then couple to other modes at lower energy, such as lattice vibrations.

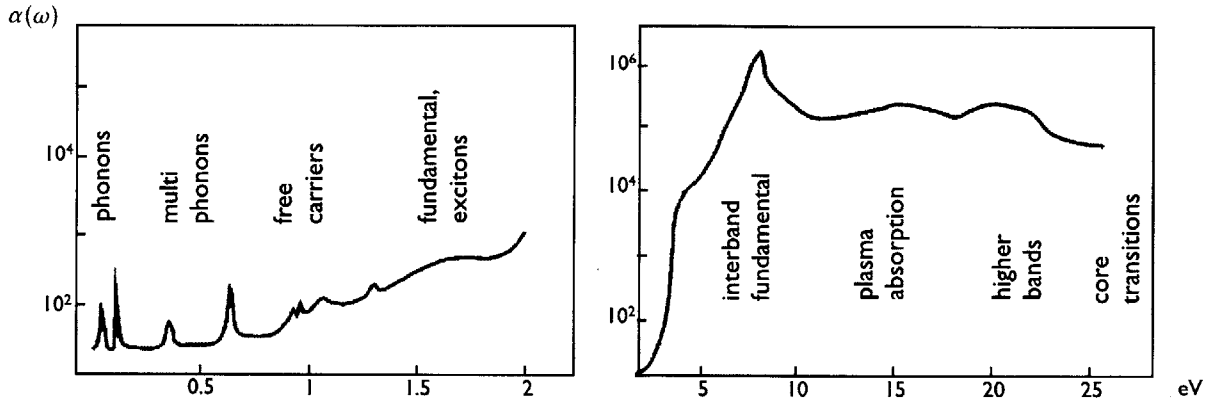

Figure 1-4: Sourced from Kuzmany, 1998.[19] A generalized plot of absorption coefficient for low (left) to high (right) excitation energies in solids.

Optical transitions contribute to light absorption (and thus the dielectric function) with a strength determined by the transition probability between the initial and final system states (typically the energetic ground state and an excited state, respectively). The quantum mechanical probability of transition from an initial state $\langle g|$ to a final state $|f\rangle$ is proportional to the matrix element reflecting their coupling, as well as the availability of the final state (from the density of states $\rho(E)$:

$$P_{g\to f} = \frac{2\pi}{\hbar}\left|\langle g|\,\vec{H}_p\,|f\rangle\right|^2 \rho(f) \qquad \textit{Eq. 1-19}$$

where $\vec{H}_p$ is the operator representing a perturbation. Eq. 1-19 is Fermi's Golden Rule. The transitions probabilities can be estimated and assigned to spectral features (such as those in Figure 1-3) or used to generate the absorption spectrum (such as in Figure 1-4), by using the electric dipole approximation. The electric dipole approximation greatly simplifies the expression for $\vec{H}_p$ by neglecting higher-order expansion terms that are reduced by the ratio between photon and electronic length scales, which differ by $\sim 10^3$. The result is a calculation based on the dipole operator matrix element, which reports on the charge distributions between states.[23] Myriad transitions are possible in solids, from electronic transitions to defect and crystal field absorption. Descriptions and theoretical models for transitions among these and other states may be found in Kuzmany, 1998.[19]

Direct optical transitions result from coupling between the electric field and electrons. Because incoming photons have negligible momentum, the electron wavenumber in k-space is unchanged, and there is a vertical transition within the band

structure. Resonant direct transitions occur between bands when the incoming photon energy corresponds to the interband energy difference. Indirect transitions can result when lattice modes and defects are coupled into the interaction, changing the electron wavenumber and enabling a nonvertical transition in the band structure. In general, due to their low transition probabilities, indirect transitions contribute more weakly to absorption spectra than do direct transitions. The strong peak shown in the imaginary part of the dielectric function in Figure 1-1, and subsequent examples in silicon, is known as the fundamental absorption edge, and corresponds to a transition between the absolute valence band maximum and conduction band minimum. (The harmonic oscillator model does not incorporate the surrounding lattice, so the shape of $\mathrm{Im}(\epsilon)$ calculated from Eq. 1-7 is especially simplistic.) In practice for solids, both the initial state and the final state are better represented by continuum states, and the electronic transition probabilities report on the joint densities of states between bands and their populations at the incoming photon energy hc/λ.

The data presented in subsequent chapters show changes in reflectivity (or transmission) over time due to changing populations, nuclear position, band structure, and temperature. All these factors affect energetic transitions. A time-dependent spectroscopy measurement employs light both as a perturbation (inducing the types of field-matter coupling described in detail below) and as a detection method (by reporting on the changing optical properties presented in this section). Ultimately, our goal is to relate these experimental results to the workings of a material on the microscale in order to better understand and control their properties.

1.3 Ultrafast material dynamics

In §1.2, light-matter interactions were discussed without particular attention to the light and material characteristics. However, the interactions described in this thesis are between ultrafast laser pulses and solid crystalline materials, and both aspects present important considerations. A laser pulse is a roughly Gaussian-shaped envelope of electromagnetic radiation centered around a particular frequency and, in our measurements, lasting tens of femtoseconds. The parameters of the field from the laser pulse can greatly affect the dynamics. Tuning the wavelength can bring the absorbed

photons into and out of resonance with electronic transitions. Light intensity can enhance or suppress various effects of nonlinear absorption. And the pulse duration, typically on the order of a molecular vibration, can mask or effectively sample coherent dynamics. Because the materials under study have repeatable lattice structure, a unit cell's interaction with a laser pulse is generally replicated across many thousands of cells. These simultaneous events add cumulatively to the signal being measured, generating a macroscopic observable signal from events happening on the angstrom (10^{-10} meters) length scale within the crystal lattice.

Interactions and energy exchange among laser pulses, electrons, and lattice atoms happen on timescales ranging from attoseconds (10^{-18} seconds) to picoseconds (10^{-12} seconds). A summary of the relevant timescales for these material dynamics is presented in Table 1-1.[24,25] At ultrafast timescales, complex physical events are accessible to measure, understand, and potentially control. As discussed in §1.2, reflectivity and transmission are two optical properties used to observe phenomena such as electronic populations, exciton formation, and lattice structure. These parameters can report on intrinsic material properties and behavior under dynamic perturbation. Measuring the reflectivity or transmission of a material under different conditions allows us to learn about the complex exchange of energy among modes, enabling deep insights into material dynamics.

Table 1-1: Coupling between radiation and materials and the relevant timescales and processes. [25]

Interaction	Timescale	Processes
Light-electrons	Attoseconds (10^{-18})	Electronic excitation
Electron-electron	10 femtoseconds (10^{-14})	Electronic dephasing
Electron-electron	100 femtoseconds (10^{-13})	Electron thermalization
Electron-phonon	Picoseconds (10^{-12})	Electron cooling, phonon emission
Phonon-phonon	Picoseconds – nanoseconds (10^{-9})	Lattice thermalization

Drawing from Table 1-1, we expect the transitions of primary importance for optical spectroscopy to be electronic. Incoming photons transfer energy to electrons, and this energy is lost via electron-electron scattering, electron-phonon scattering, and

electron-hole recombination, or the diffusion and transport of energetic carriers. Some of these mechanisms are summarized here, including carrier excitation and relaxation and coherent phonon generation via Impulsive Stimulated Raman Scattering (ISRS) and Displacive Excitation of Coherent Phonons (DECP). The mechanisms and theory of photo-induced phase transitions are also introduced in this section, and we briefly summarize how the above mechanisms are detected experimentally. Some phenomena, including carrier diffusion, carrier transport, and thermal diffusion, are discussed in Chapter 4 in the context of measurements on and modeling of bismuth thin films.

1.3.1 Electronic Excitation, Scattering, and Recombination

Free carriers (electrons and holes) in crystals may be treated as having classical charges and masses via the effective mass approximation,[26] wherein a carrier's wavefunction is greatly simplified by its crystalline environment . Upon interacting with a very weak external electric field, the carrier distribution does not change, but carriers move collectively with a characteristic drift velocity. Under exposure to higher electric fields (greater than $10^4 \frac{V}{cm}$), carriers behave differently. We typically employ field strengths of $10^6 \frac{V}{cm}$ –$10^7 \frac{V}{cm}$ with a laser pulse. This behavior is more difficult to characterize, because carriers gain energy at faster rates than they lose energy to the lattice, rendering scattering rates and temperature undefined outside thermal equilibrium. But understanding these behaviors is critical to controlling and designing materials better. The ability to characterize such dynamics far from equilibrium on a very fast time scale is a key contribution of this work.

Upon irradiation, hot carriers (carriers out of thermal equilibrium with the lattice) are promoted into a non-equilibrium distribution. A more intense pulse photoexcites more carriers, and the wavelengths within the pulse bandwidth, the electronic band structure, and the electronic density of states determine the post-pulse population. Many processes also depend on the excitation and pulse characteristics themselves. Electron-electron scattering increases abruptly with increasing carrier density at high fluence, but the rate plateaus at very high fluences due to coulombic screening between carriers [ref]. As another example, the probability of nonlinear absorption increases strongly with laser intensity, so shorter pulse durations or higher fluence can lead to different post-pulse distributions. These effects can even affect longer timescale events.

In the case of GaAs (Figure 1-5), higher populations in the electronic side bands take longer to recombine [ref]. In a polar crystal such as GaAs, these carriers couple preferentially to long-wavelength (small momentum) phonons, thereby slowing the scattering of carriers to the lowest-lying symmetry point in k-space.

Figure 1-5 depicts the key processes of excitation and relaxation for optically excited electrons. Momentum is conserved and electrons are promoted directly in k-space, with the direct transitions with the smallest energy gaps dominating the absorption. Indirect transitions ($\Delta k \neq 0$) can also occur via phonon assistance. Subsequently, thermalization via electron-electron and electron-phonon scattering then produces populations at low-lying states (the conduction band edge). Additional absorbed photon energy can also generate hot carriers from the conduction band edge (yielding the free carrier response demonstrated in §1.2.2). Thermalized electrons and holes eventually recombine, either directly or via phonon assistance to conserve momentum. Mid-gap localized defect states can also be produced during electron relaxation on the sub-picosecond timescale, their low energy the result of coupling with lattice vibrations.[27,28] Shaded in blue in Figure 1-5 are carrier populations where we typically can measure them reliably, after band-edge relaxation and in thermal equilibrium. The processes preceding this, shown in the dashed region, are measurable only transiently or indirectly within our time resolution.

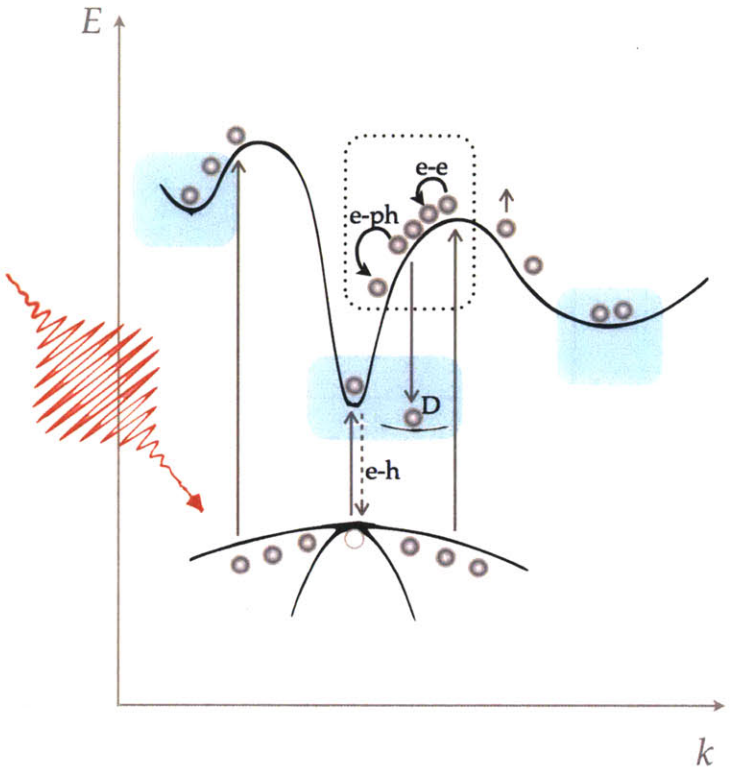

Figure 1-5: Excitations and relaxation processes after photoexcitation in GaAs (simplified band structure of GaAs from the Ioffe Physico-Technical Institute electronic archives). After photo-excitation, electrons lose energy via electron-electron scattering (e-e), electron-phonon scattering (e-ph), electron-hole recombination (e-h), or relaxation to defect states (D). The blue shaded regions indicate thermalized populations; processes enclosed in the dashed region are only transiently measureable.

To illustrate why this is the case, a simplified calculation of electron distribution $f(E,t)$ above the Fermi level after laser pulse excitation using Keldysh rate equations is shown in Figure 1-6.[27,29] Our measurements typically employ probe pulses ~70 fs in duration, their temporal centers spaced 23 fs apart. Electron thermalization occurs on the timescale of our pulse duration, and the electronic distribution is already changed considerably via multiple processes by the point at which only twenty temporal points have been collected (~500 femtoseconds).

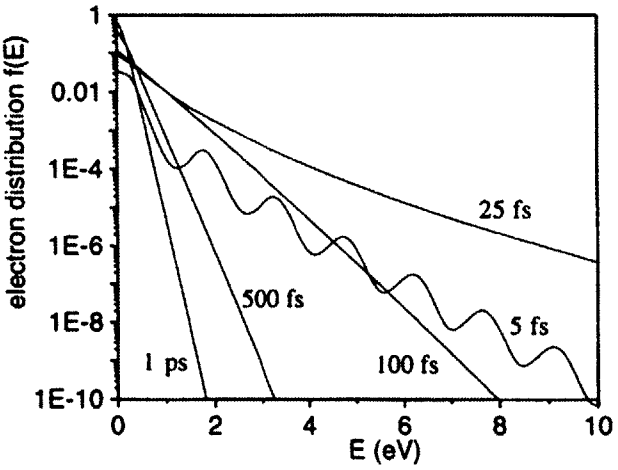

Figure 1-6: From Mero et al., 2005.[27] Electron energy distribution post-excitation at different timepoints, as calculated using the Boltzmann distribution and Keldysh rate equations. The 5 fs instance is modulated at the photon frequency due to multiphoton processes and polarization; these modulations are quickly averaged out.

To attribute optical data in the time domain to microscopic processes, we look for signals displaying characteristic timescales and features and for the interplay between competing or coupled processes. As one set of examples, consider the sample signal in Figure 1-7, consisting of signal from electron-electron, electron-phonon, and electron-hole interactions on overlapping but generally increasing timescales. Carriers gathering at the local conduction band minima (different symmetry points in k-space, as in Figure 1-5) may have varying relaxation rates that together dictate the material's dynamics. Further, these dynamics can be tuned according to the desired application if we understand their underlying drivers. In the first few tens of femtoseconds, we can expect quickly changing nonequilibrium behavior. On the picosecond timescale, electrons at k=0 may undergo direct electron-hole recombination—typically observed as an exponential decay (~10 ps)—while electrons at other symmetry points may preferentially couple to certain optical phonon modes (whose oscillation amplitudes can be measured as a function of electron population if the coupling is faster than the oscillation period).[30] Similarly, defect excitation in the mid-gap range is possible in certain circumstances and is an important parameter in device design. Defect formation is detectable as low-frequency lattice vibrations if relaxation into the state is faster than the oscillation period. The pathways and timescales along which electrons and phonons interact are complex and highly variable.

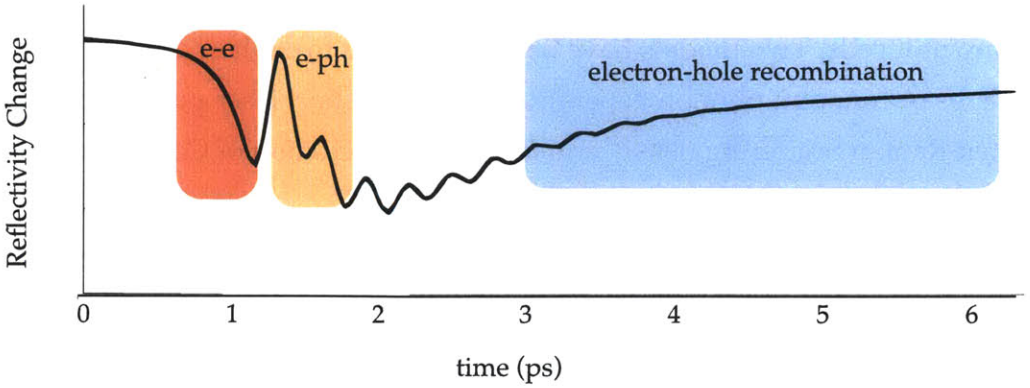

Figure 1-7: Examples of possible microscopic dynamics leading to a typical time-domain reflectivity signal in a crystalline band-gap material with a Raman active phonon mode. Electron-electron interaction occurs on the 100 fs timescale; electron-hole recombination on the several ps timescale, and electron-phonon interactions on intermediate timescales.

Complicating further our observation of the above mechanisms is the reality that in a probed area of sample, carriers can leave the region entirely. Typically, we approximate transport out of the region as one-dimensional, since the optical penetration depth in materials of interest is much smaller (tens of nanometers) than the pulse spot size (tens of micrometers), creating steep temperature and population gradients into the depth of the sample relative to the lateral dimension. The effects of carrier diffusion and transport on the fundamental processes will be explored further in our treatment of bismuth dynamics in Chapter 5. Heat transport by phonons, acoustic waves, and pressure gradients, can also occur.

1.3.2 Coherent Phonon Generation via ISRS and DECP

Crystalline materials have characteristic vibrational modes resulting from their structure; coherent phonons are their elementary excitations. Phonons are lattice vibrations generated by dynamic perturbations such as ultrafast laser pulses and detectable by spectroscopic methods when coherent, as highlighted in the orange-shaded region in Figure 1-7. Coherent control has been demonstrated by selective enhancement and cancellation of specific modes using time-separated optical pulses of select photon energies.[31] [32] The generation and relaxation of coherent phonons depends strongly on coupling with photo-excited electrons. Together, the lattice and electronic properties can yield real-time information about the state of the system. Because coherent phonon generation results from incoming photons ($k \approx 0$) as described below,

the wavepackets do not propagate throughout a crystal, and are generally delocalized over many unit cells. Two models have been developed to explain different mechanisms of coherent phonon generation from ultrashort laser pulses: Impulsive Stimulated Raman Scattering (ISRS)[33] and Displacive Excitation of Coherent Phonons (DECP),[34] summarized in Figure 1-8.

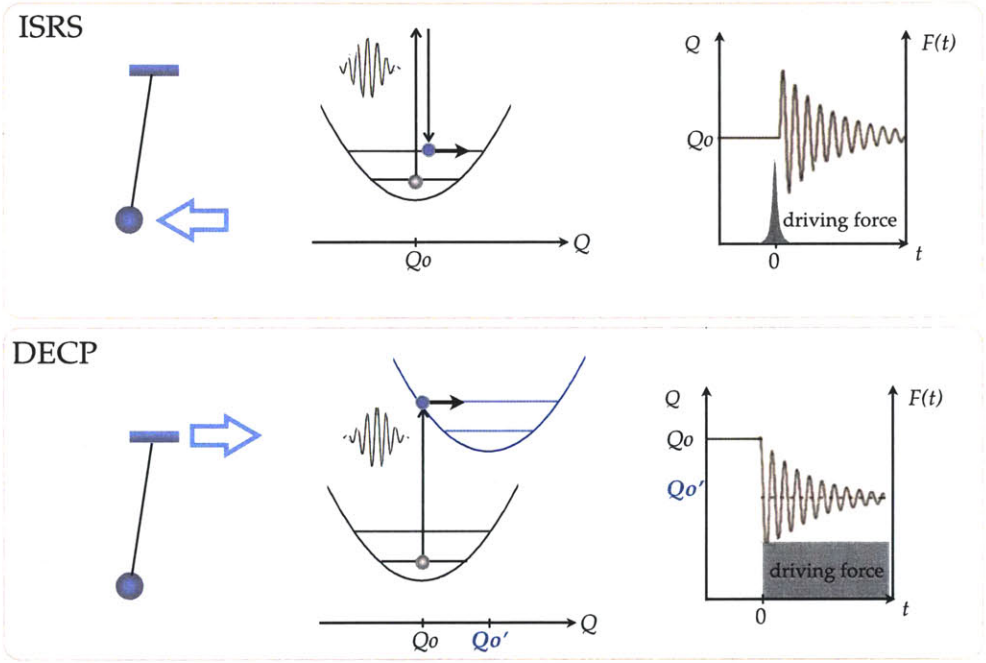

Figure 1-8: Adapted from Ishioka, 2012.[35] Depictions of generation mechanisms and example nuclear trajectories for coherent phonon generation via ISRS (top) and DECP (bottom). The greyed portions beneath the time-dependent traces represent the driving force—a delta function for ISRS (similar to striking the pendulum ball) and a step function for DECP, (analogous to translating the pendulum string). The ISRS mechanism maintains nuclei equilibrium positions generating sine function oscillations about those positions, while the DECP mechanism displaces nuclei equilibrium positions generating cosine function about the new positions when the wavepacket is launched.

ISRS may be understood in the context of conventional Raman scattering. When light scatters inelastically with a material, it can emerge frequency-shifted due to its interaction with Raman-active vibrational modes. When multiple fields are involved with difference frequencies matching a Raman mode, the scattered light is coherent and the signal amplified. As long as an ultrafast pulse is of shorter temporal duration than the vibrational period, many frequency combinations within the pulse's spectral bandwidth exist to achieve resonance with vibrational modes, allowing a single pulse to launch a wavepacket.[36] The effect is an impulsive launch of nuclear motion in the ground electronic state, similar to striking a pendulum ball from its equilibrium

position to generate kinetic energy. Nuclear motion about the equilibrium position yields a characteristic sine function from the coherent phonon signal as illustrated in Figure 1-8.

Formally, the laser pulse driving force is given by the Raman polarizability tensor, the change in dielectric function with respect to nuclear coordinates Q: [37]

$$F(t) = \frac{\partial \epsilon_{kl}}{\partial Q} E_k(t) E_l(t) \qquad \textit{Eq. 1-20}$$

where the optical fields E_k and E_l have frequencies such that $\omega_k - \omega_l = \omega_{phonon}$ for Raman-active modes.

In contrast, the DECP model employs photo-excited carriers to launch coherent phonons via strong electron-phonon coupling in the material.[34] Photo-excited carriers are promoted to an excited electronic state, and the equilibrium position on the new potential energy surface is shifted. The nuclear positions are initially unchanged (following the Franck-Condon principle), so the potential surface shift launches a vibrational wavepacket along the excited state potential as the nuclei experience a restoring force around the new equilibrium positions. In the molecular picture, electrons are excited from bonding to anti-bonding orbitals, causing decreased shielding among nuclei, bond lengthening, and a reduced force constant as the restoring force launches a vibration. Beginning away from the equilibrium position of the excited state, the DECP mechanism yields a characteristic cosine function oscillation.

From our discussion of carrier excitation (§1.3.1) and model dielectric functions, (§1.2.1 and §1.2.2), we expect that the laser pulse will drive an excited population of carriers $n(t)$ and that both the electronic redistribution and any nuclear motion will modulate the complex dielectric function. The DECP framework as formulated by Zeiger, et al. characterizes the change in electronic distribution in the perturbed region as

$$\dot{n}(t) = \rho P(t) - \beta n(t) \qquad \textit{Eq. 1-21}$$

where $P(t)$ is the power density of the arriving pulse, β is an electronic decay constant, and ρ is a constant related to the material's refractive index η.[34] Additionally, there will be a temperature change $\Delta T(t)$ as electrons above the Fermi level absorb photon energy and equilibrate.

For DECP to occur, there must be electron-phonon coupling along the vibrational mode such that lattice parameters are sensitive to electronic redistribution. This coupling is assumed to be linear:

$$Q_0(t) = \kappa n(t) \qquad \textit{Eq. 1-22}$$

where Q_0 is the equilibrium configuration toward which nuclei are restored in the excited potential. Qualitatively, we have $n(t)$ as a function of the driving force and the equilibrium nuclear position as a function of $n(t)$, and we note that a similar relation to Eq. 1-21 exists for $\Delta T(t)$. Because reflectivity is a function of the complex dielectric function, we expect that transient reflectivity measurements will reflect modulation via these parameters in the form:

$$\frac{\Delta R(t)}{R} = \frac{1}{R}\left(\frac{\partial R}{\partial n}n(t) + \frac{\partial R}{\partial T_e}\Delta T(t) + \frac{\partial R}{\partial Q}Q(t)\right) \qquad \textit{Eq. 1-23}$$

These dominating factors can be understood by the timescales of the measurement: on a fast timescale, electrons have thermalized so that their populations and temperature are well-defined; similarly, nuclear motion (lattice vibrations) proceed on the timescale of several hundred femtoseconds. The differential transient reflectivity reports on changes in carrier density and temperature as well as nuclear motion, allowing insights into energy transfer and relaxation processes in the time domain. Noting again the relation between reflectivity R and the dielectric function $\epsilon(\omega)$, the third term on the right hand side of Eq. 1-23 (nuclear displacement) recalls Eq. 1-20. While vibrational mode excitation via DECP is not related to the Raman process, Eq. 1-23 suggests that the detection of coherent phonons will be limited to Raman-active modes.

DECP was developed in part to explain the sole detection of the fully symmetric A_{1g} mode in bismuth and antimony without detection of the orthogonal E_g mode.[38] Density functional theory calculations have shown the A_{1g} mode to be selectively coupled to photo-excited carriers; a potential shift exists along the inter-nuclear axis of the A_{1g} mode, the direction of Peierls distortion.[39] [40] Subsequently, modifications have been proposed that express DECP as a special case of ISRS.[41] [42] Specifically, the excitation terms for the two generation mechanisms contain related Raman tensor components, with the real part related to the impulsive mechanism and the imaginary to the displacive mechanism.

1.4 Watching Dynamics Unfold: Experimental Techniques

We have now encountered many of the fundamental ultrafast processes of interest in materials discussed in this thesis. The observables discussed thus far have been discussed as a function of frequency, while we are interested in watching these processes as they unfold dynamically. How are the fundamental excitations shown in Figure 1-4 be captured in order to generate a time-dependent picture like the one shown in Figure 1-7?

1.4.1 Pump-probe Spectroscopy

Just as a sports photographer uses fast shutter speeds to capture players in action, monitoring events that occur on ultrafast timescales (Table 1-1) requires a 'shutter' as fast as the events themselves. Thus, we use femtosecond laser pulses for two purposes in a measurement: to induce the material dynamics of interest and to monitor the dynamics themselves. Femtosecond lasers pulses are at present the fastest that are also robust and adaptable to spectroscopic requirements such as those met by the single-shot instrument presented subequently. As attosecond laser technology and attosecond spectroscopy techniques continue to develop,[43] spectroscopists will be able to watch even faster events unfold.

A robust tool of time-domain ultrafast laser spectroscopy is the pump-probe technique (Figure 1-9). This method uses a pair of short (femtosecond timescale) laser pulses: an intense 'pump' pulse (the perturbation) and a weaker 'probe' pulse (for detection) separated by a delay Δt. When the pump excites the sample, it induces a change in state. The probe interacts with the sample and 'reads' the response. Measureable probe properties that are sensitive to the change (e.g. via reflection or transmittance) report on the changed state for a given Δt. When Δt is negative, the probe reaches the sample before the pump and no pump-induced change is detected. When $\Delta t = 0$, the pulses arrive together and the probe response describes the instantaneous response. For $\Delta t > 0$, the pump arrives first and the probe response captures the system at $t = \Delta t$. Thousands of data points (for varying Δt) combine to yield a picture of the time-evolving material response to the pump pulse. One critical assumption for most pump-probe techniques is that the system recovers between each

pump-probe pulse pair, so that effects measured by each pair are independent of effects from previous pairs.

Advantages of the technique are many. The time delays between pump and probe pulses (effectively yielding the total time window of the measurement) and the time delay between pulse pairs (the time resolution of the measurement) can be varied easily, enabling observation of many physical phenomena. Importantly, the technique supports balanced detection and multiple scans, allowing even very weak signals to be detected after averaging. If a pump-induced change in the sample relaxes before the next pump arrives, the measurement can be performed on a single spot. If fresh sample is required, a sample may be flowed (liquids and gases) or scanned (solids) to yield a time-dependent response.

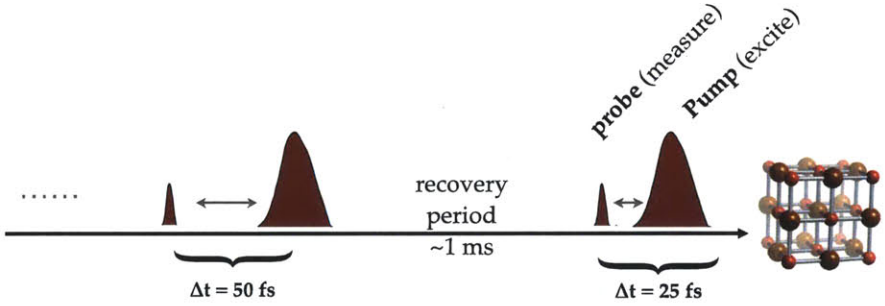

Figure 1-9: In a conventional pump-probe time-domain measurement, an intense pump pulse induces a change in the sample via light absorption and a probe pulse reports on the resulting measurable change in optical or electronic properties. This pump-probe sequence is repeated while varying the inter-pulse time delay, and a time-dependent response is reconstructed

The conventional pump-probe spectroscopy technique has key limitations, however. Chief among them is our inability to study irreversible dynamics in most solid-state samples with the method. While irreversible dynamics can be measured by flowing samples in the liquid and gas states, solid-state samples are often non-uniform at surfaces and interfaces and are challenging to synthesize in large quantities, limiting the viability of scanning solutions. Constrained to a very small area, repeated pump-probe pairs cannot measure a true time-dependent response of an irreversible event. The very first pump changes the material such that subsequent pump-probe pairs see the material in an altered state. Thus, the time-dependent response cannot be accurately reconstructed. Instead, the conventional measurement in this case yields an evolving

time-average of cumulative material change. A different way of observing the material response must be employed for watching irreversible events in the solid state.

1.4.2 Single-shot Spectroscopy

Materials under extremely high-density excitation showcase novel far-from-equilibrium phenomena that are inaccessible by other means. In many cases the events that take place following intense irradiation are irreversible or only slowly reversible, and either sudden or cumulative sample damage prevents conventional pump-probe measurements. "Single-shot" methods that allow the entire time-dependent response to be monitored in real time after sample excitation offer improved prospects for learning about far-from-equilibrium states. This thesis describes the adoption, improvement, capabilities, and results of single-shot femtosecond spectroscopy measurements on solid-state materials of interest. The single-shot measurement yields a complete time-dependent response to photoexcitation from one laser shot, reporting in real-time as the system undergoes irreversible change.

Interesting phenomena far from equilibrium are many. Laser annealing, an alternative to slow-baking in industrial annealing processes, occurs via high-energy excitation processes that permanently move surface atoms into place after damage.[25] Micro- and nano-structuring of materials can be achieved with laser pulses through material ablation, which occurs at high excitation densities and cannot be studied via conventional methods due to its irreversible nature.[44,45] The precision and predictability of the effects of femtosecond pulses on material machining hold great promise, since non-thermal localized change can preserve the properties of the surrounding material structure. Additionally, photo-induced events in high-energy crystals are largely unstudied and hold great promise for understanding and controlling chemical decomposition and detonation events.

We will take 'irreversible' to mean *irreversible on the timescale of the measurement or longer*. For our purposes, any event that does not relax fully to its original state after approximately 1 millisecond (corresponding to a typical 1 kHz laser repetition rate) is irreversible, because it precludes conventional measurements. Additionally, permanent change, such as occurs in ablation or explosive events, is of key interest, and can be uniquely accessed by the single-shot instrument.

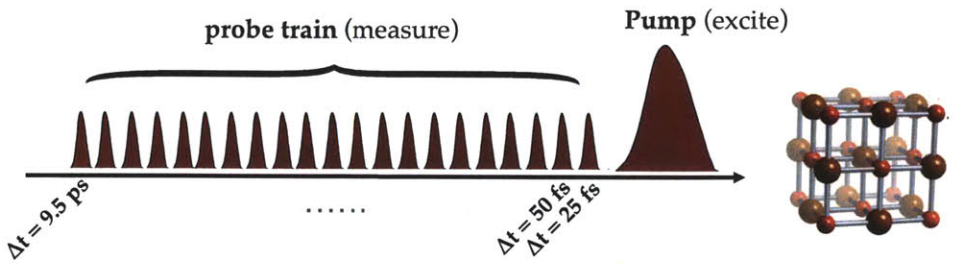

Figure 1-10: In a single-shot spectroscopy measurement, an intense pump pulse induces a change in the sample. Because either the recovery timescale or the strength of response renders the event irreversible on the femtosecond timescale, a temporal stream of probe pulses is used to monitor the material response in real-time. One full time-sequence is constructed from one laser shot.

First introduced in 2006,[46] the single-shot spectroscopy method employs a single pump pulse followed by several hundred probe pulses in close temporal succession (Figure 1-10). The probe pulses report on material dynamics in real-time as they unfold on the femtosecond timescale. Rather than initiating the same event many times over, capturing a snapshot at just one pump-probe delay each time, and assembling a reconstructed time-sequence, the measurement described here captures the true time-sequence the first and only time it occurs. This enables visualization of dynamics that have not been measurable by other methods. Full experimental details are provided in Chapter 2 and Chapter 3; experimental results for systems showcasing new phenomena under high-density photoexcitation are presented in Chapter 4 and Chapter 5.

1.5 Photo-induced Phase Transitions

Conventional phase transitions often involve structural rearrangement induced via thermal or pressure-dependent mechanisms. When ice is placed at room temperature, heat from the surrounding air disorders the lattice into a looser network of water molecules—a solid-to-liquid phase transition. But when certain materials interact with laser light via the mechanisms described above, they can undergo phase transitions on the ultrafast timescale. These phenomena are broadly referred to as Photo-Induced Phase Transitions (PIPT), and they are distinct from the mechanisms described above but generally come about via these mechanisms. A photo-induced phase transition is conversion, via light-matter interactions, into a macroscopic excited

domain with distinct collective structural or electronic features. Mechanisms of photo-induced phase transitions are varied, and multiple theoretical descriptions have been put forth. We will be especially interested in structural photo-induced phase transitions, wherein a measureable long-range atomic order or disorder can be induced in the crystal.

PIPT research on the femtosecond timescale over the last two decades has made great strides in identifying new phenomena and possibilities.[47] Inducing structural change with ultrafast light pulses can in some cases allow states to be accessed that cannot be achieved by other means. Among other achievements, short- and long-term data storage options have resulted from this development,[48,49] and domain-switching devices remain a key application of PIPT advances.[50,51]

PIPTs also allow us to investigate the complex and intriguing interplay among various material properties. Finely-tuned perturbations can tip the balance of competing forces and interactions in favor of a new stability, enhancing our understanding of these interdependencies and ultimately contributing to the goal of better material design and control.[52] In an extension of this goal, with the single-shot measurement we can uniquely observe energetic interplay and 'tipping points' far from equilibrium in hard-to-study systems.

1.5.1 Energetics and Timescales of Photoinduced Phase Transitions

Figure 1-11 presents a potential energy schematic of the states involved in a PIPT. From the initial state $|i\rangle$, the system is photo-excited to a transient state $|t\rangle$. Under most PIPT scenarios, the system relaxes into a distinct structural state of higher energy than the ground initial state. This meta-stable non-equilibrium state $|p\rangle$ is the photo-induced phase, and it resides in a local minimum. Depending on the lifetime of the electronic states corresponding to $|p\rangle$ (which yield an energy barrier stabilizing the metastable state), measurable structural change can result. Various relaxation pathways exist to return the system to the lower potential energy curve, either to the low energy equilibrium state $|i\rangle$ or the higher energy equilibrium state $|h\rangle$. Alternately in this scenario, the system could reach state $|h\rangle$ from $|i\rangle$ via thermal excitation (e.g., melting), but the higher potential curve and its corresponding states can be accessed only through photo-excitation. Specific photo-induced phenomena observed experimentally and presented in Chapter 4 and Chapter 4 will make repeated use of this basic picture

to map the system dynamics. Because the free energy of the photoinduced states can be similar to equilibrium or thermally accessible states, with the transition toward them coordinated by a delicate balance of cooperative degrees of freedom,[52,53] PIPTs present the possibility to induce macroscopic order change with relatively weak and local perturbation.

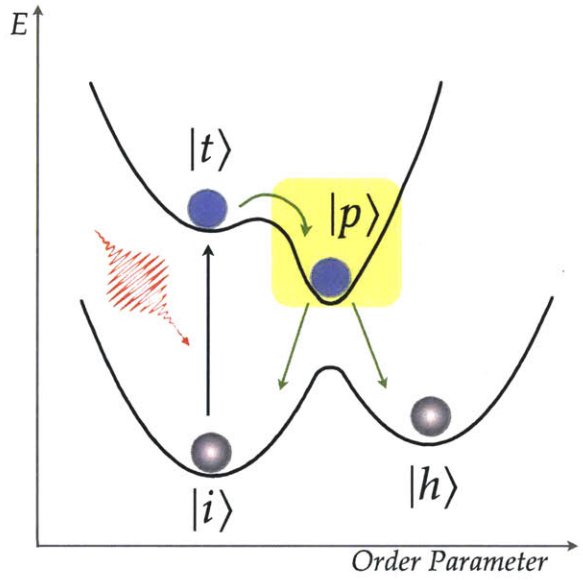

Figure 1-11: Adapted from Nasu, 2001. [54] *The system can be taken from the initial ground state $|i\rangle$ to state $|h\rangle$ on the same potential energy surface via thermal heating. Photoexcitation from state $|i\rangle$ to state $|t\rangle$ allows relaxation to the metastable photoinduced state $|p\rangle$ which can be structurally distinct. Relaxation proceeds to either $|i\rangle$ or $|h\rangle$.*

Structural phase changes can be induced thermally or non-thermally. Experiments using picosecond and nanosecond pulses in particular have shown evidence for thermal laser-induced melting, wherein the sample is heated by the laser pulse energy through the melting point into the liquid phase.[55,56] Recalling the fast timescales in Table 1-1, we note the many light-matter and matter-matter interactions that precede slow thermal diffusion. Femtosecond pulses have allowed initiation and observation of non-thermal changes that take place at faster timescales than any thermal event.[57] When a macroscopic structural change results from these events, we refer to the phenomenon as a non-thermal phase transition.

In a purely electronic PIPT mechanism, laser excitation induces a critical density of excited carriers and causes a collapse of the band gap. This can occur when the bandgap arises from coulomb repulsion in Mott insulators, as described by the

Hubbard model.[58] Because no electron-phonon coupling is required, the electronic mechanism can take place within an unthermalized lattice in a matter of femtoseconds.

Alternatively, transitions can take place via non-thermal electron-phonon interactions if strong coupling exists along key vibrational modes. In a mechanism similar to DECP (§1.3.2), the result of photoexciting carriers is to destabilize covalent bonding in the lattice. At high enough excitation densities, the lattice structure can become so destabilized as to change phase. This non-thermal mechanism can be understood within the two-temperature model of lattice heating, where electrons and the lattice are treated as separate thermal baths with a coupling factor between them. (The two-temperature model is examined in more detail in Chapter 4 in the context of measurements on bismuth films.) Energy from a laser pulse is transferred first to the electrons while the lattice remains cold, and the two baths gradually thermally equilibrate through electron-phonon thermal interactions.

Identifying the mechanism responsible for a PIPT can by difficult. Both resonant [59] and displacive [60] generation of phonon vibrations can induce electronic or structural change through a variety of interrelated pathways: extreme bond displacement,[61 62] orbital overlap and bandgap collapse,[59 63] and charge-density-wave modulation.[64, 65] For charge-density-wave transitions, a related path is via photo-induced charge-transfer, leading to a lattice shift and simultaneous bandgap collapse.[66] Consensus on mechanistic details remains elusive even for transitions that have been under study for decades, though added experimental methodology will play an important role in gaining new insights.[67,68 69]

1.5.2 Theory of Photoinduced Phase Transitions

To understand PIPT phenomena in the context of conventional phase transitions, consider that phase transitions are typically characterized by an order parameter (e.g., inter-atomic distance, viscosity, magnetic moment, etc.) rather than by the external parameter that effected the change (such as temperature or pressure).[70,71] A commonly borrowed concept in photo-induced melting studies is the Lindemann criterion, which states that melting occurs as an order parameter δ_L— the ratio of RMS fluctuations about equilibrium atomic positions to unit cell distance—exceeds a critical value.[71,72] This rule is applicable to both thermal and non-thermal transitions and even provides a straightforward means to estimate non-thermal melting thresholds via the interatomic

potential energy surface dependence on excited carrier density. Typically, the dimensionless δ_L falls in the range between 10% and 20%.[73-75] While this metric provides a useful intuitive understanding for PIPT phenomena, below we outline thermodynamic and quantum-mechanical theories of PIPT as outlined in other sources. The former is a useful starting point; the latter is a powerful means to estimate many useful quantities and dynamics. Other approaches are mentioned briefly.

Thermodynamic Description

Thermodynamically, a state is stable if the chemical potential μ is minimized. In the case of PIPT, electronic excitations change μ by changing the bonding. For a comparable structural change that can be induced thermally or non-thermally, the phase transition rate $\Gamma = \Gamma(t)$ from $A \rightarrow B$ is given by:

$$\Gamma_{A\rightarrow B} \propto e^{-\beta \Delta G} \qquad \textit{Eq. 1-24}$$

where $\beta = 1/kT$ influences the rate thermally and Gibbs free energy ΔG influences the rate non-thermally. We here summarize the formal thermodynamic treatment by Bennemann, 2011, and references therin.[76] One example of a useful thermodynamic treatment of the PIPT phenomenon is in describing the role of electronic excitations on supercooling or supersaturation, since certain excited states may lead to the creation of nucleation sites. Hereafter, transition quantities refer to differences with respect to phases A and B. The thermodynamic free energy ΔG is given generally by

$$\Delta G = -S\Delta T - N\Delta\mu + \sigma\Delta s + \cdots \qquad \textit{Eq. 1-25}$$

with entropy change S, the number of particles involved in a nucleation process N, surface energy per unit area σ, and surface area change Δs. Using a supercooling transition as an example, $\Delta T = T_0 - T_{nuc}$ with T_0 the temperature at the phase boundary and T_{nuc} the final temperature where we will consider nucleation to be occurring. To transition to the photoinduced picture, we replace the entropy term with $(\frac{Nq}{T})\Delta T$. The parameter q, the molecular latent heat from a change in binding, can be straightforwardly related to electronic excitations since both interpretations change the bonding. We approximate Δs as $4\pi r^2$ for a spherical nucleation site and split $\Delta\mu$ into two terms:

$$\Delta\mu_{A\to B} = \Delta\mu_{therm} + \Delta\mu_{ph} \approx T\ln(p/p_0) + \Delta\mu_p' \qquad \textit{Eq. 1-26}$$

Here, p_0 is the pressure at the thermodynamic phase boundary and p/p_0 gives the extent of saturation. The term $\Delta\mu_{ph}$ is the photoinduced contribution, which can be understood as the difference in binding energies per molecule in response to light for phases A and B. It is proportional to the effective change of energy per particle in the nucleation site $\Delta\mu_p'$, which can be expressed in terms of electronic excitation-induced bond energy changes. Replacing N via the particle density per spherical volume $\rho = N/V$, we obtain from Eq. 1-25 and Eq. 1-26:

$$\Delta G \approx -\frac{4\pi r^3}{3}\frac{q}{T}\rho\Delta T - \frac{4\pi r^3}{3}\rho T\ln(p/p_0) + \frac{4\pi r^3}{3}\rho\Delta\mu_p' + 4\pi r^2\sigma \qquad \textit{Eq. 1-27}$$

In approximating $N\Delta\mu_{ph} \approx \frac{4\pi r^3}{3}\rho\Delta\mu_p'$, we have assumed uniform excitation for all molecules at the nucleation site, which is only true at high excitation fluence.

To determine where the free energy change is favorable, we can simply set $\Delta G < 0$ in Eq. 1-27 and solve for the critical nucleation radius that yields a global phase change:

$$r_c = \frac{3\sigma/\rho}{\frac{q}{T}\Delta T + T\ln(\frac{p}{p_0}) - \Delta\mu_p'} \qquad \textit{Eq. 1-28}$$

Thus the further the system has been cooled toward saturation (larger ΔT and p/p_0), the smaller the critical radius. More relevant for the photoinduced picture, a larger extent of electronic excitation yields a smaller critical radius necessary for global change (since $\Delta\mu_p' < 0$). The quantity $\Delta\mu_p'$ must be proportional to the absorbed light and thus the incident fluence F, since the probability of electronic excitation is proportional to F. Thus we have developed a thermodynamic picture that illustrates cooperative effects in photoexcited systems and relates the laser fluence to the threshold for global phase change.

Other non-electronic descriptions of PIPT phenomena also emphasize (by design or result) the importance of cooperativity in the lattice. Statistical treatments have included a linear chain system with stochastic processes generating appropriate Hamiltonian terms[77] and a mean-field Ising model treatment with excited and ground states

characterizing the spin-up and spin-down states.[78,79] These models successfully showed that excited molecules were stabilized by aggregation along a chain.

Quantum-Mechanical Description

To describe the quantum-mechanical interpretation of PIPT phenomena, we will use as an example the PIPT observed in tetrathiafuluvalene-p-chloranil (TTF-CA) depicted in Figure 1-12 following Nasu et al.[54,66] At 83 K, TTF-CA undergoes a transition between an ionic spin-density wave state (SDW, wherein charge is uniformly distributed but spin is spatially modulated) and a neutral charge-density wave state (CDW, wherein spin is uniformly distributed and charge is localized in space), abbreviated here as phases I and N, respectively. The transition can also be induced with a laser pulse.[66] As depicted in Figure 1-12, the change from N to I can be described via a charge transfer from the highest occupied molecular orbital (HOMO) of the TTF molecule to the lowest unoccupied molecular orbital (LUMO) of the CA molecule. This system (as do many others that exhibit structural PIPTs) exhibits strong electron-lattice coupling, so the model must build in the interdependence of the electronic distribution and vibrational mode along the axis of charge transfer.

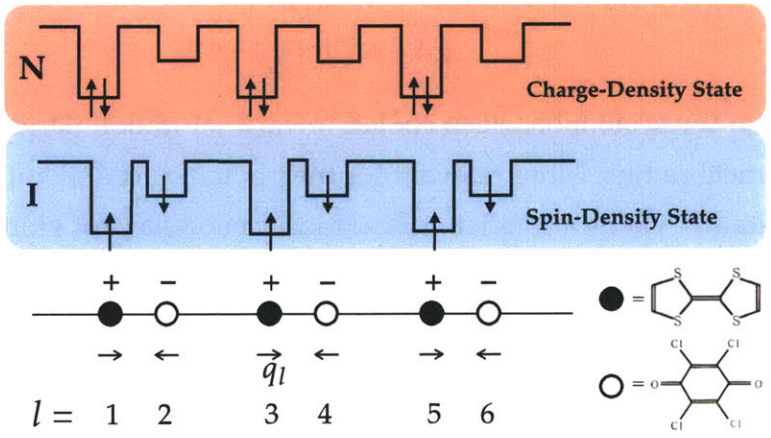

*Figure 1-12: Adapted from Nasu et al., 2001.[54] Representation of phase change between CDW (**N**) and SDW (**I**) states in TTF-CA. Lattice displacement q_l is the site-specific displacement parameter; sites l are labeled for reference in the equations. Black and white circles represent TTF and CA ions, respectively.*

The Hamiltonian operator corresponding to the total energy of the system is

$$\widehat{H} = \hat{H}_{el} + \hat{H}_{ph} + \hat{H}_{inter} \qquad \textit{Eq. 1-29}$$

with the terms on the RHS corresponding to the electronic, phonon, and inter-chain Hamiltonians, respectively. For simplicity, we neglect $\hat{H}_{inter}$ since the inter-chain interaction is expected to be very small. The electronic and phonon Hamiltonians proposed by Nasu, et al. are given here for completeness:[1]

$$\hat{H}_{el} = -T_0 \sum_{l,\sigma} (c^{\dagger}_{l,\sigma} c_{l+1,\sigma}) + \frac{E_{\mathrm{LUMO}} - E_{\mathrm{HOMO}}}{2} \sum_{l} (-1)^l n_l + U \sum_{l} n_{l,\uparrow} n_{l,\downarrow} + \sum_{l} V_l \delta n_l \delta n_{l+1} \quad \textit{Eq. 1-30}$$

$$\hat{H}_{ph} = \frac{S_1}{2} \sum_{l} (q_l - q_{l+1})^2 + \frac{S_2}{4} \sum_{l} (q_l - q_{l+1})^4 \quad \textit{Eq. 1-31}$$

In $\hat{H}_{el}$ (Eq. 1-30), $c^{\dagger}_{l,\sigma}$ and $c_{l,\sigma}$ are the creation and annihilation operators for an electron n with spin σ ($\uparrow$ or $\downarrow$) at site l as labeled in Figure 1-12. δn terms denote the charge on alternating atoms or molecules: $\delta n_l = n_l - 2 \;\; (l \in odd)$ and $\delta n_l = n_l \;\; (l \in even)$. T_0 is the transfer energy for an electron between the HOMO and LUMO on neighboring molecules, U is the intra-molecular electronic Coulomb repulsion term, and V_l is the Coulomb interaction between adjacent molecules. This last quantity, which describes electron-phonon coupling, must depend on the intermolecular distance, so it is given relative to the repulsion strength for the ground-state lattice V_0 by:

$$V_l(q_l, q_{l+1}) = V_0 + \beta_1 (q_l - q_{l+1}) + \beta_2 (q_l - q_{l+1})^2 \quad \textit{Eq. 1-32}$$

where β_1 and β_2 are the linear and quadratic coefficients. In $\hat{H}_{ph}$ (Eq. 1-31), second- and fourth-order coefficients S_2 and S_4 accompany the potential terms; the kinetic term is omitted because we are using the adiabatic approximation in which electronic motion is much faster than, and therefore independent of, nuclear motion.

T_0, E_{LUMO}, E_{HOMO}, U, V_0, β_1, β_2, S_1 and S_2 can all be estimated to a good degree from *ab initio* calculations, visible and IR spectroscopy experiments, and X-ray diffraction if the system is well studied. With the Hartree-Fock method, which permits iterative calculation of the electronic energies as a function of nuclear coordinates, the potential energy surface can be calculated. Results from Nasu et al. are shown in Figure 1-13 in the top panel.[54] Phase I, the SDW state in red, is shown to be the true ground state, but both phases are locally stable with respect to small changes in lattice

[1] *Hermitian conjugate terms are omitted*

displacement. The calculation predicts the adiabatic energy barrier ΔE between the states and the crossover point for specific values of the unperturbed lattice parameter q_0.

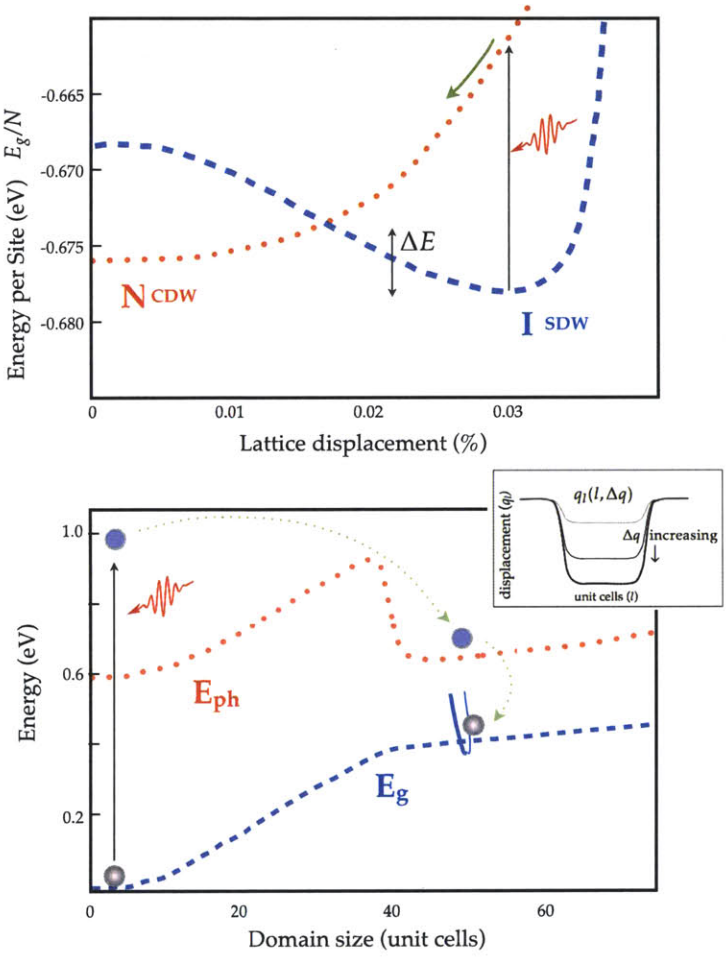

Figure 1-13: Adapted from Nasu et al, 2001.[54] ***Top:*** *Calculated energies per site from the Hartree-Fock method for the phases depicted in Figure 1-12. Phase I (SDW; blue dashed) is shown to be the true ground state; both phases are locally stable. Photoexcitation is indicated from the ground state to the Phase N energy surface (CDW; red dotted); the green arrow describes the relaxation along the excited surface.* ***Bottom:*** *Cross-sections of ground (blue dashed) and first excited (red dotted) potential energy surfaces as a function of domain size. After photoexcitation, the system relaxes to a metastable N phase on the excited surface and to the ground-state N phase after exciton relaxation. The three-dimensional valley around the cross-section is indicated for visualization; the functional form for displacement as a function of amplitude and unit cell site is sketched, inset.*

The top panel of Figure 1-13 describes the energetics of the transition between phases, and is the starting point for determining the dynamics of relaxation to the photoinduced phase (depicted by the green arrow) after photoexcitation. The Hartree-

Fock-derived displacement q_0 per site is a function of the lattice displacement amplitude and the molecular site itself, since neighbors affect the energetics. A typical functional form is sketched inset in Figure 1-13 for different amplitudes Δq.[79] Then, the two-dimensional potential energy surfaces can be calculated as a function of amplitude and domain size. We expect the amplitude (extent) of lattice displacement Δq to depend on the laser fluence F, since greater photon absorption continues to decrease the covalent nature of the intermolecular bond. Local minima on both the electronic ground state and the photoexcited state can then be located to find the conditions for the thermal and photoexcited phase transitions, respectively. A cross-section of both surfaces is shown in the bottom panel of Figure 1-13, with Δq (and consequently F) chosen to demonstrate the steepest changes. N-phase local minima are located on the ground state surface ($\Delta q > 0.5$, well is parallel to the page) and on the excited state surface near 45 unit cells.

This quantum-mechanical picture describes the trajectory of relaxation after photo-excitation, predicts the nucleation (domain) size and energetics of phase switching, and can be formulated in terms of absorbed photons or laser fluence. Further, because the spins and charges have been assigned to molecular sites via Eq. 1-30 and Eq. 1-32, the charge and spin densities can be plotted as a function of real space. This outcome provides the basis for relevant calculations on metal-halide chains for comparison with our experimental data, which will be presented in Chapter 4.

In this work, we use coherent phonon generation to provide an indication of the structural phase, since the activity of vibrational modes is allowed or disallowed by changes in crystal symmetry. Probing the electronic band structure can also report on the structure indirectly, since the periodic representation of electronic energies in k-space results from the periodic lattice structure in real space. The development of a single-shot method to observe these dynamics and novel phenomena can extend the study of PIPT into non-equilibrium regimes with important and fundamentally interesting applications.

1.6 Summary and scope of work

Motivated by multiple perspectives—fundamental science, engineering materials, and a gap in measurement abilities—single-shot spectroscopy offers a way to observe and understand solid-state physical and chemical dynamics far from equilibrium on the

micro-scale. With the above described needs, capabilities, and core principles behind the measurement in mind, this work will describe details of the instrument's development, operation, and measurement results. In this thesis we are primarily considering the control of vibrational modes excited via optical light. These modes typically have frequencies in the 1-3 THz regime, enabling the possibility of driving coherent vibrations directly with THz radiation (instead of indirectly via electronic optical absorption) as that method matures. Information from single-shot optical spectroscopy data not only enables understanding of systems far from equilibrium, but may lay the groundwork for future work in other spectroscopy regimes.

Chapter 2 describes the femtosecond single-shot spectroscopy method in detail, from the laser system and optical instruments to pulse characteristics and sample considerations. This chapter also lays out key challenges and solutions, as well as perspective on challenges yet to be overcome. Chapter 3 details noise sources and their contributions in the single-shot measurement, including a full analysis of their fundamental lower limits, their interactions with other sources, and strategies for noise management. Chapter 3 also describes detection and processing in the single-shot measurement—a topic intrinsically related to instrument noise—in an analysis ranging from image acquisition and processing to data filtering and analysis. In Chapter 4, results from a study on one-dimensional platinum-halide chains are presented. High-fluence measurements on this model material are discussed, providing insight into the properties and timescales of localized excitations within the crystal. Additionally, a basic model for cooperative electronic and lattice effects leading toward the phase transition of this 1-dimensional prototype material is presented. Measurements on the bulk and thin film semimetal bismuth are presented in Chapter 5. Quantum confinement effects, timescales of relaxation, and photo-induced phase transitions at high excitation densities are examined. At the close of each chapter, contributions are summarized with a look toward future measurements, potential improvements, and a perspective on how the technique or measurements can shape materials science and physical chemistry in the future.

Chapter 2

Femtosecond Single-shot Spectroscopy

The single-shot spectroscopy method employs a unique combination of optical, detection, and analysis techniques to achieve real-time measurement of solid-state dynamics and energy exchange among light, electrons, and lattice modes. Measuring these dynamics allows us to examine interesting physics far from equilibrium that are largely unexplored. This chapter describes the experimental details that enable this measurement. Because the method is still in development, much opportunity remains for further optimization. Chapter 3 provides an analysis of the instrument as a basis for future developments.

2.1 Light Source Generation

2.1.1 Laser system

Laser pulses for the single-shot experiment are generated from the integration of three commercial systems: a laser seed source (Coherent Vitesse oscillator), a pulse amplifier system (Coherent Legend), and a pump laser (Coherent Evolution-30). The oscillator produces a train of ultrashort pulses, which are then amplified in intensity via light from the pump laser inside the Legend amplifier. The components and core principles of these systems are described here briefly, and the reader is referred to texts

in laser engineering for more formal treatments of the mechanisms mentioned, as well as discussions of the many challenges involved in generating robust ultrafast pulses.[80] The outline of the laser system and the most important measurable properties of the light at each stage are summarized in a block diagram in Figure 2-1. Figure 2-2 depicts key processes in the laser system that change pulse properties, referenced in the discussion below as applicable.

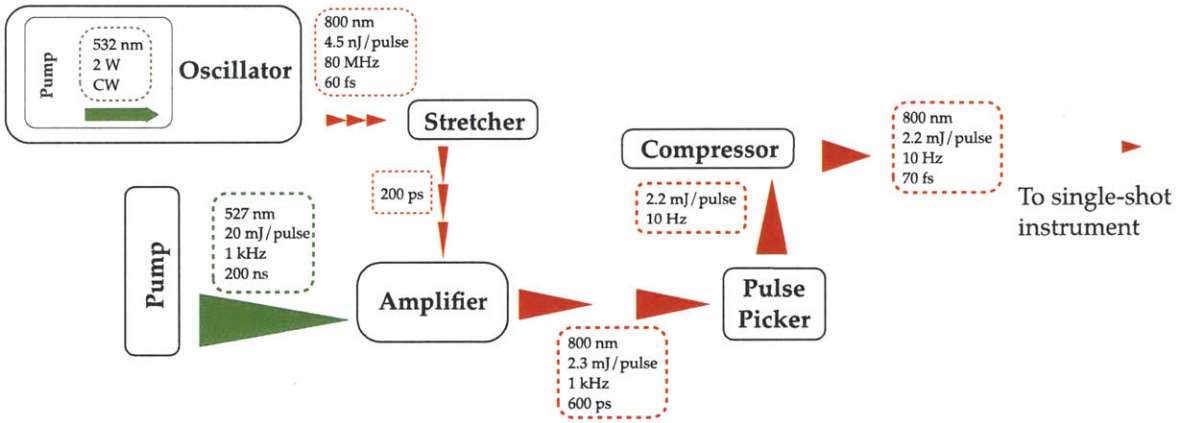

Figure 2-1: Key elements of the laser system used for single-shot spectroscopy measurements. Pulse properties (or their pertinent changes) are summarized between each block diagram element. Not to scale, arrowheads schematically represent wavelength by color, repetition rate by spacing, pulse duration by length, and pulse energy by base width.

Inside the oscillator box there is an additional laser head. Pumped by a continuous optical diode pump source emitting at ~810 nm, an Nd:YVO_4 crystal continuously emits light at 1064 nm by stimulated emission. This light is frequency-doubled (see §2.1.3) to 532 nm in an LBO (Lithium Triborate, LiB_3O_5) crystal. The output from this laser head (532 nm at 2W power) is used to pump a Ti:Sapphire crystal in the oscillator box. Under continuous-wave (CW) operation, light centered at 800 nm is continuously emitted. Distinct frequencies supported by the laser cavity length form standing waves (longitudinal modes) that have no fixed phase relationship to each other. Their constructive and deconstructive interference with is constantly changing in time, resulting in a continuous light source.

The oscillator employs a *passive mode-locking* technique via the optical Kerr effect, diagrammed in Figure 2-2 [B]. Very high intensity can instantaneously change a medium's refractive index such that a lensing effect is produced, reducing the spatio-temporal pulse profile and thus preferentially amplifying short pulses. An aperture in

the cavity ensures that losses to the CW beam are high relative to the pulsed light. This process is initiated by a finely calibrated momentary change in cavity length to generate a very large power fluctuation. Exiting the oscillator is an 800 nm (~40 nm bandwidth FWHM) pulse train at 80 MHz with a power of ~350 mW. Pulses are ~60 fs in duration, yielding pulse energies of 3-4 nJ .

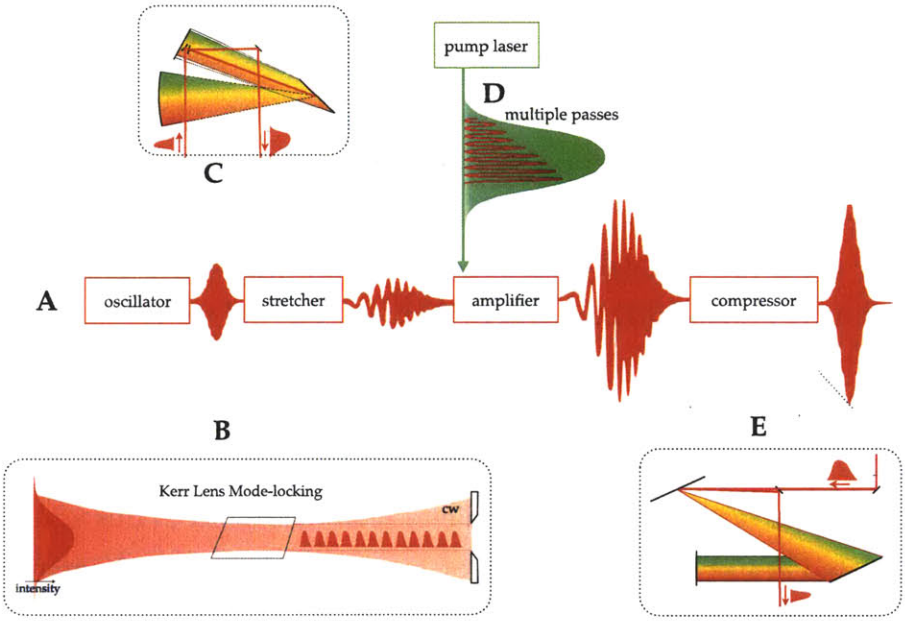

Figure 2-2: [A] *Chirped pulse amplification (CPA): an ultrafast pulse is stretched in time, amplified, and then compressed in time to near its original pulse duration.* [B]**:** *Kerr lens mode-locking (KLM): the optical Kerr effect and an aperture are employed in the oscillator to produce a train of ultrafast pulses.* [C] *Stretcher: group velocity dispersion (GVD) is introduced by varying the path lengths of separated frequencies with a grating, mirror, and curved mirror.* [D] *Amplification: within the amplifier cavity, the 800 nm seed pulse makes many round trips while the crystal is pumped with a single high-energy nanosecond pulse.* [E] *Compressor: GVD is reduced via multiple passes between a grating and retro-reflectors.*

To observe the effect of high fields inside materials of interest and study dynamics far from equilibrium, we want very high peak intensities:

$$I_{peak} = \frac{E_{pulse}}{A\Delta t} \qquad \textit{Eq. 2-1}$$

with beam area A and pulse duration Δt. We increase the energy of 800 nm oscillator pulses via pumped amplification. Because very high pulse energies are generated and damage to the gain medium and cavity optics must be avoided, we stretch the pulse in time before it is coupled into the amplifier cavity and compress the pulse after amplifying. This process is called *chirped pulse amplification* (CPA), depicted by the pulse

profiles in Figure 2-2 [A]. Pulses are sent through a stretcher (a configuration of mirrors and a grating, Figure 2-2 [C]) that separates the pulse frequencies and increases their time delays relative to one another via path length differences. The pulse is stretched in time by a factor of $\sim 10^4$ to a few hundred picoseconds.

The 800 nm oscillator seed pulses are amplified at the Ti:Sapphire crystal of the Legend by pumping the crystal with an external Nd:YLF Evolution pulsed laser. 527 nm pump pulses exit the Evolution at 20 W as a 1 kHz pulse train. Pulse durations are on the hundred-nanosecond timescale, and are generated via *active Q-switching*. As compared to mode-locking, Q-switching is an alternative approach to producing pulse trains that yields higher pulse energies, longer pulse durations, and lower repetition rates. An acousto-optic modulator (AOM) in the cavity is used to selectively diffract and couple out light via the modulator crystal's acousto-optic response. The AOM ensures that cavity loss is initially high so that the energy from a diode light source can accumulate inside the Nd:YLF gain medium without inducing lasing. When gain saturation is reached, the cavity loss is drastically removed via an electric signal and piezoelectric transducer to the AOM, leading to immediate high power in the cavity that depletes the built-up population inversion by stimulated emission. The effect of this sudden lasing process, modulated at 1 kHz, is a kHz train of 20 mJ ~200 nanosecond green pulses (527 nm).

The high-energy 527 nm pump pulses are overlapped at the amplifier's Ti:Sapphire crystal with the 800 nm ultrafast seed pulses from the oscillator. The green pump pulses create population inversion in the crystal, which amplifies the seed pulses in the cavity. Even after stretching the pulses in time, the ~200 picosecond seed pulses are much shorter than each ~200 ns pump pulse. This is exploited in *regenerative amplification* by passing the shorter pulse through the cavity many times during the nanosecond pulse duration such that gain medium saturation and seed pulse amplification are co-optimized (Figure 2-2 [D]). Once the optimal amplification is achieved after many round trips, the pulse is coupled out of the cavity. Out-coupling, or *cavity dumping*, is accomplished using an optical switch to shift the cavity loss from low to high. A Pockels cell and polarizer are used as the optical switch. A Pockels cell applies voltage to an electro-optic crystal, which can tune the polarization of propagating light. The polarizer then retains the pulse in the cavity for amplification or

directs it out of the cavity. The pulse amplification process can be observed and optimized by coupling out to a photodiode detector, which enables precise calibration of the Pockels cell switching times.

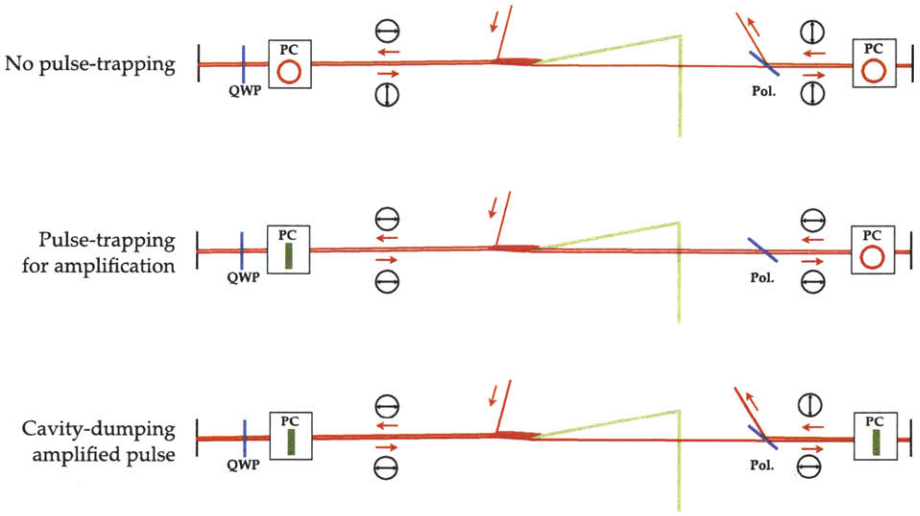

Figure 2-3: Mechanism of a regenerative amplifier in a simplified cavity. A pulse is rejected from (or trapped inside) the cavity by switching off (on) the left-most Pockels cell, rendering the polarization changed (unchanged) after two passes and consequently reflected (transmitted) by the polarizer while the right-most Pockels cell remains off. Multiple round-trips are made, and the right-most Pockels cell is switched on to change the polarization after two passes and dump the amplified pulse from the cavity.

The optical switching steps for amplification and cavity dumping are demonstrated in Figure 2-3. When the left-most Pockels cell is turned off, a single pulse passing through the cavity exits via the polarizer. It is not trapped, and there is no amplification. After the arrival of the nanosecond pulse and gain saturation, the left-most Pockels cell is switched on, trapping the pulse in the resonator for amplification. When maximum amplification is achieved (typically after ~30 roundtrips), the right-most Pockels cell is switched on to act as an out-coupler in concert with the polarizer. The 800 nm pulses coupled out of the amplifier cavity have a repetition rate of 1 kHz, and energies are 2.3 mJ/pulse.

We employ a pulse-picking scheme to down-count the pulse train from 1 kHz to 10 Hz. Operating at this lower repetition rate facilitates single-shot measurements, since many coordinating elements (TTL signals, mechanical shutters, image acquisition and download, etc.) accompany each measurement. In the pulse-picker, we apply a voltage across a Pockels cell to switch the polarization of one pulse for every 100 out of the amplifier (i.e., every 100 ms). A polarizer directs the 10 Hz pulse to the single-shot

setup. For alignment and characterization, it is often preferable to have a higher power laser beam. This is easily accomplished by firing the Pockels cell every other millisecond to achieve a 500 Hz repetition rate.

2.1.2 Pulse optimization and characterization

To deposit energy into a material on a non-thermal timescale (less than 1 ps) or to resolve lattice vibrations (whose periods are in the single picosecond range), the pulse must be compressed to the sub-picosecond timescale.

Thermal lensing, diffraction off dust particles, and other effects can lead to irregularity across the beam's irradiance distribution. These effects can be largely suppressed by focusing the light inside a very small aperture, since scattered light from defects does not focus as tightly as the direct beam. Before the compressor, pulses are expanded by a 3× telescope to avoid damaging the diffraction grating with high peak intensities. This enables spatial filtering at the focus of the first telescope lens with a $50\mu m$ pinhole, which smoothes the irradiance distribution significantly in preparation for the optical imaging to follow in the single-shot measurement.

The pulse is then shortened to below 100 fs by a compressor assembly—a grating and two retro-reflectors (Figure 2-2 [E]). The compressor compensates for a significant amount of group velocity dispersion introduced by the stretcher. The total path length traveled by the pulse inside the compressor is greater than its path length in the stretcher, allowing optimal compensation of the first-order dispersion that was introduced by the gain medium in the amplifier cavity. Pulse durations are characterized using the frequency resolve optical gating (FROG) technique.[81]

Since there is no high-speed electronic means to measure an ultrafast pulse in time, the pulse itself is used to characterize its own temporal profile (optical gating). This is accomplished by splitting the pulse at a beam-splitter, directing one path along a scanning variable delay stage, and crossing the focused beams inside a nonlinear optical crystal such as β-Barium Borate (BBO) to yield second harmonic generation (SHG), described in the next section. Because SHG occurs most efficiently while the pulses overlap in time, the autocorrelation of two identical pulses via a scan delay gives the temporal duration of the pulse.

The temporal duration, however, is not a full enough characterization for our purposes. Many of the optical techniques discussed in §2.1.1 introduce chirp—variation

of the frequency with time. By incorporating frequency resolution with a spectrometer as the detector, and thus measuring the signal spectrum versus delay, the FROG technique demonstrates temporal chirp present in the pulse. The spectral measurement of the pulse as a function of time also allows reconstruction of spectral intensities and spectral phases through a two-dimensional phase retrieval algorithm.[82] Thus the intensity profile and frequency content of the pulse can be visualized in addition to the pulse duration. Typically, FROG traces are obtained continuously while the compressor delay stage is varied, changing the relative path lengths of the pulse's frequency components to shorten the pulse in time. Pulse durations near 70 fs are possible using this method. The intensity profile gained from the FROG measurement also enables important troubleshooting capabilities for the single-shot measurement. As one example, satellite pump pulses, which result from reflections off cavity optics, can arrive a few picoseconds ahead of our pump pulse and compromise the integrity of the single-shot measurement. The FROG measurement allows us to identify such artifacts and verify their suppression.

2.1.3 Tunable-wavelength pulses

In many cases, it is valuable to pump and/or probe the sample of interest at wavelengths other than 800 nm. This may become necessary when a resonant excitation or strong absorption exists at higher energies than 1.55 eV. Additionally, wavelength-dependent measurements can uniquely report on electronic band structure, since a pump (or probe) of varying wavelength can excite (or interrogate) carriers with different wavevectors, i.e., in different regions of k-space. Tunable pulse wavelengths can be achieved by exploiting nonlinear optical effects.

From Eq. 1-1, the polarization of a medium is related to the incident electric field by its susceptibility χ. Eq. 1-1 describes linear light-matter optical phenomena, such as the absorption spectra presented in Chapter 1. However, it is only the first order term in the expansion:

$$P = \epsilon_0(\chi^{(1)}E + \chi^{(2)}E^2 + \chi^{(3)}E^3 + \cdots) \qquad \textit{Eq. 2-2}$$

Because the time-varying polarization of a medium can act as a source of changes to the electric field, Eq. 2-2 is of key interest for manipulating optical properties. A medium's (non-zero) second-order optical susceptibility $\chi^{(2)}$ is responsible for *sum and difference*

frequency generation, discussed below, while the third-order optical susceptibility $\chi^{(3)}$ is involved in the optical Kerr effect.[83] Sum frequency generation (SFG) is an example of a *parametric* effect, where interacting photons at high intensity mix to yield new frequencies without imparting energy to the medium, as in:

$$\hbar\omega_1 + \hbar\omega_2 = \hbar\omega_3 \qquad \textit{Eq. 2-3}$$

Generation of the outgoing photons can be efficient and coherent—and therefore useful for our measurements—when the incoming beams satisfy the phase-matching condition:

$$\hbar k_1 + \hbar k_2 = \hbar k_3 \qquad \textit{Eq. 2-4}$$

with $k_{1,2,3}$ as the photon wavevectors. An energy-level description of SFG is shown in Figure 2-4 [A]. One particularly useful case of SFG is second harmonic generation (SHG), where $\omega_1 = \omega_2 = 2\omega_3$. SHG can be exploited with one color of light, as in the FROG example in the previous section, while SFG more generally requires two. For spectroscopy, generation of a 400 nm pump or probe pulse is easily accomplished by SHG of 800 nm light through a nonlinear optical crystal. However, the need to employ other wavelengths for certain measurements remains.

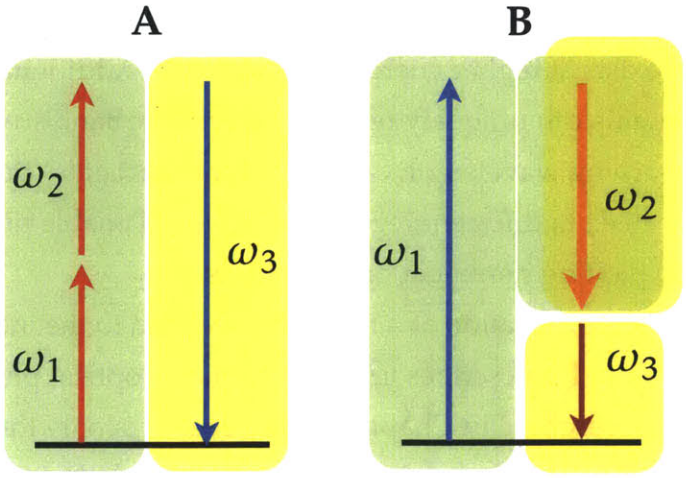

Figure 2-4: Energy-level picture of second-order optical processes for new frequency generation. Green shading indicates incident photons; yellow shading indicates emitted photons. [A]: *SHG of 800 nm light to 400 nm, a special case of SFG.* [B]: *In parametric amplification, one DFG mechanism is favored, and we amplify a chosen seed frequency* ω_2.

A straightforward method for obtaining tunable frequencies is to generate a broadband continuum and select the wavelength of interest using a frequency filter. In

this scheme, weak (~$1\mu J$) 800 nm pulses are focused into a 2 mm sapphire plate. (Stronger fields result in stronger non-linear effects as suggested by Eq. 2-2, but unwanted effects and instabilities necessitate a balance determined by the application.) The Kerr effect causes the center part of the beam to travel more slowly through the medium so that the beam starts to self-focus. At the resulting high peak intensities, new frequencies are generated across the optical continuum via non-linear interactions through an as yet unresolved mechanism.[84,85] The output is a spatially coherent white light. Wavelengths from ~420 to 750 nm can be isolated by placing a filter in the beam path. This method of frequency-tuning is sufficient for conventional pump-probe measurements, which are often useful for sample characterization preceding single-shot measurements. Taking 600 nm light generation as an example, $1\mu J$ / pulse of 800 nm light incident on the sapphire generates about $0.1nJ$ / pulse of 600 nm light using a 20 nm bandpass filter. For measurements that average over many scans and employ a photodiode detector, this pulse energy is typically sufficient.

For single-shot measurements, however, we employ little to no averaging and detect signal by spatially resolving photon intensities on a photodiode array. The low photon counts that result from using the above method are not sufficient to overcome experimental noise challenges. Pulse energies in the sub-nJ range at the sapphire result in downstream CCD detector counts of 10-100 above background, using at most 2% of the 12-bit camera resolution. Instead we use a non-collinear optical parametric amplifier (NOPA) to amplify selected frequencies from the broadband continuum. NOPA operation is based on several nonlinear processes, summarized briefly here. Further experimental details and specifications developed for single-shot operation are outlined in Poulin, 2005.[86]

Similar to an amplified laser system, a NOPA employs two inputs: a pump pulse and a seed pulse. The pump pulse 'prepares' the conditions for amplification, and the seed is amplified. The pump is generated by SHG of 800 nm light after the compressor. By focusing the 400 nm pump close to a nonlinear BBO crystal, new frequencies are emitted via difference frequency generation (DFG). This mechanism is shown schematically in Figure 2-4 [B] with ω_1 incident and ω_2 and ω_3 emitted. Strictly, the pair of photons preferentially emitted should be determined by the phase matching angle. However, by employing a non-collinear geometry incident on BBO, wavelengths over a very broad bandwidth may be phase-matched simultaneously, as first reported by Gale,

et al.[87] Thus many frequency pairs ω_2 and ω_3 are emitted. In an OPA application, the lower frequencies ω_3 are in the infrared range and collectively called the *idler*, and the higher frequencies ω_2 are in the optical range and called the *signal*. The generation of these frequencies occurs in a cone-shaped geometry and is called parametric fluorescence.[88] This is spontaneous two-photon emission from a virtual energy level created by the incident photon.

We note from the energy picture in Figure 2-4 that for every ω_1 photon annihilated, an ω_2 photon is created. In this way, the ω_2 frequency can be amplified: ω_1 prepares the state, and the decay process for a given two-photon pair ω_2 and ω_3 is stimulated by the presence of ω_2. By seeding the DFG process with a chosen wavelength, we can amplify that wavelength. For amplification, the broadband seed is generated using a sapphire crystal by the process described above. The continuum is then focused into the crystal and spatially overlapped with the pump. Because of the different velocities of frequency components in the continuum, only a small portion will be temporally overlapped with the signal and idler photons being generated. This is precisely the frequency portion that is amplified, and we tune its selection by an upstream delay stage in the seed path. The process introduces significant chirp as pulses travel through lenses and nonlinear crystals, so the pulse is passed through an additional compressor and optimized using the FROG technique.

2.2 Single-shot Optical Instrument

2.2.1 Measurement via spatio-temporal mapping

Key to the single-shot measurement is an optical probe that encodes temporal dynamic information across its spatial profile after interacting with the sample, avoiding the need for repeated measurements. The probe is derived from a single laser shot that also produces the pump pulse, and all dynamical information is collected in real-time after the single pump perturbation. This section introduces the concept and optical details of the time-dependent probe pulse; the full optical layout of the single-shot instrument is presented in §2.2.2.

A single probe pulse passes through two crossed echelon optics, which resemble glass staircase structures about 1 cm across. Each echelon has 20 discrete and uniform steps in thickness, formed by stacking layers of fused silica. The echelons were

manufactured by *Okamoto Optics*. When the beam propagates through an echelon, space-dependent time delays are introduced over the beam cross-section. A schematic illustration of the echelons and the resulting probe beam array is shown in Figure 2-5. The thickness of each step on the thicker echelon is $300\mu m$; the thickness of each step on the thinner echelon is $15\mu m$. Due to the refractive index of fused silica ($\eta = 1.45$), light passing through fused silica of thickness d will be temporally delayed relative to light propagating in air. This leads to characteristic and discretely increasing time delays for light propagating across each echelon given by the relation:

$$\Delta t = (\eta - 1)\frac{d}{c} \qquad \textit{Eq. 2-5}$$

For 800 nm light, the thick and thin steps impart temporal delays of 453 fs and 22.7 fs, respectively. When one echelon is rotated 90° relative to the other, a pulse propagating through the echelons is deconstructed into a temporal grid. That is, the 20 portions of light that experience 453 fs delays relative to one another are each further sliced into 20 portions that experience 22.7 fs delays relative to one another. This array of 400 pulses is shown schematically in Figure 2-5. The slowest pulse is delayed 9.1 ps relative to the first (20×22.7 fs).

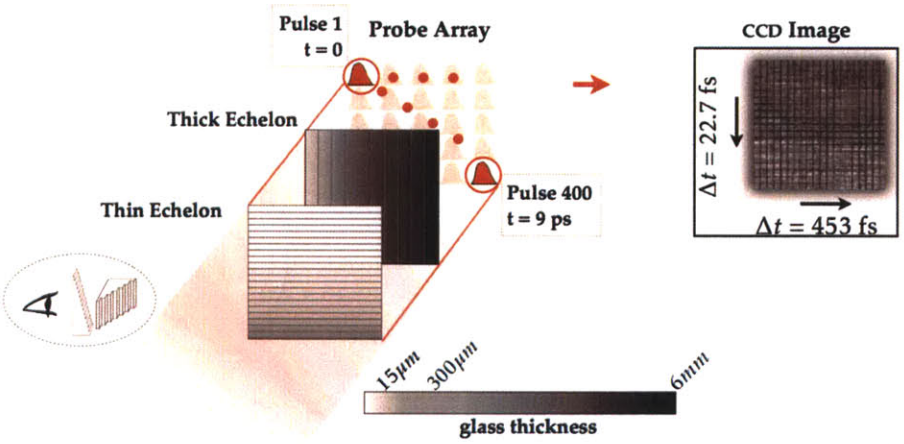

Figure 2-5: Concept of the dual-echelon single-shot measurement. A beam is passed through a thin echelon with 15μm steps running down and a thick echelon with 300μm steps running across, imparting relative time delays of 22.7 and 453 fs, respectively, and a total time window of 9.1 ps across 400 pulses. The beam array is eventually imaged onto a CCD camera, as shown on right.

The experimental implementation of the echelon concept is shown in Figure 2-6. The Gaussian beam is expanded significantly, and its center is selected and collimated so that the intensity is nearly uniform over the echelon area. After generation of the spatio-temoral pulse array by the echelons, the array is focused onto the sample. Each pulse arrives at the same sample location so that the sample spot experiences a train of incident pulses spaced by 22.7 fs and lasting 9.1 ps due to their relative delays. The probe pulses interact with the sample, typically after a perturbation by the pump. The probe pulses transmit through or reflect off the sample, containing time-dependent intensity information that reports on the photo-excited dynamics of the sample. The probe is collimated after the sample so that the pulses reconstruct the echelon grid. Finally, the grid is imaged onto a CCD camera, and we extract the time-dependent signal by analyzing the intensity as a function of location within the grid image.

An example image is shown to the right in Figure 2-5. Time delays increase down each column in increments of 22.7 fs, and the time difference between any two grid squares in a row is 453 fs. In the image, each grid square (timepoint) is identifiable from its neighbor due to diffraction off the echelon steps. As is described in detail in §2.3.3, for a successful measurement we require various correction images. One correction is sourced from a reference grid that is generated by the echelons but bypasses the sample, and the other is sourced from a background measurement in the absence of the pump pulse.

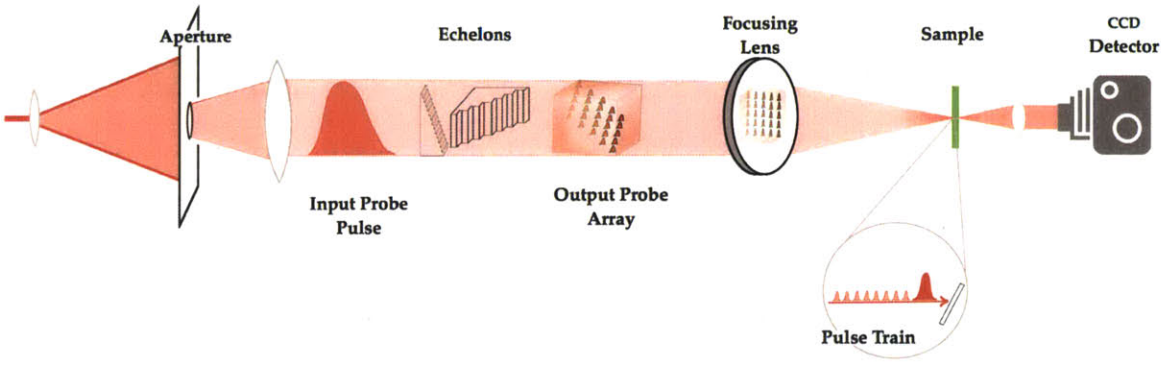

Figure 2-6: Experimental implementation of the dual-echelon time-dependent probe concept. The probe pulse is expanded and the center is collimated before echelon grid formation. The spatio-temporal grid of pulses is formed and focused onto the sample by a lens. The sample experiences a stream of pulses at the same location, and the pulse grid is then reconstructed onto a CCD detector. A strong pump pulse is indicated preceding the probe pulse train.

2.2.2 Optical layout

We have described the generation of high-energy ultrafast pulses and the dual-echelon single-shot concept. Here we describe the experimental details of employing amplified ultrafast pulses for single-shot spectroscopy measurements. Figure 2-7 shows an overview of the single-shot experimental setup operating in a reflection mode geometry with a single pump path.

Before the compressor and spatial filter, 10 Hz pulse energies are 2.2 mJ/pulse to 0.2 mJ/pulse. A half-wave plate and polarizer pair upstream in the pulse-picker setup enable this tunability. The light polarization is adjusted by the wave-plate angle, and the polarizer permits only horizontally polarized light. The pulse-picker is 95% efficient when operated for the maximum 10 Hz pulse energy. Values referenced below as 'maximum' are derived from the highest wave-plate setting; 'minimum' values from the lowest.

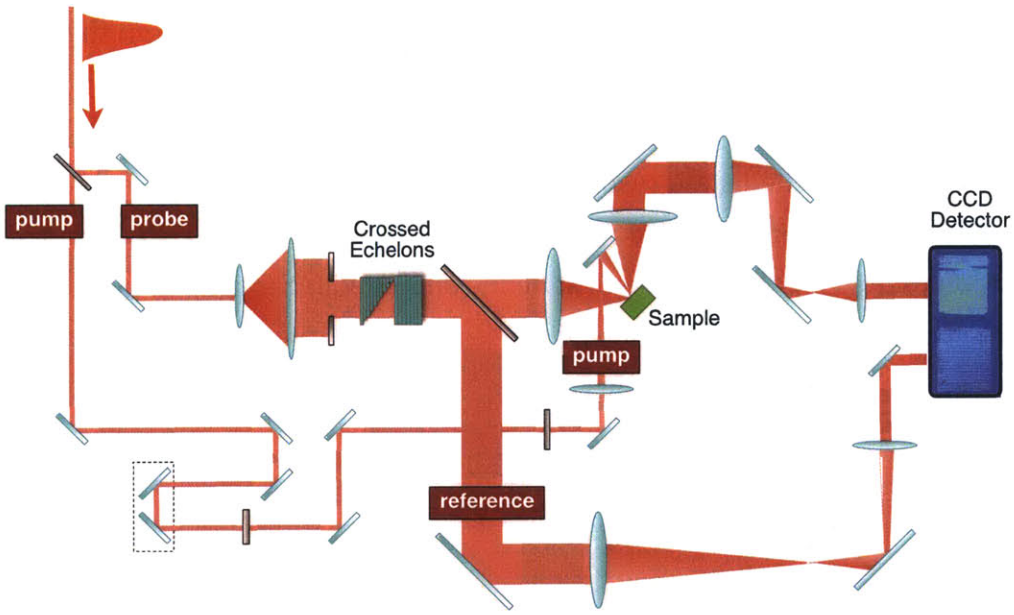

Figure 2-7: Schematic illustration of the single-shot instrument after pulse generation and compression. The pulse energy is split along pump and probe paths of varying relative path lengths. The probe beam is expanded and separated into a spatio-temporal grid via crossed echelons. A reference grid is split off from the probe, and both grids are imaged onto a CCD detector. The layout is shown in the reflection geometry; Figure 2-9 shows both reflection and transmission options.

There is a combined loss of ~50% power over the spatial filter and the grating compressor. This can be reduced to a 25% loss by increasing the spatial filter size; however, this results in a loss of mode quality and yields little practical gain. The beam is then split along two paths by an 80/20 beam-splitter, with the majority of power retained in the pump pulse. The maximum pump energy after the beam-splitter is 0.7 mJ/pulse, and the maximum probe energy is 0.2 mJ/pulse. We first consider the pump path.

Pump Path

A mechanical shutter permits or blocks arriving pump pulses via an electronic signal. This shutter allows a true single-shot experiment by ensuring that all measured material dynamics result from the one pump pulse that interacts with the sample and also enables a reference measurement (described below). Details on the shutter timing and electronic signal integration are described in §2.3. The permitted pump pulse then passes through a series of mirrors, beam-splitters, and retro-reflectors that enable an optional two-pump measurement. Figure 2-8 shows this assembly. From the one pump pulse that the shutter admits, we can create two pump pulses with different path lengths (arrival times at the sample) and intensities (perturbation strength) to perform spectroscopy on an excited state system. In practice, the first pump is used to photo-excite the sample far from equilibrium, and the second pump is employed as a weak perturbation to interrogate the system state in concert with the time-dependent probe. Data from two-pump measurements are presented in Chapter 4 and Chapter 5.

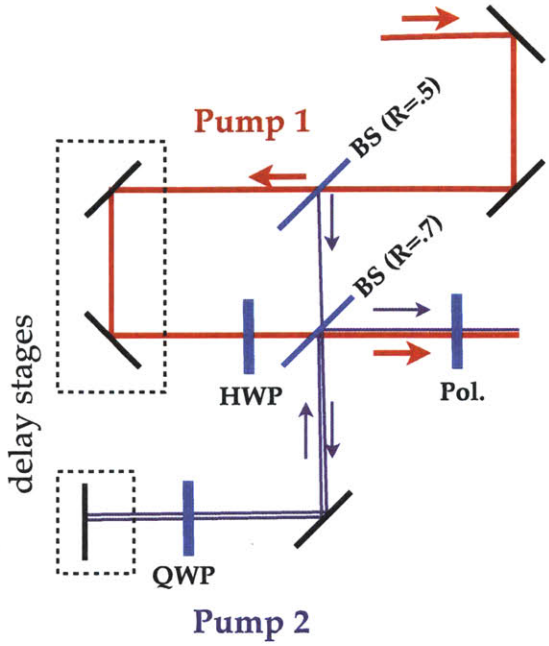

Figure 2-8: Two-pump setup. An 800 nm pump is split into two pumps using a series of beam-splitters and retro-reflectors. The path of pump 1, which retains most of the incoming power, is shown in red; the path of pump 2, which acts as a weak perturbation, is shown in purple. Both pulses are 800 nm; color is for clarity. A single pass through a half-wave plate (pump 1) and a double-pass through a quarter-wave plate (pump 2), when paired with a polarizer, provides independent power attenuation.

When the two-pump setup is in use, the stronger pump pulse (*pump 1*) retains 55% of the incoming pulse energy, and the weaker pump pulse (*pump 2*) retains 15% of the incoming pulse energy. (30% is lost to multiple reflections off beam-splitters). The pump 1 retro-reflector is mounted on a delay stage that introduces time differences relative to the probe path, permitting flexibility in measurements. While our optical measurement is limited to a 9.1 ps probe window, we are able to translate the relative timing of this observation window to occur during or up to 1 nanosecond after pump excitation by shortening the pump path by up to 30 cm. The pump 2 retro-reflector, a single mirror, is mounted on a short delay stage. While the pump 1 delay stage is moved in discrete steps for a set of two-pump experiments (e.g., to observe the system both 5 ps and 50 ps after pump 1 arrival), the pump 2 delay stage is used for fine-tuning the relative temporal overlap between pump 2 and the probe pulse. The pump 1 delay stage is never scanned continuously as it is during a conventional pump-probe

measurement. Rather, our ultrafast time sampling is introduced solely by spatio-temporal mapping of the probe pulse.

Each pump path contains a half-wave plate: pump 1 passes once through a half-wave plate, while pump 2 passes twice through a quarter-wave plate. Together with a single downstream polarizer common to both paths, the wave-plates independently allow up to 90% power attenuation for each pump pulse. Such polarizer-regulated attenuators also enable quick switching of pump and probe polarizations during an experiment. This can be valuable either for the measurement itself—when polarized light preferentially interacts with a material excitation—or for noise reduction using an additional polarizer before the detector. A variable neutral density filter wheel is in the collinear pump path to allow for additional continuous attenuation up to a factor of 10^4. Thus, the energies of pump pulses 1 and 2 can be tuned from 0.4 and 0.1 mJ/pulse, respectively, to the single nJ/pulse range.

A lens (200 mm focal length) focuses the pump pulse of beam radius 5.2 mm (half-width at $1/e^2$ intensity) onto the sample at an incident angle of 22.5 degrees. The lens is mounted on a delay stage and can be adjusted so that the pump's focus is between 3 and 1 cm behind the sample. This varies the beam radius on the sample from 700 to 300 μm. It is typically preferable to employ a larger pump spot on the sample for two reasons. As in all pump-probe measurements, if the probe size on the sample is larger than the pump size, we reduce the signal-to-noise ratio (SNR) by gathering information from an unperturbed area. Unique to our measurement, in practice individual probe pulses do not focus to one identical spot and may overlap with a gradient of pump intensity. In this case, probe pulses will report on variability in the perturbation strength that is inseparable from real signal. Both effects can be minimized by ensuring that probe pulses interact only with the large, uniform center of the pump intensity profile. In all, the measures described above enable a tunable pump fluence incident on the sample from 100 mJ/cm^2 to 10 nJ/cm^2.

Probe and Reference Paths

We next consider the 20% of beam power —a maximum of 0.2 mJ/pulse after the beam-splitter—directed to the probe path. Pertinent calculations referenced below are shown in §3.3 in the context of instrumental analysis. After losses over reflective optics and an additional polarizer, the maximum probe energy before the optics in Figure 2-6

is typically 0.1 mJ/pulse. The probe path also contains a neutral density filter wheel for variable intensity, which can decrease this pulse energy down to 0.01 μJ/pulse.

Preceding the telescope that prepares the probe beam for the echelons, the probe beam radius is 4.7 mm (half-width at $1/e^2$ intensity). The probe passes through the first lens of an 8× magnifying telescope (focal length 75 mm). Prior to the telescope's collimating lens, we employ a 1″ spatial filter as described above. The spatial filter selects 25% of the original probe power at the beam's center, and the selected portion continues to diverge. A 600 mm lens collimates the selected portion. After collimation, the non-Gaussian beam is 29 mm in total diameter and the maximum pulse energy is 25 μJ/pulse.

The probe pulse passes through the crossed echelons. The echelons are placed as close to each other as their mounting will allow with both sets of steps facing inward to optimize the quality of the echelon image on the CCD camera. There is significant diffraction off the outer edges of the echelons, and we also employ a square aperture of the echelon cross-area size (1 cm × 1 cm) to render the propagating grid well defined. The beam power is reduced by an additional 80% by the echelon aperture, rendering the probe grid array energy (all 400 pulses) 5 μJ maximum after grid formation.

After the temporal array is generated, we employ a beam-splitter (R = 0.4) to create a reference grid from the same pulse as the probe. The reference grid is reflected, bypassing the sample, and is imaged onto the CCD camera alongside the probe grid. Because the grid that interacts with the sample contains the time-dependent signal, we distinguish the two grids as *signal* and *reference.* Their paths are shown in Figure 2-9. The reference grid enables correction for laser shot noise variation, as described in §2.3.3.

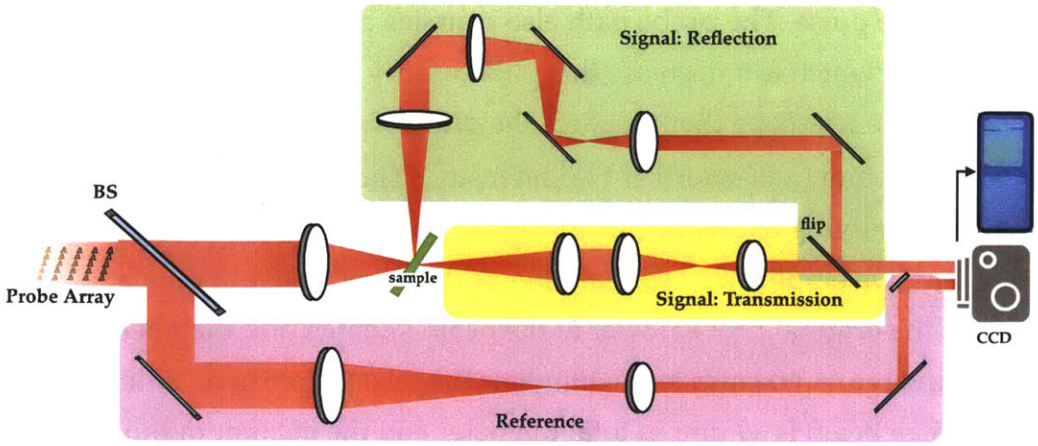

Figure 2-9: Optical layout after generation of the echelon array. The reference path is shaded in purple. The signal grid travels in either the reflection (shaded in green) or transmission geometry (shaded in yellow) depending on the measurement details. A flip mirror activated for reflection mode enables easy switching. The CCD camera sits at the imaging plane for all three imaging systems shown. Focal lengths are not drawn to scale.

At the sample, the probe array has maximum total energy 3 μJ / pulse, and each of the 400 probe pulse that interact with the sample carries ~8 nJ. The array of temporally and spatially separated probe pulses is focused onto the sample by a 100 mm focal length lens to an approximate size of 45μm across. Thus when the pump (of radius 700-300 μm) and probe are perfectly overlapped, each probe pulse experiences 1-5% variations in pump intensity, depending on the focused pump spot size. The intermediate case is shown in Figure 2-10.

After interacting with the sample, the majority of the non-absorbed probe pulse intensity from the signal grid is either reflected from or transmitted by the sample, depending on the sample properties, its thickness, and the light wavelength. The single-shot instrument can operate in either geometry by simply flipping a mirror before the CCD camera, as shown in Figure 2-9. The camera is mounted on a translation stage to accommodate the slight variations in imaging optics.

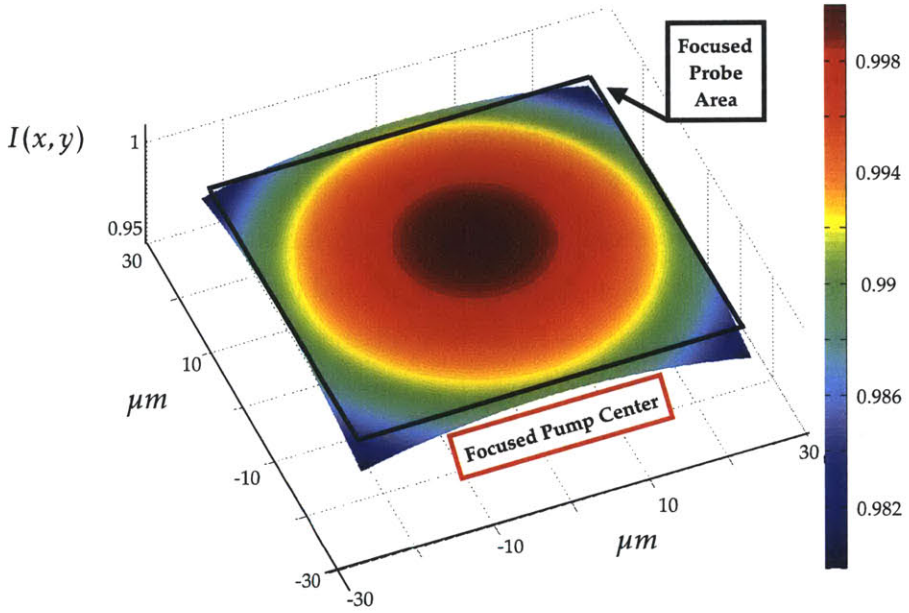

Figure 2-10: Centermost part of pump's focused Gaussian intensity (with a focused beam radius at $1/e^2$ intensity of $500\mu m$). The open black square shows the focused probe region. At this pump size and for near-perfect overlap, each probe pulse sees up to a 2% variation in pump intensity.

Imaging and detection

Signal detection in our single-shot measurement is achieved by imaging the echelon grid of pulses onto a CCD camera as shown in Figure 2-9. Because the echelon pair occupies about 1 cm in the beam propagation direction, no exact object plane exists for perfect imaging onto the CCD. In practice, placing the object plane between the two inward-facing echelons optimizes reconstruction of the image. In the reference arm, a single telescope is employed to reduce the grid size by 3× (600 mm focusing lens, 200 mm collimating lens). This process inverts the image, which is accounted for in our analysis. In the signal arm, we employ a $4f$ imaging system before reducing the grid size by ~2.5× (reflection geometry: 300 mm focusing lens, 125 mm collimating lens, transmission geometry: 200, 75mm collimating lens). Within the $4f$ imaging telescope (both lens focal lengths 100 mm in both geometries), the signal echelon grid is focused onto the sample and reconstructed. Because the signal grid passes through two telescopes, the final image is in the correct upright position. The side-by-side signal and reference images that arrive at the camera are processed as described in §2.3.3.

The CCD camera detector employs a micro-lens and a 1344 × 1024 array of detector elements that serve as pixels. Photons incident on the chip generate electron counts proportional to the light intensity. Employing the chip's pixel array enables the spatial resolution of the light intensity—retaining the temporal information carried by the spatio-temporal probe array. Each pixel is a bin which retains for a time the number of electrons corresponding to incident light intensity at that pixel location. The image is created in a storable form when an analog-to-digital (A/D) converter adjacent to the pixel array processes the electrons in each pixel and stores the result. The counting is accomplished by the consecutive charge transfer from one bin to the next until all have been read. This process also gives the charge-coupled device (CCD) its name. There is some error in this process which is called *read noise.*

The camera employed for single-shot measurements is the ORCA-ER from Hamamatsu. It has an effective area of 8.6mm (H) × 6.9 (V) mm and 1344 × 1024 pixels, with each pixel being 6.5μm square. Under normal operation, it can acquire up to 8 images per second, and it is triggered electronically as described in the next section. The camera is cooled by a Peltier heat pump, which maintains the A/D converter temperature and reduces both read noise and *dark noise* (movement of electrons from thermal rather than photon energy). The camera's dynamic range is 2250, its read noise is 8 electrons, and the A/D converter is 12-bit. These important camera properties determine the sensitivity of our detector. The dynamic range is the ratio of a pixel's full well capacity and the read noise. Thus each bin, or pixel, can contain about 18,000 electrons. The camera's quantum efficiency (percent conversion of photons to electrons) is shown in Figure 2-11. At 800 nm, the quantum efficiency is ~15%.

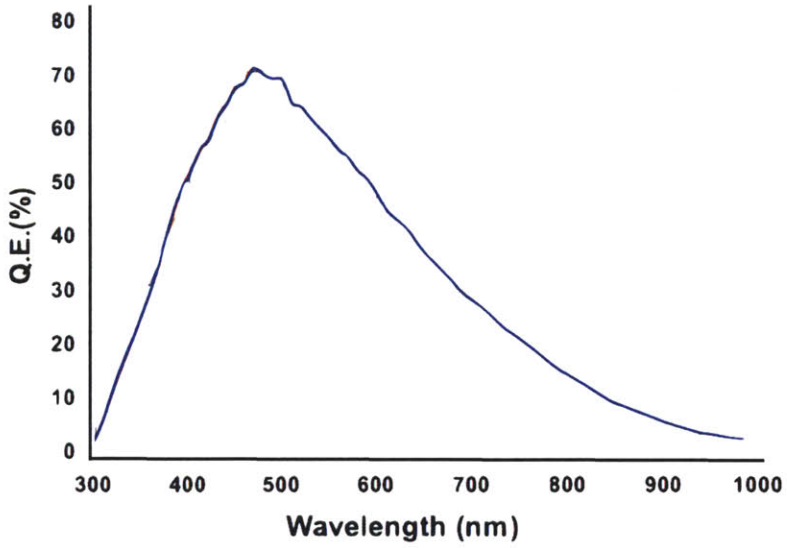

Figure 2-11: ORCA-ER spectral response curve shows the camera's quantum efficiency under high light conditions. From Hamamatsu Corporation. Available online: http://www.spectracore.com/cameras/pdf/QECurves.pdf

Given the image reduction by both the lenses in the optical setup and the camera's micro-lens, each grid point from the probe array occupies about 30×30 pixels on the CCD chip. On average then, 800 nm light will saturate the camera when the incident photons per echelon square exceed 1×10^8 ($\frac{18000\times30^2}{0.15}$), or when the grid-pulse energy exceeds 25 picoJoules. Grid pulses can be well above that range as discussed previously (8 nJ maximum), so we frequently place neutral density filters before the camera lens to reduce absolute intensity without changing the intensity profile. The standard procedure is to use as near to the full dynamic range as possible without saturating the camera. Pixel capacity does not convert directly to image resolution; the A/D converter must be sufficiently sensitive to avoid excess information loss. The 12-bit converter can encode an analog input (electrons) to $2^{12} = 4096$ different levels. Roughly, this corresponds to 4-5 electrons per pixel value level. Thus the stored image is a matrix of pixel values between 0 and 4096, where the value scales with the number of incident photons (tempered by the read noise, dark noise, and quantum efficiency).

2.3 Single-shot Instrument Operation

§2.2 described the optical details of the single-shot measurement; this section describes the implementation of a successful measurement by alignment procedures, instrumental electronics, and image collection.

2.3.1 Alignment

Careful alignment is critical to the success of a single-shot measurement, because any spatial variation experienced by the signal probe array left uncorrected yield error in our time-domain data. Spatial variation can be introduced by many factors, such as the probe beam intensity profile (signal and reference beam paths differ, yielding imperfect correction), the pump beam intensity profile, imperfect alignment through lenses, sample irregularity, and damage or dust on the instrument optics.

The echelons are mounted on three-dimensional adjustable stages and aligned by their retro-reflection (vertical and transverse echelon axes) and by their diffraction patterns relative to the beam propagation axis downstream (longitudinal echelon axes). The sample is mounted on a 360° full-rotation Gimbal mount so that the surface interacting with the signal probe array remains in its focal plane when translated along any axis. The Gimbal mount is further mounted on translation stages that enable x, y, and z adjustments in either the reflection or transmission geometry. Movement out of the plane can increase the effective size of the probe signal array during the measurement and/or change its incident angle, causing probe pulses to experience greater variations in pump intensity and thus decreasing the data reliability. Additionally in the reflection geometry, movement of the sample out of the focal plane causes misalignment in the imaging optics and compromises the final image quality. Full rotation capability at the mount's center minimizes these effects.

The alignment procedure for the reflection geometry is outlined here. If needed, temporal and spatial overlap between pump and probe are first identified via a strong signal on lithium niobate, which is relatively insensitive to optimal overlap. This signal can be identified without data processing by inserting a polarizer in the transmitted probe light and observing strong light attenuation in the echelon image. The sample for the intended measurement is placed in the mount, and the sample rotation axes are optimized so that the echelon grid is aligned well through the downstream imaging

optics. A camera trained on the sample and a video output are used to mark the beam sample location on the monitor. This is a relative measure of the distance between different sample planes. If the sample is moved, the probe beam will appear to be translated on the video output. To achieve alignment of the sample in the probe signal array focal plane, the sample stage is swapped with a mounted razor blade. The razor blade is translated until it sits in the same plane as the sample, as marked on the monitor.

At the focus of a laser beam, all of the beam information is at its most concentrated. We exploit this fact to place the probe signal array focus at the sample (razor blade) location by translating the razor blade through the beam and optimizing the probe focusing lens location for a uniform disappearance of the echelon grid as the razor blade passes through the beam. To accomplish this, the probe signal array's focusing lens is mounted on a translation stage in the beam propagation direction, and the CCD camera is operated in a continuous capture mode. At this stage, the probe echelon array is focused onto the sample surface location and the downstream imaging optics are aligned for reflection off the sample.

Still using the razor blade to avoid pump damage to the sample, the pump is directed to the probe location using a mirror and the sample camera video output. Both pump and probe beams must be attenuated significantly to distinguish the center of each beam and thereby achieve good overlap. After alignment of the pump and probe beams on the razor blade, the sample stage is returned and an alignment check (of probe focusing and pump-probe overlap) is performed. It is advantageous to check pump-probe alignment on the sample near the edge or a region of damage, since doing so provides some scattered light for observation. Finally, the probe signal array propagation through the downstream imaging optics is checked for slight variations in alignment on the CCD camera video output, and adjusted as needed using mirrors in the imaging path. If the sample is rotated in this process, the process must be repeated iteratively.

The image plane for the three imaging systems shown in Figure 2-9 is approximately the same. To correct for slight variations, however, both the camera and the final lens in the reference path can be translated in the beam propagation direction (z). First, the camera position is adjusted for the chosen geometry (reflection or transmission) by optimizing the signal image quality, and then the reference path lens

position is adjusted by optimizing the reference image quality. The camera can also be translated in the x (horizontal) and y (vertical) directions to locate the probe signal array in the desired location on the CCD chip. A mirror immediately before the camera in the reference array path places the reference array alongside the signal array in the desired location.

2.3.2 Electronics and Timing

Laser pulse generation and the single-shot measurement are possible only with precisely controlled fast electronics that orchestrate the process. We here outline the electronics that facilitate 10 Hz ultrafast pulse generation (described in §2.1.1) and detail the electronic timing scheme built for the single-shot measurement. Figure 2-12 diagrams the connectivity (curved black lines), synchronization (dotted blue lines), and electronic signals (dashed red lines) that enable a single-shot measurement.

A synchronization and delay generator (SDG II from Coherent) coordinates the mode-locked output of the oscillator with the Q-switching of the pump laser to facilitate amplification. The RF driver from the mode-locked system sends an 80 MHz pulse, and the Q-switch driver receives feedback from the SDG to synchronize its 1 kHz Q-switching at even intervals of oscillator pulses. This kHz signal becomes an electronic 'clock' or trigger that is synchronized with the amplified laser pulse output. To amplify a laser pulse, the SDG fires the first Pockels cell to couple a pulse into the cavity and fires the second Pockels cell at a time delay relative to the first to couple the pulse out. The time delay between cell firing dictates the number of round trips. Synchronization with the mode-locking driver and the kHz clock ensures that only one pulse is amplified and that the output is at 1 kHz.

The SDG sends a 1 kHz trigger to a delay generator (DG). The delay generator uses two output TTL pulses to turn the pulse-picker Pockels cell on and off via a high-voltage power supply. The Pockels cell is fired every 96 ms (relative to an initial pulse from the 1 kHz clock) and turned off after 10 μs, generating a train of 10 Hz laser pulses directed to the single-shot apparatus by a polarizer (Figure 2-12 [1]). The timing is adjusted to optimize 1 kHz pulse extinction in the 10 Hz line with a photodiode and oscilloscope after the pulse-picker setup. Though we employ a 10 Hz repetition rate pulse train, during single-shot measurement acquisition only isolated pulses are released. We employ two mechanical shutters—one upstream of the compressor, and one in the

pump line to permit background measurements in the pump's absence. At the start of a measurement, both shutters are closed.

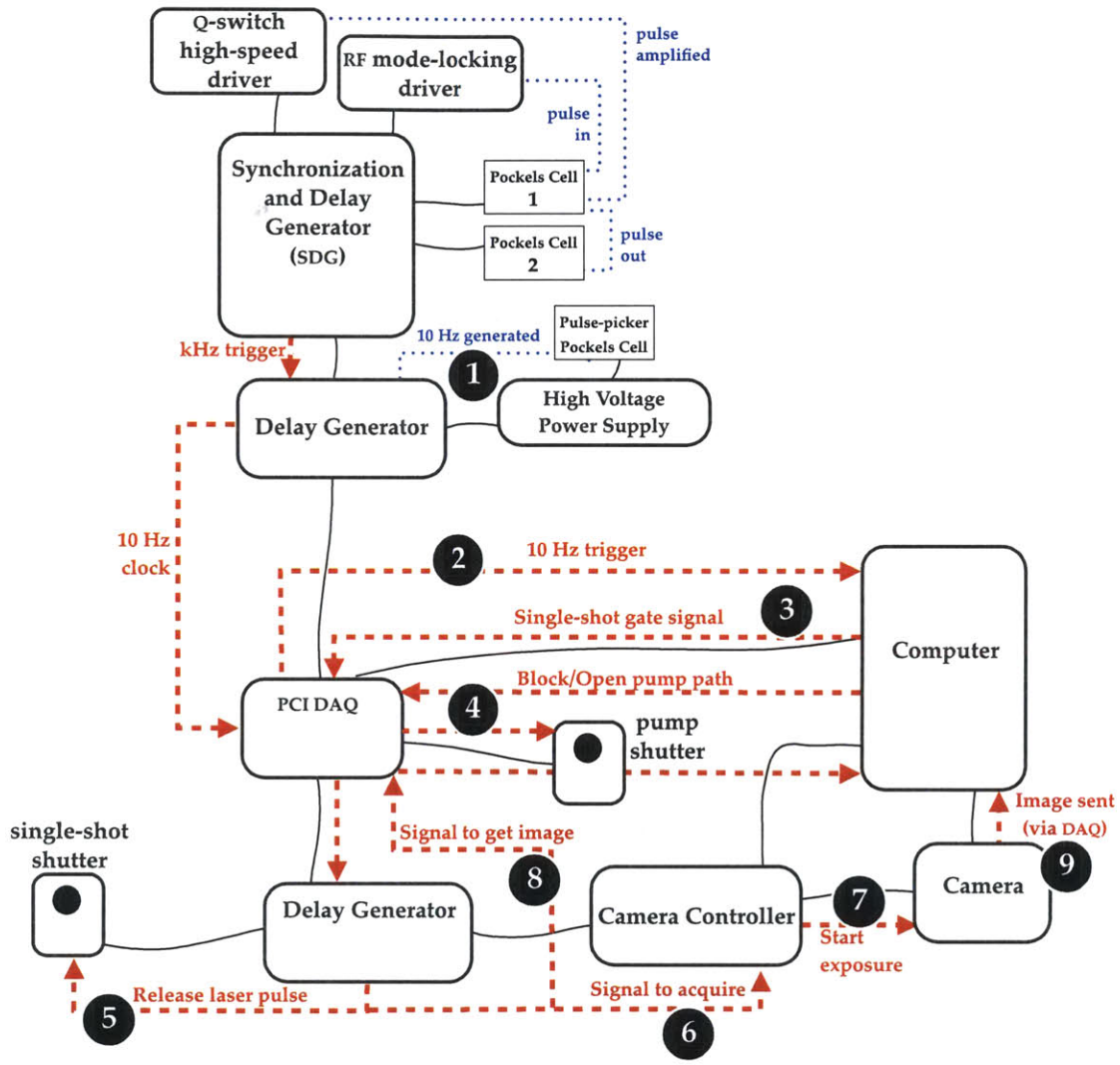

Figure 2-12: Connectivity diagram for the laser system and single-shot instrument. Curved black lines show physical connections. Dotted blue lines indicated synchronized processes in the laser system described in §2.1.1. Dashed red arrows indicate the sending of TTL pulses that facilitate the single-shot measurement. Numerals indicate an approximate time-ordering of signals; this time-ordering is set by the delay generators and the LabView acquisition code.

The DG also creates a pulse every time the Pockels cell is fired that is offset by 50 ms. This 10 Hz 'clock' is used to tell the electronics when a laser pulse will arrive after the user starts the measurement process. The 10 Hz clock is sent to the computer as a trigger pulse via a PCI data acquisition card (DAQ) (Figure 2-12 [2]). When the

measurement process is launched (via a user interface on a LabView program), the program monitors the trigger line from the PCI to wait for a TTL pulse. When a pulse arrives, a timer is set, and the following sequence is set in motion to coincide exactly with a single laser pulse's arrival at the camera. In fact, this sequence is performed *twice*—once with the pump shutter blocked to permit a background measurement, and once with the pump shutter open to photo-excite the sample and measure the resulting dynamics—the data measurement. The sequence is diagrammed in Figure 2-13, with the probe and pump pulses used for the measurement displayed as though there were a photodiode in the pump and probe paths monitoring for the released pulses.

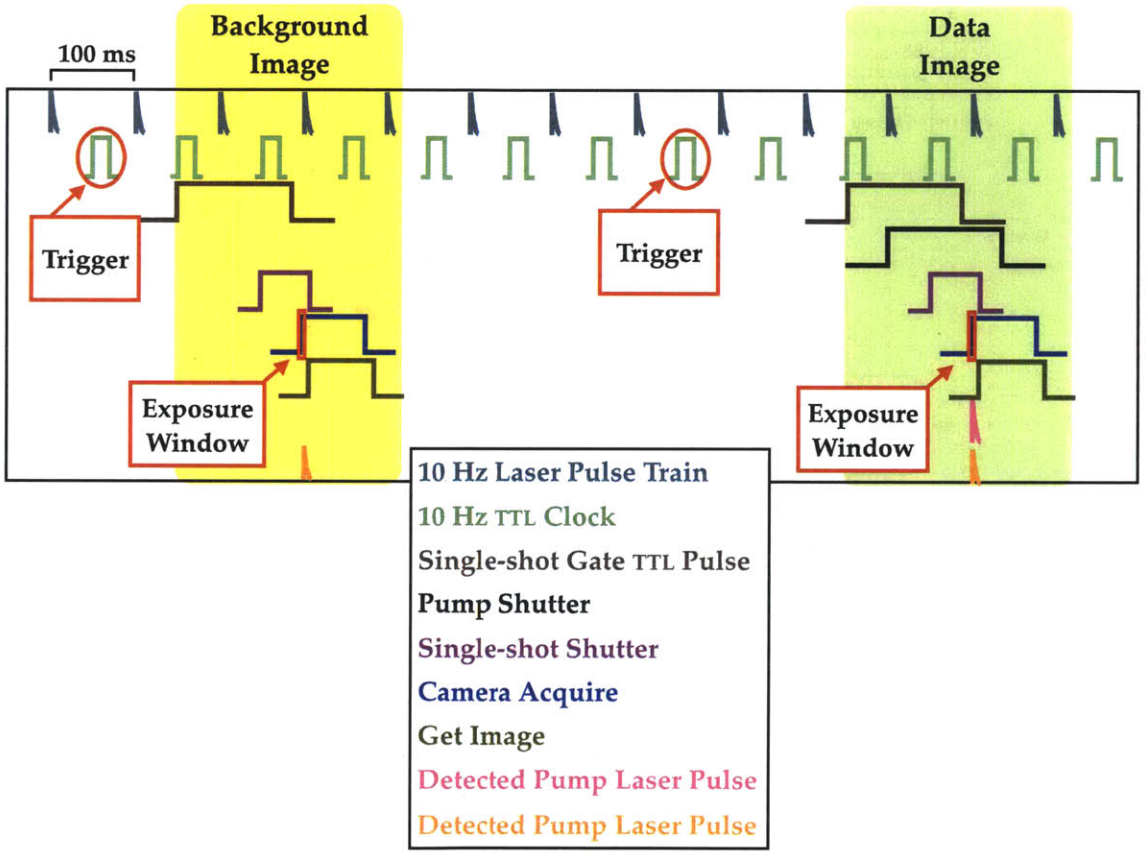

Figure 2-13: Pulse ordering for a single-shot measurement. Shaded in yellow is the first iteration without pump for a background image; shaded in green is the second iteration with pump for a data image. Circled are the two trigger pulses that launch the process. The exposure window is shown as a red rectangle, its width set by the computer program. The 10 Hz pulse train and the admitted single pulses for measurement are shown as photodiode traces on an oscilloscope; detected laser pulses are shown as photodiode traces downstream of the shutters.

The program generates a digital TTL pulse called the 'gate' pulse 100 ms after the 10 Hz trigger. There is one gate pulse per image capture. The pulse is sent to a second

DG via the PCI (Figure 2-12 [3]). A second digital TTL pulse is sent to the pump shutter controller via the PCI if the shutter is to be opened (i.e., on the program's second iteration) (Figure 2-12[4]). When the DG receives the gate pulse trigger, it triggers three more pulses at specified time delays. The first, 100 ms later, opens the upstream shutter for 60 ms to allow one laser pulse from the 10 Hz train through (Figure 2-12 [5]). The second, 149.8 ms after the gate pulse arrives, sends a signal to the camera controller to acquire the image (Figure 2-12 [6]). The camera controller immediately opens the camera shutter (Figure 2-12 [7]) to expose the CCD detector for ~1 ms just as the echelon grid arrays arrive at the camera—the signal probe array having interacted with the sample, with or without the pump excitation. The third triggered pulse, 10 ms after the acquire signal, tells the PCI to find the image in the camera's temporary memory (Figure 2-12 [8]), and the image is transferred to the computer via the DAQ functionality of the PCI (Figure 2-12 [9]). The exposure time window is set by the acquisition program.

Each timing function described above is an important variable in the measurement design, and is integrated with parameters in the LabView code that runs the single-shot measurement. The 10 Hz clock is offset by the 10 Hz laser pulse train by 50 ms; thus, the camera exposure timed 149.8 ms after the single shot gate pulse arrival captures a laser pulse at the camera. The timings are calibrated using a digital oscilloscope, a photodiode in the pump path for reference, and the echelon grid image capture. The 1 ms exposure time window can be translated so that it captures exactly one pulse, eliminating the background 1kHz signal from the pulse-picker inefficiencies.

2.3.3 Image Collection and Analysis

One single-shot measurement—the real-time visualization of a material's response to a single laser pulse—involves obtaining two images. The two images are the *background image*, taken with the pump blocked, and the *data image*, taken with the pump unblocked. The first enables us to filter out the probe's interaction with the sample from the second image, so that the signal is due primarily to the pump's presence on the sample. Each captured image has two grid arrays—the *signal grid* on the left, the *reference grid* on the right, which arrive at the camera after being split after the echelons and propagating down different paths. Normalizing the *signal* grid in the *data* image by the *signal* grid in the *background* image isolates the response of the pump pulse from the probe-sample interaction. By comparing the two *reference* grids between the

background and *data* images, we can approximately correct for variation in laser intensity from the first shot to the second.

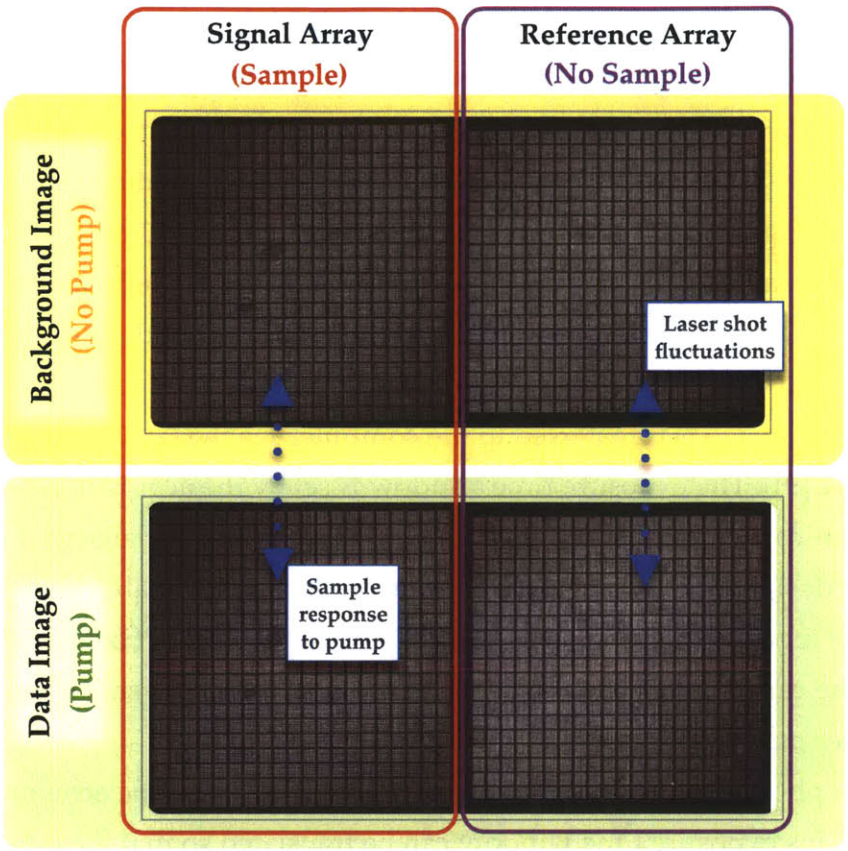

Figure 2-14: Pair of images with (data) and without (background) pump pulse, each containing a signal and reference array that derive from the same laser pulse. Blue arrows mark key difference between the grid arrays that are exploited in image analysis.

The process diagrammed in Figure 2-13 is implemented by a LabView code, which writes both images to text files upon completion. Each 15 MB text file is a 1344 x 1024 matrix of integer values between 0 and 4096. (Strictly, these values are shifted upwards by ~200 to avoid the computational challenge of negative electron counts that would result from dark current fluctuations if the minimum digital value were zero.) A pair of images is shown in Figure 2-14 annotated with the relationships described above. Note that the pump's presence is not visible by eye in the data image.

A MATLAB code was written to analyze the image data and obtain the time-dependent material response. A threshold is determined (~250 counts) below which points are not included in the data and background images for further processing. This

results in a clean background and relaxes the dependence on perfect boundary identification, since non-valued (NaN) pixels are not tabulated in the processing.

We wish to report on $\Delta R/R$:

$$\frac{\Delta R}{R} = \frac{R_f - R_i}{R_i} = \frac{R_f}{R_i} - 1 \qquad \textit{Eq. 2-6}$$

where R_f is the reflectivity in the pump's presence, and R_f / R_i the fractional change due only to the pump's presence. We divide the *data image* by the *background image* in a pixel-to-pixel division to obtain the ratio between the signal arrays with and without the pump. This step normalizes the data to isolate the effects of the second shot, resulting in the division image shown in Figure 2-15. The pump's arrival is clearly visible in the 3rd echelon column of the signal array. From the divided image, we can also observe an approximate view of the dynamics (with 453 fs time resolution) by simply tilting the signal array to look 'up' the columns, as shown in Figure 2-15.

Though the pump response is the dominating feature, laser shot variation is also contained within the divided signal array. Since the measurement is accomplished using single laser shots, we must account for fluctuations resulting from shot (Poisson) noise and beam pointing variation from air and thermal currents. The reference array, which bypasses the sample, is unchanged between the two images except for shot-to-shot intensity variations intrinsic to the laser operation. Therefore, the reference array in the divided image contains the corrective information. We divide the signal array response by the reference array response, both from the divided image, by first converting the pixel array to two 20×20 matrices of average pixel values.

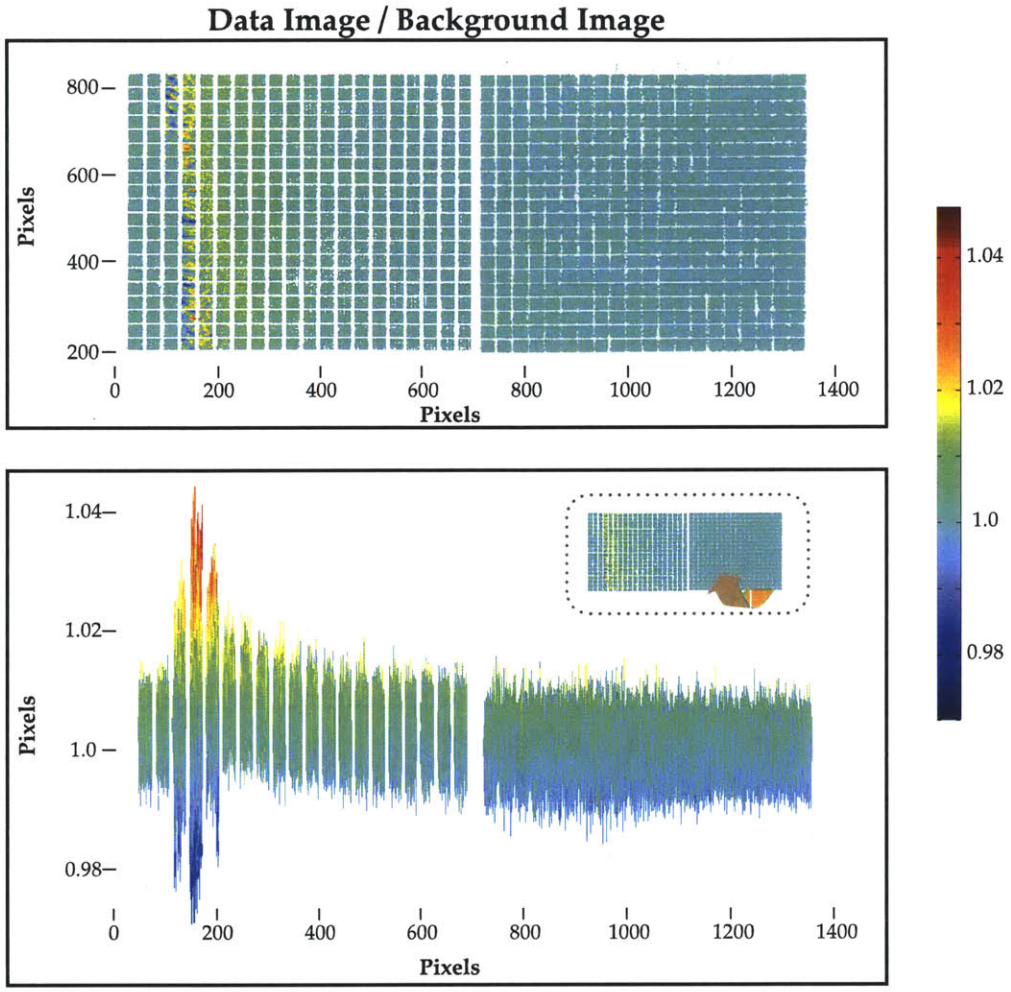

Figure 2-15: Top: the result of dividing the data image by the background image (after discarding values under threshold). The pump arrival is visible in the 3rd echelon column of the signal image. Bottom: a coarse view along the columns of the thick echelon show the material response in 453 fs steps.

For a given data set, the four vertices of each array are identified by the user. Typically, this is only necessary once for a large group of data, as the echelon images do not move appreciably on the CCD chip during a set of measurements. Longitudinal tilt in either array is detectable by the input vertices, and is corrected by masking each array and performing a rotational image transform. Boundaries are then defined as even divisions inside the specified grid area, yielding two 20×20 grids of pixel groups for each image that correspond to consecutive 22.7 fs time delays. Pixels within each square are then averaged to yield the 20×20 *averaged signal matrix* and *averaged reference matrix* depicted in Figure 2-16.

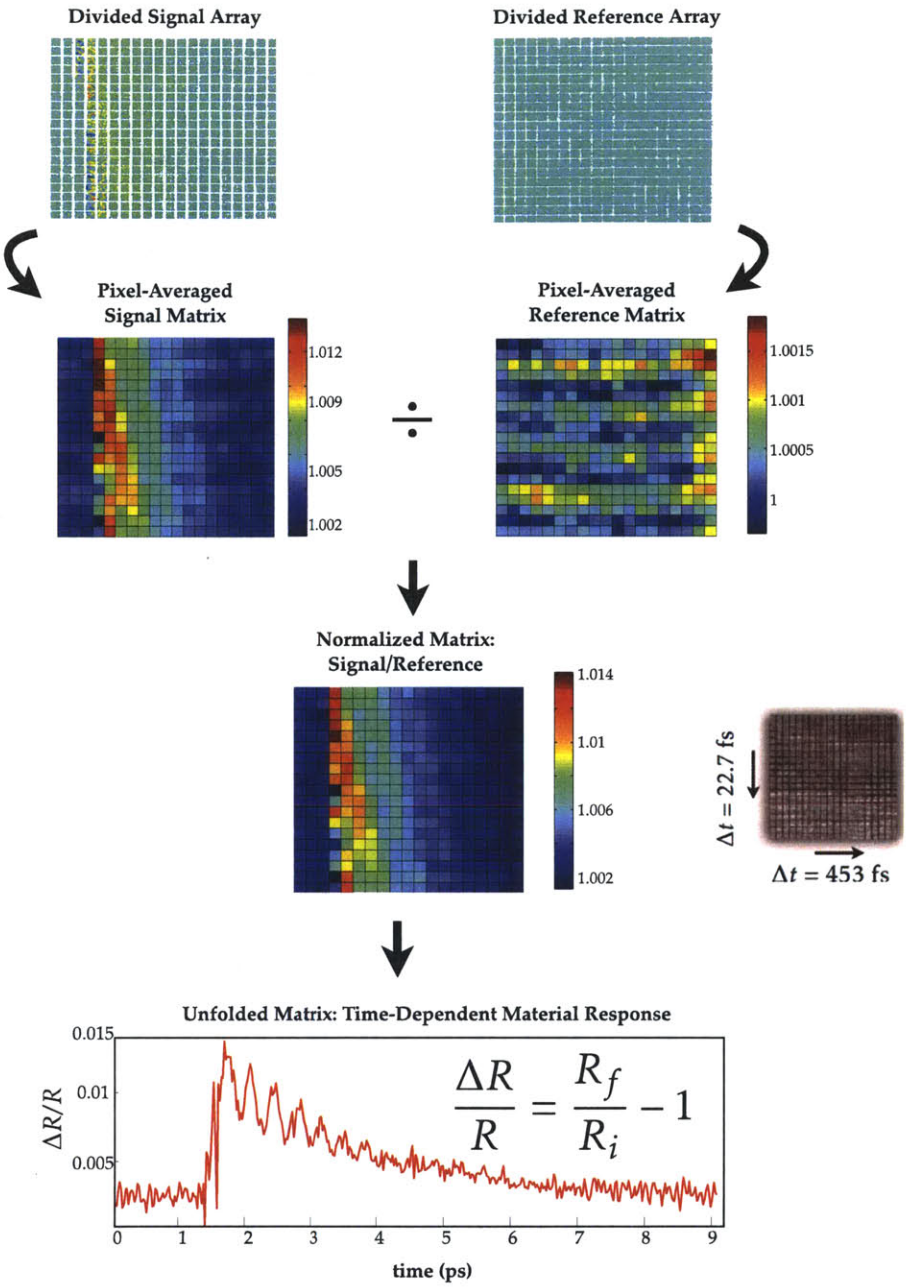

Figure 2-16: Image processing steps. After obtaining the divided image, the signal and reference arrays are separately processed. Pixel-averaging yields 20x20 matrices from the signal and reference arrays. Their quotient minus unity gives the time-dependent material response when unfolded into one dimension.

After the *signal* and *reference* matrices are obtained via pixel-averaging, their quotient is taken to yield the signal matrix normalized for shot fluctuation. Finally, this 20×20 matrix is re-dimensioned into a 1×400 vector. Following Eq. 2-6, we subtract

unity to give $\Delta R/R$ as the values of the vector. Their corresponding time values are given by the echelon-induced delays. A final unfolded trace is shown in Figure 2-16.

The single-shot method enables measurements far from equilibrium by avoiding the cumulative damage that would result from thousands of high-intensity shots. This presents a significant challenge, however, since multiple averaging is used to wash out random noise and is often key in attaining a sufficient SNR for the phenomenon being measured. While high-volume averaging is disallowed by our method, we can gain significant averaging advantage by performing even a few measurements repeatedly. Figure 2-17 displays the results of the above image analysis algorithm on two measurements, 1-shot and 10-shot, in the absence of a pump (to emphasize the baseline noise). That is, the *background* and *data* images processed come from separate laser shots, but are otherwise identical. In the case of 10 laser shots, the images were averaged in real-time as 1344×1024 pixel matrices. 20×20 signal and reference matrices were then extracted from the composite averaged image post-measurement. The suppression of random noise is significant, with an improvement factor of $\sigma_{10}/\sigma_1 = 2.8 \approx \sqrt{10}$.

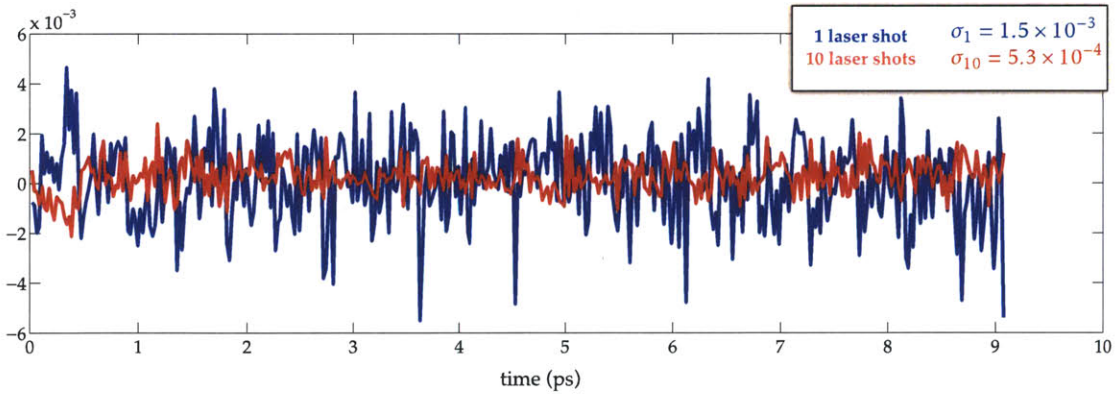

Figure 2-17: $\sqrt{N}$ improvement in baseline noise is observed when the number of measurements N is increased. Acquiring 10 single–shot measurements allows significant improvement of the noise level while still preserving the integrity of real-time near-threshold dynamics measurements.

Most 'single-shot' data presented in this thesis are the result of 10-50 laser shots averaged in this manner. When multi-shot data are taken, the order of background and data images is preserved; however, the division between the averaged signal matrix and averaged reference matrix becomes less critical to overall noise reduction as the number of shots is increased. In each instance of a multi-shot measurement, we verify

that no cumulative damage results from the multiple shots that is not also observable at the same order of magnitude for a single shot by examining the unfolded time traces. In most cases, this process also determines the number of shots used for a measurement. Averaging multiple shots enables a wider set of potential measurements while still preserving the unique capability of the method.

2.4 Summary

In summary, we employ a novel method to resolve solid-state femtosecond dynamics in real-time under intense photoexcitation. At the core of this measurement is a grid of probe pulses generated by crossed echelon optics that encodes temporal data into spatial regions of the grid. This spatial resolution is preserved by detection with a CCD array. We generate images of the probe array after it interacts with the photoexcited sample and analyze the intensity variation over the grid image to yield a time-resolved trace of the material response. The laser system for generating ultrafast pulses, the single-shot optical instrument, the electronic signaling driving the measurement, and the processing technique were all introduced, and practical considerations for sample preparation and instrument alignment were discussed.

Our real-time single-shot spectroscopy method is a unique and powerful tool for monitoring light-matter interactions and material dynamics in previously unmeasured regimes. The method continues to be optimized toward the measurement of physical phenomena unreachable by other methods. The next chapter provides a framework for future improvements to the method. Subsequently, we present single-shot spectroscopy data on two systems to explore fundamental questions of electronic and structural dynamics and energy transfer among material modes photo-excited far from equilibrium.

Chapter 3

Analysis of Single-shot Detection

The single-shot spectroscopy technique described in Chapter 2 offers tremendous potential to observe material dynamics far from equilibrium—a pursuit of high interest in condensed matter but one that remains in its infancy. Detection and noise management remain key challenges of the single-shot technique; future improvements to the current capabilities will derive in large part from attention to these matters. The image analysis algorithm described in Chapter 2, as well as reduced camera exposure time and an increased acquisition rate have led to a factor of two improvement in noise over our prior work,[89] yet additional opportunities remain. This chapter develops a formal connection between the single-shot optical experiment and the spatio-temporal CCD detection scheme. Laser noise, diffraction, field interactions, and the sample response all influence signal detection. Here we explore the manifestations of these parameters in using the single-shot detection method and image analysis. In so doing, a framework is developed for targeting and assessing other opportunities in the measurement's single to noise ratio (SNR) improvements. First, the signal sizes of potential interest in our optical solid-state measurements are related to the units of digital CCD detection and evaluated relative to noise sources. Pixel value averaging and variation is then discussed, with attention to relevant tradeoffs and a presentation of possible interference effects of physical interest embedded in our signal. Finally, a

mathematical model is presented for evaluating the probe beam array explicitly in terms of electric fields at the sample and detected intensity at the camera. These calculations provide a framework for understanding the detection scheme in greater detail, investing in improvements, and modeling processes of interest.

3.1 Digital Signal Detection and Noise Level Calibrations

If we assume typical magnitudes of relative reflectivity changes $\Delta R/R$ due to instantaneous electronic excitation and lattice oscillations, we can estimate the corresponding signal sizes on the CCD detector. In Table 3-1, we assume $(\Delta R/R)_{el} = 0.02$ and $(\Delta R/R)_{ph} = 0.005$. Knowing that there should be a maximum of 1×10^8 photons incident per echelon square at the camera's maximum threshold (§2.2.2), let us assume a probe beam whose intensity yields a maximum of 9.8×10^7 photons per echelon square, or 1.09×10^5 per pixel, making close to full use of the camera's dynamic range. As is clear from Table 3-1, we must rely on relatively small numbers of digital counts to resolve signals of interest even using the camera's full dynamic range. A ΔR_{el} of 2% is expected to manifest as ± 75 counts, and a ΔR_{ph} of 0.5% as ± 19 counts when employing the full dynamic range (DR) of the camera. Employing a more narrow range with weaker incident light yields correspondingly lower detection thresholds. The values in Table 3-1 were calculated considering a quantum yield of 0.15 at 800 nm and an electron-to-count conversion factor of 4.5, in accordance with the camera specificiations described in §2.2.2.

Table 3-1: Sample response pixel detection for full and half dynamic range (DR)

	Full DR: avg. photons/pixel	Full DR: avg. electrons/pixel	Full DR: avg. digital counts	Half DR: avg. digital counts
$R_{baseline}$	1.09×10^5	16,350	3720	1860
ΔR_{ph} (.5%)	± 545	± 82	± 19	± 9.5
ΔR_{el} (2%)	± 2180	± 327	± 75	± 38

To put this estimate in context, we return to the data used to illustrate the image analysis procedure in Chapter 2. The observed electronic signal change $(\Delta R/R)_{el}$ from

the pre-pump baseline to the maximum of the electronic background (exponential fit amplitude) is 0.007 (Figure 3-1 [A]). Roughly, we observe from the divided signal matrix that a strong signal (the electronic response) is visible down the 4th column (Figure 3-1 [B]). Taking the difference between the average pixel values of the 4th and 1st columns of the data image signal grid (Figure 3-1 [C]), less average pixel values of the 4th and 1st columns, respectively, of the background image signal grid (Figure 3-1 [D]) to correct for probe beam variation, we have a difference of roughly 27 counts, corresponding roughly to what is expected for a 0.7% signal near full dynamic range, from Table 3-1.

The calibration suggests that noise sources must cumulatively contribute less than 10-20 counts per measurement point to successfully resolve an oscillatory phonon signal. As will be demonstrated in the following section (see Figure 3-4), averaging over at least 100 pixels is necessary for most grid points to achieve a stable reported average, while 300-400 are needed to fully sample the distribution. As a conservative threshold for a good SNR, averaging over 100 pixels should yield uncertainties of no larger than ±10 counts.

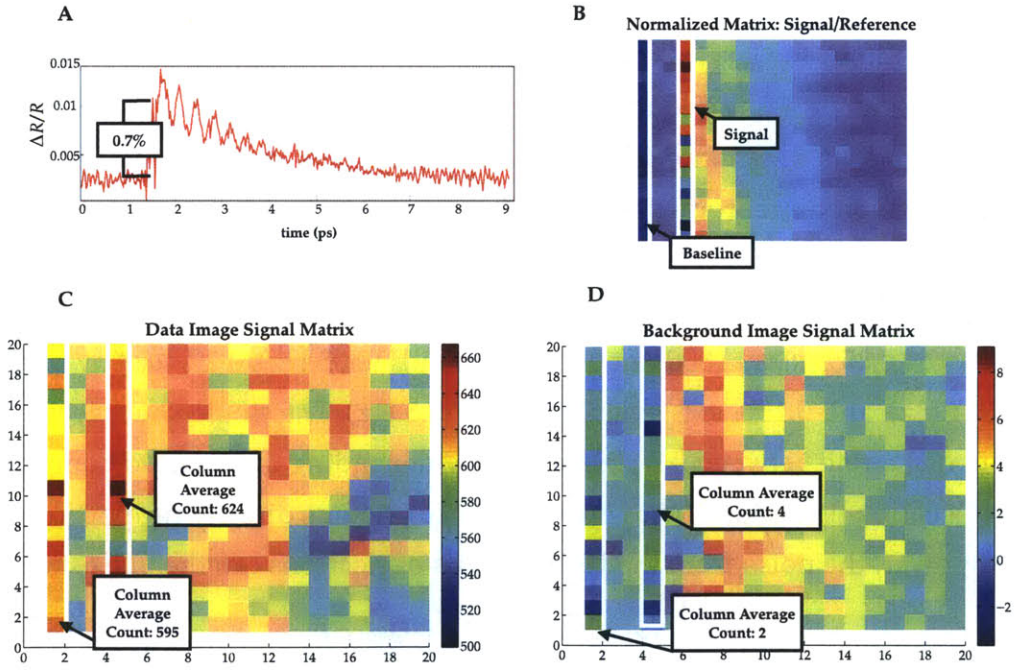

Figure 3-1: Illustration of orders of magnitude in signal detection. [A] *Sample signal, exhibiting a 0.7% differential reflectivity change.* [B] *The result of averaging each grid point of the divided image (signal/background) illustrates the baseline and signal locations on the grid.* [C] *The data image signal matrix yields a difference of 29 counts, adjusted to 27 when corrected by the difference between data and background images* [D].

Three noise parameters are typically relevant in CCD imaging applications: electron counts from thermal energy, rather than photon energy, variation in the number of photons, and noise in the charge-coupling and digital readout of the camera. Camera dark noise, n_d, yields a background count level that is proportional to exposure time. The dark current per unit time for our camera was measured to be 0.2 counts per 100 ms, so that $n_d = (\frac{1\text{electron}}{100\text{ms}})t$. Variation in the number of photons measured per pixel is the photon noise n_P. The photon noise reflects the random arrival of photons fundamental to the nature of light and is expected to follow Poisson statistics, with the measured deviation per unit time varying by up to $\sqrt{N_{photons}}$. Finally, the camera readout noise n_r is 8 electrons, and is assumed to be constant. The total expected noise per pixel from the CCD image acquisition over the $t = 1ms$ exposure time may be calculated from the separate noise sources by converting to uniform units of electrons per pixel:

$$n_{CCD} = \sqrt{n_d^2 + n_P^2 + n_r^2} = \sqrt{0.01^2 + (0.15)N_{photons} + 8^2} \qquad \textit{Eq. 3-1}$$

Assuming photons incident on the camera in the range of 1×10^5 per pixel (following Table 3-1), the expected noise per pixel is 122 electrons, or ~27 counts. As expected for high light conditions, the largest contributing factor by far is photon noise. While pixel non-uniformity can be a noise source in some CCD imaging applications, our pixel array was characterized via a standard flat-field calibration using an incoherent light source and found to exhibit no reproducible irregularity among pixels.

Because our measurement uses two images for signal extraction, we must also account for variations in the laser intensity. Laser shot-to-shot fluctuations were measured to be 0.25% RMS at 800 nm over 20 seconds (0.05 Hz), 0.2% RMS over 10 seconds (0.1 Hz), and 0.15% RMS over 2 seconds (0.5 Hz). The single-shot measurement is performed at a rate between 0.5 Hz and 0.8 Hz depending the selected computer memory allocation procedure. With the number of photons directly proportional to measured power, the noise from the laser in units of electrons can then be estimated by

$$n_{Laser} = QE_\lambda \text{RMS}_{acq} N_{photons} \qquad \textit{Eq. 3-2}$$

We obtain 22 electrons, or 5 counts when evaluating Eq. 3-2 for 800 nm, 1×10^5 photons per pixel, and the RMS value of 0.15% (conservatively at the lower end of our acquisition

rate range). We estimate the fundamental noise floor per pixel via the CCD and laser noise sources to be 27.5 counts at 800 nm via:

$$n_{pixel} = \sqrt{n_{CCD}^2 + n_{Laser}^2} \qquad \text{Eq. 3-3}$$

Assuming a factor of $\sqrt{N_{pixels}}$ reduction in the noise level upon averaging over N_{pixels}, averaging over 100 pixels will yield a noise level of ~3 counts per echelon square measurement, which is acceptably within the desired range. Averaging over a large fraction of the ~700 pixels per echelon grid point should yield a lower variation of ~1 count per measurement. Inevitably, additional sources of noise exist that add to the 3 count base level. Electronic interferences among camera system components are present due to the contrast between microvolt-level signaling of the internal CCD electronics and the more noisy operation elements used to cool, send voltage signals, and transfer collected data. These interferences are typically highly correlated in the frequency domain, and have been characterized in our lab to occur chiefly in the 10-20 Hz region. Thus their effects can typically be isolated from our oscillatory signals of interest (in the 2-4 THz regime), but their presence in the time domain nonetheless can obscure relevant phenomena and render very sensitive measurements irreproducible.

Optical alignment also plays a role in noise management. Sources of noise in alignment and optical aberrations in the single-shot experiment are discussed in Shin, 2010.[89] Of particular note is a recurring periodic feature at 2.2 THz corresponding to the step size of the thick echelon used in our experiment. Because beams separated by 453 fs are also the most spatially separated from each other, any spatial variations experienced by the grid of pulses, such as pump intensity, sample irregularity, and focusing plane, will manifest themselves as periodic noise at 2.2 THz. The periodic effect can range from being undetectable to overwhelming the signal at several percent when several spatial variation sources are present. (There is an analogous variation over the other echelon dimension that manifests as a uniform $\Delta R/R$ drift over the experimental time window, but it is typically of less concern in signal analysis.) Additionally, interference effects from phase variation in the array of probe beams may introduce noise. Section 3.3 presents a framework for interpreting noise sources intrinsic to beam interactions in the dual echelon optical setup.

3.2 Pixel variation and averaging

We here explore the importance and effect of averaging over pixels in the single-shot experiment. Twenty images without a pump pulse were taken in close succession to directly measure typical pixel value variation. Figure 3-2 shows the standard deviation of each pixel across the set of images, with representative standard deviations labeled in the background (σ = 3.9), in the echelon signal grid (σ = 22.4), and in a boundary (σ = 9.5). The measured variation per pixel when measuring laser intensity across the grid is found to be close to the calculated value of 27.5 counts reported in the previous section.

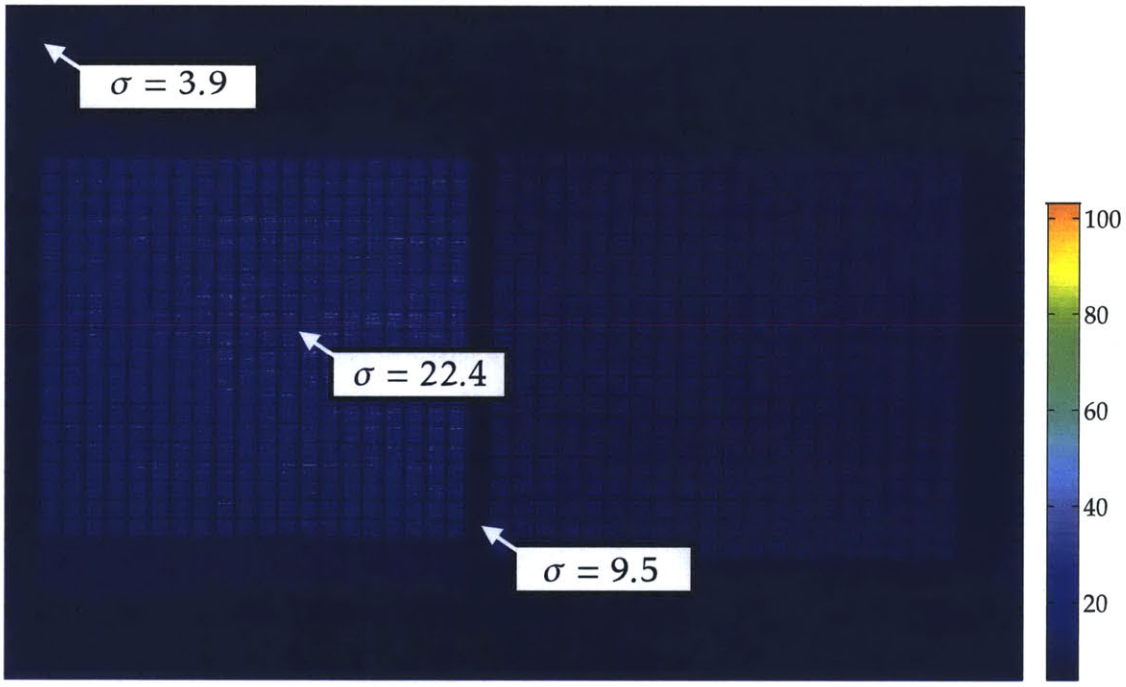

Figure 3-2: The pixel-by-pixel standard deviation across 20 images taken at a rate of about 1 Hz. The experimental acquisition rate is 0.8 Hz.

The standard deviation per pixel value in the echelon grid region ranges between 20 and 100, well into the range of signal levels in Table 3-1, necessitating an average over many pixels. However, image edge-finding algorithms lack precision, so there may be cause to favor conservative boundary estimation over full pixel averaging. Figure 3-3 shows the effect on the measured signal [A] and the baseline noise level [B] of averaging over successively more pixels per echelon square, from the center outward. Here, the baseline noise is defined as the standard deviation of the last 2 picoseconds of

$\Delta R/R$ data. Increasing the averaging up to about 300 pixels (1/3 of the total 700-900 per square), there is significant noise suppression, and averaging beyond that point does not substantially decrease the baseline noise.

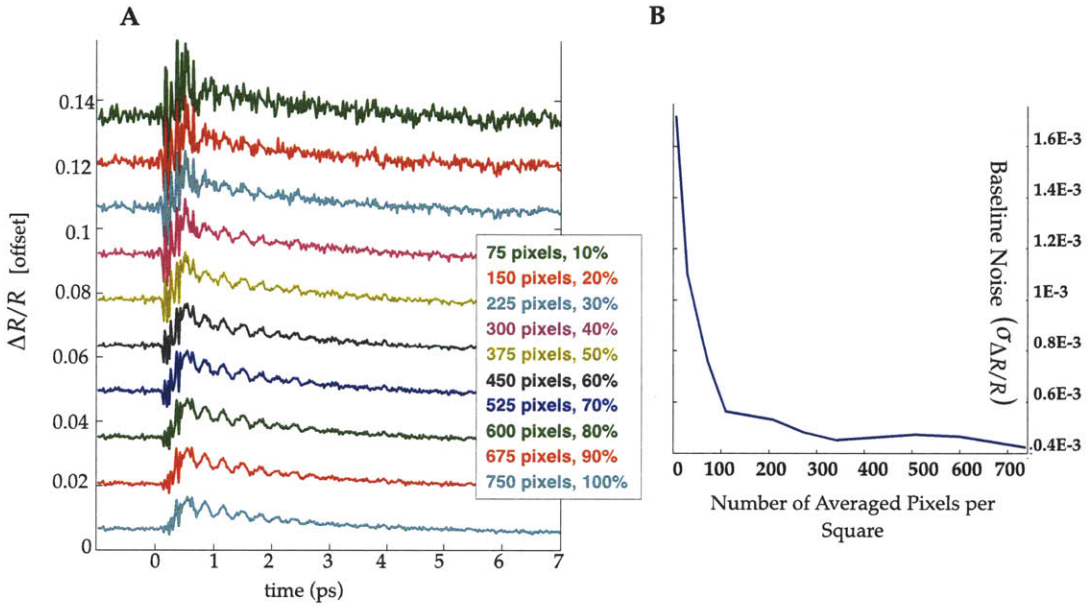

Figure 3-3: [A] *Signal obtained by averaging over increasingly large fraction of pixels per square, from 10% (top) to near 100% (bottom).* [B] *Standard deviation of last 2 picoseconds of data as a function of the number of averaged pixels per square.*

To take a closer look at this result, we tabulate the reported average of each square (the value that appears per time-point in each unfolded time trace) as a function of the number of pixels averaged for a random selection of squares. Figure 3-4 shows one such instance. We find that the reported average for most squares converges after only about 100 pixels have been counted (~13%). The reported average for some squares, however, continues to change until nearly all have been averaged. We note that in the instance shown in Figure 3-4 (and in other iterations performed) the grid square requiring the most averaging to converge corresponds to the [10,4] square, or 1.6 ps in time. In this data, as shown in Figure 3-4, the 1.6 ps time-point corresponds to a very strong signal.

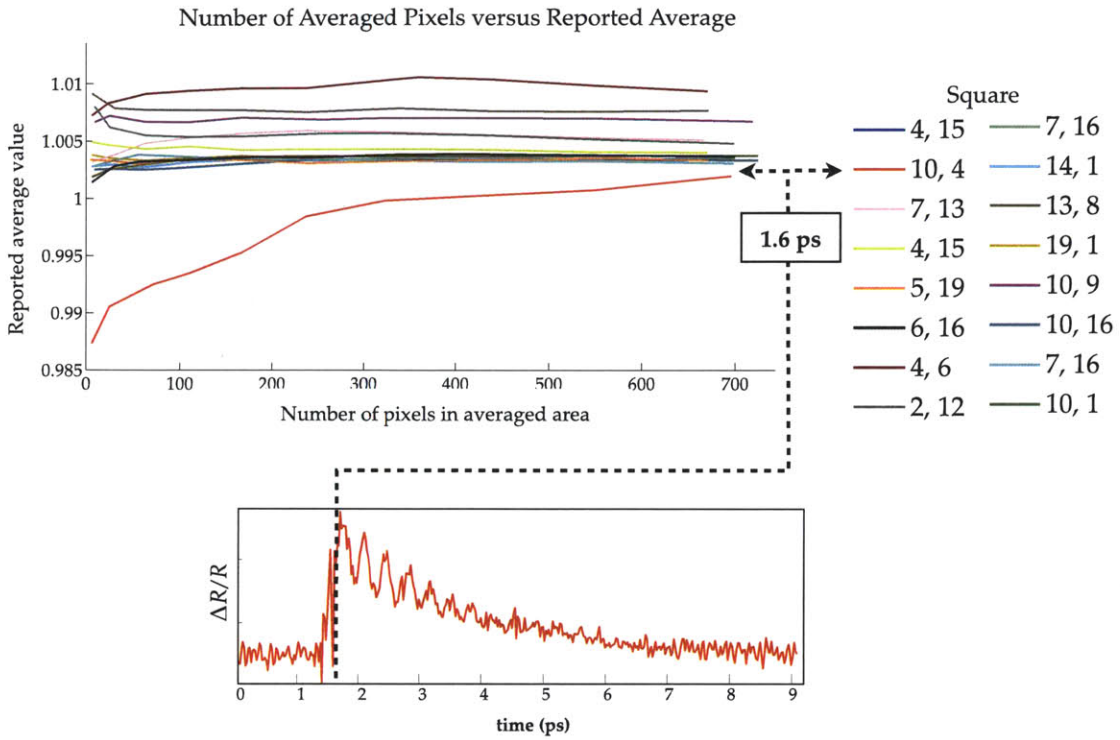

Figure 3-4: The reported average over randomly selected pixel squares is shown as a function of pixel area averaged. The instance seen to change most appreciably as the number of averaged pixels increases beyond ~300 is [10,4], which corresponds to 1.6 ps—in this data, the time of a strong pump response.

To explore the unexpected result that grid squares corresponding to strong signal points require more averaging, the divided signal image corresponding to this data (which is then pixel-averaged to yield the unfolded trace) is shown in a colormap scheme in Figure 3-5, which highlights variation. The [10,4] square is highlighted. In that grid point and the surrounding ones, we observe strong variations of light and dark intensity relative to the pre-pump intensity (e.g., the first two columns). The strongest variations are observed between the grid points of [18,3] and [10,4], or between 1.3 and 1.6 ps. This region corresponds closely to the rise observed in the data that we attribute to electronic excitation.

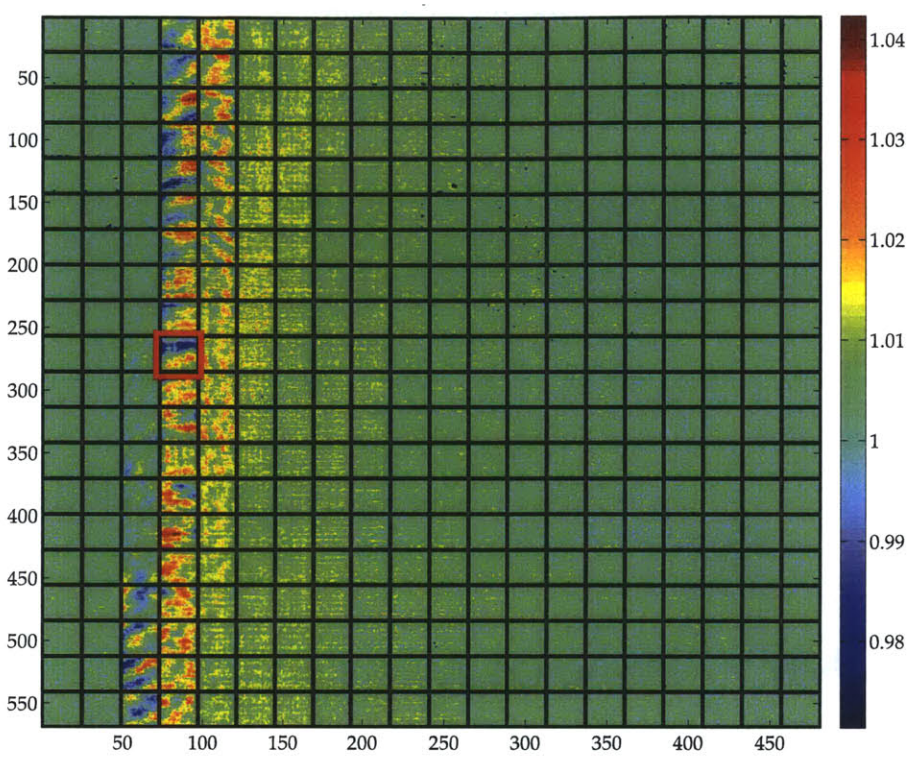

Figure 3-5: The signal side of a divided image (data image / background image) shows strong variations in each grid square during the time of the electronic rise in the data (1.3 to 1.6 ps), and moderate but distinct variations after 1.6 ps.

Figure 3-6 displays the familiar unfolded trace, as calculated by pixel-averaging the image in Figure 3-5 and dividing by the reference pixel-averaged grid. Also displayed is an unfolded trace derived from pixel value standard deviations over each grid square instead of pixel value averages. Comparing the two measures, a sharper rise is apparent in the standard deviation trace, and the measured standard deviation returns to the pre-pump level after ~1 ps, whereas the measured average decays over the time of the probe window. A phonon signal at 2.9 THz (corresponding to the Raman active mode in Bismuth) is visible in the averaged trace; however, the standard deviation trace does not display an oscillatory component. Oscillatory structure in the standard deviation trace was found by Fourier transform to occur at 2.2 THz, the

periodic noise feature common to our measurement from thick echelon time steps.

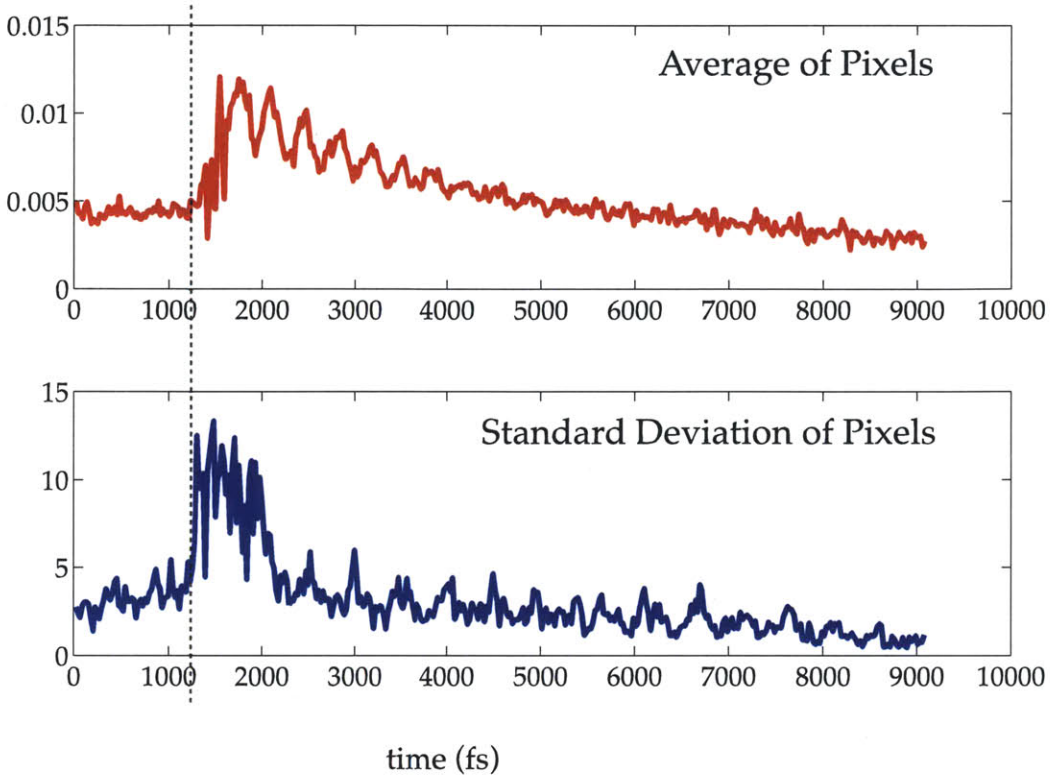

Figure 3-6: Unfolded traces of the image in Figure 3-5 derived from the average of pixel values in each grid point (top) and the standard deviation of pixel values in each grid point (bottom). The dashed line is a guide to the eye placed on the rising edge of both time traces.

The image's noticeable variation in individual grid squares over the timescale of average intensity rise suggests the possibility of interactions between the pump and probe pulses that we can uniquely detect on the CCD array. In a typical pump-probe experiment, photon counts are averaged by a photodiode without a mechanism to resolve intensity variation in a single pulse. The structure visible in the divided image is suggestive of beam interference patterns, a possibility explored and modeled in §3.3.3, and may provide an independent measure of a short-time electronic response as compared to the pixel-averaged trace.

3.3 Modeling the Spatio-Temporal Probe Array

Details of the probe beam array employed in the single-shot experiment are calculated and modeled in this section to provide a framework for understanding phenomena of interest and evaluating prospective changes to experimental operation.

3.3.1 Beam Power and Intensity Profile

Before the lens that expands the probe beam and prepares it for echelon imaging, the probe has a beam radius of 4.7 mm (half-width at $1/e^2$ intensity). A one-inch round aperture selects the beam center 61 cm downstream. By the ABCD matrix propagation method, the beam was calculated to have a radius of 3.35 cm immediately before the aperture. To calculate the beam power $P = I/A$ through the aperture, we model the expanded beam intensity profile as a two-dimensional Gaussian (Figure 3-7 inset) and integrate under the circular area of radius 0.50″ (12.7 mm). The volume under the normalized intensity surface at a specified radius outward yields the percent power permitted by an aperture of that size. The integration result is shown for several values of aperture radii in Figure 3-7. We find that 25 % of the incoming beam power is selected by the 12.7 mm aperture. This result was also measured experimentally, but verified here due to the difficulty of measuring low-intensity beams over large areas.

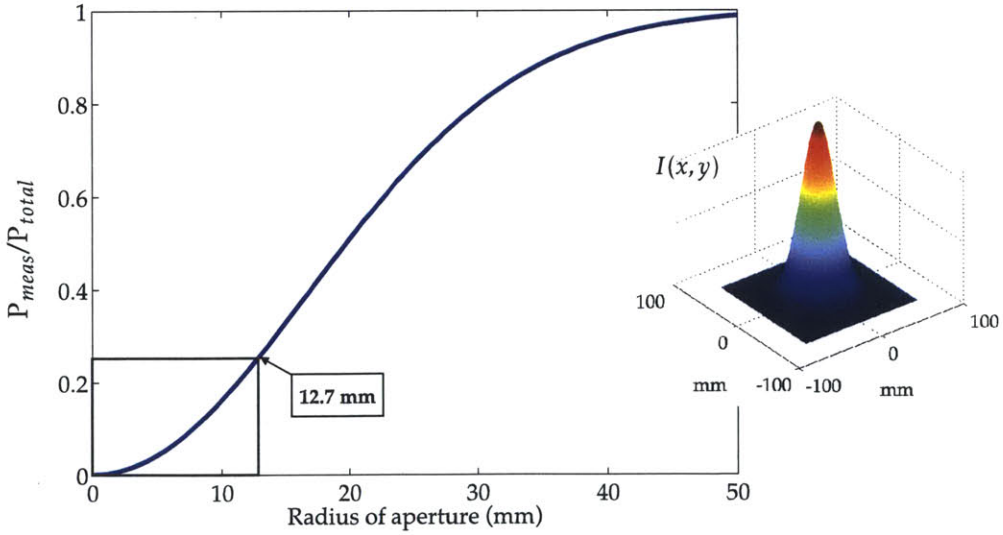

Figure 3-7: Power of input Gaussian beam of radius 3.35 cm (inset) permitted by an aperture of varying size, determined by integrating under the Gaussian intensity surface (inset). After expansion, the single-shot probe encounters a 1″ diameter aperture (12.7 mm radius) that permits 25% of the power.

The selected beam propagates for 8 cm before the collimating lens. Again by ABCD matrix propagation, we obtain 29.2 mm as the total diameter of the selected beam at the collimating lens. The beam now resembles the tip of a two-dimensional Gaussian. The collimated beam propagates through the echelons and a square aperture of the echelon cross-area size (1 cm ×1 cm). We calculate the power and new intensity profile through the echelons by treating the echelons as a square aperture. Ignoring reflection and diffraction, we obtain the intensity profile of the probe grid, containing 20% of the incoming beam power, shown in Figure 3-8. We find that the echelon grid profile varies by ~6% from the center to the corners, and by 3-4% from the center to the edges.

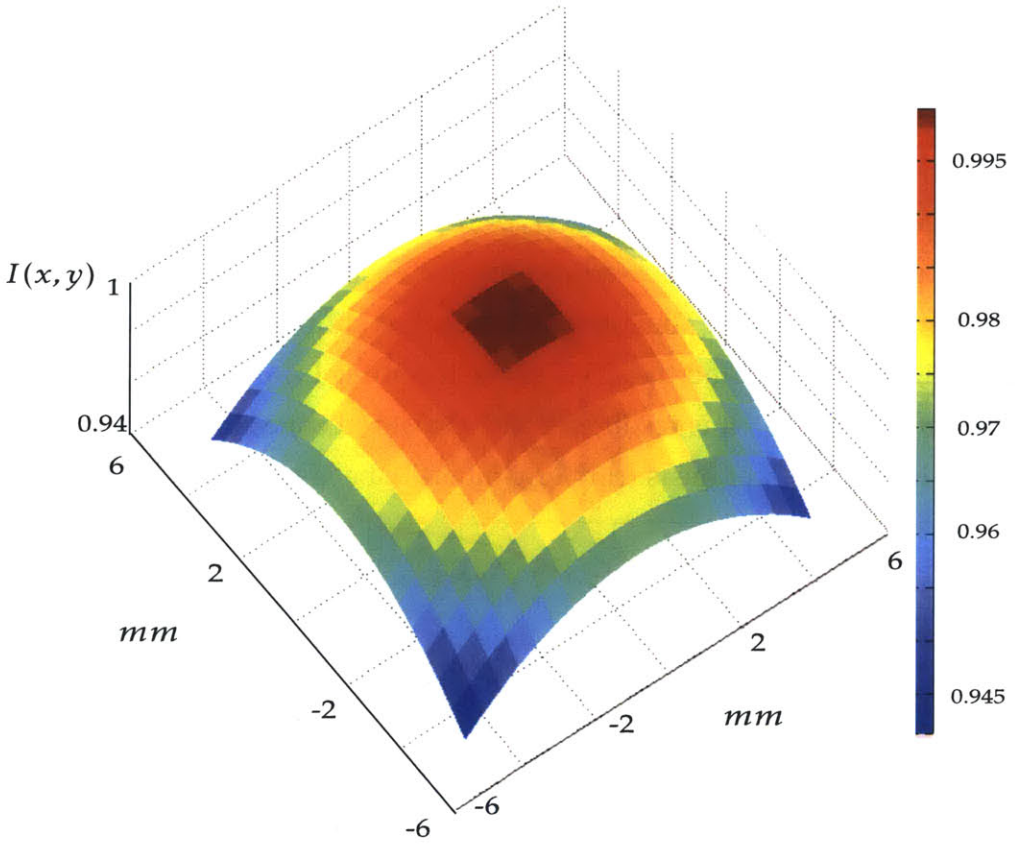

Figure 3-8: Intensity profile of the probe beam across the echelon grid before being focused onto the sample. The beam is ~1 cm across, and its intensity varies up to 6% from the beam center to the corners.

3.3.2 Spatio-Temporal Interactions Among Probe Pulses

We would like to understand the behavior of probe beams at the sample and quantify the outcomes of changing various parameters such as pulse duration,

irradiance distribution, and wavelength for experimental optimization. We can then translate this information to make predictions about the detected signal on camera.

Each probe beam portion experiences four glass edges as it propagates through the crossed echelons. If we treat each group of edges as a square aperture, we can proceed to model the beam from diffraction theory. The calculated diffraction pattern will be inexact, because the light experiences the edges at different points in time and space. That is, a beam that experiences edge diffraction on its left side propagates a short distance before experiencing edge diffraction in its right side, and so on. The result will be a blurring of the calculated pattern, because each diffraction edge acts as a point source whose plane waves propagate and interfere, creating a new pattern, before experiencing the next edge. Additionally, as discussed in §2.2.2, because the echelon pair thickness precludes a precise object plane, our imaging system deviates significantly from the ideal.

The far-field distribution of an electric field that propagates through a single rectangular aperture is a two-dimensional sinc function:[90]

$$E_1(X,Y,t) = C\left(\frac{\sin\alpha}{\alpha}\right)\left(\frac{\sin\beta}{\beta}\right)\cos(\omega t - kD) \qquad \textit{Eq. 3-4}$$

$$\alpha = \frac{ka}{2D}Y\ ,\ \beta = \frac{kb}{2D}X \qquad \textit{Eq. 3-5}$$

where $k = 2\pi/\lambda$, a and b are the vertical and horizontal dimensions of the aperture, respectively, D is the far-field distance, and C is a constant reflecting the maximum field amplitude, which we subsequently neglect. A pair of rectangular apertures separated by a distance w either horizontally or vertically create an interference pattern that is simply the sum of their separate fields. To evaluate the resulting interacting field $(E_1 + E_2)$ at an observation point in front of one aperture, we modify the kD term in Eq. 3-4 for the second field E_2 to reflect its different path length to the observation point in terms of w:[90]

$$E_2(X,Y,t) = \left(\frac{\sin\alpha}{\alpha}\right)\left(\frac{\sin\beta}{\beta}\right)\cos(\omega t - kD + 2\phi_{x,y}) \qquad \textit{Eq. 3-6}$$

$$\phi_x = \frac{kw_x}{2D}X\ ,\ \phi_y = \frac{kw_y}{2D}Y \qquad \textit{Eq. 3-7}$$

Similarly, the result of adding more apertures symmetrically about a center aperture can be calculated by adding additional fields with the appropriate path lengths. For $t = 0$, calculated electric field distributions are shown in Figure 3-9 for a single aperture, three apertures, and five apertures in the geometries shown.

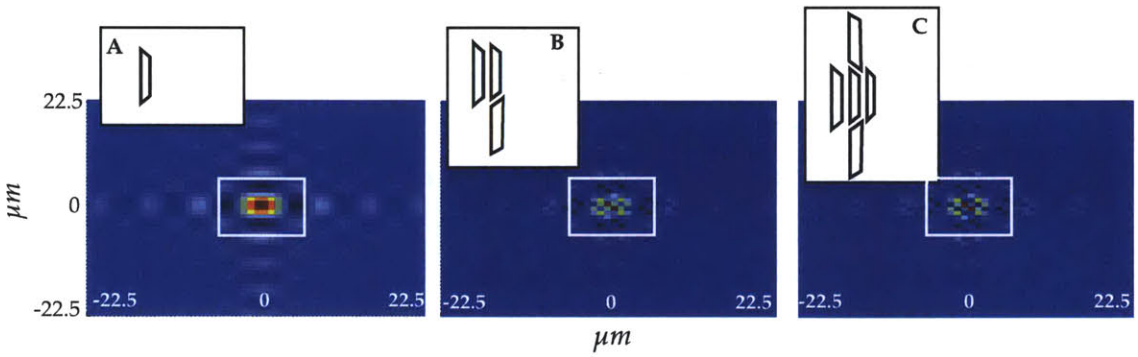

Figure 3-9: Far-field diffraction patterns from [A] *a single rectangular aperture,* [B] *3 apertures, one above and one below the original, and* [C] *5 apertures, with 4 placed symmetrically about the original. The values used for center-to-center distances between apertures were equal to the aperture dimensions.*

In our optical system, the focusing lens after the echelon pair maps the far-field diffraction pattern of the preceding apertures onto its focal plane, so we replace D in the above equations with the lens focal length f, and expect patterns like those shown in Figure 3-9 to arrive at the focus. Noting that a Gaussian distribution, rather than a sinc function, interacts with the sample in a conventional spectroscopy experiment, we wish to ascertain the effects of this diffraction distribution on our detected signal. As described in §2.2, the probe array focuses to about 45 μm across. This sets our scaling for the aperture dimensions at the focus, yielding the axes in Figure 3-9. This is the primary region we image onto the CCD camera, and The center region, highlighted by a white square, becomes more complex as more apertures contribute to the diffraction pattern. Because this complexity is encoded at the focal point where we obtain dynamical time-domain data, we seek to know the patterns or variation the beam interaction imparts to the data.

For light propagating uniformly through an array of identical apertures, the overall diffraction pattern becomes the product of one aperture's diffraction pattern and a set of point sources in the shape of the array. However, phase shifts and temporal delays prevent us from utilizing this convenient result. The added term in Eq. 3-6 accounts for the angular phase shift ϕ_{ang} between beams traveling from different points

of the echelon grid to the focus. If the coordinate system that determines path lengths is devised so that the origin is placed at the grid center, these phase factors form a symmetric distribution as they increase from the center point (Figure 3-10 [A]). However, an additional phase term ϕ_{trans} must be added that results from light propagating through the glass:

$$\phi_{trans} = k(\eta - 1)d \qquad \textit{Eq. 3-8}$$

where η is the refractive index and d is the amount of glass a beam passes through. These phase factors collectively form an asymmetric distribution that follows the cumulative echelon thickness (Figure 3-10 [B]). For the field of an individual probe beam, the total phase is the sum of ϕ_{ang} and ϕ_{trans} (Figure 3-10 [C]).

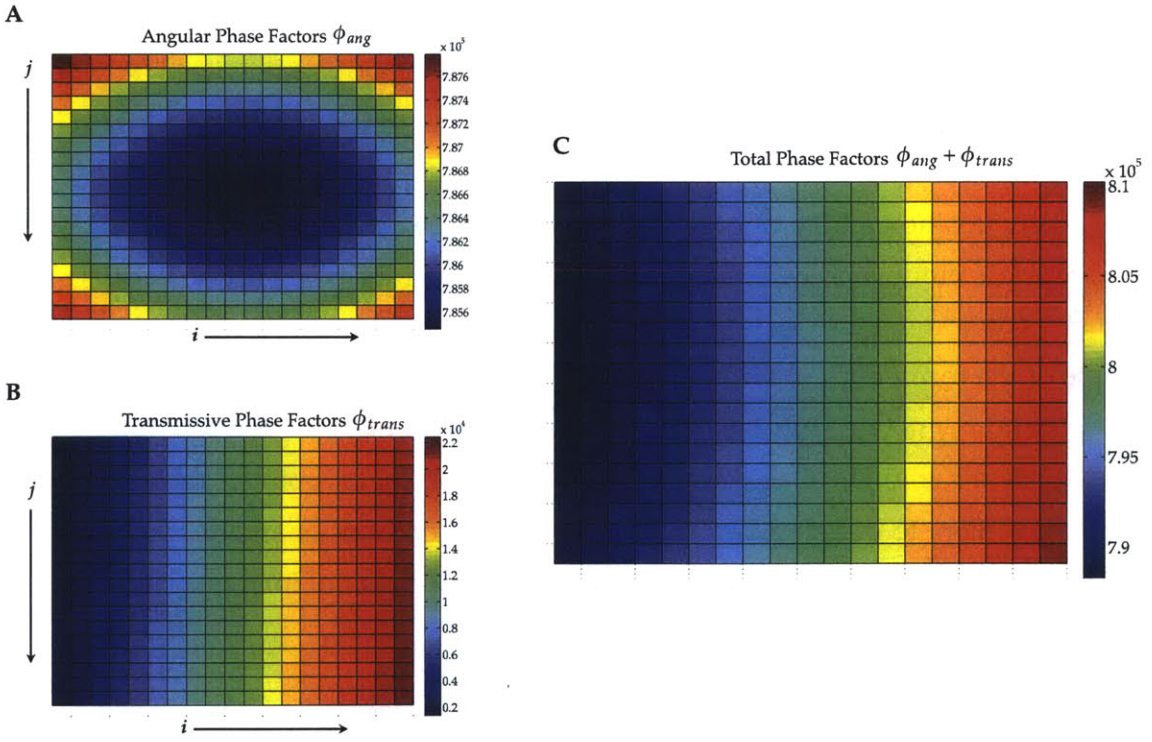

Figure 3-10: [A] *Angular phase factors relative to center result from varying path lengths traveled by individual probe beams.* [B] *Transmissive phase factors relative to the first timepoint result from varying thickness of glass in individual probe beam paths. Calculated for 800 nm.* [C] *The sum of the two phase factors defines each beam's phase delay relative to the others. The slight asymmetry present in the angular phase factor distribution is due to numerical rounding from an even number of echelon columns and rows.*

Denoting the rows of the echelon grid as j and its columns as i, the field of an individual, isolated (no interferences) probe beam at the focus is given by:

$$E_{j,i}(X,Y,t) = \left(\frac{\sin\alpha}{\alpha}\right)\left(\frac{\sin\beta}{\beta}\right)\cos(\omega t - kf + \phi_{ang} + \phi_{trans}) \qquad \textit{Eq. 3-9}$$

$$\phi_{ang} = \frac{ka}{f}[|j-10.5|+0.5]Y + \frac{kb}{f}[|i-10.5|+0.5]X \qquad \textit{Eq. 3-10}$$

$$\phi_{trans} = k(\eta-1)[j(15\mu m)+(i-1)(300\mu m)] \qquad \textit{Eq. 3-11}$$

$$\alpha = \frac{ka}{2f}Y\ ,\ \beta = \frac{kb}{2f}X \qquad \textit{Eq. 3-12}$$

Each aperture's height and width is set by the echelon dimensions to be $a = 600\mu m$ and $b = 500\mu m$, respectively, which are scaled by a factor of 222 (1.2 cm at the echelons/45 μm at the focus) when evaluated at the focus $f = 10cm$ away from the echelons. Eq. 3-10 has taken on a specialized form of Eq. 3-7 due to the geometry of the problem, where the center-to-center distance between apertures is equal to the aperture length in that dimension.

Array position and temporal delays must also be considered in order to devise an appropriate model and evaluate interactions in the probe beam array, because both parameters determine the fields with which any one probe beam interacts. As an example of the former, $E_{10,10}$ will interact with other beams in a symmetric way (i.e. with $E_{9,10}$ and $E_{11,10}$,$E_{10,9}$ and $E_{10,11}$) while $E_{1,1}$, in a corner of the grid, will not. Eq. 3-9 defines a beam's angular phase term in reference to the center point of the grid, but it will be convenient to define ϕ_{ang} as zero for the beam of interest, and calculate the fields of neighboring beams with phase factors relative to the beam of interest. Then for modeling interactions with beam $E_{j,i}$, ϕ_{ang} of beam $E_{n,m}$ is given by:

$$\phi_{ang_{n,m}}\Big|_{j,i} = \frac{ka|j-n|}{f}Y + \frac{kb|i-m|}{f}X \qquad \textit{Eq. 3-13}$$

If the pulse duration is long, probe beams overlap for a greater length of time on the sample. Put another way, the extent of interaction between two beams is determined by the pulse duration. By modeling the intensity of each pulse as a Gaussian in time, we can formulate a time overlap matrix to determine this interaction extent as a function of the input pulse duration. The center of each Gaussian $I_{j,i}(t)$ is the arrival time of the pulse on the sample $T_{j,i}$ relative to the first probe pulse such that

$T_{1,1} = 0$. For 800 nm light, all pulses are spaced by 22.7 fs. The width of $I_{j,i}(t)$ is the pulse duration $\tau_{j,i}$, which is determined by the input pulse duration and the dispersion introduced by the material, set by the group velocity dispersion (GVD) and the thickness. These parameters are governed by the following equations:

$$I_{j,i}(t) = e^{-\left(\frac{t-T_{j,i}}{\tau_{j,i}}\right)^2} \qquad \textit{Eq. 3-14}$$

$$T_{j,i} = \frac{\eta - 1}{c} d_{j,i} \qquad \textit{Eq. 3-15}$$

$$\tau_{j,i} = \tau_0 \sqrt{1 + \left(\frac{4 \ln 2 \,(\mathrm{GVD})\, d_{j,i}}{\tau_0^2}\right)^2} \qquad \textit{Eq. 3-16}$$

$$d_{j,i} = j(15\mu m) + (i-1)(300\mu m) \qquad \textit{Eq. 3-17}$$

$$\mathrm{GVD} = \frac{\lambda^3}{2\pi c^2} \frac{\partial^2 \eta}{\partial \lambda^2} \qquad \textit{Eq. 3-18}$$

where τ_0 in Eq. 3-16 is the input pulse duration. A time overlap matrix $O_{j,i}$ is then formed for each probe beam to describe the extent of time overlap with the other beams:

$$(O_{j,i})_{n,m} = I_{j,i}(t) \cdot I_{n,m}(t) \qquad \textit{Eq. 3-19}$$

where n and m each vary from 1 to 20, and the matrix $O_{j,i}$ is normalized so that $(O_{j,i})_{j,i} = 1$. The time overlap matrix $O_{10,10}$ is shown in Figure 3-11 for input pulse durations of 100 fs (left) and 400 fs (right).

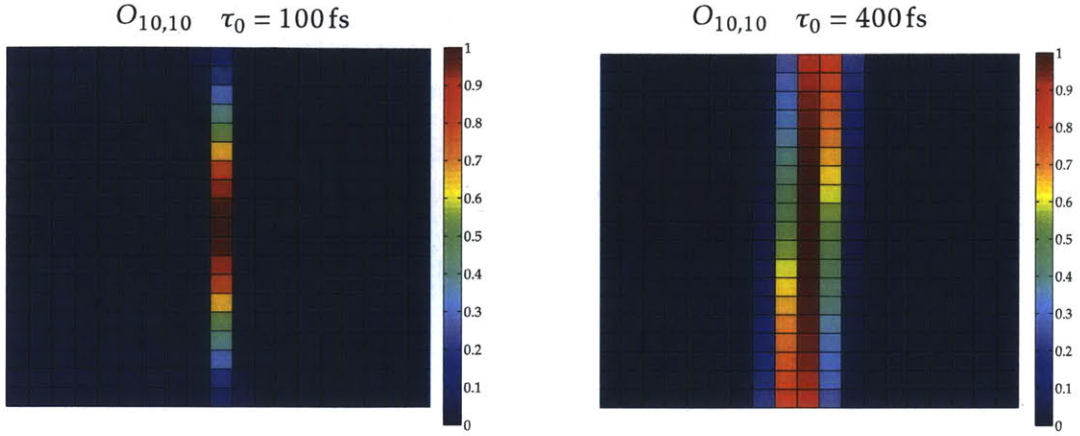

Figure 3-11: Time overlap matrices for the grid square [10,10], where each element is formed by the dot products of two Gaussian intensity profiles in time. Left: an input pulse of 100 fs confines the time overlap to a single column of pulses. Right: an input pulse of 400 fs induces very strong overlap over a single column and moderate overlap with the preceding and following columns.

Because the relevant time parameters are contained within the phase factors (controlling the amplitude of the field at a moment in time relative to its launch) and the Gaussian intensity distribution (placement of the field arrival relative to other pulses), we can drop the time dependence of Eq. 3-9. Incorporating the convention of $\phi_{ang} = 0$ for the field of interest, Eq. 3-9 becomes:

$$E_{j,i}(X,Y) = \left(\frac{\sin\alpha}{\alpha}\right)\left(\frac{\sin\beta}{\beta}\right)\cos(\phi_{trans}) \qquad \textit{Eq. 3-20}$$

where the term $-kf$ has also been dropped since it appears in every cosine term.

We now have a description of each probe pulse in space (Eq. 3-20) and in time (Eq. 3-14), as well as a description of how other probe pulses surround that pulse in space (Eq. 3-13) and in time (Eq. 3-19). The result of a probe field $E_{j,i}$ having interacted with other probe fields in our experiment is given by $E_{I_{j,i}}$:

$$E_{I_{j,i}}(X,Y) = \left(\frac{\sin\alpha}{\alpha}\right)\left(\frac{\sin\beta}{\beta}\right)\cos(\phi_{trans_{j,i}}) + \sum_{m=1}^{20}\sum_{n=1}^{20} E_{n,m}\Big|_{j,i}(O_{j,i})_{m,n} \qquad \textit{Eq. 3-21}$$

$$E_{n,m}\Big|_{j,i} = \left(\frac{\sin\alpha}{\alpha}\right)\left(\frac{\sin\beta}{\beta}\right)\cos\left(\phi_{trans_{n,m}} + \phi_{ang_{n,m}}\Big|_{j,i}\right) \qquad \textit{Eq. 3-22}$$

Representative fields $E_{I_{j,i}}$ resulting from the calculation of Eq. 3-21 and Eq. 3-22 are shown below in Figure 3-12; those selected are from along the diagonal of the probe pulse array ([1,1], [2,2], etc.). We note that there is an intrinsic variation in the range of values (reflecting field strength at the sample) that result from the interactions. The input pulse duration was 100 fs, the wavelength was 800, and the input intensity distribution was uniform.

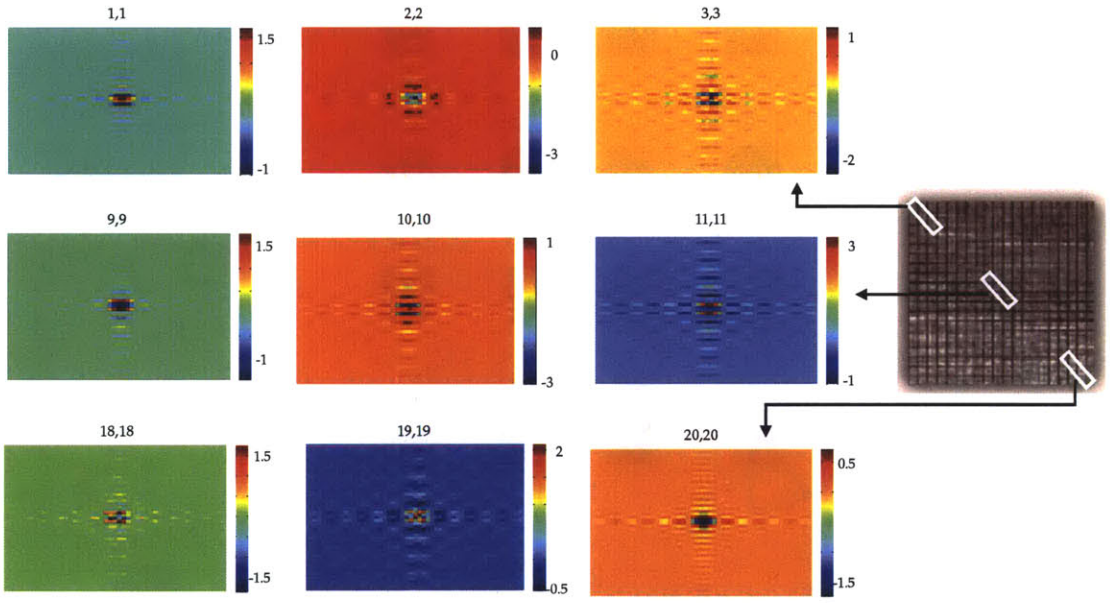

Figure 3-12: Representative examples of calculated interacting fields $E_{I_{j,i}}$ along the grid array diagonal. Variation in background intensity is observed, as well as structure both in the fringes and the central region.

At the focus we would observe the square of the interacting field $|E_{I_{j,i}}(X,Y)|^2$, and at the camera we observe its two-dimensional inverse Fourier Transform $\mathcal{F}^{-1}\left(|E_{I_{j,i}}(X,Y)|^2\right)$. In this way the resulting image from any probe beam interactions (neglecting the pump and sample) can be calculated, as shown for representative grid squares in Figure 3-13. We note that there is generally more structure contained within the edge images (e.g., [1,2] and [20,1]), and that the center images are nearly identical when compared symmetrically about the center. These calculations assume that the dielectric constant does not change with time. That is, we are calculating the *intrinsic variation from a single shot*, which is present underneath the signal produced via time-dependent variations in the reflectivity.

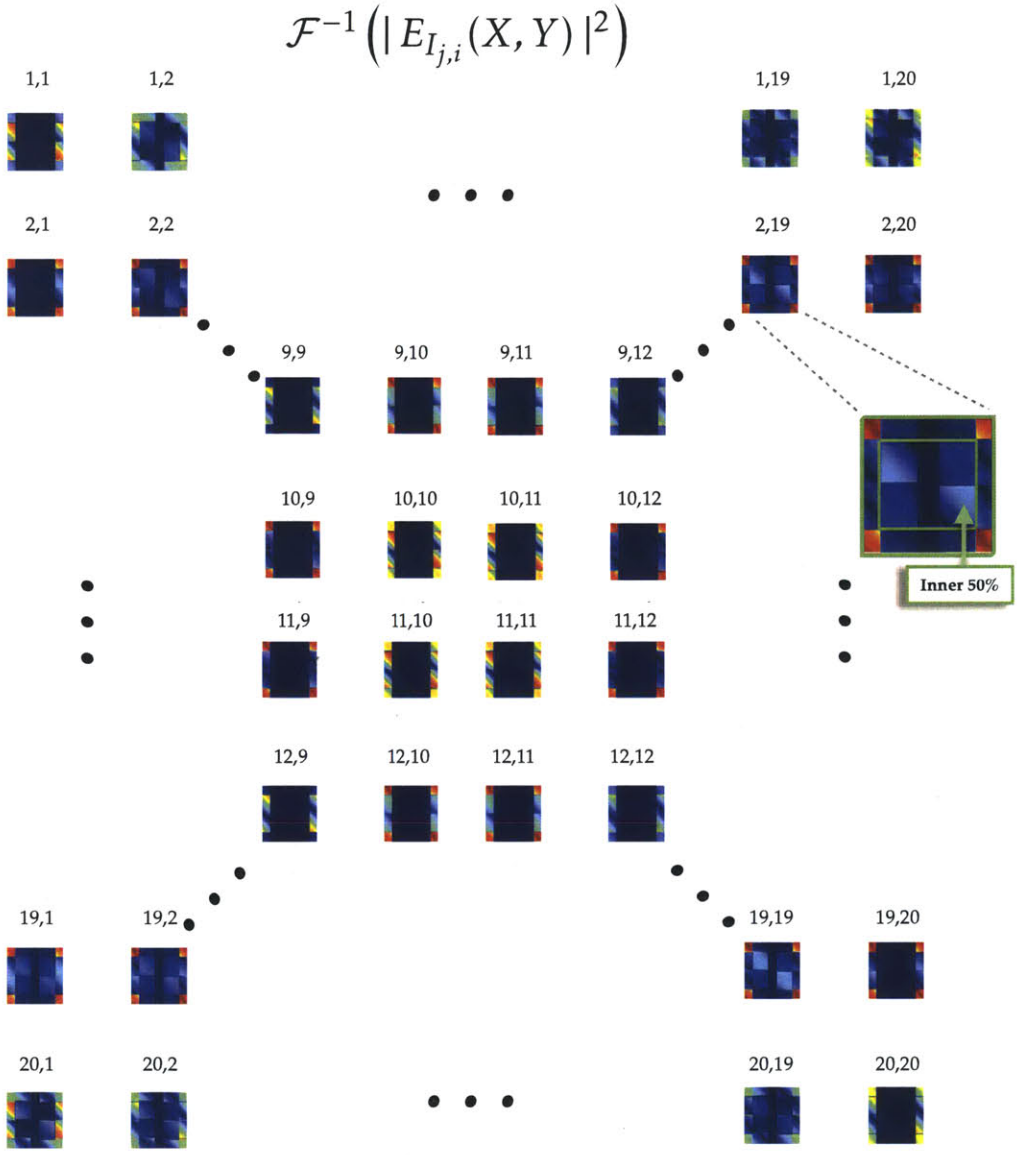

Figure 3-13: Examples of calculated grid squares on the camera, the result of taking the inverse Fourier transform of the square of interacting fields at the focus. Examples from the central area are shown along with examples from each corner. The [2,19] square, representative of squares along the corners and edges that have internal structure, is magnified. The area covered by the inner dimension is 50% that of the outer.

The calculated grid square images resemble windows with varying degrees of complexity toward the center. A detailed section of an actual CCD image is shown in Figure 3-14; the grid squares highlighted are the last 5 columns of the first 5 rows. Interference effects are clearly visible in each grid square, with the patterns and intensities of variation seeming to vary from square to square. Many of the calculated grid square images toward the edges have distinct inner structure, as emphasized in the

[2,19] square in Figure 3-13. The inner square area was found to be 50% of the total square area, corresponding closely to the 40% of pixel area found to be most critical to reducing the baseline noise (Figure 3-3).

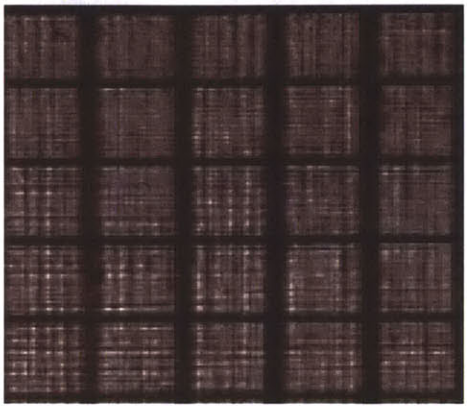

Figure 3-14: 5×5 echelon grid square detail of a CCD image, showing the first five columns of the last five rows. The section was taken from a signal image in the absence of a pump.

To proceed in the analysis, we extract relevant parameters such as mean and standard deviation from intensities at the camera (i.e., of $\mathcal{F}^{-1}\left(|E_{I_{j,i}}(X,Y)|^2\right)$). To do so, we collapse each plot to a single number (the parameter of interest) to obtain a 20×20 matrix representing all 400 grid points, as was demonstrated in the analysis of real images in §2.3. Matrices displaying the average intensity and standard deviation of the intensity at the camera are shown for four different cases in Figure 3-16 and Figure 3-17, respectively. The averages are expected to underlie our experimental signal as it is typically reported; the standard deviations hold potential interest given the discussion in §3.2 regarding variation within individual echelon squares. In both figures, [A] is calculated from a 100 fs input pulse at 800 nm and with uniform intensity across the input beam array. [B] is the result of a 100 fs input pulse at 800 nm superimposed with the truncated Gaussian distribution shown in Figure 3-8. [C] results from a 400 fs input pulse at 800 nm with a uniform intensity distribution, and [D] from a 100 fs input pulse at 400 nm with a uniform intensity distribution. For each calculation, all initial isolated fields (Eq. 3-20) were normalized to the largest field strength in the array. The field strengths before and after the interaction are shown in Figure 3-15 for a 100 fs 800 nm input pulse as a demonstration of this normalization.

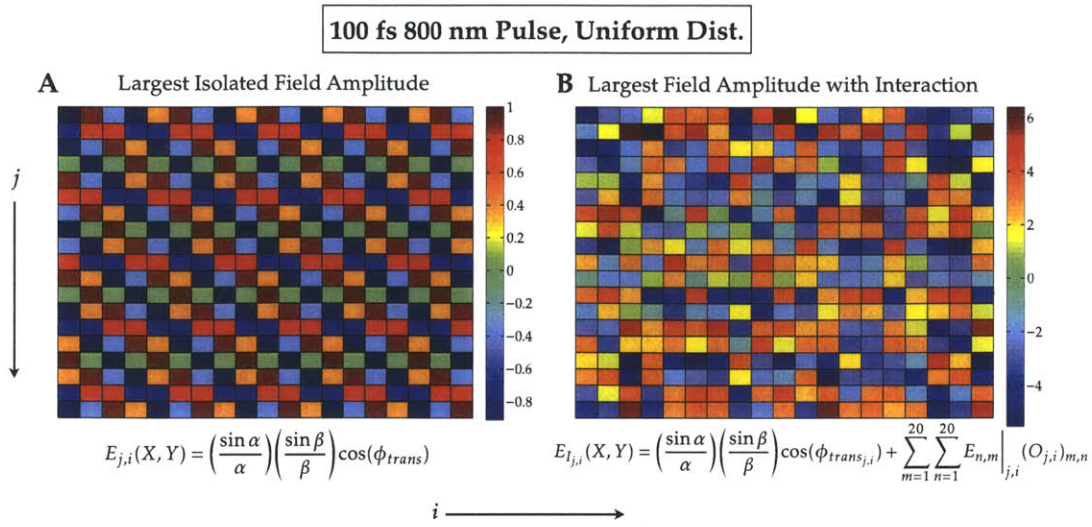

Figure 3-15: Demonstration of normalization procedure used. [A] *The isolated field amplitudes were calculated according to Eq. 3-20. Their largest values were computed, and all 400 fields were scaled so that the largest amplitude of any one field was unity.* [B] *Interacting fields, calculated according to Eq. 3-21, result in higher amplitudes due to constructive adding in the time domain.*

We see from Figure 3-16 that there is intrinsic variation to the measured values on the camera that is completely independent of camera noise or laser fluctuations. Instead, these variations are derived purely from beam interactions and the experimental geometry. Given a uniform distribution and a 100 fs 800 nm input pulse (Figure 3-16 [A], average values across grid squares fluctuate ±110% from the center value. This variation is slightly more (±125%) for an input pulse with a Gaussian distribution as expected (Figure 3-16 [B]). Since the order of magnitude of reported averages and their variation does not change when comparing uniform versus Gaussian intensity distributions, we proceed with uniform intensity distributions for the remaining calculations. The Gaussian distribution is more physically accurate, but the intensity variation may obscure other observations of interest for this analysis.

The calculated averaged matrix for a 400 fs 800 nm input pulse (Figure 3-16 [C]) demonstrates one greater order of magnitude in reported averages relative to the 100 fs case, yet a similar variation in average grid square values from the center value (±110%). This reflects the additive interaction of several fields (higher field strengths overall), as well as the expanded time overlap matrices used for a 400 fs (Figure 3-11) pulse that effectively provide averaging effects. The averaged matrix for a 100 fs 400 nm input pulse (Figure 3-16 [D]) demonstrates a slightly narrower range of reported

averages than the equivalent 800 nm case, with a variation of ±100% from the center value. This could result in a slight averaging effect as the pulse duration increases more over the time window than in the 800 nm case (Eq. 3-16, ($\eta_{400} = 1.47$, $\eta_{800} = 1.453$).

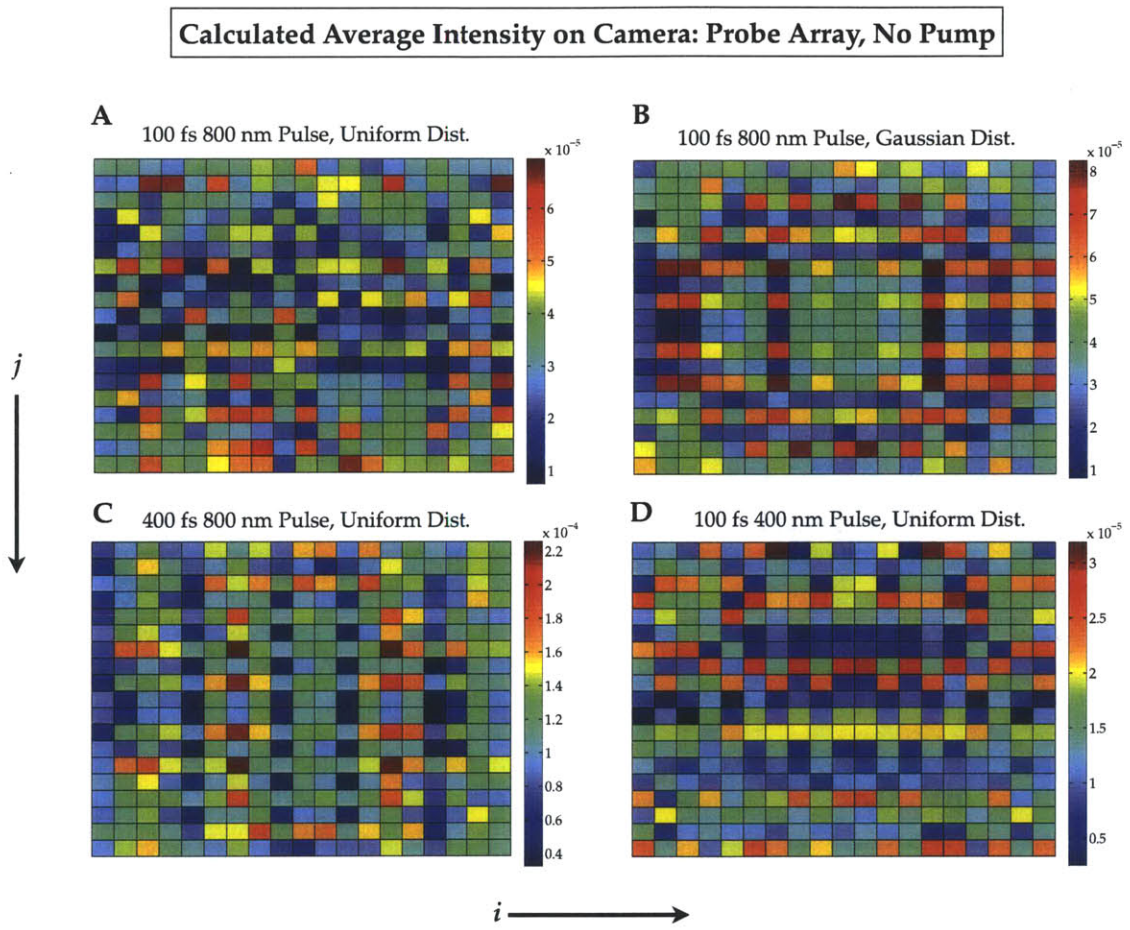

Figure 3-16: Calculated average intensities from probe array beam interactions. Each value is the two-dimensional mean of the inverse Fourier transform of the square of the corresponding interacting field—i.e., $\mathcal{F}^{-1}\left(|E_{I_{j,i}}(X,Y)|^2\right)$, examples of which are shown in Figure 3-13. The calculation parameters are specified in each case, separately varying the initial intensity distribution, the pulse duration, and the wavelength.

We observe the same orders of magnitude in standard deviations across all four test cases. For a given calculated distribution, features such as a large standard deviation in certain echelon squares suggest the possibility of new data analysis methods that devalue the corresponding time points or interpolate them based on values from other squares that are neighboring in time.

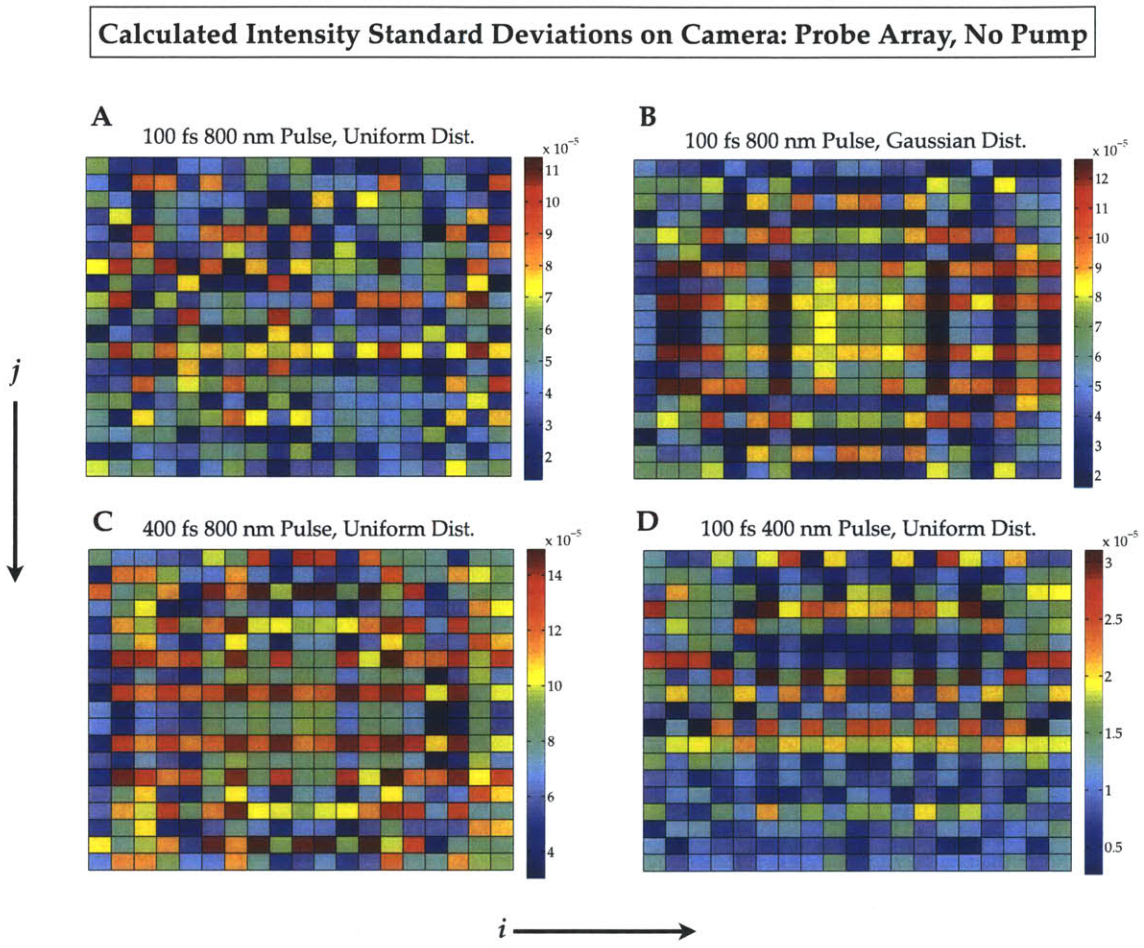

Figure 3-17: Calculated intensity standard deviations from probe array beam interactions. Each value is the two-dimensional standard deviation of the inverse Fourier transform of the square of the corresponding interacting field—i.e., $\mathcal{F}^{-1}\left(|E_{I_{j,i}}(X,Y)|^2\right)$, examples of which are shown in Figure 3-13. The calculation parameters are specified in each case, separately varying the initial intensity distribution, the pulse duration, and the wavelength.

The results shown in the preceding figures suggest that parameters such as probe wavelength and temporal duration can affect signal detection due to intrinsic properties of the probe beam array and the experimental geometry. The units provided do not have physical relevance, however. To connect these calculations to experimental results

and CCD electron counts, we examine the reference grid from a CCD image. Figure 3-18 [A] shows the result of pixel-averaging the reference side of an image to a 20×20 matrix. The resulting array is dominated by a large-scale intensity variation due to the probe beam profile. We take the difference of two pixel-averaged matrices from images collected in close succession to eliminate the beam profile variation. The result should reflect *changes* in probe beam interactions from one image to another, which are presumed to be less than the variations across any one image, as well as changes in the CCD and laser noise sources (calculated to be 27.5 counts per pixel in §3.1, or ~1 count per echelon square when all pixels are averaged $(27.5/\sqrt{700 \text{ pixels}})$. The difference between two pixel-averaged reference matrices, neglecting outliers, varies by ±5 counts about zero as shown in Figure 3-18 [B]. This suggests that the variation from probe beam interactions may lie in the 4-count range. Unlike the noise sources discussed in §3.1 (with the exception of periodic noise), this variation cannot be treated by pixel averaging. Rather, it is the intrinsic variation between pixel-averaged regions.

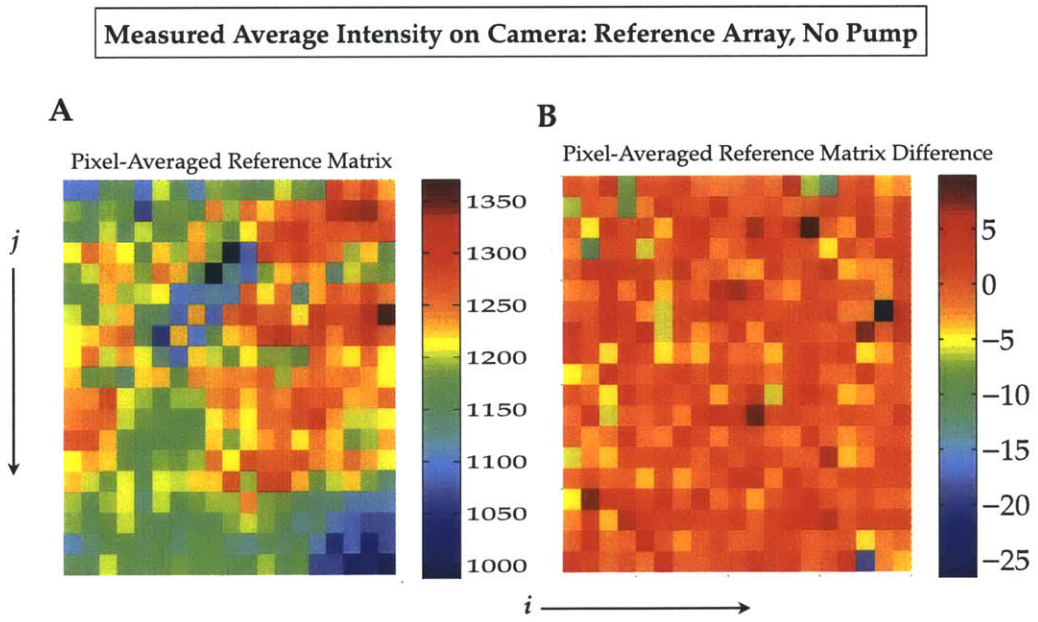

Figure 3-18: [A]: The pixel-averaged reference matrix computed as described in 2.3.3. The large-scale intensity variations are due to the probe intensity profile. [B]: *The difference of two pixel-averaged reference matrices from separate laser shots shows the variation underneath the probe beam intensity profile. While not ordinarily used in processing, this averaged matrix provides a rough calibration for scaling the averaged values calculated in the probe array simulations.*

3.3.3 Probe Beam Array Interactions under Photoinduced Change

In addition to analyzing intrinsic noise levels, the model presented here supports calculations of the imaged signal response to strong external pulses, as additional pulse interactions and time-dependent refractive index changes are straightforward to introduce by exploiting the spatio-temporal mapping. The calculation for a 100 fs 800 nm input probe pulse of uniform intensity was repeated with an introduced pump response: a step function change in the refractive index between square [18,3] and [2,5] (i.e., between timepoints 58 and 82, or between 1.3 and 1.9 ps) as shown in Figure 3-19 [A]. The -10% change in η, from 1.45 to 1.3 during those timepoints, was chosen to be larger than is physically likely for illustrative purposes. ($\Delta\eta_{pump} \approx 10^{-2}$ has been observed in several systems.[91,92]) The aggregated 20×20 matrices for isolated field amplitude [B], average intensity [C], and standard deviation [D] are also shown. For more straightforward comparison, in Figure 3-20 we compare the average and standard deviations between the pumped (Figure 3-19) and unpumped (Figure 3-16 [A] and Figure 3-17 [A]) calculations.

From the difference of the 'pumped' and 'un-pumped' averaged matrices in Figure 3-20, we observe the effects of the refractive index change well before the change has been introduced in time, as is seen easily by visual comparison with Figure 3-19 [A], as well as throughout the time of the lowered η. This may be interpreted in the context of the time overlaps between pulses, which for a 100 fs input probe pulse were shown to extend appreciably 10 grid points in either direction (Figure 3-11 [A]).

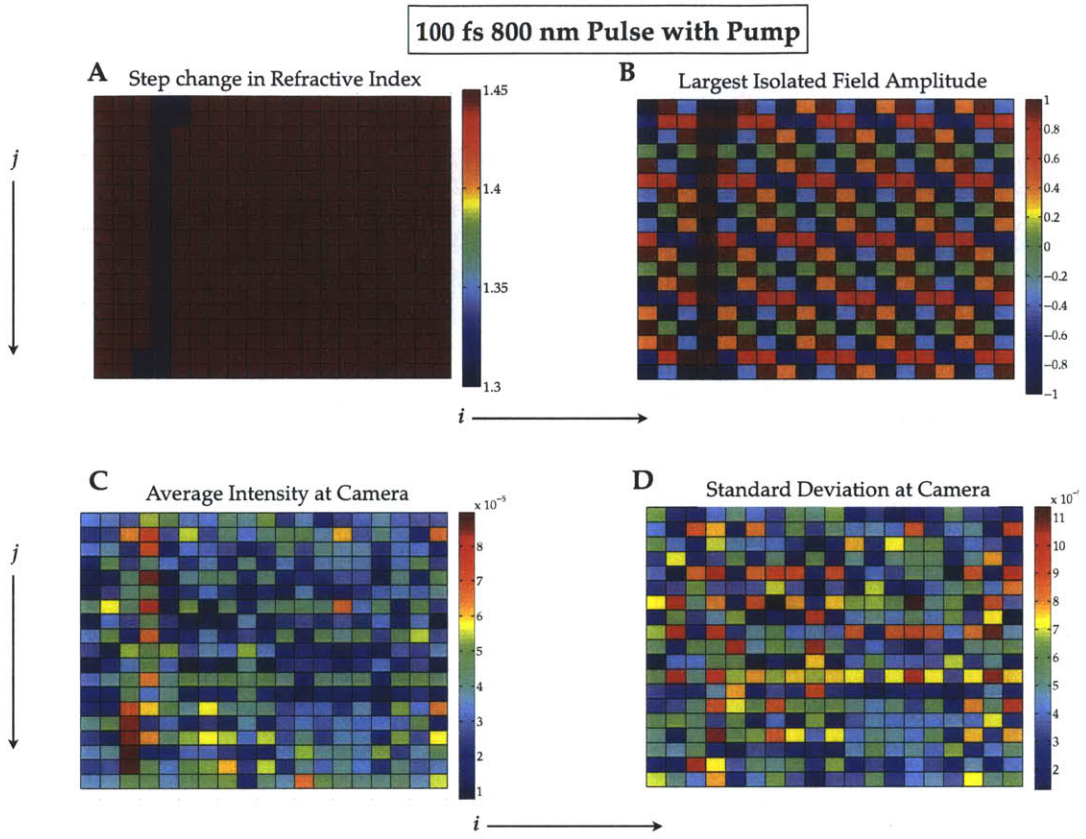

Figure 3-19: [A]: *A step change in refractive index was introduced for the timepoints shown to simulate a material response to a pump pulse.* [B]: *The largest isolated field amplitude, calculated without beam interactions, demonstrates the effect of a refractive index change confined to specified grid points.* [C]: *Average intensity per grid point under a simulated pump pulse.* [D]: *Standard deviation per grid point under a simulated pump pulse.*

The unfolded traces of both grids are shown in Figure 3-20 [C], with the earliest and latest perceptible change noted, as well as the temporal region of refractive index change induced. In this simulated case with no laser shot fluctuations, changes we observe are due solely to predicted interactions of probe fields under varying conditions. The (difference) average unfolded trace reports on the net changed values of interacting probe fields under a step change in refractive index. The (difference) standard deviation unfolded trace reports on the changed extent of variation within each square resulting from the step change. In reference to the discussion of variation in individual echelon squares in 3.2, we postulate that strong interference patterns result from the nearby (in space and time) interaction of probe pulses that see significantly different optical material properties during their centered arrival time on the sample. Notably, the most significant sustained changes in standard deviation in

Figure 3-20 [C] (the rising and falling edges) occur before and after the induced refractive index change, rather than during.

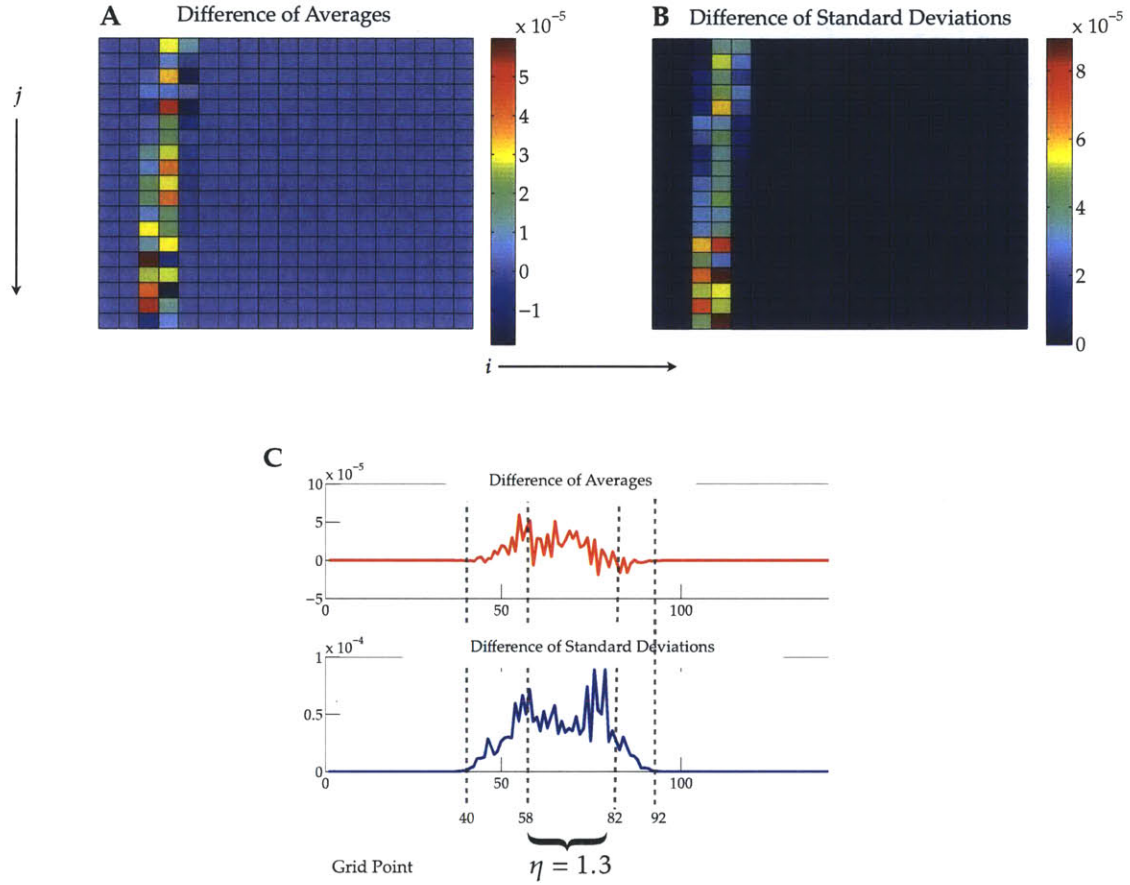

Figure 3-20: [A]: *The effect of a simulated pump response on the averages measured at the camera. Shown is the difference of the matrices shown in Figure 3-19 {C}* and *Figure 3-16 {A}.* [B]: *The effect of a simulated pump response on the standard deviations measured at the camera. Shown is the difference of the matrices shown in Figure 3-19 {D} and Figure 3-17 {A}.* [C]: *Unfolded traces of both difference matrices, with time points specifying the first {40} and last {92} perceptible changes, as well as the temporal region of changed refractive index {58-82}.*

The interaction of probe beams, as analyzed in detail in this section, presents important considerations for data analysis. We conclude that the temporal duration of the probe pulses is likely to play a significant role in the reported dynamics of the measurements. Care should be taken for precise temporal characterization of the pulse. However, the beam interactions that result from our unique experimental geometry may also be uniquely sensitive to changes in material properties or optical pulse interactions, providing an alternate means to inform our analysis and complement our measurements of time-resolved material dynamics.

Chapter 4

Photo-induced Structural Change in Platinum-Iodide

Photoinduced dynamics in crystalline metal-halide chain compounds have stimulated decades of interest due to their straightforward structure yet complex interplay between electronic and vibrational degrees of freedom and between chemical and structural rearrangements.[93-96]

In this chapter, single-shot two-pump femtosecond optical measurements of PtI(en) are presented that have permitted analysis of cooperative effects and real-time visualization of a photoinduced electronically distinct state. Interactions among photoinduced excitations are monitored in the context of cooperative models, and evidence for a photoinduced response lasting more than 100 picoseconds upon exciton generation at high densities is shown, as measured by electronic signal amplitudes and lattice phonon properties. The achievement and observation of a distinct long-lived response may indicate collective structural rearrangement in this and related compounds. The experimental observations are discussed in the context of significant background literature and theoretical descriptions, and future measurements are proposed.

4.1 Metal-halide chain crystals

In seeking to understand how energy is stored, moved, and transferred in materials, it is often helpful to study simple systems. Though even in structurally simple systems the dynamics remain complex, reducing the complexity in particular ways can help us isolate parameters of interest and understand fundamental principles that extend to more complex systems. In this spirit, we turn to a prototype material of long-standing interest in condensed matter physics and chemistry: metal-halide crystalline chains.[97-102] Improved understanding of the mechanisms involved in light-induced changes to electronic and lattice structure in this material could yield applications in molecularly engineered electronic and photonic devices.

Quasi-one-dimensional metal-halide chain compounds exhibit mixed valency across the metal centers and competition or cooperation among key energetic terms that determine their structure and dynamics. In particular, Coulomb repulsion energy (U) competes with electron-phonon interaction (S) to dictate the ground state lattice structure and electronic configuration. Mixed-valence chain materials were originally classified by Robin & Day according to the extent of their valence delocalization.[103] Class I comprises structures with stable and highly localized valencies that cannot interconvert. Class III comprises highly delocalized valencies, with each metal site exhibiting an intermediate oxidation. This effect, rendering a Mott-Hubbard symmetric state, is ascribed to a strong coulombic term yielding degenerate half-filled shells. Because the lattice structure is symmetric, mixed-valency Mott-Hubbard states cannot be easily distinguished with spectroscopy. Intermediate between these, Class II materials exhibit moderate valence delocalization with a low conversion barrier between atomic sites. The mixed-valence ground state that results is ascribed to strong electron-phonon coupling, wherein a stabilizing electron configuration induces a particular lattice structure. The mixed-valence structure is frequently referred to as a charge-density wave (CDW) state. Figure 4-1 illustrates this picture for a linear metal-halide chain with competing U and S terms. Nickel and Platinum compounds are known examples of Mott-Hubbard and CDW ground state structures, respectively.

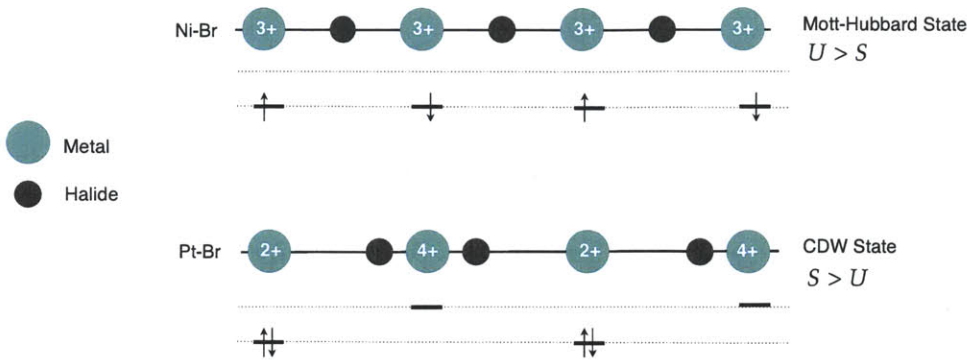

Figure 4-1: Structural and electronic configurations typical of mixed-valence metal-halide ground-state chain configurations when coulombic interactions U yield the symmetric ground state (top, Mott-Hubbard state, e.g. Ni-Br chains) and when electron-phonon interactions S yield the distorted ground state (bottom, Charge Density Wave state, e.g. Pt-Br chains.)

The ground state structures are depicted as concrete cases in Figure 4-1, but the extent of lattice distortion and valence localization varies continuously for groups of synthesized crystals with even only slightly varying properties.

One such group is Pt-X chain crystals, where X = Chlorine, Bromine, or Iodine. Here we will emphasize measurements on Pt-I crystals, but detailed studies elsewhere have described the extent and direction of measurable property differences across these related compounds.[98,99,101,104-107] Our focused measurements on one structure are an effort to observe new thresholds of behavior for these materials generally rather than to affirm established trends across them. Nonetheless, future studies on other related compounds remain a compelling possibility, as discussed in §4.6. For reference in comparing to the literature (where Pt-Cl has been the most widely-studied), we summarize the trends briefly here. Strong electron-phonon coupling is observed in Pt-Cl complexes, with Pt-I demonstrating the weakest coupling. As a result, the extent of valence localization and the ratio of bond lengths in the disordered ground state decrease across the Cl, Br, I series. The absorption spectra for this category of materials exhibit decreasing frequency of the main (charge-transfer) absorption band from Pt-Cl (highest frequency) to Pt-I (lowest). While the precise values of these properties depend on the ligand and counterion structure, the trends hold true across the halogen series for a consistent given structure.

The crystals, typically recrystallized from solution, form linear chains of alternating metal and halide atoms. The chains are separated by ligands that reduce steric effects between chains and can fine-tune certain structural properties. The

distance between chains is on the order of 10 angstroms, while the inter-nuclear distance along a chain is on the order of 1 angstrom. This geometry, in addition to a primary electronic transfer path coupling to an in-chain lattice mode, renders a one-dimensional approximation appropriate. This approximation is especially accurate for Pt-I crystals of the form studied here, as they lack the two-dimensional phase alignment of halogen distortions observed in the similar Pt-Br structure.[106]

The compound studied here is $[Pt(en)_2][Pt(en)_2I_2](ClO_4)_4$—hereafter PtI(en). A simplified structure is depicted in Figure 4-2. Ethylenediamine (en) ligands occupy the platinum binding sites, and perchlorate counterions (not pictured) link the chains. Laser-induced electron transfer along the 1D chain axis launches halide motion and coherent vibration along the same axis, creating a well-defined microscopic laboratory to showcase the interplay among optical, electronic, and vibrational energies and their roles in local crystalline chemistry and collective, long-range lattice structure.

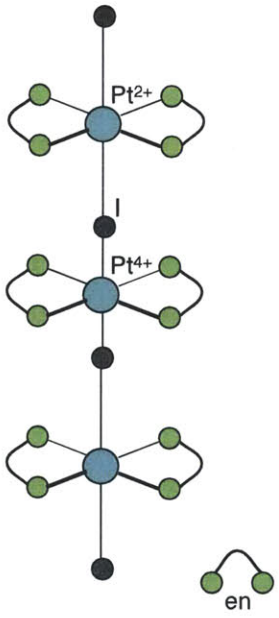

Figure 4-2: PtI(en) lattice structure with a symmetry-breaking, energy-lowering Peierls distortion of alternating valences and bond lengths. Perchlorate counterions neutralize the overall charge and minimize steric effects while linking parallel chains; ethylenediamine (en) ligands occupy the metal binding sites.

4.2 Excitations and Phase Transitions

4.2.1 Fundamental excitations in Metal-halide chains

The electron-lattice coupling that produces a characteristic lattice distortion in PtI(en) also yields a Peierls band gap that minimizes the electronic energy. In the ground state, Pt centers exhibit alternate valences of 3-δ and 3+δ, and Pt-I bond lengths alternate as well (with a length ratio of 0.92 from one Pt-I bond to the next).[108] Even slight perturbations to the electronic ground state can induce structural change. While in a metal it is typically sufficient to describe promoted electrons as free carriers evenly distributed, the one-dimensional constraint disallows that description for PtI(en). Instead, a variety of quasi-particle excitations are possible. Excitons may propagate along the chain when a valence electron is promoted; specifically, charge-transfer excitons correspond to the inter-valence energy gap caused by the Peierls distortion. Excitons interacting strongly with surrounding atoms can become immobilized, or self-trapped. Additionally, mid-gap states are reported to exist in platinum-halides, and may be reached either by absorption or exciton decay. Polarons, a coupling of a charge carrier with an atomic polarization field, are one such excitation—first predicted for strong electron-phonon coupling materials by Landau in 1933.[109] Self-trapping generally requires a barrier-surmounting transition toward a trapped potential that is defined by short-range atomic forces.[110,111] In contrast, pure polarons arise from the coulomb interaction between electrons and a polar lattice, and may or may not become immobilized.[112] Solitons, solitary self-reinforced waves without dispersion, have been predicted theoretically to exist in platinum-halides,[113] but their identification has proved more elusive. Additional excitation types, including kinks and bipolarons, may also be present when excitations interact with the surrounding lattice.[114]

Polaronic behavior is observable via Raman spectroscopy.[100,115] Absorption from polaron states grows in to the red of the inter-valence charge transfer absorption band with red-shifting of the excitation wavelength. These observations have allowed phenomenological descriptions of vibrations both in the ground state and in excited states. Still, the lack of experimental study on lattice dynamics in various electronic excited states has been noted in the literature.[114] In particular, observation of polaron absorption in PtI by Raman spectroscopy has been difficult since the excitation

absorption (1.3 eV) lies in the infrared,[102] though absorption at 0.6 eV has been ascribed to photo-generated polarons.[106] Numerous nonlinear pathways have been proposed for the decay and creation of defects.[100,101] Evidence of defect features changing with temperature, excitation energy, or other parameters may lend insight into their properties.[102,114,116]

The charge-transfer exciton is the excitation most directly related to the lattice symmetry. Transitions from charge density wave to free exciton to trapped exciton are illustrated in Figure 4-3, which shows the highly localized two-site limit.[117,118] More realistically, the excitation has been proposed to exist over approximately twenty unit cells, calculated via the spatial electronic wavefunction solution in the excited state to a tight-binding model.[117]

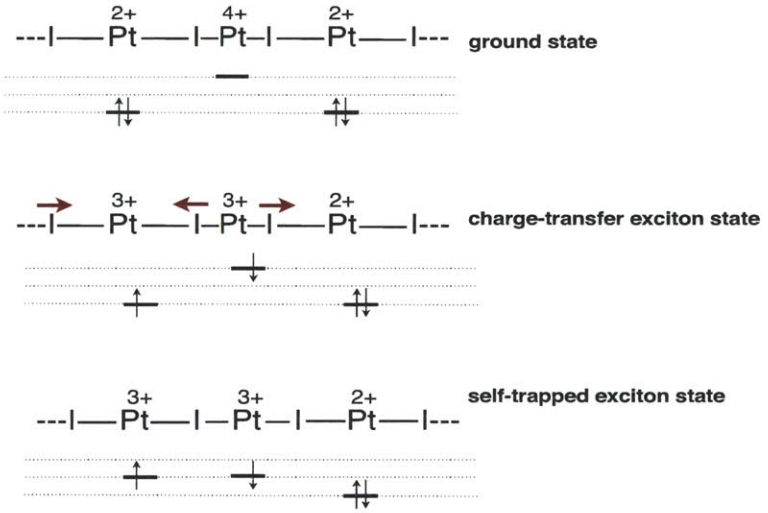

Figure 4-3: Structure and electronic distribution in the highly localized extreme for the ground state, charge-transfer exciton state, and self-trapped exciton state. (Sourced from [118]).

Photo-induced charge-transfer excitation and self-trapping in metal-halide chains have been studied in the time domain via ultrafast spectroscopy and luminescence measurements. The symmetric I-Pt^{IV}-I stretch is Raman active and shows strong resonance enhancement and vibronic coupling near the charge-transfer transition, onset at 1.3 eV.[108] Photoexcitation into a charge-transfer exciton state with the ground-state Peierls-distorted geometry initiates a large excursion along the symmetric stretch coordinate as a locally equivalent self-trapped exciton (STE) species is generated. PtI(en) lattice vibrations associated with STE formation around 125 cm^{-1} have been reported from time-domain studies,[119] corresponding to the symmetric stretch in the resonant

Raman spectrum.[120] In addition, wave packet motion at 110 cm^{-1} along the fully formed STE state has been resolved in the time-domain spectrum of photo-excited PtI(en).[121] The STE lifetime in PtI(en) has variously been reported as 0.65 ps via time-resolved luminescence measurements[122] and as 1.4 ps via time-resolved reflectivity measurements with a 150 fs formation or thermalization time.[123] Most likely, these differing timescales reflect not discrepancies in measurements but instead result from complex multi-pathway decays into localized excitations and strong electron-hole coupling due to restricted dimensionality.[124]

Though conventional time-resolved pump-probe spectroscopy has provided descriptions of STE formation in PtI(en) and related materials,[95-97,104,125,126] the technique's investigative utility is restricted to reversible material changes due to the thousands of repeated pump-probe sequences required. This limits probing the high-excitation-density region where cooperative effects are expected and where proposed dynamics for localized excitations may be further scrutinized.

4.2.2 Structural Transitions

The intermediacy of Class II mixed valence chains render them especially attractive for our study of phase transitions and control over material dynamics. The strong electron-phonon coupling characteristic of this class provides a means of studying and controlling energy transfer at the molecular scale, and the prospect of controlled low-barrier structural switching is a key goal of materials science that our measurement is uniquely positioned to explore.

Platinum-halide chains exhibit temperature-dependent structural phase transitions. At very low temperatures (20 K), stacking of ethylenediamine ligands has been observed via neutron diffraction.[127] Near room temperature (20-30 $^{\circ}C$ depending on the structure), platinum-halide chains undergo a phase transition from a monoclinic (low temperature) to an orthorhombic (high-temperature) structure.[128-130] The temperature-dependent conformational change has been attributed to increased motion of perchlorate counterions that modify the hydrogen-bonding network formed by the counterions and ligand $-NH_2$ groups, affecting the packing of parallel chains. Due to this conformational change at ambient temperature, significant variation in reported structures exists.[107] Comparison among certain measurements can be difficult as a result, but we will mostly be concerned with electronic and structural dynamics along

the chain axes, rather than across the two-dimensional chain structure. Raman spectroscopy measurements performed across the ambient temperature phase transition have identified an increase in the breathing mode frequency (motion of the halogens and metal ions along the chain as electronic degeneracy lifts) with increasing temperature, indicating that an increase in CDW strength occurs alongside the conformational packing change.[107]

An additional structural phase transition is possible along the platinum-halide chain by a different path. The distortion in the ground state lattice may be lifted due to an inter-valence charge transfer, causing the chain to move toward a symmetric non-distorted structure. This electron-phonon coupling effect has been well-characterized in platinum halides, and in PtI(en) the charge-transfer absorption peak is at 1.3 eV.[108] The phase transition is referred to as a charge-density to spin-density wave (SDW) transition, characterizing the redistribution of uniform charge in space, or alternatively as a reverse Peierls transition, suggesting the joint rearrangement of electrons and atoms.[100,131] Importantly for our purposes, the resulting atomic motions along the inter-nuclear chain can be resolved as phonon oscillations.

The reverse Peierls phenomenon—charge transfer and subsequent atomic motion—can occur on either a very local scale (across one pair of platinum ions) or, theoretically, across a large region (many hundreds to thousands of unit cells). Theoretical treatments such as the Peierls-Hubbard model have shed light on the behavior underlying localized transitions, but the magnitude and spatial extent of structural change induced by a charge transfer event are more difficult to model and require assumptions about interactions.[117] Localized instances of structural rearrangement are typically characterized as excitations that propagate along the chain, or as valence defects that become immobilized and are semi-stable. While localized excitations exist without interaction, cooperative effects are likely to play a role in inducing macroscopic structural change, with stability from one altered region inducing stability in a nearby region. Materials that undergo macroscopic change from a localized trigger are of significant interest due to their potential application in future switching devices, and the exploration of Pt-X materials toward this end has in part motivated our study.[132] In either observed case—localized or macroscopic—the relevant experimental signatures are largely unexplored, yet their distinction and control would be a valuable tool.

Photoinduced charge transfer is an attractive route toward chain-axis structural change, particularly because the charge transfer transition is in the optical to near-infrared range. Photoinduced creation of localized defects has been demonstrated,[106,129,133] and theoretical treatments have proposed routes to macroscopic phase changes by photoexcitation.[134,135] Additionally, a photoinduced insulator to metal transition in platinum-halides has been reported to take place for high excitation densities (near 0.5 absorbed photons per Platinum ion).[136]

Due to fundamental interactions (electron-phonon coupling), reduced dimensionality, distinct well defined excitations, and the potential to exhibit cooperative effects, metal-halide chain complexes have served as prototypes in solid-state theory and modeling. Rudolf Peierls predicted the existence of charge density waves in quasi-one-dimensional materials through his work in the 1930's and 1940's,[137] and they were identified experimentally in the 1970's in compounds bearing resemblance to metal-halide chains.[138,139] The metal-halide chain compounds have been evaluated extensively within the Peierls-Hubbard model,[140] and have also been treated as prototypes in the development of a theory for PIPT.[54,79,141] Further theoretical treatments have been developed to characterize the normal mode vibrations of metal-halide chains and the energetics of possible excitations in the material.[113,114,142]

Metal-halide chains have also been explored as model compounds for high temperature superconductors based on work by Frohlich in 1953.[141] The symmetric breathing mode frequencies of platinum-halide compounds increase as the excitation energy increases, an effect attributed to the extent of valence delocalization and induced conductivity along the chain.[143] It has been shown that several high-temperature superconductors exhibit charge density wave behavior under some circumstances, and in general CDW behavior is thought to compete with superconductivity.[144,145] Recently, at least two important works have elucidated this competition experimentally. Chang and co-workers characterized the superconducting-CDW competition near the critical temperature in $YBa_2Cu_3O_{6.67}$,[146] and Ghiringhelli et al. found CDW behavior above the superconducting temperature in a related material and demonstrated improved calculation of critical temperatures when incorporating the CDW character into superconducting models.[147] An advanced understanding of electronic interactions and control in quasi-one-dimensional CDW crystals such as PtI(en) may help us design better superconducting devices in the future.

4.2.3 Key Questions for Single-shot Study

Several factors render the metal-halide family a prime candidate for single-shot study. Optical and crystallographic properties of the materials are well known, and expertise has developed around synthesizing high optical quality crystalline samples—an important criterion for our noise-sensitive imaging detection system.

Metal-halide chains have been discussed as prototypes for the field of photo-induced phase transitions; however, the cooperative effects proposed to yield macroscopic change have been treated theoretically without experimental corroboration. A photoinduced macroscopic phase change is one possibility, but many variants are also possible, from long-range delocalized excited structures and isolated domains of high symmetry to long-lived defect states. The single-shot measurement, capable of studying irreversible events at the high intensities proposed to be necessary for cooperative phase change effects, is uniquely positioned to examine dynamical evolution of this system even very far from its equilibrium state.

Key experimental needs have been identified in the literature, the fulfillment of which would yield a fuller picture of metal-halide chain behavior. Koshihara et al. observed threshold behavior in the photoconverted fraction of low-dimensional organic charge transfer crystals leading to macroscopic change, but specified that experiments with a repetition rate less than 10 Hz would be required for confirmation that the effect did not result from accumulated thermal change.[66] In addition, the need for dynamical lattice measurements to connect directly with electronic population data has been stressed.[101]

In other low-dimensional strong coupling materials, semi-permanent states lasting for several hours have been reported after photoexcitation.[133,148] This intriguing observation may have relevance in short-term data storage and other applications. However, conventional spectroscopy measurements cannot reveal the development of such states. Nor, in most cases, can they distinguish between pure one-photon excitations and cumulative effects derived from heating or continuous carrier population pumping. The single-shot measurement can both observe the dynamics of far-from-equilibrium states in real-time and distinguish between isolated and cumulative measured effects.

Finally, theoretical works have proposed significant non-linear effects in metal-halide chains that may lead to structural photoinduced phase transitions.[135,149,150] These works have proposed various mechanistic pictures of excitations leading to structural change. The interplay between excitation and structural change is expected to be complex; self-trapping and other excitations occur due to induced changes from previous excitations, and cooperative change is likely an emergent result of such excitations themselves. Preliminary efforts to characterize exciton interaction in a generic one-dimensional electron-lattice coupled system have suggested that a precursor to long-range phase domain formation exists when 4-exciton aggregates interact along a chain, suggesting that high excitation densities are necessary for true structural change.[150] Our single-shot study of platinum-halide chains is positioned to complement such developing mechanistic pictures experimentally since the structural phenomena of interest are expected to occur at high excitation densities. As previously discussed, conventional time-domain spectroscopy measurements cannot accurately measure dynamics beyond a certain material-dependent threshold of absorbed photons. As we show below, single-shot measurements allow us to accurately portray the material response under extremely high photon excitation densities without cumulative damage effects. This provides a unique means by which to monitor cooperative effects, evaluate proposed theoretical models, and gain insight into the nature of photo-induced phase transitions.

4.3 Measurement and Analysis

4.3.1 Experimental Details

The pump wavelength was 800 nm, corresponding to a photon energy of 1.55 eV, above the charge-transfer transition energy of 1.3 eV for PtI(en). As described in Chapter 2, a sapphire crystal for white light generation was paired with a filter for probing at wavelengths less than 800 nm to conduct conventional pump-probe measurements, while a non-collinear optical parametric amplifier (NOPA) was employed for single-shot measurements. For the measurements presented here, the probe wavelength was 600 nm, and both pump and probe polarizations were parallel to the chain axis. A bandpass filter was used to block scattered pump light from the detector.

We are interested in the material's response to a single pulse rather than to the cumulative result of many pulses; however, averaging several shots of data significantly improves signal-to-noise levels (Figure 2-17). The single-shot-regime data presented here were collected over 60-100 laser shots whose separations are long enough to ensure the full relaxation to the ground state, and their average is displayed. In each case, cumulative degradation was avoided by ensuring that low-fluence conventional measurements following the high-power shots yielded the expected and reproducible response.

Damage measurement checks were instituted for each pump power employed for both conventional pump-probe and single-shot measurements. This procedure involved data collection at low fluence (~1 $\frac{mJ}{cm^2}$), followed by irradiation on the same sample spot at the desired fluence for measurement. For conventional pump-probe measurements, the sample spot was irradiated on the order of 10,000 times, corresponding to several tens of seconds and a comparatively fast scan. For single-shot measurements, the sample spot was irradiated at most 100 times for these tests, which yielded the desired signal-to-noise ratio given the expected signal strength. After irradiation, the fluence was lowered to the original fluence and data were collected again. If the sample response before and after the irradiation period were identical, it was assumed that no cumulative damage was incurred. This was the case for all data shown here except conventional pump-probe data presented for illustrative purposes in Figure 4-13.

Single crystals of PtI(en) were synthesized from perchloric acid ($HClO_4$) solutions of the complexes $[Pt(en)_2I_2]I_2$ and $[Pt(en)_2](ClO_4)_2$, and were recrystallized from the water solution by collaborators in the laboratory of Jun Tanaka at Osaka University.

4.3.2 Data Analysis

Separating electronic and lattice components

Typical measured reflectivity traces exhibit modulations from lattice oscillations superimposed on an exponentially decaying electronic background signal from carrier absorption. To separate the electronic and oscillatory contributions, the signal after t=0 was fit to a multi-decaying exponential:

$$(\Delta R/R)_{el} = Ae^{-t/\tau_a} + Be^{-t/\tau_b} \qquad \textit{Eq. 4-1}$$

Phonon frequency and damping parameters were determined by performing both conventional and short-time Fourier transforms on processed data of the isolated oscillatory component, and a uniform error for all frequency parameters was estimated to be 0.2 THz by fitting representative oscillatory data to the form:

$$(\Delta R/R)_{ph} = Ce^{-t/\tau_{ph}} \sin(\omega t + \beta t^2 + \phi) + D \qquad \textit{Eq. 4-2}$$

This level of uncertainty is also supported by the $\frac{1}{50\,\text{fs}}$ sampling frequency and number of timepoints. Phonon amplitudes relative to electronic absorption amplitudes were extracted directly from the raw data to retain directly comparable values across data scans. Errors are given by the instrumental variation in $\Delta R/R$ values, 0.001.

Fourier Analysis

We analyze the instantaneous lattice response to photoexcitation at different fluences by performing a discrete short-time Fourier transform (hereafter STFT). This is accomplished by weighting the signal function with a sliding time 'window' that acts as a low-pass filter, and then Fourier transforming the result to analyze the frequency components within each window. In a continuous time domain, the short-time frequency spectrum is given by

$$X(f,t) = \int_{-\infty}^{\infty} w(t-\tau)x(\tau)e^{i2\pi f\tau}d\tau \qquad \textit{Eq. 4-3}$$

with $x(\tau)$ as the input signal and $w(t)$ as the window function. In our measurements, and for any practical signal processing application, the time-varying signal $x(\tau)$ is sampled discretely. For pump-probe measurements we sample every 50 fs; for single-shot measurements every 22.7 fs. If we define this characteristic sampling interval as T_s and the number of samples as N, then the sampling rate is $F_s = \frac{1}{T_s}$ and we can evaluate each timepoint $t_n = nT_s$ or equivalently each frequency point $f_m = \frac{mF_s}{N}$, up to the Nyquist frequency $\frac{F_s}{2}$. Accuracy is improved when windows are chosen to be mostly overlapping in time. Assuming the sampling rate is more than double the highest frequency of interest, the spectrum can be evaluated discretely for values of n and m with minimal information loss:[151]

$$X_{nm} = \sum_{t_n=0}^{T-1} w(nT_s - t_n)x(t_n)e^{i2\pi t_n f_m/T} \qquad \textit{Eq. 4-4}$$

with total time $T = NT_s$. Eq. 4-4 is evaluated for all frequencies of interest, and the result is often depicted in a spectrogram which shows the power spectrum of the time-varying signal's frequency components as a function of time. A sample spectrogram from the lowest pump fluence measurement for our PtI(en) measurements is shown in Figure 4-4. Any STFT must be performed with careful attention to detail. It should be clear from the above definition for a discretely sampled spectrum that the maximum possible frequency resolution is determined by particulars of the experiment. Further, the actual frequency resolution equal to or less than this maximum must be selected for the application at hand (discussed below). In addition, the type of window function applied and its width can lead to drastically different apparent results, so it is essential to understand the signal well before performing the analysis. For a thorough discussion of artifacts that can result from improper treatment, including degradation, spectrum leakage, and truncation error, the reader is referred to Stuller, 2008 or other signal processing texts.[152]

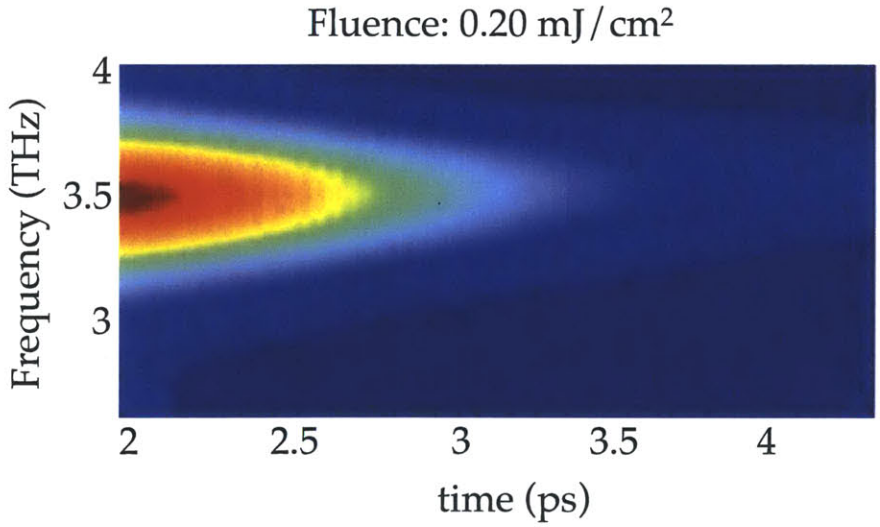

Figure 4-4: Spectrogram showing the power spectrum as a function of time and frequency, for the data collected at the lowest pump fluence in Figure 4-6. A time window of 1.95 ps was used. Intensity is centered at the breathing mode frequency near 3.5 THz, with the strongest contribution in the first few picoseconds of measurement time.

In the STFT data presented here, we use the Hann window to minimize aliasing. The functional form with specified full width at half maximum a is given by:

$$w(t) = \frac{1}{2}\left[1 + cos(\frac{\pi t}{a})\right] \qquad \textit{Eq. 4-5}$$

The choice of parameter a is an important one related to the Gabor limit. The Gabor limit states that there is an inherent tradeoff between time and frequency resolution when performing an STFT.[153] This presents a particular challenge for our application: we are interested in subtle frequency shifts (begging good frequency resolution), but since the initially red-shifted phonon oscillation is expected to relax in time, and at increasingly high fluences we observe fewer cycles for analysis, longer time-windowing (poorer time resolution) yields a result that is averaged over a significant range of time-varying frequencies. This effect is displayed in exaggerated fashion in Figure 4-5. For these data, the window width has been chosen by increasing the frequency resolution (widening the window) until, for each fluence and at the initial timepoint (where physically we expect the greatest frequency spread and will conduct subsequent analyses), one frequency component was clearly dominant in the frequency region of interest (2.7 - 3.7 THz). If the time resolution is increased beyond this point, frequencies for different fluences merged so as to be indistinguishable. The time window used for all conventional pump-probe data was 1.9 ps; the time window used for all single-shot data was 1.7 ps.

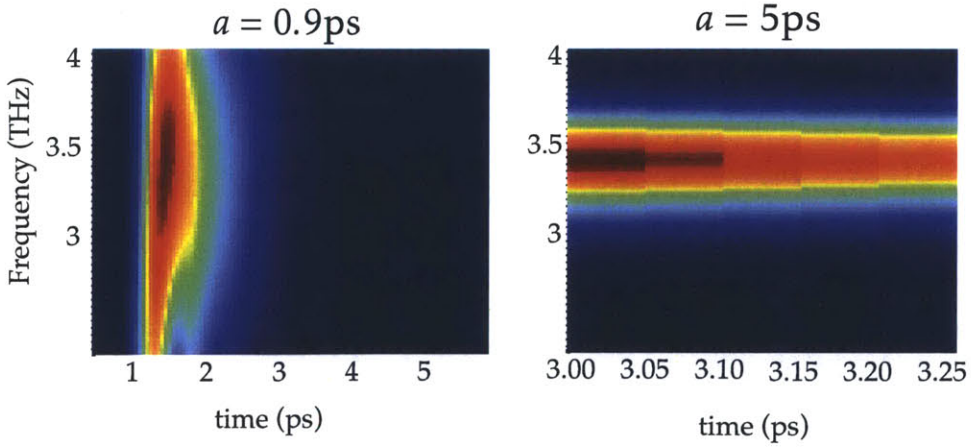

Figure 4-5: Two representative spectrograms constructed from the same data trace (lowest pump fluence in Figure 4-6, 0.2 mJ/cm^2). On the left a time window of 0.9 ps was used; on the right a time window of 5 ps was used. While the frequency resolution from the wider time window is excellent, in our case the loss of time resolution is costly because the frequency is expected to change perceptibly within a few vibration cycles.

4.4 Experimental Results

In this section, PtI(en) photoinduced responses to a range of pump pulse intensities across varying timescales are presented to formulate perspectives on the key questions outlined in §4.2.3. Our single-shot measurement technique can uniquely address questions of interactions at high excitation densities. While it has been proposed that defect states occur via non-linear decay channels and that macroscopic phase changes may depend on high-density cooperative effects, no experimental studies have systematically examined the photoexcitation fluence continuum in metal halides.

We here present conventional pump-probe measurements to characterize the sample response at low and medium fluence excitation, noting dynamical trends of interest for further study, and demonstrate the insufficiency of the conventional pump-probe method at higher fluence. We then present single-shot measurements that monitor photoinduced dynamics in real-time under higher excitation. Finally, we present single-shot two-pump measurements, in which a second pump pulse excites the lattice weakly after a strong pump pulse has already perturbed the system at high fluence. This enables spectroscopy of the excited state itself up to 100 ps after its creation, whereas one-pump measurements resolve the evolution of the excited state from the ground state. Section 4.5 then discusses and develops all experimental results presented here toward a description of photoinduced electronic and lattice dynamics in PtI(en) across different excitation density regimes and from the femtosecond through 100 picosecond timescale.

4.4.1 Conventional Pump-Probe Measurements: the reversible photoexcitation regime

Low to moderate fluence excitation

Figure 4-6 shows time-dependent reflectivity data from PtI(en) recorded using conventional pump-probe methods. Responses following 800 nm pump pulses with fluences between 0.20 $\frac{mJ}{cm^2}$ and 1.6 $\frac{mJ}{cm^2}$ were probed by weak 600 nm probe pulses. The data show a near-instantaneous reduction in reflectivity upon pump arrival followed by a rise, and an oscillatory component. The slowly varying background is assumed to be

due primarily to carrier excitation and subsequent changes to carrier populations or the system temperature, while the oscillatory component results from lattice vibrations.

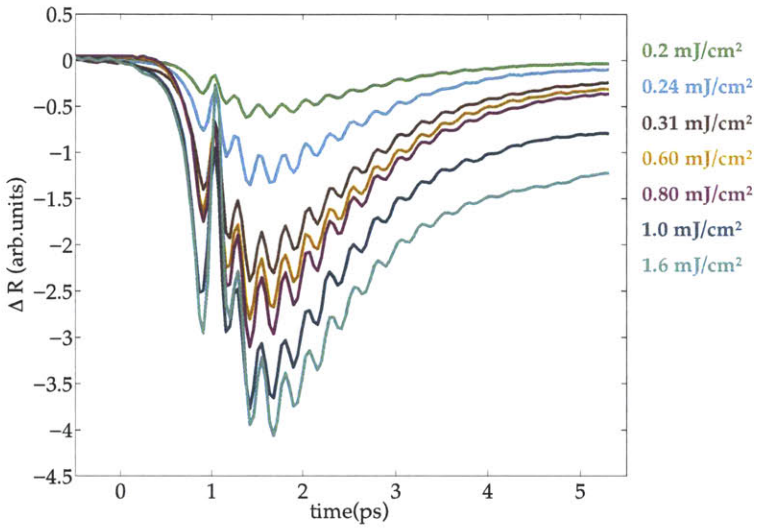

Figure 4-6: Reflectivity response of PtI(en) versus time for pump fluences between 0.20 and 1.6 mJ/cm². Fourier spectra are inset, showing a time-averaged 3.6 THz frequency for the launched mode.

The slowly varying components were fit to exponential decay functions to extract relevant parameters for the description of carrier dynamics. It was found that a single exponential fit gives satisfactory results for the PtI(en) electronic response below 0.6 mJ/cm^2 fluence; however, above this fluence a biexponential fit was needed to sufficiently describe the data. Results from the fits are presented in Figure 4-7 and Figure 4-8.

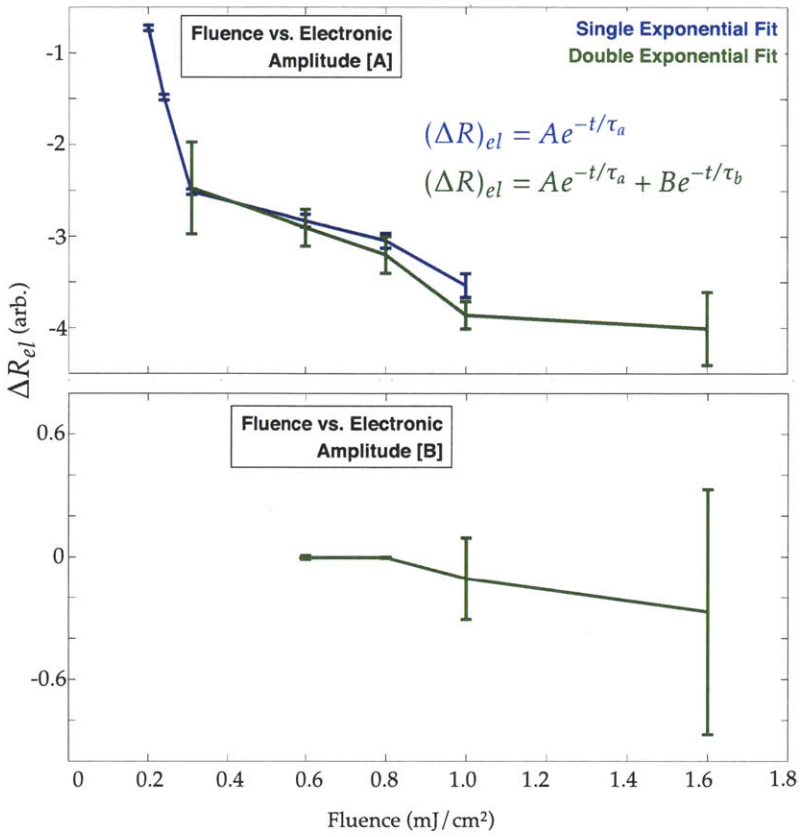

Figure 4-7: The electronic amplitudes resulting from exponential decay fits to the data in Figure 4-6 are shown as functions of pump fluence. A single exponential fit was found to be sufficient for pump fluences below 0.6 mJ/cm²; above this fluence a biexponential fit was used. Increasingly negative amplitudes are observed for both fit parameters, with the second amplitude decreasing only slightly within error.

Based on the fits, we observe that a second, longer-lived electronic component is induced above 0.6 mJ/cm2 that is not present upon lower photoexcitation. In this fluence regime, the component appears to have a lifetime of >4 ps (Figure 4-8) and its contribution (negative amplitude) increases slightly with fluence (Figure 4-7). The contribution of the shorter-lived electronic component (<4 ps) increases sharply with fluence up to 0.3 mJ/cm^2, and then continues to increase with fluence, albeit less drastically. While the STE lifetime has previously been reported to be 5 ps via luminescence measurements,[121] we observe behavior suggestive of a longer-lived response in the non-oscillatory component as the pump fluence is increased.

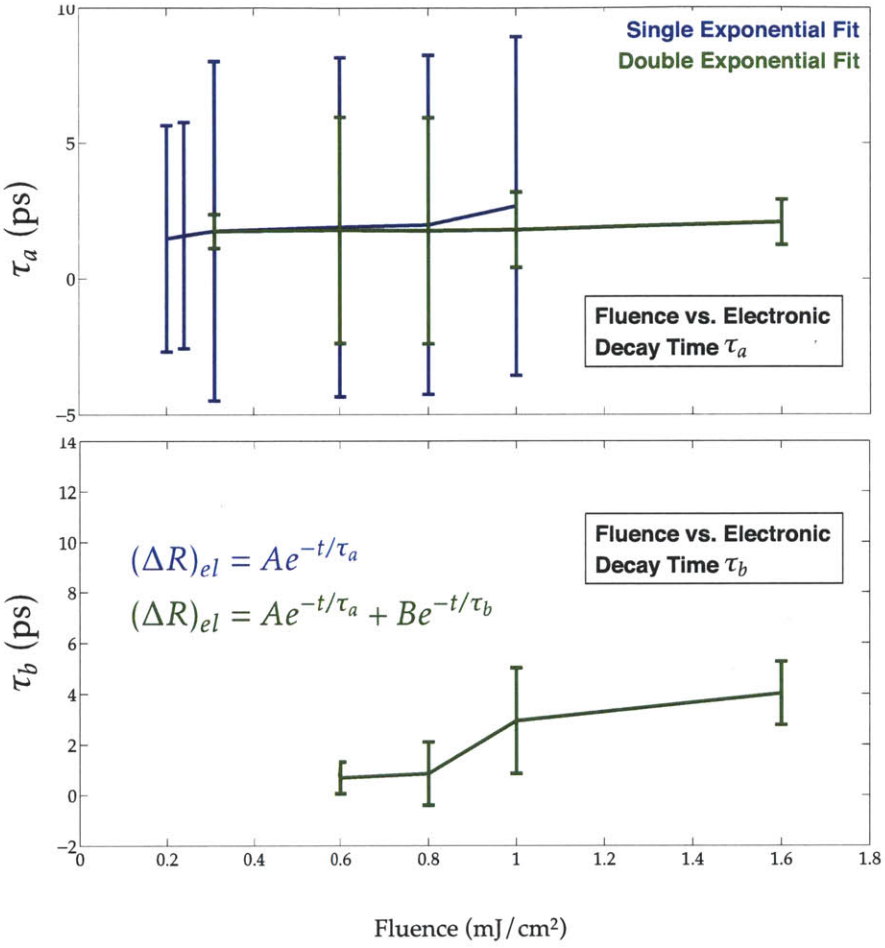

Figure 4-8: The decay times resulting from exponential decay fits to the data in Figure 4-6 are shown as functions of pump fluence. A single exponential fit was found to be sufficient for pump fluences below 0.6 mJ/cm²; above this fluence a biexponential fit was used. The first decay time is near constant with fluence, while the second increases.

We expect higher pump fluence to initiate correspondingly more charge-transfer and STE formation events in the pumped region, manifesting in stronger electronic signal. However, the changing dependence of the short-lived electronic amplitude on fluence suggests nonlinearity in the electronic response. Figure 4-9 shows the data from Figure 4-6 rescaled by pump fluence, emphasizing a dramatic nonlinear response that peaks at 0.31 mJ / cm². The magnitude of the electronic response from the pre-pump baseline to the third oscillation null (at 1.5 ps) is also plotted in arbitrary ΔR units in Figure 4-9 for direct comparison among the fluences.

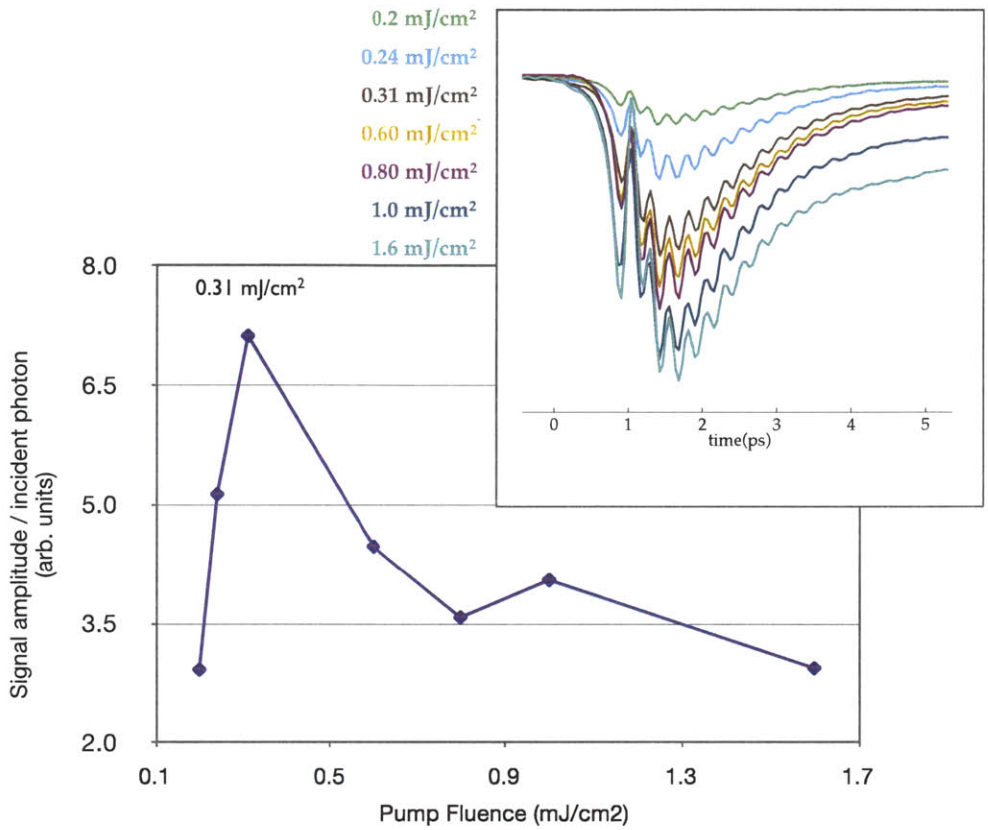

Figure 4-9: Signal amplitudes based on exponential fit scaled by pump fluence, exhibiting a maximum in multi-exciton effects at 0.31 mJ/cm². Reflectivity traces from Figure 4-6 and scaled by incident pump fluence are also displayed.

To extract information on lattice dynamics, the exponential fits for each data sweep were subtracted from the data in Figure 4-6 (single exponential below 0.6 mJ/cm^2; double exponential above 0.6 mJ/cm^2). The resulting oscillatory signal components, shown in Figure 4-10 [A], were analyzed in the frequency domain by a Fourier transform. A lattice mode near 3.6 THz frequency (120 cm^{-1}) indicates relaxation of the initial photoexcited state to the STE state. The normalized set of peaks at the STE formation frequency are shown in Figure 4-10 [B], and the non-normalized spectrum is shown in Figure 4-10 [C]. The peak widths indicate a dephasing time of 1.6 ps ($\tau = \frac{2}{\mathrm{FWHM}}$). Little change in decay time is observed, and within our experimental error of 0.2 THz (set by the $\frac{1}{50\ \mathrm{fs}}$ sampling frequency and number of timepoints), there is no perceptible shift in measured phonon frequency. The spectrum shows significant structure at frequencies below the main peak, but they are not resolvable above the noise.

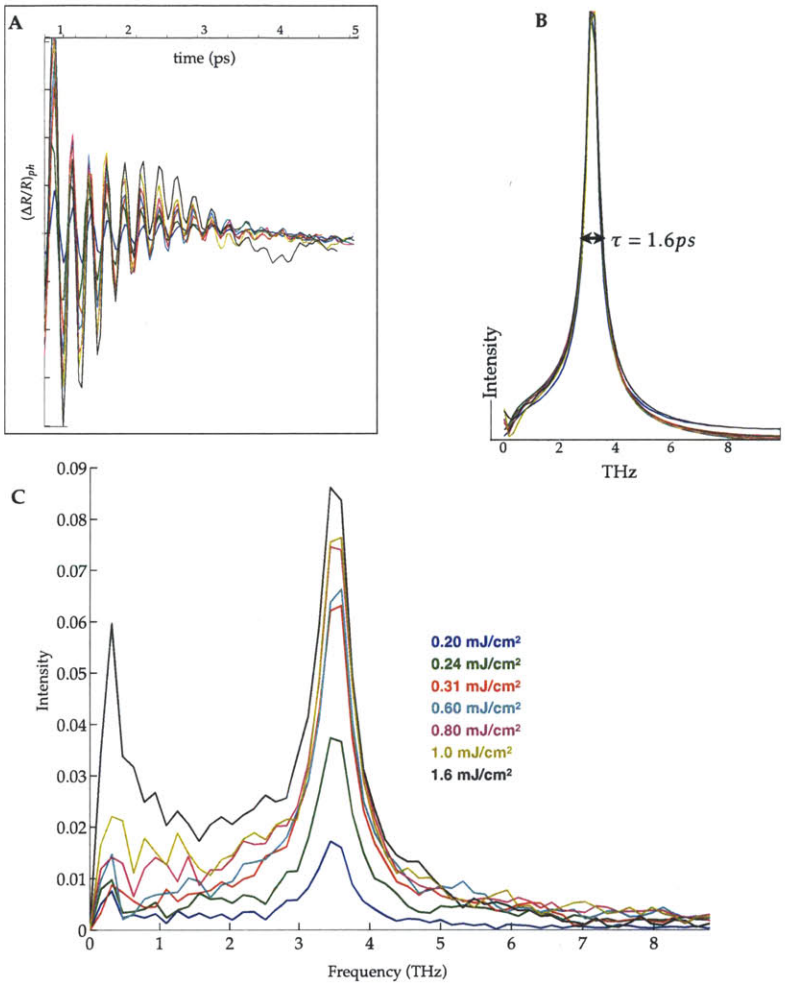

Figure 4-10: [A]: *Oscillatory components extracted by subtracting exponential fits from the raw data.* [B]: *Normalized Fourier peaks at the main* STE *lattice frequency.* [C]: *Full non-normalized spectrum with experimental frequency steps of 0.2 THz.*

Figure 4-11 shows spectrograms from conventional pump-probe measurements in the 0.75-2.4 THz frequency range to emphasize the structure not resolvable above the noise in Figure 4-10 [C]. A time window of 1.95 ps was used. We observe a distinct mode at 1.7 THz at the lowest fluence, blue-shifting to 1.8 THz at a slightly higher fluence, and the loss of mode structure for increasing fluence. At the highest fluences employed for conventional pump-probe measurements, we observe increased frequency amplitude centering around 1.9 THz with a short lifetime relative to the low-frequency mode at the lowest fluences. Also shown is the instantaneous (first 1.95 ps)

non-normalized frequency spectrum as a function of fluence, with the lowest amplitude peak corresponding to the lowest fluence.

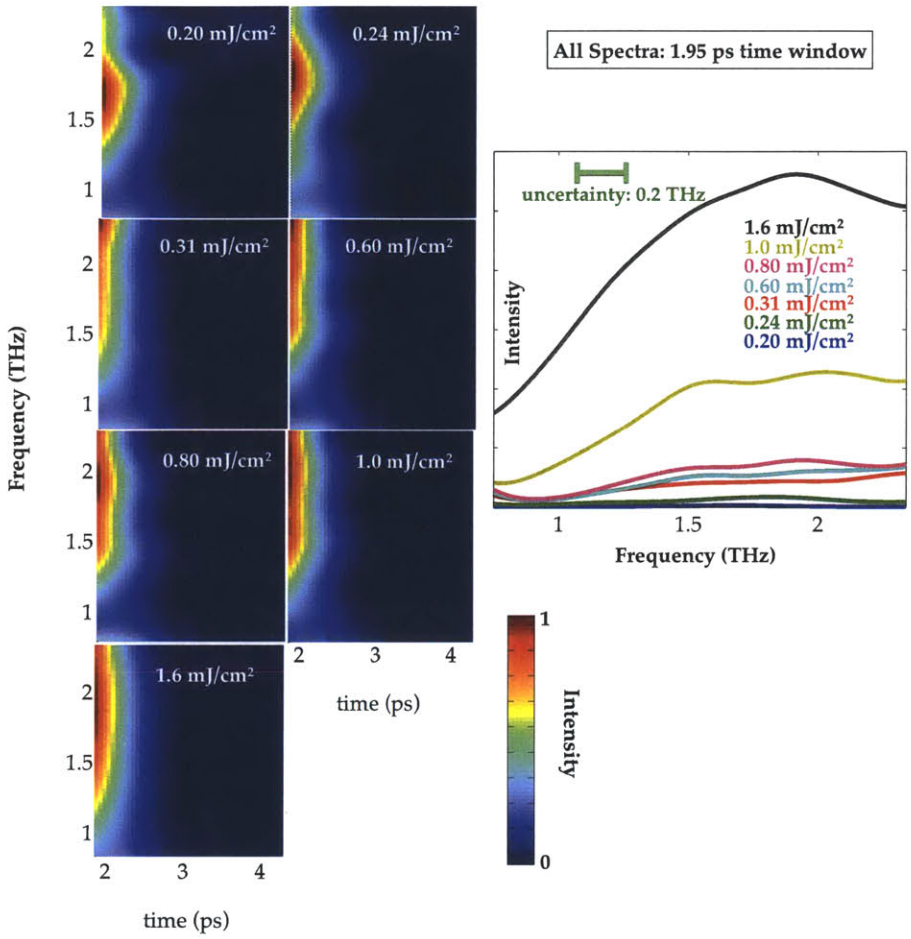

Figure 4-11: Low-frequency mode observed from conventional pump-probe measurements (color axis is normalized for each plot so that the color codes ranges from 0 (blue) to 1 (red) across 2D plots). The time and frequency axes are identical in all 2D plots. A mode at 1.7 THz is present at the lowest fluence, blue-shifting slightly (to 1.8 THz) for slightly increased fluence but losing its distinct shape upon further increasing fluence. At the highest fluences shown here, a low-frequency band is observed that peaks at 1.9 THz. Non-normalized early-time cross-sections (lower left-hand plots) suggest two modes are present.

For reference and for comparison with single-shot measurements to be presented in the next section, a 1.95 ps windowed Fourier transform around the main STE peak from low-fluence conventional pump-probe data is shown in Figure 4-12. We observe slight red-shifting upon increasing fluence, as well as peak broadening indicating a faster dephasing time for the mode corresponding to creation of the STE state.

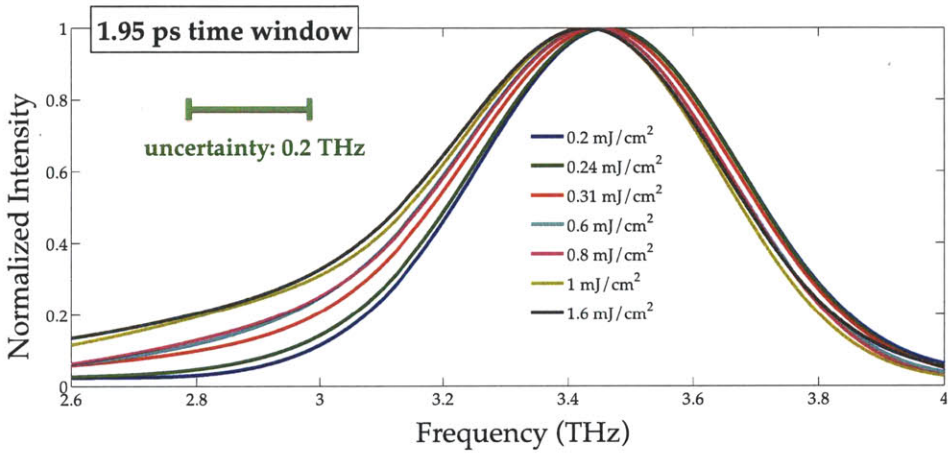

Figure 4-12: 'Instantaneous' (earliest measureable STFT time) breathing mode frequency in PtI(en) extracted from conventional pump-probe measurements (time window = 1.95 ps).

High fluence excitation

We obtained measurements using the conventional pump-probe technique at high fluences to explore the PtI(en) optical damage threshold. At the high excitation fluences (2.4 to 9.4 $\frac{mJ}{cm^2}$) whose responses are shown in Figure 4-13 [A], the material response reveals drastically different time-dependent profiles than those at low fluence (Figure 4-6). However, the observed responses were shown to result from cumulative degradation of the sample over more than one million shots (20 minute scan at 1 kHz repetition rate). After each long-time exposure to high intensity laser pulses on a single sample spot, we performed low-fluence measurements on the same sample location to test for long-term damage. If damage did not occur under high fluence excitation, the same responses known to occur upon low fluence excitation should be measured. Results of low-fluence excitation on regions of high intensity exposure are shown in Figure 4-13 [B]. They differ markedly from the low-fluence response without prior high-fluence excitation (red curve in Figure 4-13 [A], 1.6 mJ/cm^2). If all curves in Figure 4-13 [B] were identical to that obtained on fresh sample, it would indicate no cumulative

damage had occurred. Instead, we conclude that cumulative damage occurs above 4 $\frac{mJ}{cm^2}$ (and possibly lower), rendering conventional pump-probe measurements near and above this threshold unreliable.

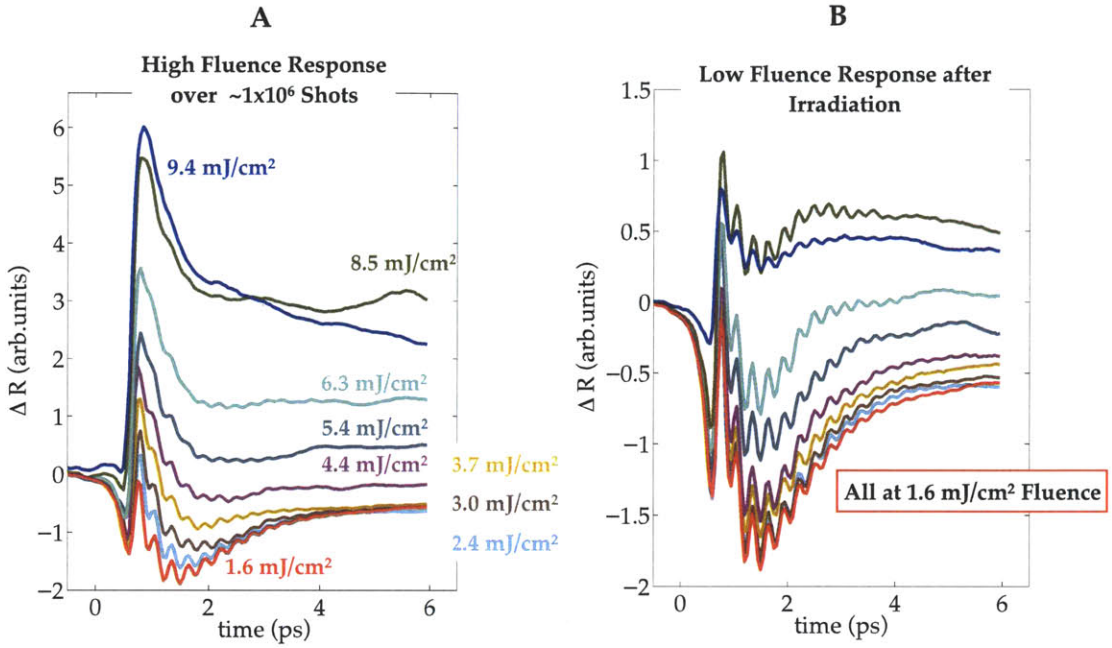

Figure 4-13: [A]: Reflectivity response of PtI(en) versus time for pump fluences between 1.6 and 9.4 mJ/cm². [B]: Reflectivity response of PtI(en) versus time for 1.6 mJ/cm² pump fluence. In each case, the measurement was taken on the sample region that was previously irradiated with the indicated fluence. The bottom curve, from 1.6 mJ/cm² on a fresh sample spot, is re-plotted from Figure 4-6 for reference.

4.4.2 Single-Shot One-Pump Measurements: the irreversible photoexcitation regime

To examine the real-time photoinduced dynamics of PtI(en) above the damage threshold measured by the conventional pump-probe results, we performed single-shot measurements for a range of pump fluences from 1.0 $\frac{mJ}{cm^2}$ to 12 $\frac{mJ}{cm^2}$. We observed significant changes in reflectivity and in phonon behavior over this range, as shown in Figure 4-14. At the lowest fluence (1.0-1.4 $\frac{mJ}{cm^2}$), the familiar lattice vibrational response associated with STE formation is observed. As the fluence increases up to 4.5 $\frac{mJ}{cm^2}$, we observe coherent vibrational oscillations but with decreasing amplitude (relative to the peak electronic signal level), frequency, and dephasing time. At still higher pump fluence (12 $\frac{mJ}{cm^2}$), no coherent vibrational oscillations were observed in the data. The

apparent disappearance of the mode at high excitation warrants further investigation. Because observation of the Raman-active mode is a hallmark of the distorted ground phase, its absence suggests the possibility of structural change. In the symmetric state, vibrations of the equidistant Pt-I bonding pairs are predicted to be Raman-inactive, so the absence of observed oscillations at 12 $\frac{mJ}{cm^2}$ pump fluence could suggest possible rearrangement to a high-symmetry state in the pumped region. Alternatively, the absence of oscillations could be due to dephasing trends. A solution to this ambiguity will be discussed below with presentation and analysis of results from single-shot two-pump measurements. The data exhibit a slight null before the full reflectivity drop, which is likely related to non-equilibrium carrier dynamics and is reminiscent of the initial reflectivity drop in the pump-probe data of Figure 4-6. The effect was confirmed not to result from a pre-pulse by performing an autocorrelation measurement.

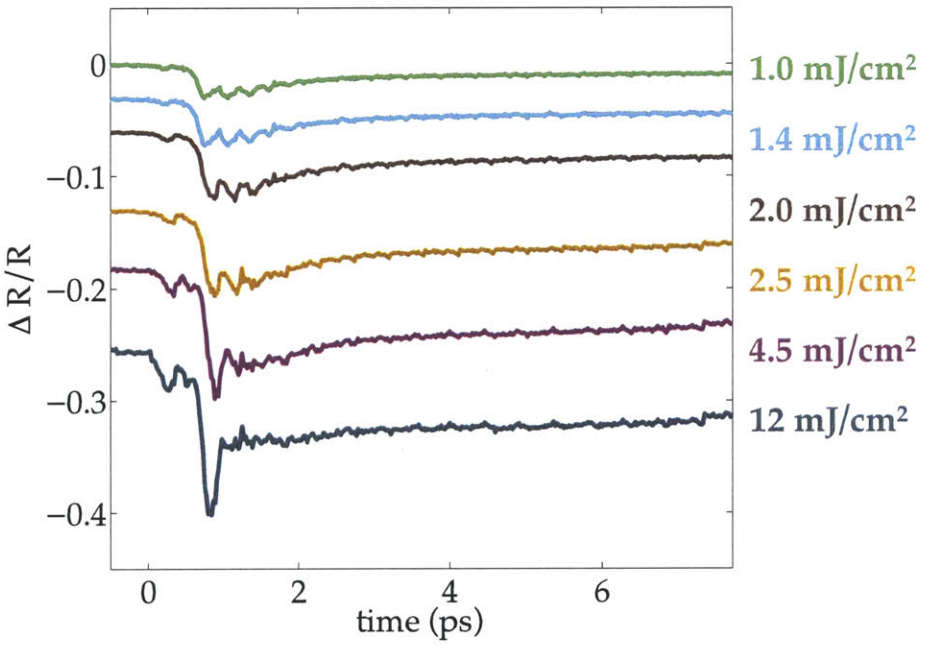

Figure 4-14: Single-shot differential reflectivity of PtI(en) versus time, showing fast dephasing at higher pump fluences. The data are offset for ease of comparison.

The single-shot data in Figure 4-14 were fit to biexponential decay functions, and the resulting parameters that could be reasonably extracted are plotted as functions of fluence in Figure 4-15 and Figure 4-16. We observe that the shorter-lived electronic component increases in (negative) amplitude until ~2.5 mJ/cm^2, and then decreases in

amplitude with increasing fluence. The second electronic component, which we ascribe to a longer-lived state, continues the trend of increasing amplitude with fluence observed in the lower-fluence conventional pump-probe measurements. The second decay parameter could not be accurately fit without artificial constraints (of increasing minimum decay time with increasing fluence) because the electronic trace after pump arrival is nearly flat in the highest-fluence case. However, it is clear from the raw data itself in Figure 4-14 that at 4.5 and 12 mJ/cm^2, very minimal electronic recovery occurs toward the pre-pump level for the 7 ps of data obtained. This long-lived response is explored in more detail via two-pump measurements.

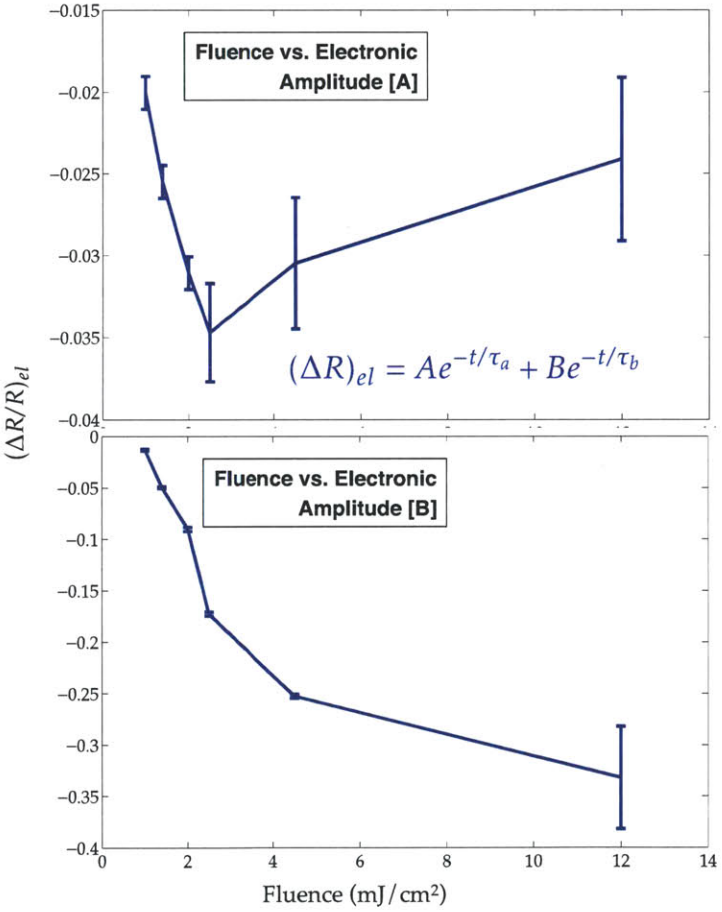

Figure 4-15: The electronic amplitudes resulting from biexponential decay fits to the data in Figure 4-14 are shown as functions of pump fluence. The first amplitude increases until 2.5 mJ/cm^2 and then decreases; the second increases with fluence.

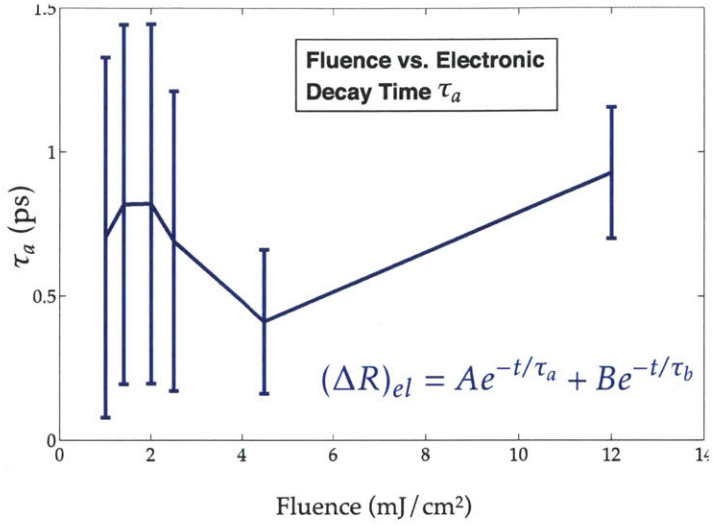

Figure 4-16: The short-lived electronic component decay time resulting from biexponential decay fits to the data in Figure 4-14 is shown as a function of pump fluence. The decay, of <1 ps, is relatively constant with fluence within error.

Figure 4-17 shows the response of PtI(en), scaled by incident fluence, to fluences ranging from 1 – 12 $\frac{mJ}{cm^2}$ using the single-shot apparatus. The response per incident photon is of increasing but comparable magnitude for increasing fluences up to 4 $\frac{mJ}{cm^2}$, and a sharp drop-off is visible above that fluence. While the raw signal (Figure 4-14) shows an increased signal magnitude throughout this fluence range, the photoexcited material does not yield a uniform response per incident photon.

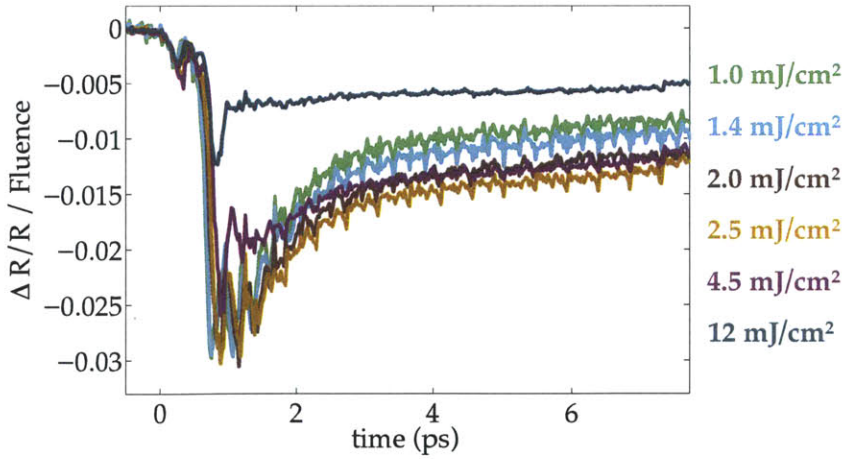

Figure 4-17: Single-shot differential reflectivity of PtI(en) versus time, with the y-axis scaled by incident number of photons (fluence). Scaled signals increase with increasing fluence until 4.5 mJ/cm², and the scaled signal drops off sharply for the highest fluence, 12 mJ/cm².

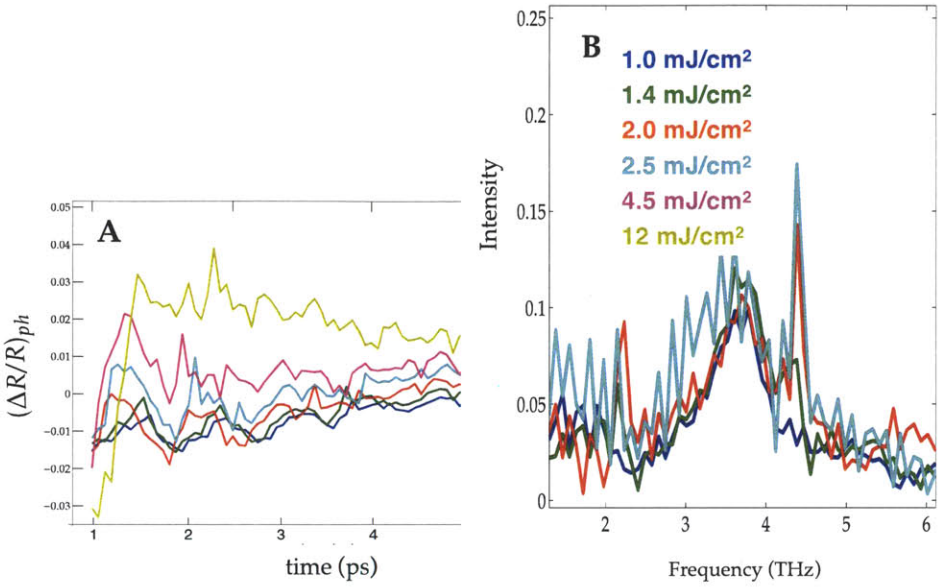

Figure 4-18: [A]: *Oscillatory components of single-shot data shown in Figure 4-14 obtained by subtraction of biexponential fits to the electronic background.* [B]: *The normalized* STE *lattice mode peaks from the single-shot data through 2.5 mJ/cm²*

To extract lattice dynamics, the exponential decay fits generated for the slowly varying electronic backgrounds of the data in Figure 4-14 were subtracted from these data, yielding the oscillatory components shown in Figure 4-18 [A]. Normalized Fourier components near the STE lattice mode are displayed in Figure 4-18 [B]. The noise in the frequency data results from a combination of few cycles, poor long-time fits leading to a slowly varying component that presents as a DC peak, and either the incorporation of systematic noise toward the end of the time trace or the truncation of those timepoints, which compromises the frequency resolution. We turn instead to windowed discrete Fourier transforms to examine the data in greater detail, since these noise factors preclude further analysis of the lattice dynamics. The results from a windowed STFT with a time window of 1.7 ps are displayed in Figure 4-19.

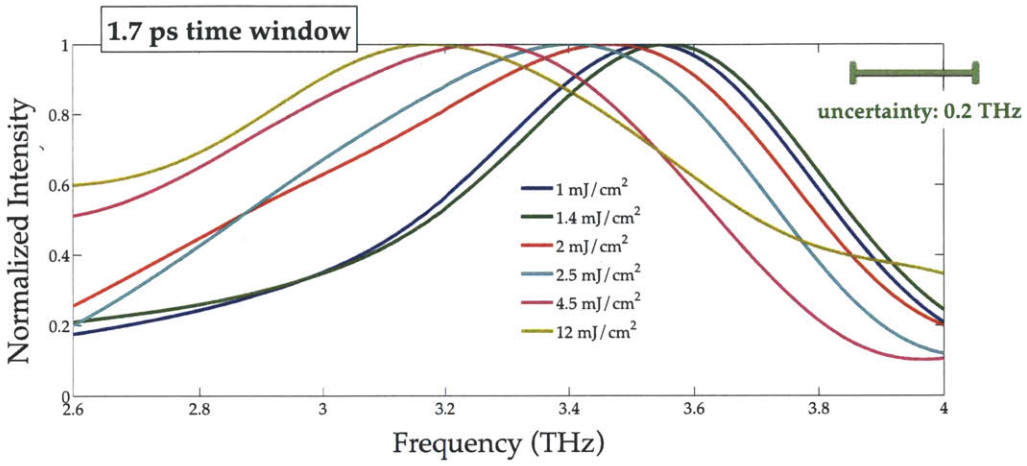

Figure 4-19: 'Instantaneous' (earliest measureable STFT time) breathing mode frequency in PtI(en) extracted from single-shot measurements (time window = 1.7 ps). Significant red-shifting is observed as fluence increases, and the peak is broadened, indicating faster dephasing or a broader range of frequencies.

To summarize the data presented from the one-pump measurements on PtI(en) from low to high fluence excitation, we have observed a short-time electronic component that grows strongly at low fluence that peaks at 0.3 mJ/cm^2, and gives way to a longer-lived electronic component at fluences above 0.6 mJ/cm^2. We propose that, counter-intuitively, interaction effects between excitation dominate at the lowest fluence. This result is explored and explained in an interaction model in §4.5.2. Our measurements at high fluence using conventional pump-probe methods indicate a damage threshold of at most 4.5 mJ/cm^2. The high-fluence longer-lived component becomes prevalent at high fluence in single-shot measurements. The component, which lasts longer than our 9.5 ps single-shot probe window, has not been previously reported, and is further explored in two-pump measurements presented in the following section.

We observed low-frequency modes in the 1-2 THz range in conventional pump-probe measurements that are highly dependent on pump fluence (Figure 4-11) in the same region as the nonlinear electronic response (Figure 4-9). Observation of the STE formation, near 3.5 THz, shows clear red-shifting and increased dephasing at increasing fluence. At the highest fluence employed, we observe the near-disappearance of lattice vibration, though the one-pump measurement cannot distinguish between rapid dephasing and structural change as possible sources of the effect. A reproducible *t=0* feature remains, and did not vanish upon higher fluence excitation as expected and

observed for lattice vibrational modes. For this reason, we ascribe the feature to nonequilibrium carrier excitation rather than to lattice vibrations.

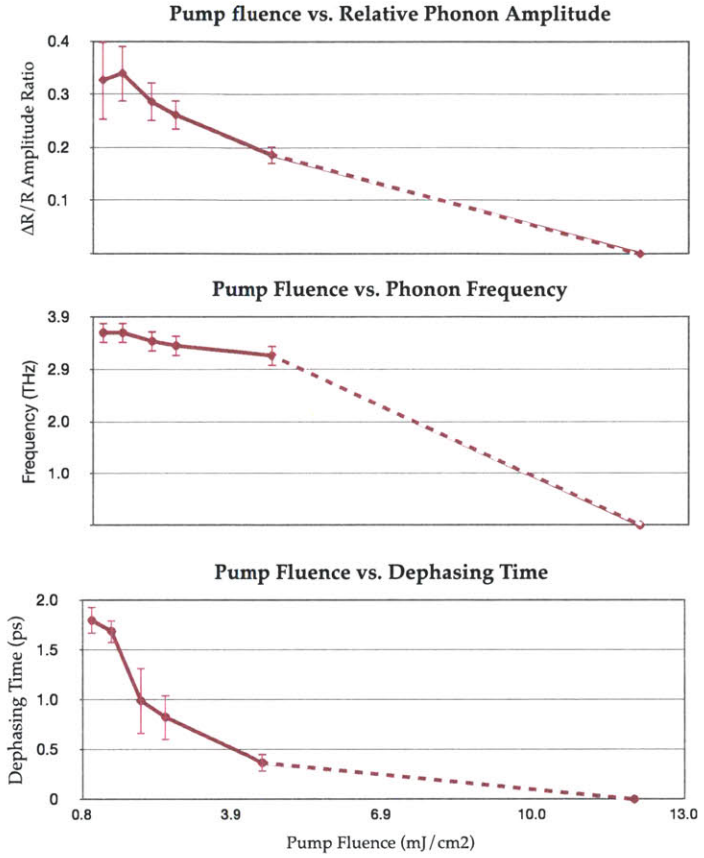

Figure 4-20: Summary of single-shot one-pump results in the regime of high excitation density. Top: Relative phonon amplitude (oscillatory amplitude relative to electronic amplitude). Middle: STE phonon frequency. Bottom: Phonon frequency dephasing time. No oscillation is reported for the 12 mJ/cm^2 data, but a dotted line is shown to emphasize the trend.

4.4.3 Single-Shot Two-Pump Measurements: measuring dynamics on the highly photo-excited state

To address the ambiguity between fast dephasing and structural change, as well as to investigate the carrier population and lattice structure after strong pump excitation, we performed two-pump measurements with a second pump pulse that acted on the photoexcited state produced by the first pump pulse. Low fluence ($0.8\ \frac{mJ}{cm^2}$) ensured that the second pulse itself did not drive the lattice far from equilibrium, but the time-dependent response—observed with 400 probe pulses that accompany the weak second pump pulse—depended on the fluence of the first pump pulse and the time delay Δt between it and the second. For three fluences of the first pump pulse (F = 1.4, 4.5, and $12\ \frac{mJ}{cm^2}$), we pumped the lattice a second time at seven different time delays (Δt) after the first pump: 0, 4, 10, 30, 50, 70, and 100 ps, and several seconds (effectively infinite time). These measurements answer the question: what is the state of the system Δt picoseconds after we excited the ground state material with a pump of fluence F? Put another way, we know the response of the ground state to a $0.8\ mJ/cm^2$ weak pump pulse (purple curve in Figure 4-6). How does the response of the highly excited state to this same perturbation differ, at different points in its lifetime, and for varying degrees of initial excitation?

Results with $1.4\ \frac{mJ}{cm^2}$ first-pulse fluence are shown in Figure 4-21; $4.5\ \frac{mJ}{cm^2}$ first-pulse fluence in Figure 4-22, and $12\ \frac{mJ}{cm^2}$ first-pulse fluence in Figure 4-23. Key parameters from all three measurement sets are summarized in Figure 4-25. After the first pump pulse, the $0.8\ \frac{mJ}{cm^2}$ second pump pulse induces a response that reports on the system's state. In the $1.4\ \frac{mJ}{cm^2}$ excitation case, within experimental error, the measured lattice properties (oscillation amplitude, phonon frequency, and dephasing time) remain unchanged from Δt of 4 ps through Δt of 100 ps after the $1.4\ \frac{mJ}{cm^2}$ pump pulse. The electronic amplitude increases slightly over the Δt range, indicating that a photoinduced electronic state persists beyond 10 ps even after moderate excitation from $1.4\ \frac{mJ}{cm^2}$ fluence (below the material's damage threshold).

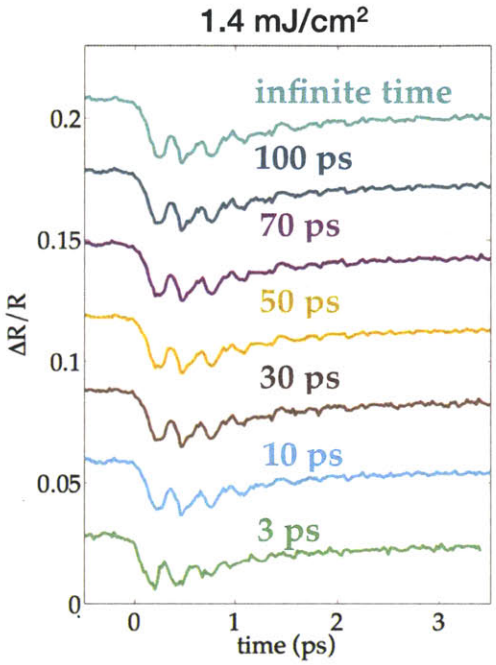

Figure 4-21: Reflectivity versus probe window time for time delays Δt (4 ps through infinity) after a 1.4 mJ/cm² pump pulse

The excited lattice created by the 4.5 $\frac{mJ}{cm^2}$ pump pulse (Figure 4-22) is clearly distinct from the STE state generated from the 1.4 $\frac{mJ}{cm^2}$ pulse since both the short-time dynamics and the long-time electronic state differ between the two photoexcitation fluences. We postulate that this change is due to a high density of STEs or absorption by STEs into other states, which may result in correlated regions of altered lattice structure in which the reflectivity at the probe wavelength is reduced and in which the phonon properties are changed.

After the 4.5 $\frac{mJ}{cm^2}$ pump pulse, the oscillatory and non-oscillatory signals induced by the second pulse are less than half their amplitudes after the 1.4 $\frac{mJ}{cm^2}$ pump pulse, the phonon frequency is reduced to 3.2 THz, and the phonon dephasing time is reduced to 0.8 ps. The excited lattice relaxes toward a final state that is not fully returned to the initial state, as shown by the continued reduced oscillatory and non-oscillatory signal amplitudes even after 'infinite' time delay. The results of a first pump fluence of 12 $\frac{mJ}{cm^2}$ (Figure 4-23) show all the same trends, with a somewhat greater reduction in the oscillatory signal amplitude.

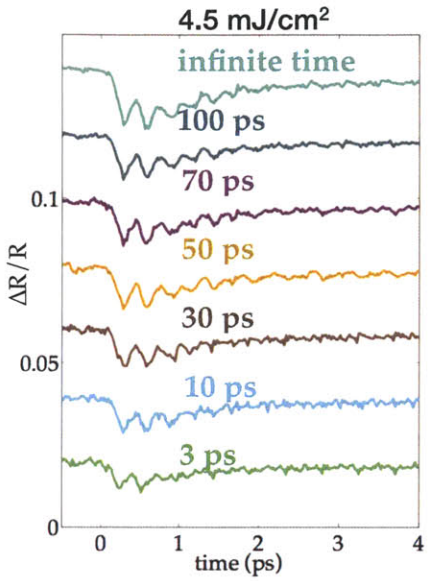

Figure 4-22: Reflectivity versus probe window time for time delays Δt (3 ps through infinity) after a 4.5 mJ/cm² pump pulse

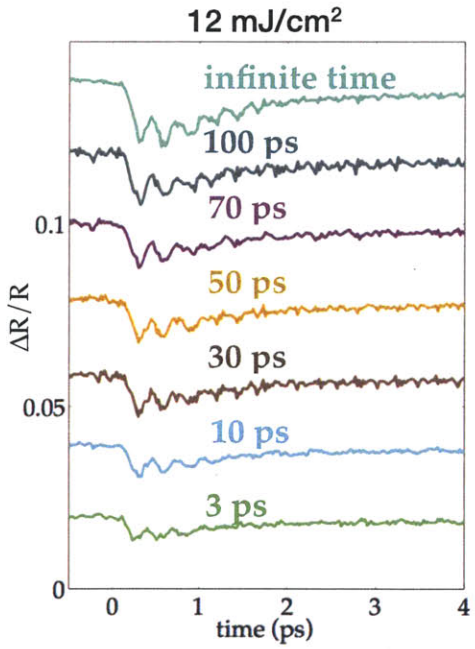

Figure 4-23: Reflectivity versus probe window time for time delays Δt (3 ps through infinity) after a 12 mJ/cm² pump pulse

Figure 4-24 shows the instantaneous frequencies for the three sets of data as obtained from an STFT with a 1.7 ps time window. The electronic and phonon properties resulting from varied excitation levels and time delays are summarized in detail in Figure 4-25 for reference in the data discussion (§4.5).

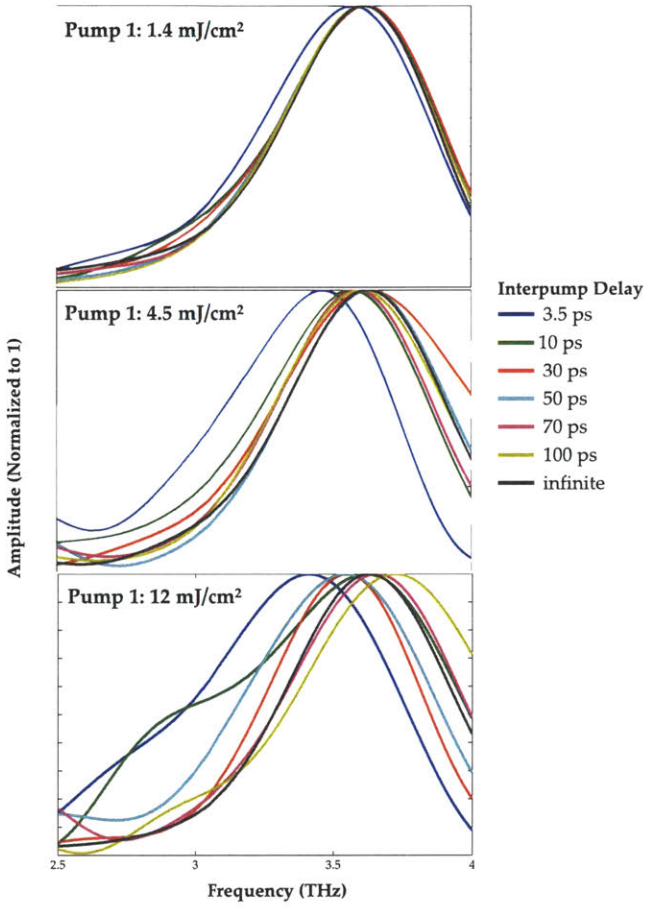

Figure 4-24: Instantaneous frequencies from two-pump data of varying initial pump fluences and interpump time delays. A time window of 1.7 ps was used, which corresponds to the first 1.7 ps of the probe window following excitation. At higher initial fluences, the frequency is significantly red-shifted after $\Delta t \sim 3.5$ ps after the initial pump pulse, and the recovery to ground-state levels is on the order of hundreds of picoseconds. In addition, the mode is broad and exhibits lower-frequency structure at the earliest interpump delay times.

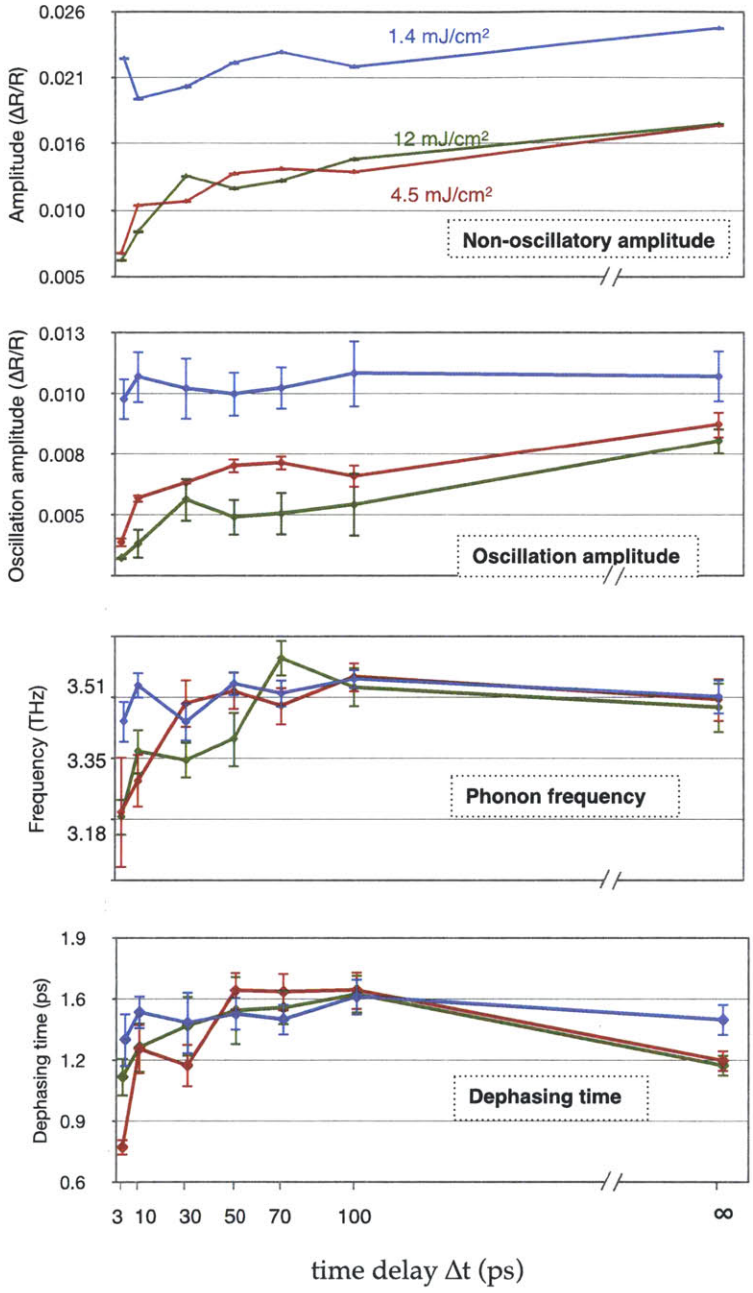

Figure 4-25: Single-shot two-pump results. Amplitudes, phonon frequencies, and phonon dephasing times versus Δt for each of the above three pump fluences. The amplitudes of oscillations launched by a fixed pump fluence are directly comparable to one another.

4.5 Discussion of Results

We have presented a widely varying set of measurements on photoexcited PtI(en). First, conventional pump-probe measurements were presented at low fluence, which report on electronic and lattice behavior, and then at high fluence, which report on optical damage. Single-shot one-pump measurements were then presented at moderate to high fluence, and electronic and lattice properties were extracted from the data, prompting questions about the photo-induced state. Single-shot two-pump measurements were then presented, which report on the photo-induced state from between 3 and 100 ps after its creation. In this section we first evaluate the trends in electronic and lattice dynamics from the ground state across the measured excitation regime. Second, we develop an interaction picture based on these data that enables framing our measurements in the context of cooperative photoinduced structural change and organizes the observations from different absorption regimes from all one-pump data on the ground state. Third, we evaluate the photo-excited state (created by different first-pump intensities) in the context of fluence-dependent behaviors observed from the preceding measurements.

4.5.1 Excitation Dependence of Electronic and Lattice Dynamics in Photo-excited PtI(en)

From the exponential fits across conventional pump-probe and single-shot one-pump data, we observe an interplay between short- and long-lived electronic components (see Figure 4-7, Figure 4-8, Figure 4-15, and Figure 4-16). A longer-lived component >4 ps is observed to be induced at a pump fluence greater than ~0.6 mJ/cm^2. This can be seen qualitatively in the data in Figure 4-6, but is verified by the result of single exponentials adequately describing the slowly varying background below the 0.6 mJ/cm^2 fluence, and a biexponential function being required to describe the data above that fluence (Figure 4-7 and Figure 4-8). This longer lived component increases significantly with fluence in its amplitude and decay time, and we observe qualitatively from the data in Figure 4-14 that the decay time increases to far beyond 6 ps, though this parameter could not accurately be fit given our 9.5 ps time window. The short-lived component increases dramatically in amplitude for our lowest set of fluences. Its growth increases slowly with increasing fluence until about 2.5 mJ/cm^2,

beyond which point the component is suppressed. Thus, there is an interplay between the shorter-lived and longer-lived electronic components as the fluence changes, which suggests either that the dominant absorbing state changes with increasing fluence, or that absorption occurring at lower fluences is further excited to a long-lived state at high fluences.

From the one-pump single-shot results, we observe that upon 4.5 $\frac{mJ}{cm^2}$ fluence excitation the signal per absorbed photon drops slightly, and upon 12 $\frac{mJ}{cm^2}$ fluence excitation the signal per absorbed photon drops sharply. We conclude that the additional signal produced under 4.5 $\frac{mJ}{cm^2}$ fluence, and especially under 12 $\frac{mJ}{cm^2}$ fluence (Figure 4-9), is *not* due primarily to increased exciton population. The net increase in signal, however, indicates that photons are still absorbed at these high excitation densities. The electronic decay trends (shorter component dominating at low fluence, longer component at high fluence) results can be understood in terms of an absorption that saturates at low fluence and gives way to another, longer-lived state. Within this picture, we suggest that the added signal upon 12 $\frac{mJ}{cm^2}$ fluence excitation is due to the further excitation (i.e., ionization) of excitons or self-trapped excitons formed at low or moderate fluence to generate carriers. This is consistent with the short electronic lifetime measurement upon 12 $\frac{mJ}{cm^2}$ excitation (~100 fs), as carriers are expected to contribute to the signal but also relax to the band edge within hundreds of femtoseconds. This interpretation is also supported by two-pump measurements, which show that a similar state is created under photoexcitation at the two highest fluences.

The low-fluence lattice frequency spectrum shows the STE formation mode at 3.6 THz, with an approximate lifetime of 1.6 ps as determined by the linewidth (Figure 4-10). We observe structure in the low-lying frequency range (from 1-2 THz) which is investigated using an STFT windowed at 1.9 ps, as shown in Figure 4-11. A 1.7 THz mode is visible at the lowest fluence, which appears to blue-shift to 1.8 THz before disappearing upon increasing fluence. At 1.6 mJ/cm^2, there is an increased frequency amplitude at 1.9 THz. The mode amplitude is significantly larger for increasing fluence, and two modes appear to be present at 1.6 and 1.9 THz, with the lower frequency mode dominating at the lowest fluences and contributions from the second mode growing in upon moderate increased excitation density.

Notably, the observed features around 1.7-1.9 THz change significantly in the fluence regime we know to be subject to changing absorption patterns. Therefore, these features may reflect extended motions along a chain, physically consistent with low measured frequency and likely to be suppressed by a change in excitation density along the chain. Low-frequency defect modes residing in the electronic bandgap have been identified via IR absorption measurements and associated with solitons and kinks, though precise vibrational assignments have been elusive. A charged kink structure in PtCl(en) is predicted to have yield a mode with frequency 56% down-shifted from the fundamental,[114] and a similar feature might be expected at 1.6 THz for PtI(en), in accordance with our results. This defect structure for PtI(en) is illustrated in Figure 4-26.

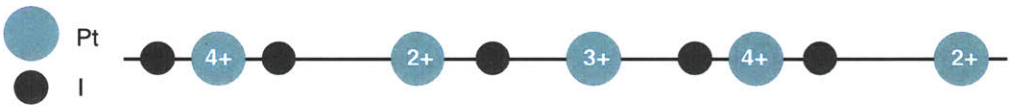

Figure 4-26: Charged kink defect, projected to have a frequency roughly 56% below the ground-state Raman stretching mode.

Other possibilities for the low fluence low frequency result include a soliton mode, defined in this context as a propagating domain, which we would expect to decrease in contribution as propagation becomes limited.[106] In addition, Gammel et al. predicted long-period 'superlattice' modes,[117] and Araoka more recently identified a mode at 65 cm^{-1} (relative to the 175 cm^{-1} fundamental) in PtBr(en)—previously unreported—attributed to an asymmetric vibration of the STE state.[154] The low-frequency mode dependence on fluence could also reflect relaxation of the STE state into multiple mid-gap states at low fluence, as predicted by Peierls-Hubbard models in previous works, while other channels dominate at higher fluence.[155-158] This interpretation is less likely than others, however, as the feature's appearance at instantaneous times suggests no relaxation precedes the vibration. Regrettably, this feature cannot be explored in our single-shot experiments due to a prominent systematic noise feature at 2 THz peculiar to our echelon optics, which would preclude making definitive assignments in this frequency range. Nonetheless, the result is intriguing, and can be further clarified in future measurements as described in §4.5.

The single-shot data at higher fluence yields noisy Fourier spectra (Figure 4-18), but the main lattice peak is resolvable for all but the two highest fluences when the slowly varying part of the oscillatory data is neglected. From these data, a slight red-

shifting and broadening of the peak is observed, though not outside the 0.2 THz error suggested by both the sampling parameters and estimates from functional fitting.

Figure 4-12 and Figure 4-19 show the spectrum in our primary frequency region of interest for all fluences obtained with both the conventional pump-probe measurement and the single-shot measurement from windowed STFT. Because the measurements were conducted with different sampling rates and for different durations, it is not possible to construct directly comparable frequency snapshots in time. Instead, we proceed with the STFT results optimized for each measurement type and consider the relative frequency shift across each measurement induced by increasing the excitation fluence.

At low fluence where many oscillations are resolved, the windowing provides an isolated snapshot of the instantaneous frequency. At high fluence where the data are noisy, the windowing allows us to focus on the region where signal is expected and suppress spurious noise from elsewhere in the time trace. We observe slight but perceptible frequency shifting with increasing fluence in the lower fluence regime, and more significant frequency shifts across the higher fluence regime. As expected physically for lattice ion motion launched by reduced electron screening after photoexcitation, the general observed trend is frequency softening as the excited potential curvature widens, reflecting a weaker restoring force. Though in theory the differences between Figure 4-12 and could result from differing temporal snapshots (a severely red-shifted mode at 1.7 ps recovering by 1.95 ps), we verified the result is due to fluence increase by comparing multiple time window ranges across the suite of measurements. Broadening of the mode is clearly observed, and is consistent with the known effect of mode dispersion across the metal-halide series for increasingly delocalized CDW states.[143]

In the low-fluence regime, we observe relatively minimal shifts in phonon frequency, reflecting little change to the lattice structure. At the highest excitation densities, the phonon frequency demonstrates considerably sharper red-shifting, in concert with the longer-lived electronic component's growing contribution. Even as the signal contribution per additional incident photon decreases (Figure 4-28), the frequency demonstrates a very high rate of red-shifting. This may suggest a very widespread contribution of STE oscillating states at high excitation densities, or a new,

low-frequency mode that accompanies an apparent shift in electronic absorbing states. In the PIPT picture, we expect the frequency to continue down-shifting as the system moves toward the symmetric state, until the system no longer supports this Raman-active vibrational mode. To our knowledge, no theoretical calculations have been undertaken to propose the evolving potential energy surface under photoexcitation at a single lattice site. A calculation of mode frequencies derived under varied models of interaction could supplement our measurements for a developed picture of correlation between observable lattice frequencies and excitation interactions. Though density functional perturbation theory (DFPT) has been employed for other electron-phonon coupling systems,[159] we expect that the response of lattice vibrational parameters to increased excitations could be significantly different when constrained in one dimension. (Adiabatic potentials have been calculated for general systems, but the results are qualitative and cannot inform our frequency analysis based on their curvature.[160])

It is instructive to compare our *instantaneous fluence-dependent* frequency with *time-dependent* literature values at *low fluence*, because the observed modes at low fluence are reasonably well understood, and can provide insight into changing contributions at high excitation. Time-averaged Fourier results have shown lattice red-shifting on the order of 12-14% of the ground-state Raman frequency during formation of the self-trapped state.[119,123] We observe an ~11% down-shifting of the phonon frequency across the fluence-dependent single-shot measurements, which suggests that the predominant oscillating mode at increasing excitation densities is that of STE formation. An interpretation of STE states dominating the frequency spectrum at high fluence is in keeping with our estimates presented in the following section that every unit cell is photo-excited under the highest fluences employed (Figure 4-29).

This interpretation is distinct from one that describes the red-shifting to be from the Raman mode, but does not necessarily preclude red-shifting of the Raman mode as a contributor to the red-shifted frequency. Further, measurement of the instantaneous lattice frequency at the highest fluences employed is error-prone since there are very few observable cycles. Dexheimer has performed two-pump measurements (at very low fluence, using conventional multi-shot methods) on PtBr(en), observing an excited-state wavepacket response intermediate between the ground-state and STE formation

frequencies that reports on the relaxed STE state.[161] While the steep red-shifting to ~3.2 THz at 12 $\frac{mJ}{cm^2}$ may be an analogous observation in the relaxed STE on the PtI(en) chain, it is more likely due to high-density effects than the relaxed STE state, which would likely occur at all excitation densities.

To the author's knowledge, no vibrational mode predictions have been made for low-frequency mid-gap states (e.g., polarons, bipolarons) in PtI(en). However, we can estimate these frequencies from dynamical matrix normal-mode analysis on PtCl(en) and PtBr(en). These calculations, along with corresponding Raman measurements, have assigned peaks down-shifted from the fundamental by 15-16% to electron-polaron excitations, and by 28-32% to electron-bipolaron excitations for both materials.[102,114,150] We therefore expect the electron-polaron and electron-bipolaron modes to appear at roughly 3 and 2.5 THz in PtI(en), respectively. These modes may be present and obscured by the fundamental. In all, these measurements suggest the need for DFPT calculations to predict the potential energy surface curvature as a function of excitation density and atomic distance under various interaction models. Further, they suggest a role for x-ray diffraction measurements to monitor the lattice structure directly during excitation at various densities.

4.5.2 Cooperative Effects in Structural Change

With fluence-dependent measurements on this system, we look to shed light on non-linear effects and cooperativity. In this section we present a study of cooperative effects in PtI(en).

Employing our data obtained at higher excitation than any previously reported measurements, we can inform the models of photo-induced phase transitions that have been proposed for a similar system with experimental data. Iwano has proposed that precursors necessary to 'seed' a macroscopic phase domain are likely to form when excitation densities are high enough for 4-exciton aggregates to interact along a chain.[149] That author's method prepares the system energy with a customized electron-lattice Hamiltonian reflecting the excitation level and then calculates adiabatic potential energy surfaces to determine favorable interactions among excited states. Importantly, many phases of interaction are proposed: 2- and 3-exciton aggregates are predicted to be energetically favorable in a localized manner (across ~5 unit cells), and 4-exciton

aggregates display an additional energy minimum spread over ~13 unit cells, while the 'seeds' formed by the latter process are expected to have further interactions that lead to macroscopic structural change.[149] Though the studies cited here are not specific to PtI(en), they nonetheless provide important principles to examine for low-dimensional coupled systems. Thus, we will examine threshold behavior in PtI(en) as it relates to structural change and the lifetimes of photoinduced excitations, emphasizing the connection between electronic and lattice properties where possible.

Continuous irradiation under the fluences in Figure 4-6 was shown not to induce permanent photo-damage by subsequent checks at low fluence. Nonetheless, as shown in Figure 4-9, highly non-linear effects are observed even at these moderate fluences, suggesting interactions between excitations. By contrast, in a non-interacting regime, the signal from isolated photo-excitations would scale linearly with the number of incident photons. This behavior at moderate fluences ($0.2 - 0.3\ \frac{mJ}{cm^2}$) is due in part to the one-dimensional chain structure of the material, and it presents an interesting opportunity for studying interactions in the solid state. In a typical metal, coulomb interactions ensure that photo-excited carriers are uniformly distributed. In one dimension, mobility is severely limited. Moreover, in ionic crystals such as PtI(en), excitations can become trapped in the polarization field created by photo-induced lattice distortions, further immobilizing charge carriers and potentially forcing their interaction. Thus, we might expect excitations to have low barriers to interactions, which is indeed suggested by Figure 4-9.

In Figure 4-9 and Figure 4-17, we observed that the electronic reflectivity response has regimes that deviate sharply from linear behavior with increasing excitation density. These effects are more clearly illustrated in Figure 4-27, which is a composite of data from conventional pump-probe and single-shot measurements.

Although the pump-probe data presented above in Figure 4-6 are plotted in arbitrary intensity units, having collected data at $1.0\ \frac{mJ}{cm^2}$ with both the conventional pump-probe and the single-shot instruments allows us to scale the pump-probe data appropriately. The pump-probe measurement obtained at $1.6\ \frac{mJ}{cm^2}$ fluence (Figure 4-6) is not included in the following analysis. Though a damage check after measurements at $1.6\ \frac{mJ}{cm^2}$ fluence did not reveal qualitative signs of cumulative effects, we note that the

electronic response change from 1 to 1.6 $\frac{mJ}{cm^2}$ from pump-probe measurements (18% increase) is significantly smaller than the electronic response change from 1 to 1.4 $\frac{mJ}{cm^2}$ (39% increase) from single-shot measurements. It is likely that a fluence of 1.6 $\frac{mJ}{cm^2}$ sits on the threshold for cumulative damage for PtI(en), since the measurements shown in Figure 4-13 [A] suggest muted electronic signal as one effect of cumulative damage.

The magenta points in Figure 4-27 illustrate the absolute $\frac{\Delta R}{R}$ change (relative to $t < 0$ value) in response to the calculated absorbed photons per Platinum ion; the blue points show the same response scaled by absorbed photons per Platinum ion. In both cases, the dashed lines convey behavior that would be expected in the linear, non-interacting regime. The approximate number of absorbed photons per Platinum ion (2 per unit cell) was calculated for each fluence F using the unit cell volume v (lattice parameters $a = 1.70$ nm; $b = 1.16$ nm; $c = 0.74$ nm), the penetration depth δ (30 nm), reflectivity R (0.7) at 800 nm, and excitation wavelength E_p (1.55 eV) according to the following relation:

$$n_{ph/Pt} = \frac{(1-R)F\,v}{2\delta E_p} \qquad \textit{Eq. 4-6}$$

The simple model presented here assumes a constant reflectivity of 0.7 independent of fluence in order to form a physical picture of excitation density. We observe at least three regimes where the absolute signal change has distinct slope behavior: between 0.04 and 0.06 absorbed photons per Pt atom (steep signal increases), between 0.06 and 0.8 absorbed photons per Pt atom (tapering signal increases), and between 0.8 and ~2 absorbed photons per Pt atom (plateauing signal increases). The first of these is the same effect shown in Figure 4-9; the second is that emphasized by Figure 4-17. Measurements were not taken at fluences higher than that corresponding to 2 absorbed photons per Pt atom. In the high excitation regime, we interpret multiple photons absorbed per platinum atom as additional absorption by already excited states. In this picture, we see that the sharply nonlinear reflectivity response and the subsequently more gradual (but still positive) changes in scaled signal occur before the 0.5 absorbed photons per Pt atom fluence, and then the scaled signal begins to decrease. Equivalently, the change in signal occurs when crossing the threshold of 1 absorbed photon per unit cell.

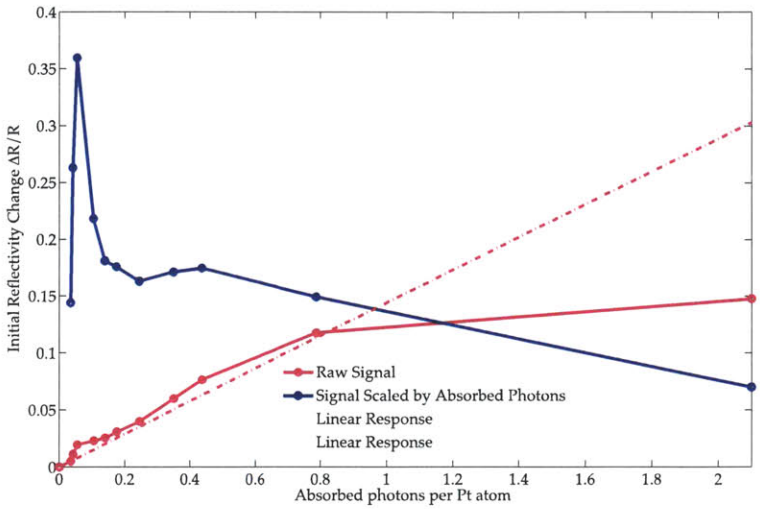

Figure 4-27: Absolute value of initial reflectivity change versus calculated absorbed photons per Platinum atom (magenta). The same data are scaled by incident fluence to emphasize regions deviating from linear behavior (blue). Both dashed lines indicate the behavior that is expected for isolated, non-interacting excitations yielding signal in the linear regime. Each point on a given line is derived from the initial t=0 rise of the conventional pump-probe and the single-shot data.

Figure 4-28 shows the sum of additional measured initial signal level per additional absorbed photon (calculated using Eq. 4-6), where each relative difference in signal is plotted vertically above the previous to yield a cumulative sum. Plotting the scaled signal contributions in this way allows us to visualize in which absorption regimes interactions are contributing most substantially to the material's changing properties and emphasizes the features specified from Figure 4-27. A large fraction of relative signal is gained from the lowest-fluence measurements (up to 0.6 absorbed photons per Pt). Fluence measurements above 0.8 photons per Pt yield almost no gained relative signal, with the middle fluence range demonstrating an intermediate contribution to the gained signal.

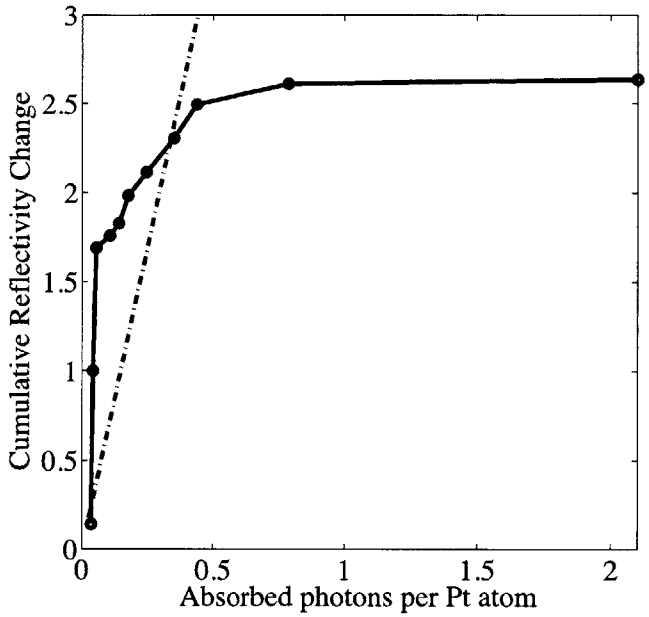

Figure 4-28: Added initial signal per additional absorbed photon. The initial signal responses are plotted cumulatively. The dashed line indicates approximate expected linear behavior in the non-interacting regime.

We are interested in understanding the extent and mechanism of interactions along the metal-halide chain. To this end, we can estimate from PtI(en) lattice parameters the distribution of excitations via the distance between nearest-neighbor excitations along the chain for a given fluence. This enables rescaling of the x-axis to chart the cumulative reflectivity change as a function of nearest-neighbor excitation distance along a single chain, as in Figure 4-29. Given the excitation volume and the crystal's lattice parameters, we have estimated 3.7×10^{12} total unit cells in the region and 7×10^{5} unit cells per chain. Here, as is standard for evaluating all electronic behavior in quasi-one-dimensional metal-halides, we have assumed no interactions between chains. From Figure 4-29 we can see directly—due to the sharp signal increase for minimal fluence increase—that at 14 unit cells apart, excitations interact to modify the material's measurable optical properties. To the author's knowledge, this is the first effort to determine the extent of delocalization in metal-halides experimentally, and it provides lower-limit support for previous calculations suggesting excitation delocalization over 20 unit cells in PtI(en).[117] (Araoka et al. used a dynamical matrix method to estimate the number of lattice ions participating in observed low-frequency modes, but the results

are offered as rough order-of-magnitude estimates).[154] Because measurements were not conducted in the non-interacting linear regime, we can only say from these measurements that the excitation delocalization length is at least 14 unit cells -- and likely longer. These results are particularly important in light of the fact that past phenomenological models have used nearest-neighbor interaction approximations to calculate defect state vibrations and other properties.[114,117,162] While our results cannot speak directly to the effect of this approximation on calculated lattice behavior, they provide evidence that a nearest-neighbor interaction model is insufficient at anyexcitation density. This is a useful metric at moderate fluence, but fails to describe the physical system at high fluence where we have presented evidence for absorption by already excited states. In this case, new photons absorbed may produce transient high-lying states, which would not result in shorter distances between excitations. Thus, in this simple picture, we neglect the estimation of nearest-neighbor excitation being less than one unit cell, and interpret that extreme as multiple excitations per unit cell.

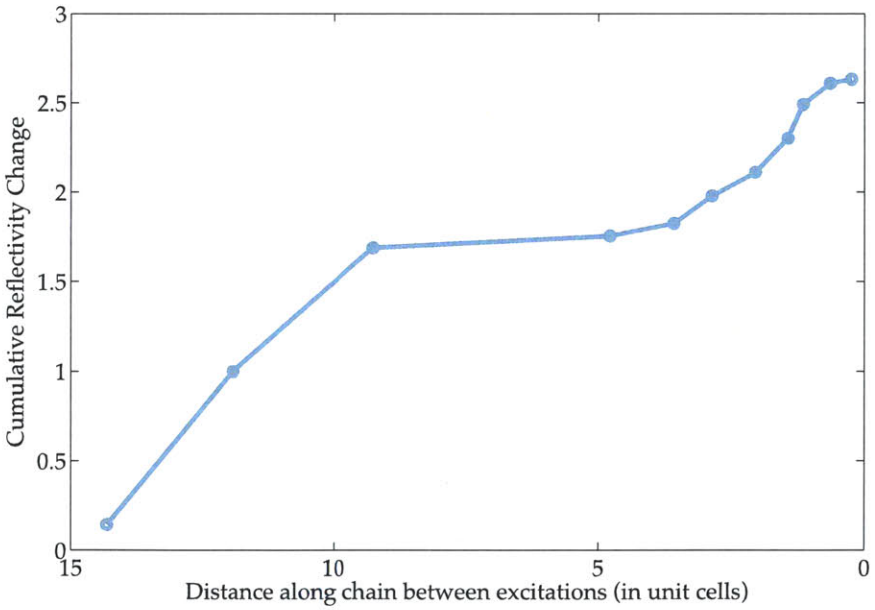

Figure 4-29: Added initial signal versus the distance to the next-nearest excitation along a single chain, estimated by experimental conditions and PtI(en) lattice parameters. The initial signal responses are plotted cumulatively.

This high-interacting regime ends as more excitations populate a single-chain, with observable drop-off at a nearest-neighbor distance of 9 unit cells. The interactions

that dominated signal contributions for the lowest fluence range in our measurements have saturated. At higher excitation densities, this simple model becomes unphysical, although less than one unit cell distance between excitations can be interpreted as high-lying excited states. Decreasing the nearest-neighbor excitation distance from 9 to 0.6 unit cells (or alternatively to the regime where high-lying states replace initially photoexcited ones), we see still significant signal gain but at a more moderate slope. Once we cross the threshold of every unit cell populated with an excitation, there is no significant signal gain per additional photon. However, from the raw data it is clear that the material continues to absorb. The additional absorbed energy may be further exciting STE states to create carriers, and the reflectivity response could be due to contributions from changes to the electronic band structure or temperature, or both.

4.5.3 Dynamics of the Highly Photo-excited State

Electronic dynamics of the excited state

In the measurements discussed thus far, we have noted four questions best addressed by two-pump measurements that probe the photo-excited lattice and electronic response. First, we observed a long-lived electronic state of increasing decay time and increasing amplitude across our fluence-dependent measurements . Second, we observed increases in absolute reflectivity for increasing fluence even after interaction effects appeared to saturate (Figure 4-27), presumably due to carrier absorption or further excitation of STEs. Third, we noted from Figure 4-14 that the breathing mode frequency appears to disappear at the highest excitation densities. The dephasing time is expected to decrease with increasing fluence (Figure 4-20). However, an alternative explanation to rapid dephasing is a structural transition to the symmetric state, which is not expected to exhibit the Raman-active breathing mode. Interrogating the excited lattice via a two-pump measurement can resolve this ambiguity. Fourth, we observed the likely formation of the STE state via an instantaneous frequency shift, but this formation is difficult to distinguish from the expected mode softening for strongly-coupled electron-phonon systems.

Two-pump measurements on the photoexcited state (see Figure 4-21, Figure 4-22, and Figure 4-23) report on the carrier population shortly after the initial photoexcitation and shed light on the population's signal contributions. Frequency analysis of two-

pump results can further inform vibrational assignments and also report on the lifetimes of the self-trapping process and the self-trapped (or other photoexcited) state itself.

Measurements above 4.5 $\frac{mJ}{cm^2}$ pump fluence demonstrate evidence of a metastable electronic state with a greater than 100 ps lifetime. This state, which may reflect underlying structural rearrangements toward a symmetric phase, is revealed through electronic and phonon properties of the photoexcited lattice measured at varying time delays up to 100 ps after self-trapped exciton (STE) formation. Phonon frequencies for the material pumped at the higher fluences (4.5 and 12 $\frac{mJ}{cm^2}$) are seen to converge near the 3.5 THz mark of the ground state over the 100+ ps timescale. A similar trend is shown for the phonon damping times. A comparison of the oscillatory and non-oscillatory amplitudes across time delays for different fluences reveals that, when pumped with fluences of 4.5 and 12 $\frac{mJ}{cm^2}$, the system continues to recover past 100 ps. These measurements of intense photo-excitation reveal a distinct state at early times relative to the sample pumped by a 1.4 $\frac{mJ}{cm^2}$ pulse. The lattice vibrational properties converge on the 100 ps timescale but the electronic state does not appear to have recovered by then, or even by many seconds after high-fluence excitation as judged by our infinite time measurement.

Trends and values for all measured properties are very similar between the 4.5 $\frac{mJ}{cm^2}$ and 12 $\frac{mJ}{cm^2}$ measurements. This mapping indicates that a threshold for lattice behavior is crossed near 4.5 $\frac{mJ}{cm^2}$, which also corroborates our excitation interaction analysis from Figure 4-27. We conclude that a similar excited state is achieved in both measurements, closely echoing the 4 $\frac{mJ}{cm^2}$ damage threshold indicated by conventional pump-probe measurements. The observed decrease in dephasing time of the oscillatory signal with increasing fluence is expected, since a high-density excitation leads to higher phonon damping rates and higher vibrational inhomogeneity due to the formation of domains that might approach or reach a high-symmetry structure. The reduction in phonon signal amplitude is consistent with the approach toward high symmetry, either uniformly or in discrete domains, since the breathing mode is Raman-inactive (and therefore its coherent oscillations do not change the refractive index and do not produce signal) in the high-symmetry phase.

We also observe indications of a longer-lived trapped state that persists for several minutes after photoexcitation above this threshold, as demonstrated by the infinite delay measurements. The deviation at infinite time (several minutes) after 4 and 12 $\frac{mJ}{cm^2}$ excitation suggests some permanent or very long-lived change to the material in the excited region. No damage was visible by eye, and the collection of data at this point with reasonable signal-to-noise suggests the surface morphology was not significantly changed. We postulate that repeated photoexcitation above a certain threshold intensity may create isolated long-lived defect states that self-stabilize and became trapped permanently or semi-permanently in the polar crystal. This effect has been observed in other systems similar to metal-halide chains, the state lasting for several hours.[133,148] However, the effect has not been previously observed at room temperature.

The top panel in Figure 4-25 shows that even 3 ps after initial photoexcitation, and continuing through all measured interpump delays, PtI(en) pumped with 4.5 and 12 $\frac{mJ}{cm^2}$ fluence yields almost identical electronic dynamics (as measurable via this method). This further confirms that the chief contributing factor to added signal under 12 $\frac{mJ}{cm^2}$ fluence excitation is exciton ionization to create hot carriers; by 3 ps post-excitation the distinction has disappeared, and the two sets of measurements relax in parallel, with presumably similar band structures and carrier populations as a function of time. Without more fluence measurements between 1.4 and 4.5 $\frac{mJ}{cm^2}$, we cannot rule out carrier heating as a contributor to the single-shot electronic signal upon 4.5 $\frac{mJ}{cm^2}$ excitation. To summarize, we suggest that added signal contributions upon 4.5 $\frac{mJ}{cm^2}$ excitation are neither the result of either exciton interaction nor of carrier heating. Instead, we suggest that the observed signal increase results from band gap closure, since the system is expected to yield larger reflectivity changes as it becomes more metallic. We can roughly estimate the fluence at which the band gap should close by referencing the molecular orbital picture depicted in Figure 4-3. For each unit cell (two Pt atoms and two I atoms), two electrons should be promoted to lift the Peierls gap. Assuming one electron is promoted per absorbed photon, this excitation density corresponds to 5.7 $\frac{mJ}{cm^2}$ (using the same calibration that was used to transform the x-axis in Figure 4-27). Thus, it is reasonable to expect band closure in the vicinity of 4.5 $\frac{mJ}{cm^2}$

excitation. Indeed, given effects of delocalization and cooperative behavior, the observable threshold for band-closing effects is expected to be lower than the calculated estimate from the localized limit. The possibility of band closure at this fluence lends additional credence to exciton absorption (or carrier heating) being the dominant effects in carrier dynamics upon 12 $\frac{mJ}{cm^2}$ excitation; as the band gap is closed, the system has a depletion of potential carriers in the disappearing valence band.

Lattice dynamics of the excited state

STFT was performed on PtI(en) two-pump data, and instantaneous frequencies (earliest time-point available) are shown in Figure 4-24 for different excitation levels of the first pump and for varying interpump time delays.

After 1.4 $\frac{mJ}{cm^2}$ excitation, we observe slight red-shifting (3.58 THz) at the earliest interpump delay time. The lattice then recovers to the equilibrium 3.6 THz value by 10 ps after initial photoexcitation. There is moderate asymmetric broadening of the mode toward the red until 50 ps after initial photoexcitation. At 3 ps after 4.5 $\frac{mJ}{cm^2}$ excitation, the breathing mode is shifted to 3.45 THz. The frequency is fully recovered to the equilibrium value by the infinite time delay measurement, with the most significant recovery occurring in the first 10 ps. Again, red-shifted asymmetry and mode broadening are observable through the first 50 ps after initial photoexcitation. The mode is most drastically red-shifted 3 ps after 12 $\frac{mJ}{cm^2}$ excitation with a frequency of 3.4 THz and recovery to the equilibrium value by 70 ps. We observe structure in the frequency spectrum at 3 and 10 ps after initial 12 $\frac{mJ}{cm^2}$ excitation centered around 2.9 THz, potentially due to gap states or extended chain modes existing several picoseconds after high density excitations. However, since gap states are expected to be extremely short-lived in the delocalized PtI(en) chain,[106] we instead attribute this feature to the very red-shifted mode rendered with suboptimal resolution during the STFT. This is supported by the continuous red-shifting observed through 12 $\frac{mJ}{cm^2}$ excitation in Figure 4-19.

Though electronic amplitude measures indicate that additional energy does not create a higher density of excitons past 4.5 $\frac{mJ}{cm^2}$ excitation , we clearly observe lattice properties affected at high excitation densities. Here too, the asymmetry (which may reflect recovery from lower frequencies) and observable broadening (which reflects

more delocalized valencies) have decreased by 50-70 ps, suggesting a coupled electron-phonon state with 50 ps duration, not previously reported in this or related materials. That this effect is more extreme in the 12 $\frac{mJ}{cm^2}$ excitation case than that of 4.5 $\frac{mJ}{cm^2}$ excitation despite our assertion that carrier dynamics post-thermalization are similar suggests that the nonequilibrium carrier population may be coupling very strongly directly to the lattice mode in this regime, an effect that has been reported previously in metals.[163]

4.6 Conclusions and Future Work

We have measured excitation interaction effects and demonstrated a long-lived photoinduced response in PtI(en). Distinct regimes of exciton interaction were observed that indicate self-trapped excitons interact over at least 14 unit cells, and these interaction effects plateau when the excitation density reaches a level that excites each unit cell. The trapped exciton wavefunction formation feature has been previously reported to persist for ~5 ps, but time-resolved measurement of the trapped state itself has been elusive. We have observed a distinct state created at high pump fluences (beyond excitation of each unit cell) with a lifetime in excess of 100 ps. This state, measured by its phonon properties and electronic signal, could reflect the formation of and recovery from a symmetric state induced by high carrier densities. Two-pump measurements also reflect an excited state persisting for ~50 ps as measured by phonon frequency and dispersion. We have also observed low-frequency long-range excitations that change significantly as exciton interaction occurs. As excitation density increases, we have proposed that domains form, the electronic band gap begins to close, and excess energy at the highest photoexcitation limit is deposited as carrier heat, which couples strongly to the lattice modes on the order of the carrier thermalization time.

These measurements illustrate that the single-shot instrument can convey interesting and new material dynamics, from electronic and phonon dynamics far from equilibrium, to cooperativity, to the creation of long-lived photoinduced states. The results suggest possibilities for future measurements to further elucidate questions we have begun to explore, summarized briefly here.

While the platinum-halide series is characterized well for certain properties in regimes of low excitation density, the high-excitation regime remains to be

characterized for these materials. As one example, the threshold for collective behavior is expected to be higher for materials that exhibit stronger electron-phonon coupling.[135] From the interaction picture developed, this is expected since nearest-neighbor excitation distance along a chain, which will always be larger for more localized excitations, is a meaningful interpretation of pump fluence. Performing the same cooperativity analysis for analogous PtCl(en) and PtBr(en) would allow evaluation of the various interaction regimes as a function of coupling, and would strengthen our understanding of the hallmarks of collective behavior. A model that accurately characterizes and predicts thresholds for collective structural change based on perturbation strength would be a valuable tool for materials scientists and device engineers; our measurements can contribute to this goal.

Similar measurements could be employed on PtI(en) over multiple excitation wavelengths. Though spectral absorption studies have long been conducted for metal-halides at varying excitation wavelengths, there has been little emphasis on identifying lattice properties of excitation states despite the electron-lattice interplay that lends these materials their interesting properties. Applying our measurement technique across excitation wavelengths could aid in assigning the low-frequency observed modes, as each gap-state excitation type is expected to be uniquely enhanced and diminished as a function of the photon energy.[102]

Pursuing lattice properties across the material series can further assist in assigning the observed modes. The lifetime of polaron states is expected to increase for Pt-Br and Pt-Cl systems relative to Pt-I; in contrast, solitons are less likely to occur in Pt-Br and Pt-Cl systems due to their more delocalized nature.[106] Additional measurements to explore the time-dependence and amplitude of vibrational features across the series could extend the measurements made here and form a more complete picture of localized photo-excitations in quasi-one-dimensional materials.

Our results provide a framework for future measurements on complex organic molecular crystals similar to the one studied here, promise advanced understanding of collective chemical and physical change in molecular crystals, and offer several intriguing directions for future work on the fundamental interactions between electron and lattice modes and photoinduced phase transitions.

Chapter 5

High-excitation Photoinduced Dynamics in Bismuth

Semimetals such as bismuth, antimony, and tellurium are of long-standing interest in the field of condensed matter due to their unique electrical and optical properties. Semimetal alloys have been developed for robust rewriteable optical data storage by exploiting their photoinduced structural response to nanosecond laser pulses.[49] Tellurium and bismuth continue to be key targets for the development of thermoelectric devices, with progress in nano-engineering material devices serving as a driving force.[164] Recently, it has been proposed that Bismuth-Antimony thin films may exhibit unique band structure behavior similar to that observed in graphene, the behavior manifesting as an ultrahigh carrier mobility, an effect of increasing interest for electronic devices.[165]

In this chapter, we present novel observations on bismuth under high photoexcitation. These measurements enable a view into how key material properties, including electron-phonon coupling and carrier mobility, behave under conditions very far from equilibrium. Previous works on bismuth, from ultrafast measurements to theoretical calculations and electron diffraction, have prompted interesting questions about the fundamental mechanisms at play when energy is transferred into the material and about our ability to control these mechanisms. We provide an overview of the material, its properties, and this past work. We then present measurements that explore

photoinduced dynamics under varying degrees of excitation, in quasi-three dimensional and quasi-two dimensional environments by variation of the sample thickness, and through interrogation of both the ground and excited states through multiple pulse spectroscopy. We develop a simple model of nonequilibrium dynamics on the sub-picosecond timescale yielding to equilibrium dynamics on longer timescales and show that the model can characterize the material response in the two-dimensional environment. In the three-dimensional environment, we present evidence for a large contribution from non-equilibrium transport that ultimately impacts both the structural photoinduced response and our ability to resolve this response.

5.1 Material and Literature Overview

Structural properties and photoinduced response

In the ground state at room temperature, the bismuth lattice structure exhibits a distorted face-centered cubic structure, which is due to the symmetry-breaking energy-lowering Peierls effect (Figure 5-1, top left).[166] In this state, the Raman-active A_{1g} mode can be resolved by coherent phonon spectroscopy, which has been well-described in the literature.[34,38,39,167-172] By the DECP mechanism introduced in Chapter 1, a redistributed carrier population created by a laser pulse instantaneously induces a shift in the potential energy surface, which leads to atomic motion by nuclear repulsion. In the case of bismuth, we resolve lattice motion along the coordinate of distortion due to the system's electron-phonon coupling. That is, the photoinduced carrier population transiently lifts the Peierls distortion and sets into motion a lattice vibration along the distortion coordinate, as also shown in our data here (Figure 5-9, inset). The lattice mode, whose ground state Raman frequency is ~2.95 THz, has been observed to red-shift with increasing photoexcitation density. This effect has been described as electronic mode softening by Fahy et al.,[172] and the lattice frequency has been observed to return to the initial value over the course of a few picoseconds after weak optical perturbation.

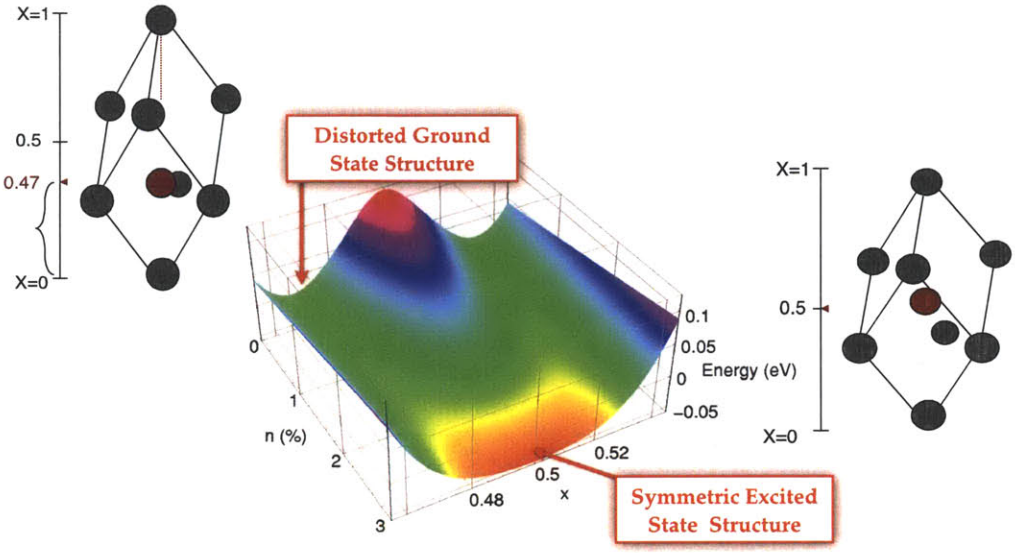

Figure 5-1: The bismuth lattice unit cell has a distorted face-centered cubic structure due to a symmetry-breaking energy-lowering Peierls distortion.
From Murray et al., 2005:[159] The potential energy surface of bismuth, calculated via density functional theory, exhibits a double-well in the ground state. When a sizeable fraction of valence electrons (~3%) are excited, the calculated surface exhibits a double well corresponding to the structurally symmetric state.

Theoretical work

Theoretical calculations have provided important insights into the understanding of laser-excited semimetals and have provided the impetus for additional experiments. Murray, et al. performed constrained density function theory (DFT) calculations to describe the potential energy surface as a function of carrier distribution, which predicts the lowest energy lattice structure (Figure 5-1, bottom left).[159] In the same work, the authors performed frozen calculations on the A_{1g} lattice mode, displacing each atom and calculating the force constant to determine frequency as a function of carrier distribution in both harmonic and anharmonic potentials (Figure 5-2, harmonic result highlighted). By comparison with optical spectroscopy experiments inducing up to 1.25% valence electron excitation, the authors confirmed the harmonic response. In a later work, the full phonon dispersion relations for equilibrium and photoexcited bismuth were calculated from first principles. The calculations explicitly show the dependence of the optical phonon modes on the carrier density.

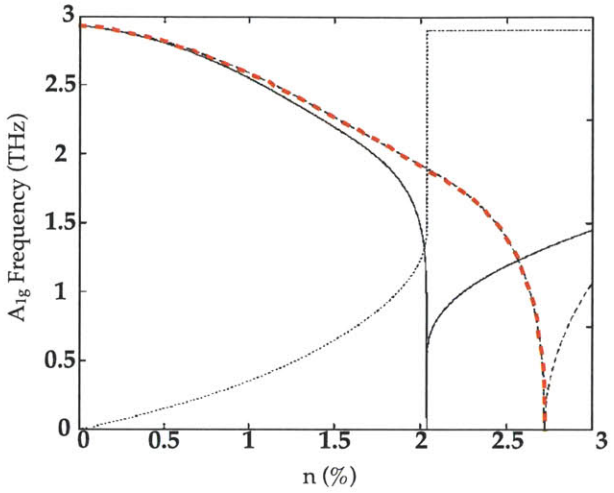

Figure 5-2: From Murray et al., 2005.[159] Frequency versus fraction of valence electrons excited, calculated by the frozen phonon method. The harmonic frequency is highlighted by the red dashed curve, and is calculated from the potential energy surface in Figure 5-1 from the same reference.

Nonthermal structural response and high-density excitation

The DFT calculation reproduced in Figure 5-1 presents an interesting possibility for photoinduced structural change. The lattice coordinate, which yields coherent optical phonons under weak optical perturbation, is predicted to reside in a local minimum in a symmetric structure under high perturbation (3% carrier density). This state, which has not been observed, is predicted to be attained nonthermally, since the lattice change is due to instantaneous carrier absorption that precedes thermal equilibrium. The prediction of the electronically induced structural *solid* state is closely tied with the exceptionally strong electron-phonon coupling. In aluminum and many other metals, carrier excitation has minimal effect on the lattice potential energy, and lattice melting proceeds through the transfer of energy from hot carriers to the initially cold lattice over a few picoseconds.[173] By contrast, in semimetals, high carrier excitation influences the lattice potential drastically on the sub-picosecond timescale, and typically causes lattice breakdown in a nonthermal melting process.[174,175] Peierls-distorted materials such as bismuth have different pathways, however, due to the energetic coupling already discussed.

Fritz, et al. reported x-ray diffraction measurements that were sensitive to the fractional lattice displacement induced under increasing carrier density.

Simultaneously, coherent phonon signal was obtained by femtosecond optical pulses, and the relationship among inter-atomic distance, carrier density, and frequency was confirmed experimentally, as shown in Figure 5-3.[40] Due to optical damage induced by the excitation laser pulse, the frequency could not be determined beyond an estimated carrier density of 1.3%, providing an important view on evolving photoinduced dynamics, but leaving the remaining potential energy surface unexplored along the carrier density coordinate.

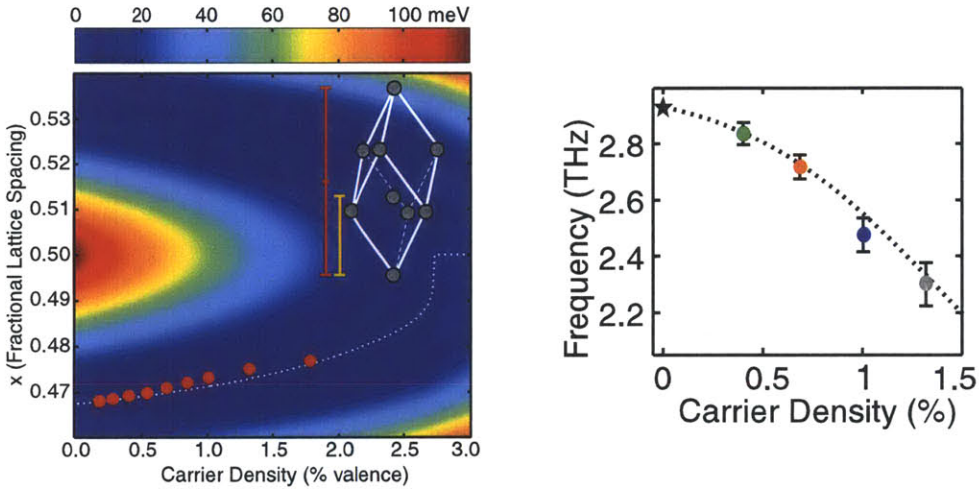

Figure 5-3: From Fritz et al., 2007.[40] Left: Bismuth potential energy surface contour superimposed with results from x-ray diffraction measurements (red circles) that report on the fractional lattice spacing and indicate a harmonic potential up to 2% carrier density. Right: optical phonon measurements, conducted simultaneously with the x-ray diffraction measurements, enable a mapping between frequency and carrier density.

The measurement limit encountered by the work of Fritz et al. emphasizes the limitations of conventional spectroscopy techniques and provides an opportunity for single-shot measurements to shed light on a fundamental physical phenomena predicted to exist. At the current state of knowledge, it is unknown if the symmetric solid state structure can be reached without melting the lattice. In an electron diffraction study of photoexcited 30 nm bismuth films, Sciaini et al. demonstrated the apparent melting of the lattice on a nonthermal timescale that is sensitive to incident fluence, as shown in Figure 5-4.[62] At the highest fluence employed, the electron diffraction peak corresponding to Peierls distorted nuclear coordinate decays with a time constant of

~200 fs. At lower fluence, the time constant is on the order of a picosecond, suggesting the possible interplay of thermal and nonthermal events as a function of fluence.

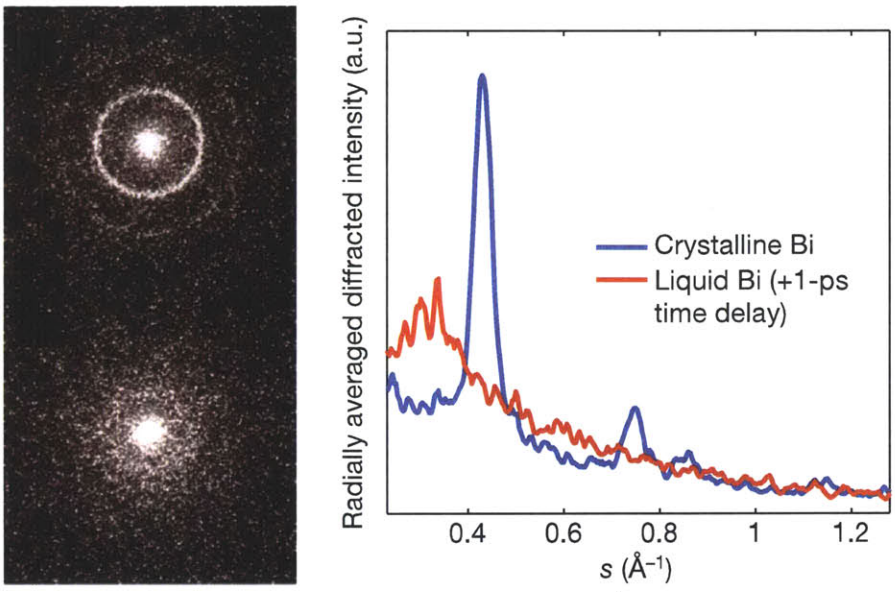

Figure 5-4: From Sciaini, et al., 2009.[62] Laser-induced melting of a 30 nm bismuth film was demonstrated via electron diffraction measurements, at high excitation and with 200 fs laser pulses, and reported to occur in less than the time of a vibrational period.

The work by Sciaini et al. provides important information regarding the ultrafast material response, but the mechanism that guides structural evolution remains unclear. Additionally, the question of a thermal versus nonthermal basis for structural change continues to be raised.[176] Other works have emphasized the need for single-shot optical measurements on bismuth under high excitation, with permanent damage thresholds at high repetition rate (> 1 kHz) reported by multiple sources to be between 22 and 25 mJ/cm^2.[167,177] At the low repetition rates employed in our measurements (< 20 shots), we do not observe permanent damage either by eye or as indicated by reflectivity measurements and image reconstruction. Therefore, we are positioned to investigate the photoinduced response of bismuth under high excitation and traverse the photoexcited potential energy surface shown in Figure 5-1. We have undertaken optical spectroscopy measurements at high excitation density that are sensitive to both electronic and lattice properties on the femtosecond timescale and extending toward the

nanosecond timescale. Additionally, we vary the sample depth to test the contribution of photoexcited carriers to the evolving dynamics.

Semimetal band structure and carrier considerations

Interpreting the ultrafast dynamics of semimetals comes with specific challenges. Semimetal electronic structure is more complex than that of metals and, in many cases, semiconductors. An illustration of the electronic band diagram for bismuth is shown in Figure 5-5. Optical transitions have been proposed to occur primarily at the Γ point, where there is an 0.8 eV band gap. However, transitions are also likely to occur elsewhere at other points. In particular, transitions near the L point, where there is a narrow gap, may contribute especially at high temperature. Melnikov et al. have proposed that carrier populations couple more strongly at certain points (such as the T point) than others.[178] Still, the mechanism of energy transfer across the Bruillion zone in response to photoinduced carriers in semimetals is largely unexplored, from both an experimental and a theoretical perspective. Additionally, the band structure in semimetals is predicted to vary as a function of temperature and film thickness,[165,179-181] although the measured dielectric function of bismuth films has been shown to be largely consistent with film thickness.[182]

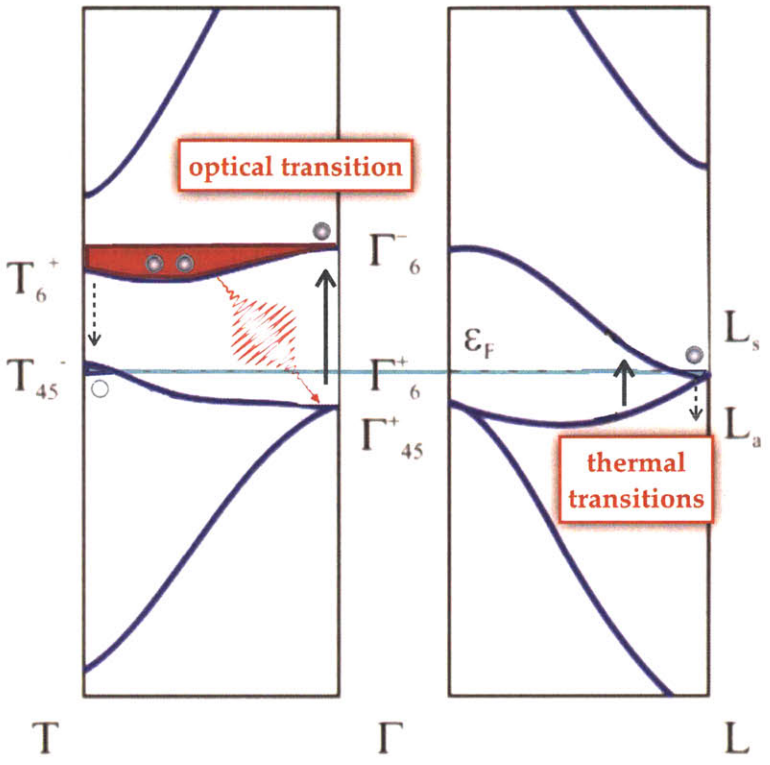

Figure 5-5: Adapted from Melnikov, et al.[178] Key symmetry points in the bismuth electronic band diagram. Optical transitions near the Γ point create carriers that collect near the T symmetry point (highlighted in red). This electronic population is thought to couple strongly with the A_{1g} lattice mode. The indirect band overlap is highlighted in blue, and occurs between the L conduction band minimum and the T valence band maximum. Thermal transitions cause the buildup of carriers near the L point, which is expected to have minimal coupling with the optical phonon mode.

5.2 Experimental Results

A wide range of data was obtained in photoexcited bismuth varying three experimental parameters: sample thickness, pump fluence, and time delay following excitation. Through separate one- and two-pump measurements, we observed the response of both the initial and photoexcited lattice under various excitation conditions.

Varying the sample depth enables a study of transport properties and may allow insight into the dependence of band structure on material dimension. We present measurements on bulk crystalline bismuth (several mm thick), 300 nm bismuth film, and 50 nm bismuth film. Because the films were vacuum deposited, high-quality data were obtained that enable direct comparison between 300 nm and 50 nm dynamics.

While surface irregularities and higher noise levels preclude direct comparisons between bulk and film samples, qualitative comparisons to the bulk can be made.

A key goal of this study is to examine electronic and lattice dynamics very far from equilibrium. For each sample, we employed a range of pump fluences to monitor the material response from moderate to very high excitation densities. The fluences were increased beyond the point where lattice dynamics were resolvable. The pump intensity required to meet this criterion varied with the sample, but in each case we obtained measurements at higher carrier densities than have previously been studied with optical pump-probe spectroscopy.

We are also interested in how the response evolves in time for different excitation intensities and for different sample thicknesses. We probed the sample photoexcitation response both instantaneously (by overlapping the pump and probe in time) and up to 800 ps after photoexcitation (by varying the pump-probe time delay) to observe the evolution of optical properties under high excitation. Finally, the photoexcited lattice was itself probed as a function of sample thickness, excitation intensity, and time delay by introducing an additional pump pulse during the probe observation time window.

Sample Preparation

Bulk bismuth was purchased from American Elements, and the surface was polished using a lapping machine with increasingly fine grits until a mirror-like surface was achieved. Thin film samples were sputter-coated on a glass substrate under vacuum. The sputtering process, which involves plasma ejection of atoms from a target and fine deposition of the atoms onto a substrate, creates high optical quality surfaces when conditions (temperature, pressure, sputtering rate) are optimized for a given material. Thin films were sputtered at 140°C and 4 mTorr at a rate of 0.4 *Å/sec.* Rates were determined by a thickness monitor during sputtering, which uses a quartz crystal microbalance to measure added mass per unit area on the crystal resonator. Thin film samples were then characterized using x-ray diffraction and found to be polycrystalline. In addition to estimation of film thickness by the crystal monitor, the thicknesses were also measured by profilometry.

5.2.1 Instantaneous Response to Strong Photo-excitation

In this section we present raw data and relevant fitted parameters resulting from 1-pump measurements on bulk and thin film bismuth samples across excitation regimes and timescales. For all data presented in this chapter, the electronic and lattice parameters are obtained as described below. Reported errors for fit parameters are one standard error above and below the reported value.

Starting at the maximum (or minimum) $_{\Delta R/R}$ value following pump arrival, each data trace was fit to a biexponential that approximates the electronic background of the signal:

$$(\Delta R/R)_{el} = Ae^{-t/\tau_a} + Be^{-t/\tau_b} \qquad \textit{Eq. 5-1}$$

No constraints were placed on the decay constants; however, for each data set, it was found that one electronic component reports on dynamics below 10 picoseconds ($\tau_a < 10ps$, with amplitude given by A) and the other reports on dynamics longer than 10 picoseconds ($\tau_b > 10ps$, with amplitude given by B). The electronic amplitudes were extracted and examined as functions of fluence. The exponential function (Eq. 5-1) is then subtracted from the raw data to isolate the oscillatory component post-pulse. The oscillatory component is fit to an exponentially damped sinusoid that approximates the lattice vibration contribution to the signal:

$$(\Delta R/R)_{ph} = Ce^{-t/\tau_{ph}}\sin(\omega t + \beta t^2 + \phi) + D \qquad \textit{Eq. 5-2}$$

In Eq. 5-2, C is the phonon amplitude, τ_{ph} is the dephasing time of the oscillation, ω the phonon frequency, β a term to account for temporal chirp, ϕ the phase, and D a constant offset.

Bulk measurements

Single-shot data from measurements on bulk crystalline bismuth are presented in Figure 5-6. The pump fluence ranges from 1.5 to 35.5 mJ/cm^2, and 8 ps of data are captured during and immediately following photoexcitation. At the lowest fluences, we observe a damped oscillatory component superimposed on a decaying background. Following the dashed blue guide, we note that the A_{1g} phonon frequency begins downshifting perceptively by eye above 5 mJ/cm^2. Above 20 mJ/cm^2, the oscillatory lattice response cannot be resolved, although the significant noise around the pump

responses may obscure oscillations. Also above 20 mJ/cm^2, the slowly-varying background takes on a new form, decreasing below the pre-pump level and not recovering within the timescale of the measurement. In contrast, at the lowest fluences, the reflectivity change is positive and returns to the pre-pump level within a few ps.

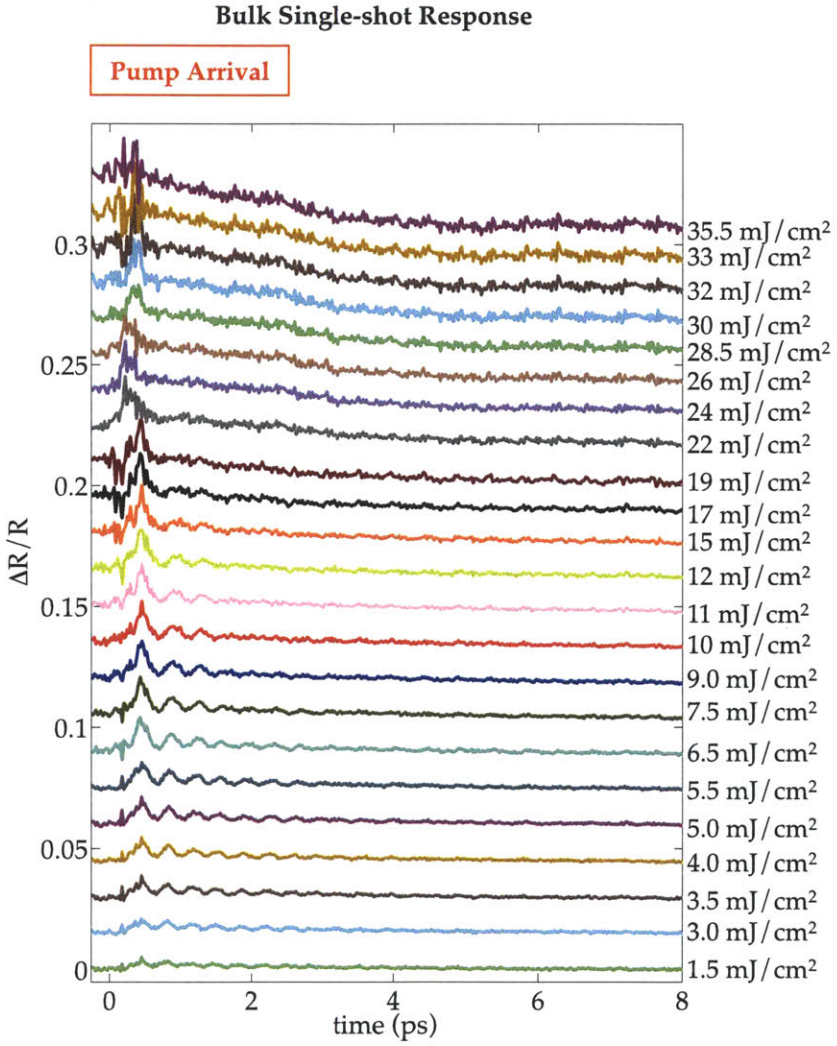

Figure 5-6: Single-shot reflectivity response of bulk bismuth at 800 nm for a pump fluence range of 1.5 to 35.5 mJ/cm^2. The red dashed line indicates pump arrival at 0 ps. The blue dashed line is a guide to the eye to emphasize the perceptible frequency down-shift upon increasing fluence.

The electronic amplitudes resulting from fitting the bulk data (Figure 5-6) to Eq. 5-1 are shown in Figure 5-7 (short-time) and Figure 5-8 (long-time).

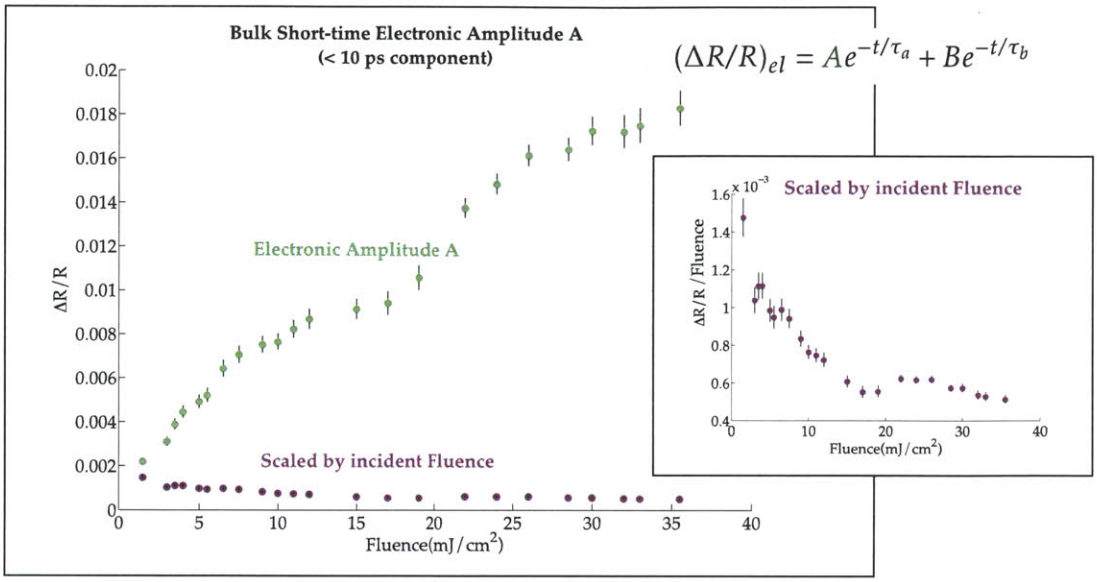

Figure 5-7: Short-time (<10 ps) electronic component A *extracted by fitting the bulk data in Figure 5-6 to Eq. 5-1. The amplitude is shown in green, and the amplitude scaled by incident fluence is shown in purple, also inset. The positive short-time electronic amplitude per incident photon decreases up to ~20 mJ/cm², and then plateaus.*

Both amplitudes increase (in absolute value) with fluence, which is expected as more lattice sites are photoexcited. When scaled by fluence, as shown in the figure insets, we observe less contribution from the short-time component upon increasing fluence, up to about 20 mJ/cm². In contrast, we observe increasing contribution from the long-time component when scaled by fluence, with no apparent plateau.

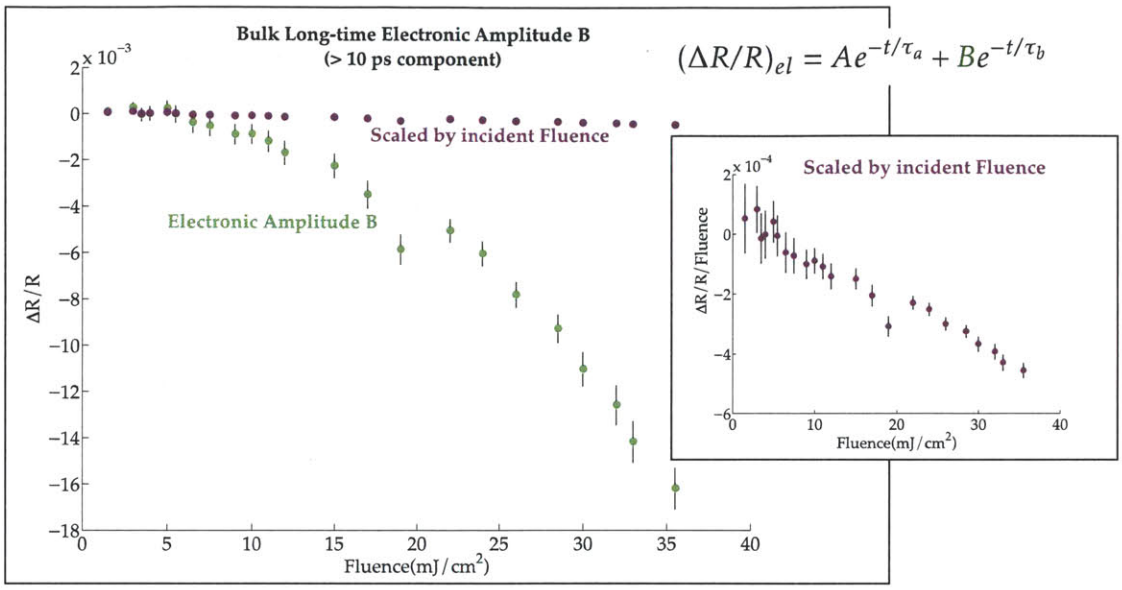

Figure 5-8: Long-time (>10 ps) electronic component B *extracted by fitting the bulk data in Figure 5-6 to Eq. 5-1. The amplitude is shown in green, and the amplitude scaled by incident fluence is shown in purple, also inset. The long-time electronic amplitude per incident photon increases near-linearly for all fluences measured.*

300 nm measurements

Select raw data traces from measurements on 300 nm bismuth films are shown in Figure 5-9. Measurements at the four lowest fluences (inset) were obtained from conventional pump-probe measurements, and the remaining data were obtained using the single-shot apparatus with a pump fluence up to 48.6 mJ/cm^2. Qualitatively, we observe a similarly increasing electronic response between the 300 nm and the bulk bismuth data following the pump pulse, with the baseline returning to the pre-pump level by ~8 ps. At 57 mJ/cm^2, the highest fluence employed, the 300 nm film (Figure 5-10) exhibits a negative response after the initial photo-excitation that descends below the pre-pump level and does not recover by the end of the 9.5 ps probe window. The frequency downshifts perceptibly from the lowest to the highest fluences, and no oscillation is visible in the highest fluence used for photoexcitation in this sample (57 mJ/cm^2, Figure 5-10).

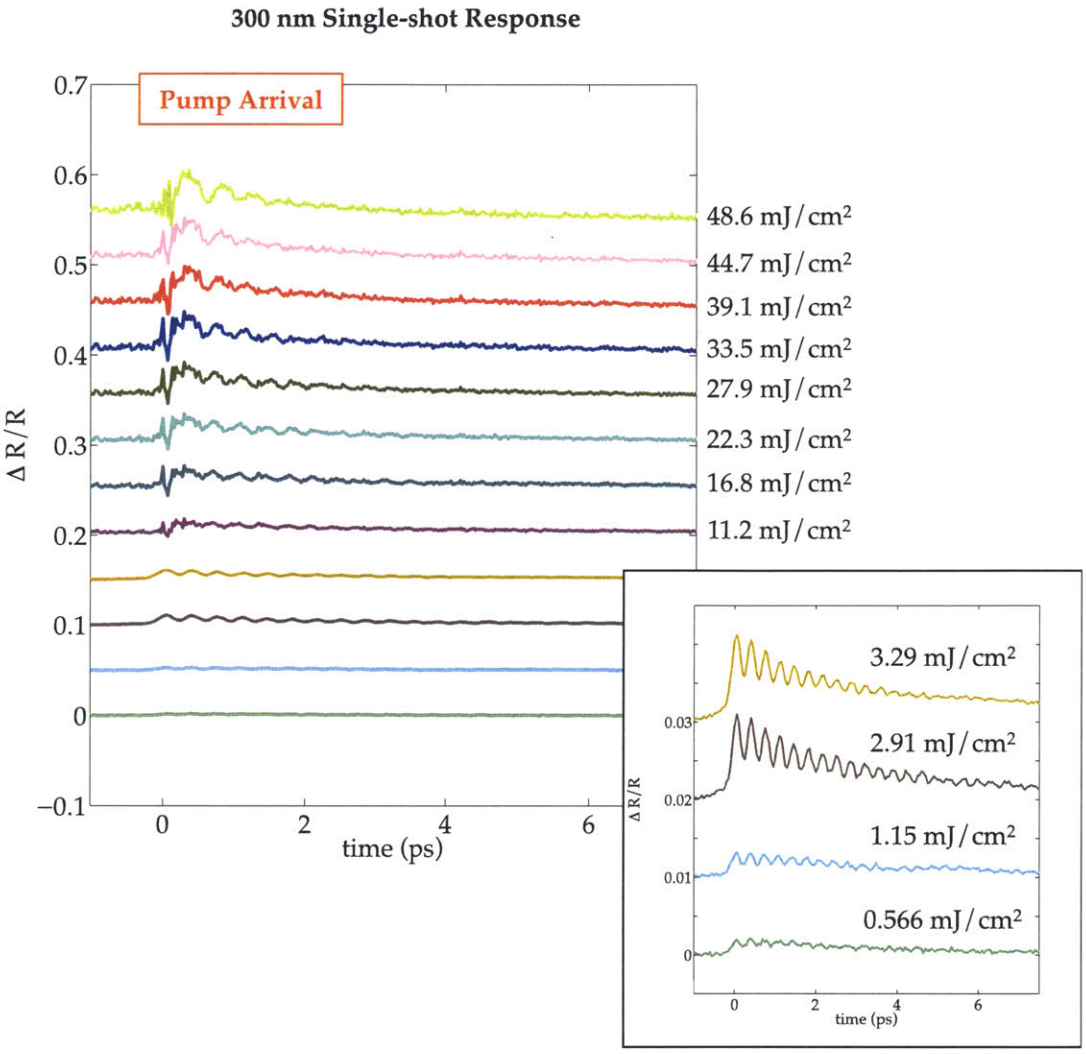

Figure 5-9: Single-shot reflectivity response of 300 nm bismuth film for a pump fluence range of 0.566 to 48.6 mJ/cm². The red dashed line indicates pump arrival at 0 ps. The blue dashed line is a guide to the eye to emphasize the perceptible frequency down-shift upon increasing fluence.

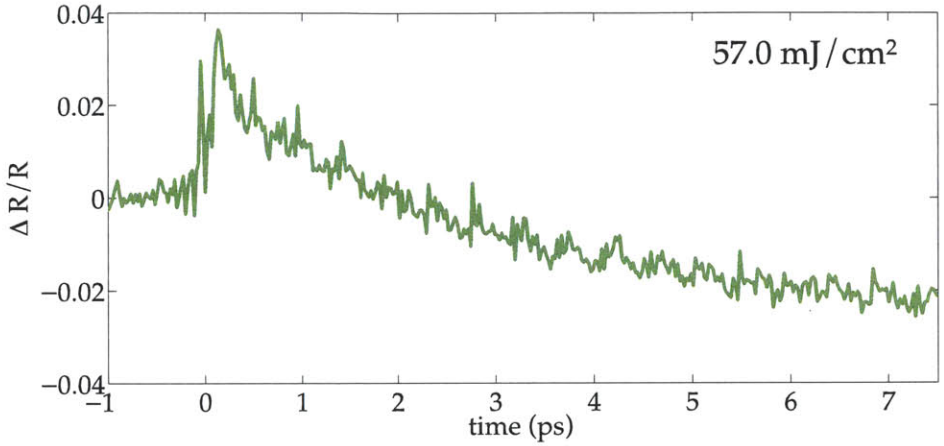

Figure 5-10: Response of the 500 nm film to the highest fluence employed in our single-shot measurements: 57 mJ/cm². The reflectivity drops below the pre-pump level after a few picoseconds and does not recover within the probe time window. No oscillations are visible.

The 300 nm bismuth film data in Figure 5-9 were fit to Eq. 5-1 and Eq. 5-2. Electronic amplitudes resulting from these fits are shown as a function of fluence (both raw and scaled by fluence) in Figure 5-11 and Figure 5-12 for the 300 nm data.

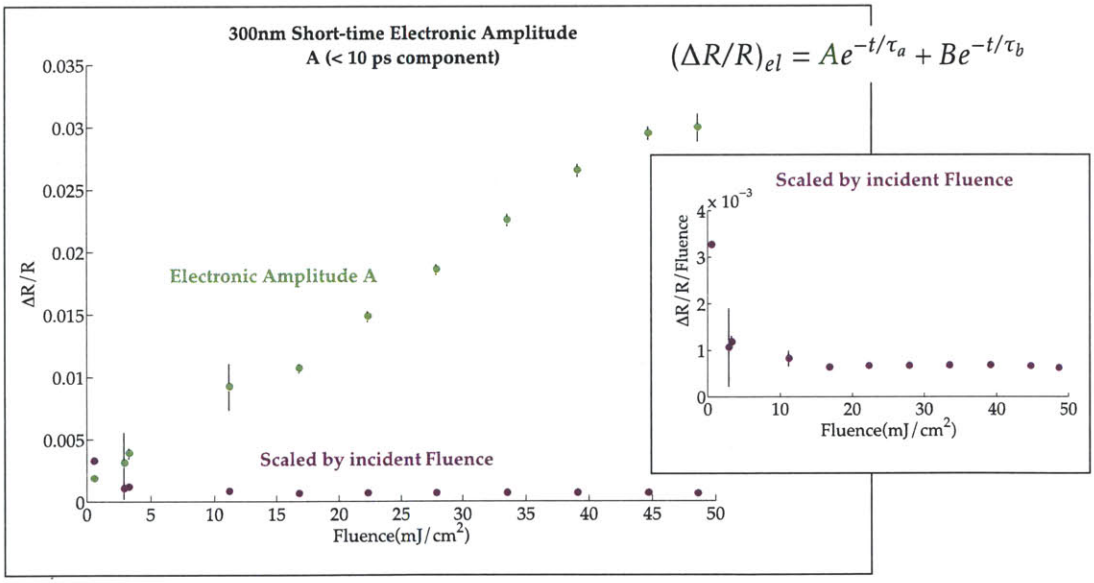

Figure 5-11: Short-time (<10 ps) electronic component A *extracted by fitting the 300 nm data in Figure 5-9 to Eq. 5-1. The amplitude is shown in green, and the amplitude scaled by incident fluence is shown in purple, also inset. The positive short-time electronic amplitude per incident photon decreases up to ~10 mJ/cm², and then plateaus.*

The short-time electronic component scaled by fluence decreases in amplitude with fluence, and levels off near 20 mJ/cm^2. The long-time electronic amplitude scaled by fluence increases with increasing fluence, and plateaus above 20 mJ/cm^2. Although the fluence values between the bulk and 300 nm data sets are not directly comparable due to measurement error, both samples exhibit decreasing scaled short-time electronic amplitudes with distinct plateaus. Both samples also exhibit increasing scaled long-time electronic amplitudes, the 300 nm component plateauing near the same fluence value as the short-term component, and the bulk long-term component increasing continuously in the measurement range.

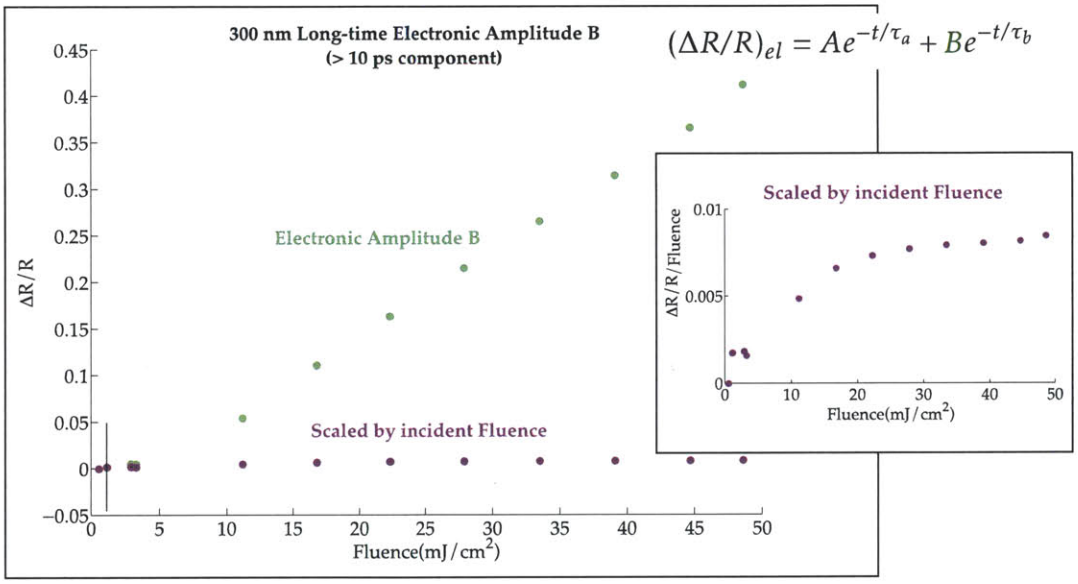

Figure 5-12: Long-time (> 10 ps) electronic component B *extracted by fitting the 300 nm data in Figure 5-9 to Eq. 5-1. The amplitude is shown in green, and the amplitude scaled by incident fluence is shown in purple, also inset. The long-time electronic amplitude per incident photon increases, then plateaus above 20 mJ/cm^2.*

Frequencies of the oscillatory parts of 300 nm photoexcited bismuth data are shown in Figure 5-13. We observe that frequency decreases with fluence moderately up to 20 mJ/cm^2, and then drops significantly with fluence, reaching ~2.05 THz at the highest fluence for which a frequency could be extracted. The most significant frequency down-shifting occurs above the same fluence (~20 mJ/cm^2) for which electronic amplitude plateaus were observed. This result is likely an illustration of the

strong electron-phonon coupling in bismuth, and will be explored in more detail in the discussion section.

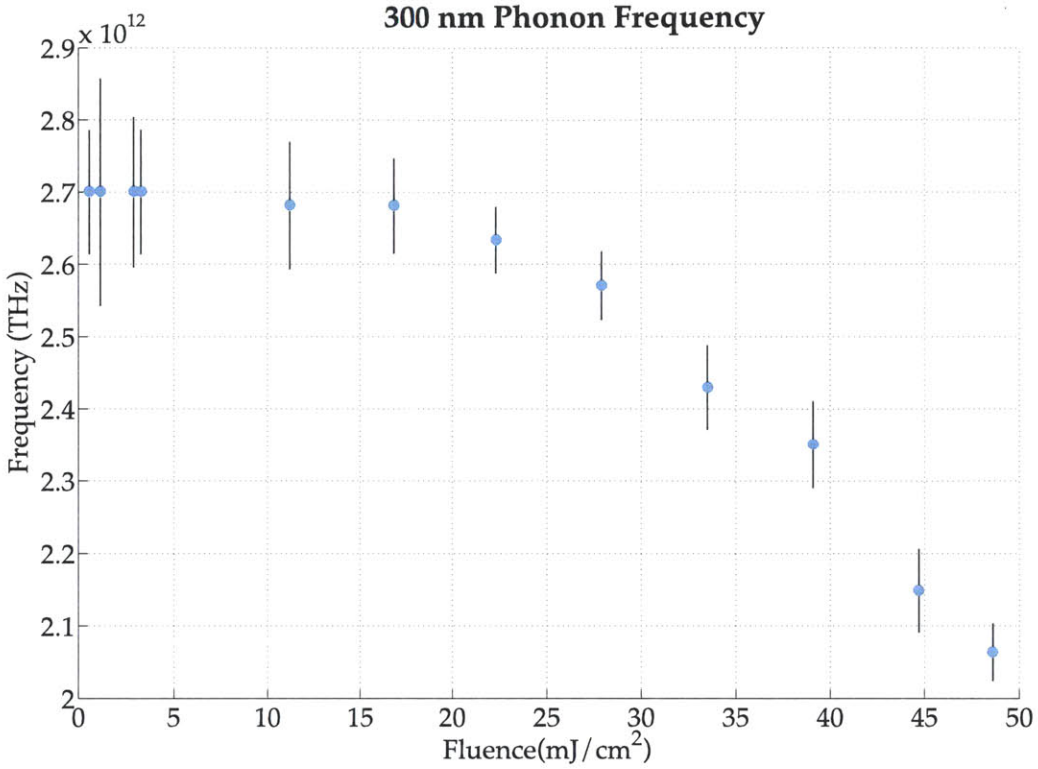

Figure 5-13: Measured phonon frequency for a range of pump fluences in 300 nm bismuth films. We observe decreasing frequency with a sharp drop above 30 mJ/cm^2. No phonon signal was resolvable in the highest fluence measurement (57 mJ/cm^2), the data for which is shown in Figure 5-10.

50 nm measurements

Raw data collected from photoexcitation of a 50 nm bismuth film is shown in Figure 5-14. In contrast to the previously presented data, we observe a negative reflectivity change upon pump arrival. We attribute this difference primarily to a change in the material band structure upon approaching the optical penetration depth (15 nm). Previous work on the probe-wavelength-dependent reflectivity change has shown that the bismuth band gap widens from 0.2 eV for bulk and 300 nm films to ~0.35 eV for a 40 nm film. Even for the lowest fluences, the reflectivity does not recover to the pre-pump value within the 8 ps window. For these measurements, the pump fluence ranged from 2.6 to 9.4 mJ/cm^2. At the highest fluence employed, oscillations are not resolvable above the noise.

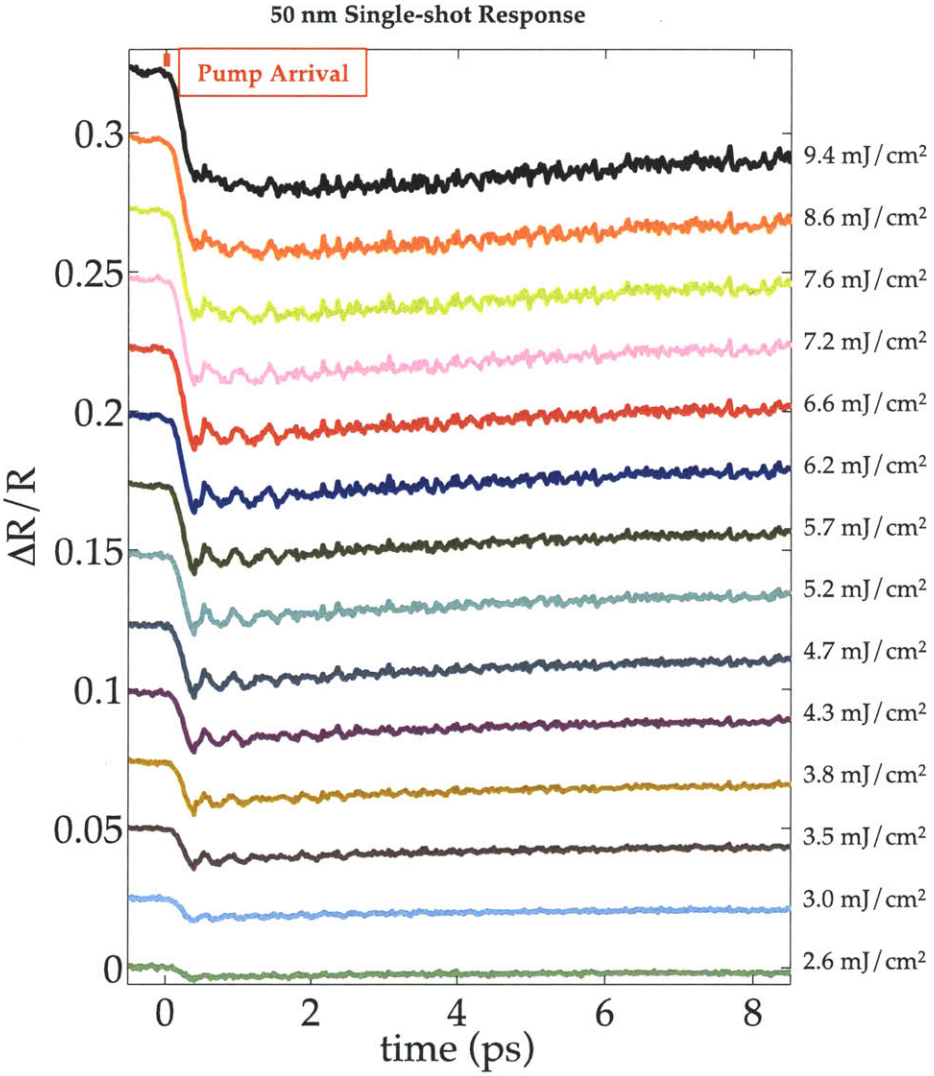

Figure 5-14: Single-shot reflectivity response of 50 nm bismuth film for a pump fluence range of 2.6 to 9.4 mJ/cm². The red dashed line indicates pump arrival at 0 ps. The blue dashed line is a guide to the eye to emphasize the perceptible frequency down-shift upon increasing fluence.

Electronic amplitudes resulting from fits to the 50 nm sample data in Figure 5-14 are shown in Figure 5-15 and Figure 5-16. We observe that for the 50 nm film, both the short- and long-time electronic amplitudes grow with fluence when scaled. The effect plateaus after 6 mJ/cm² in the short-time (< 10 ps) case, and after 8 mJ/cm² in the long-time (> 10 ps) case. The different behavior exhibited at short times in the 50 nm film could result from absorption by excited carriers constrained in the region due to the

narrow depth. This would suggest that early-time transport of photoexcited carriers may play an important role in material dynamics when the system is constrained to two dimensions. As for the other samples, it was confirmed that a biexponential was necessary to fit the post-pulse response of the 50 nm film data.

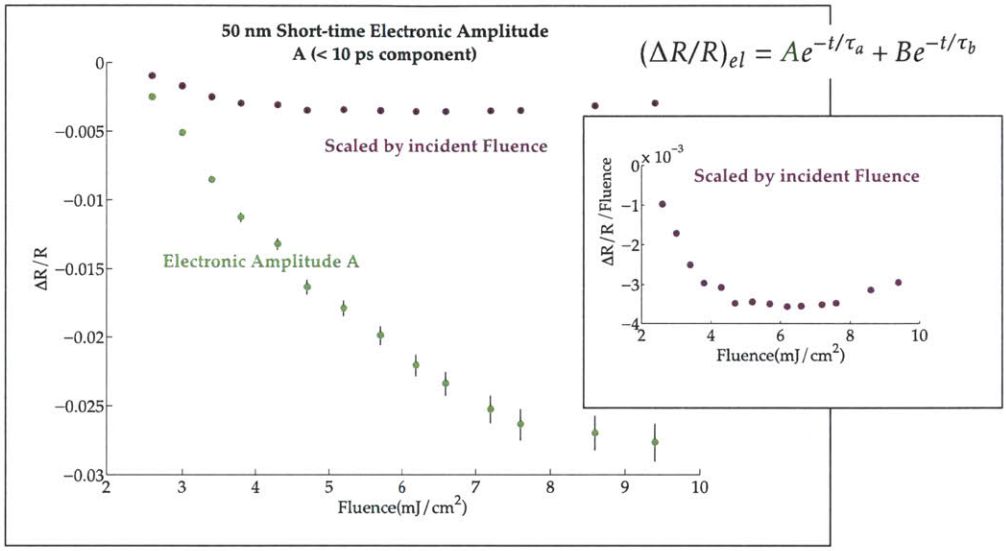

Figure 5-15: Short-time (<10 ps) electronic component A *extracted by fitting the 50 nm data in Figure 5-14 to Eq. 5-1. The amplitude is shown in green, and the amplitude scaled by incident fluence is shown in purple, also inset. The positive short-time electronic amplitude per incident photon increases up to ~5 mJ/cm², and then plateaus.*

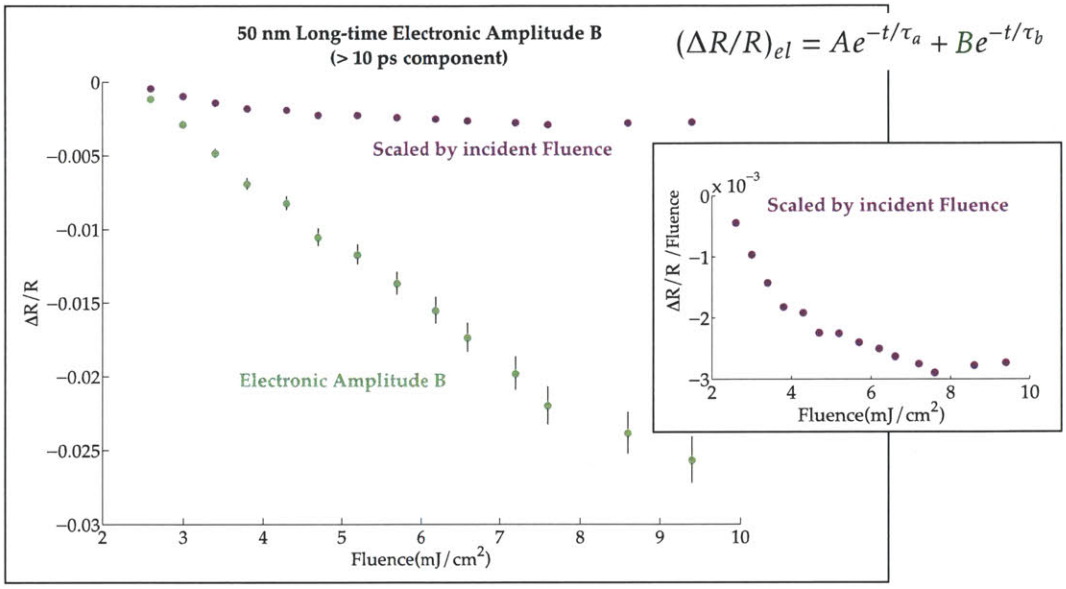

Figure 5-16: Long-time (>10 ps) electronic component B *extracted by fitting the 50 nm data in Figure 5-14 to Eq. 5-1. The amplitude is shown in green, and the amplitude scaled by incident fluence is shown in purple, also inset. The long-time electronic amplitude per incident photon increases, then plateaus above 8 mJ/cm².*

Frequencies extracted from the oscillatory part of the 50 nm film data are shown in Figure 5-17. As in the case of the 300 nm film, we observe a slight decrease up to the fluence threshold that marks an electronic signal plateau (8 mJ/cm² for 50 nm, 20 m/cm² for 300 nm) and significant down-shifting of the frequency following or slightly preceding this plateau. The lowest resolvable phonon oscillation is at ~2 THz after excitation by a 9 mJ/cm² pump pulse. While similar dynamics are observed in the 300 nm and 50 nm samples (with the exception of the short-time electronic amplitude), in all cases the thresholding behavior occurs in response to significantly reduced pump fluence in the 50 nm film case.

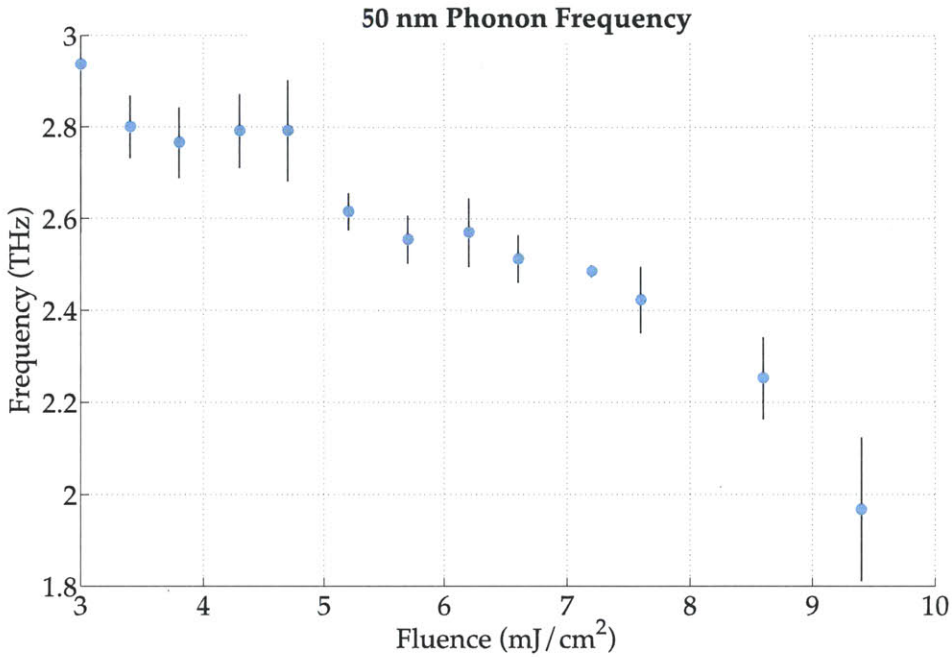

Figure 5-17: Measured phonon frequency for a range of pump fluences in 50 nm bismuth films. We observe decreasing frequency with a sharp drop above 5 mJ/cm^2. The highest fluence measurement yields a frequency below or 2 THz. The measurement at 8.5 mJ/cm^2 fluence is the highest fluence which yields a well-resolved frequency.

The time traces were fit to exponential functions after the pump pulse response (starting at the maximum reflectivity change after $t = 0$ for bulk and 300 nm, and at the minimum reflectivity change after $t = 0$ for 50 nm). Figure 5-18 shows the absolute value of the instantaneous amplitude scaled by pump fluence for the different samples, obtained by taking the range over the first 500 fs of the measurement. The scaled absorption decreases slightly with fluence for the bulk and 300 nm samples (leveling off at ~10 mJ/cm^2 in the 300 nm case and ~20 mJ/cm^2 in the bulk case), but increases sharply for the 50 nm sample until ~6 mJ/cm^2, at which point it decreases slightly. These dynamics mirror the short-time amplitudes for each sample discussed above. With the assumption that the instantaneous response reports primarily on the photoinduced carrier population, these trends suggest that the short-time electronic component is due primarily to instantaneous absorption. We propose that carriers created by the leading edge of the laser pulse absorb additional photon energy and contribute nonlinearly to the signal in the 50 nm case, where transport out of the quasi-two-dimensional region is limited. At the plateau near 6 mJ/cm^2, the sample undergoes

the same saturation in absorption observed in the bulk and 300 nm films that has been previously reported.[86]

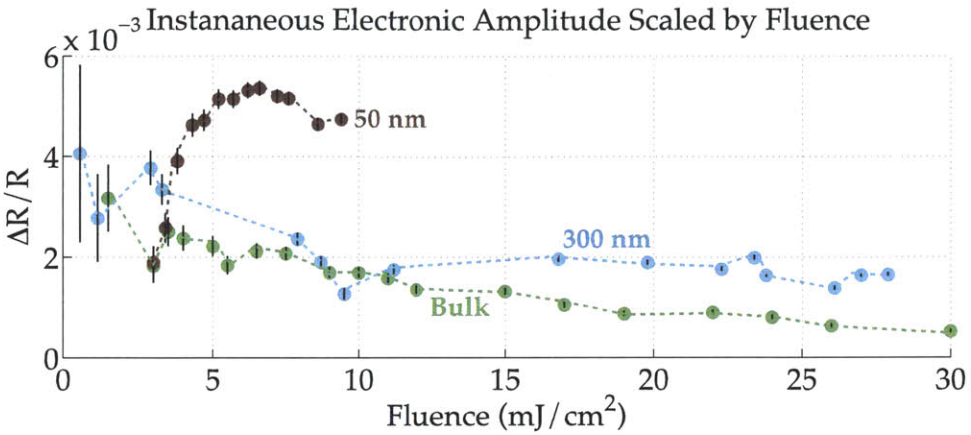

Figure 5-18: The absolute value of the instantaneous reflectivity response for pump arrival is shown for each sample. The value is defined as the maximum (bulk and 300 nm) or minimum (50 nm) ΔR/R value reached relative to the pre-pump baseline in the first 1 ps.

5.2.2 Long-time Response to Strong Photo-excitation

The previous section presented measurements on the instantaneous photoinduced electronic and lattice dynamics in bismuth far from equilibrium. By temporally overlapping the pump pulse with the single-shot probe pulse, those measurements report on the photoexcitation itself and the subsequent 8 ps of material evolution. By employing a translation stage in the optical setup, the probe can be positioned to arrive many picoseconds after the pump pulse during a subsequent measurement. Post-excitation lattice dynamics are only resolvable with a second pump, as presented in the next section. With the temporally delayed probe pulse grid alone, we can capture 9.5 ps of the evolving reflectivity of the perturbed sample at any delay of interest, as shown in Figure 5-19. The $\Delta t = 0$ measurement corresponds to zero time delay between the pump and probe, equivalent to the measurements presented in 5.2.1.

The measurement was repeated for several time delays between the pump and probe and for several different pump fluences. For each set of measurements following like fluence, probe pulse snapshots were assembled to provide a composite time trace. Each measurement set per fluence was obtained on the same sample spot, and it was verified that cumulative optical damage did not occur by reproducing the expected $t = 0$ response after the measurement. In Figure 5-19, the slowly varying structure visible

within individual 9.5 ps probe time trace results from variation across the echelon grid, a spatio-temporal artifact described in Chapter 3. In a typical measurement, this variation is masked by the larger signal. The fast-varying structure within each individual 9.5 ps probe time trace results from instrument noise. Despite these variations, the average intensity from one probe trace (time delay) to another varies reproducibly for a given fluence. Thus, long-time dynamics may be extracted from multiple measurements even upon high fluence excitation as long as the baseline noise is moderately low (below 0.1%). Because the bulk crystalline sample is not optically smooth, noise exceeds this level. However, the deposited films exhibit optically smooth surfaces, enabling a comparison of the many-picosecond reflectivity evolution of photoexcited bismuth in a quasi-three-dimensional environment (300 nm) and a quasi-two-dimensional environment (50 nm) from moderate to strong excitation.

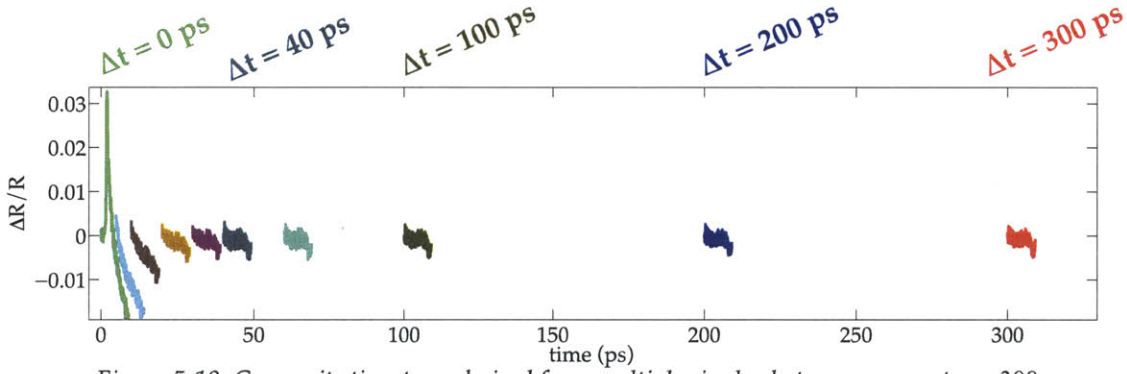

Figure 5-19: Composite time trace derived from multiple single-shot measurements on 300 nm bismuth film after varying time delays following excitation by a 26 mJ/cm² fluence pump pulse. Variations over individual 9.5 ps snapshots are due to variation over the echelon profiles, and do not bear physical meaning in interpreting the signal.

To aid in visualization and comparison, 9.5 ps data traces after the $\Delta t = 0$ trace are depicted by a single point whose y-value (differential reflectivity) is the average over the last 2 ps of the specified 9.5 ps time window, and whose x-value (time) is given by the measurement time delay (e.g., 40 ps, 100 ps, etc.) plus 8.5 ps. The resulting composite time trace gives snapshots of the material reflectivity up to many picoseconds after pump excitations of varying fluence.

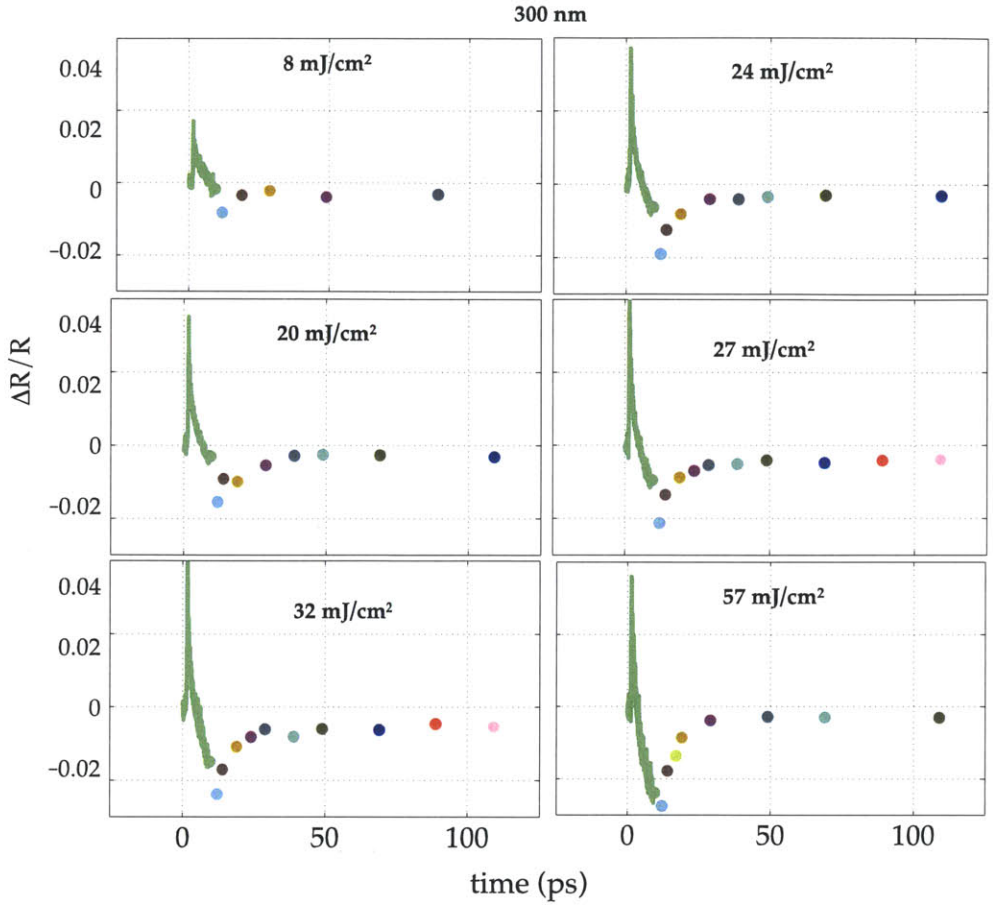

Figure 5-20: Composite time traces collected from multiple single-shot measurements of varying time delays on the 300 nm sample. The ~10 ps response increases with fluence beyond the level visible by our 9.5 ps probe pulse, and recovers by 25-50 ps for most fluences measured. Colors for a given composite time trace indicate consecutive measurements.

Composite time traces of the 300 nm bismuth film photoexcitation response, ranging from 0 to 100 ps after pump arrival, are shown in Figure 5-20 for six pump fluences ranging from 8 to 57 mJ / cm^2. With the exception of the lowest-fluence case, there is little distinction in the temporal profiles across the traces. There appears to be a slow recovery throughout the next 800 ps, but differences are smaller than the instrumental error of 0.001%, as shown in Figure 5-21. Additionally, there may be an acoustic response between 200-300 masking the long timescale recovery.

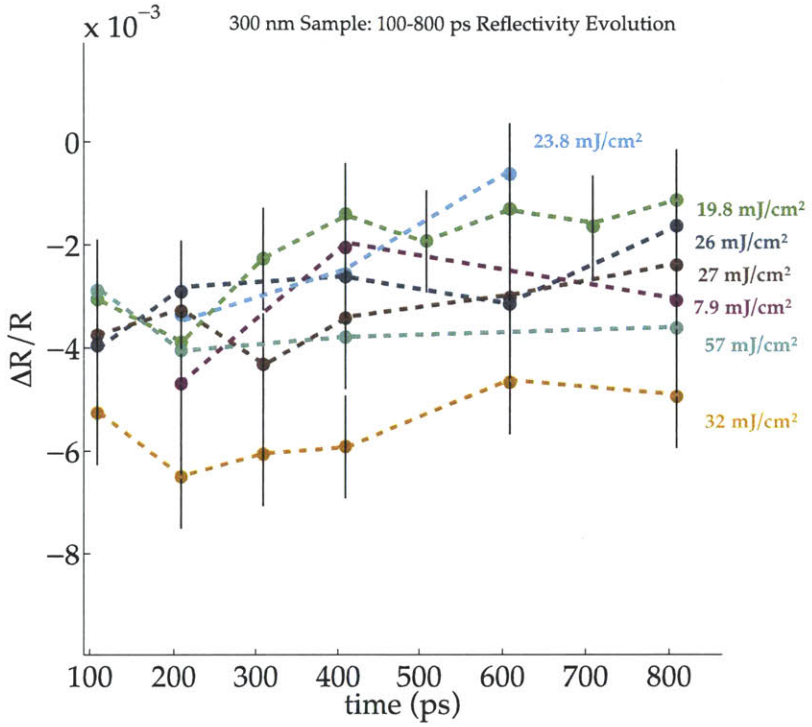

Figure 5-21: Emphasis on the 100-800 ps reflectivity evolution of 300 nm bismuth data shown in Figure 5-23, with instrumental error of 0.001%.

Figure 5-22 shows composite time traces of the 50 nm film response for a fluence range of 3 to 9.5 mJ/cm^2. In the case of the 50 nm film, the reflectivity does not return to the pre-pump zero level by 100 ps, but rather remains largely unchanged from the level 9.5 ps after pump arrival. The reflectivity response passes through a minimum near 50 ps, of moderately increasing depth with increasing fluence, which may be due to an acoustic response in the thin film upon intense photoexcitation. Because the $t = 0$ response was reproduced at infinite time (several seconds), it is clear that a slow recovery takes place on the 100 ps to ns timescale.

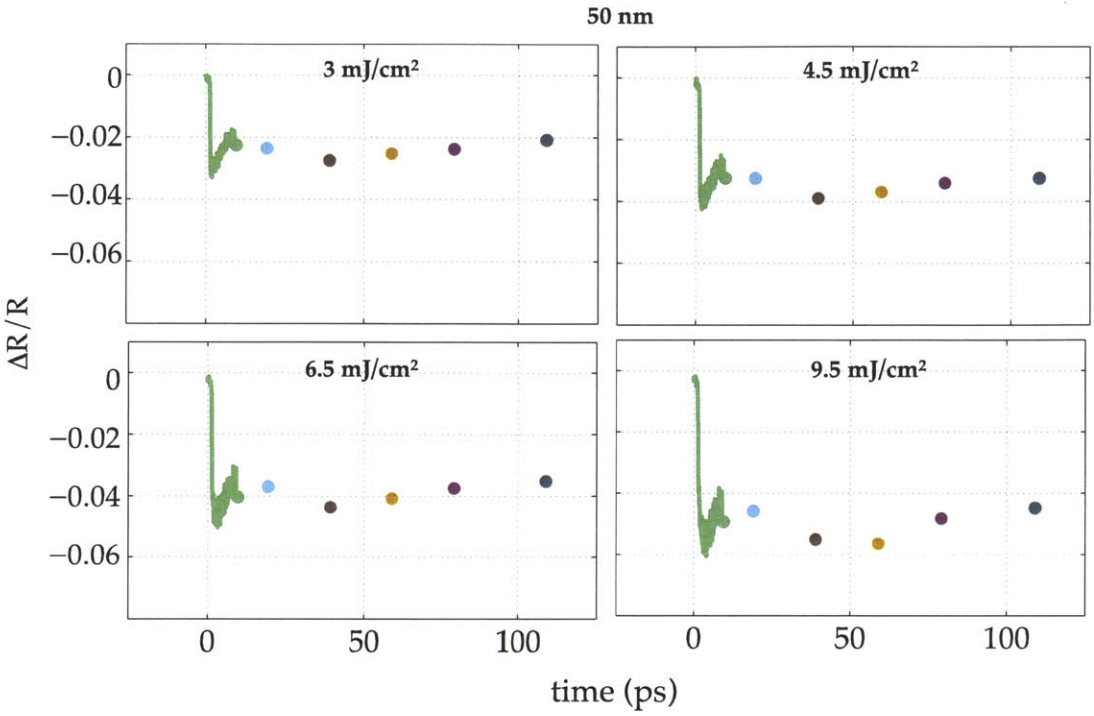

Figure 5-22: Composite time traces collected from multiple single-shot measurements of varying time delays on the 50 nm sample. The response increases toward the pre-pump level for 10-15 ps and remains relatively unchanged through 100 ps except for the acoustic strain pulse. Colors for a given composite time trace indicate consecutive measurements.

5.2.3 One-pump Thin Film Measurements: Key Results

In the measurements presented thus far, we have observed various timescales of interest that likely result from specific photoinduced dynamics. These timescales are summarized in Figure 5-23, which displays all composite single-shot time traces for both the 300 nm (top) and 50 nm (bottom) sample. (300 nm traces are displayed on a log scale in the main figure).

Generalizing, the 300 nm film exhibits a positive response on the 500 fs timescale and falls below the pre-pump level to a minimum at ~10 ps. The reflectivity recovers almost completely to the pre-pump level during the next relaxation phase (from ~10 to 50 ps). A slow recovery on the longer timescale after 50 ps is likely but not resolvable above the instrumental noise.

The 50 nm film exhibits a negative near-instantaneous response on the 500 fs timescale, recovers moderately on the 10-15 ps timescale, and undergoes a slow recovery toward the baseline level. An acoustic response is visible at ~50 ps. Though

measurements were not obtained past 100 ps in the 50 nm sample, the eventual recovery was verified by reproducing the original $t = 0$ response at the infinite-time limit (many seconds later).

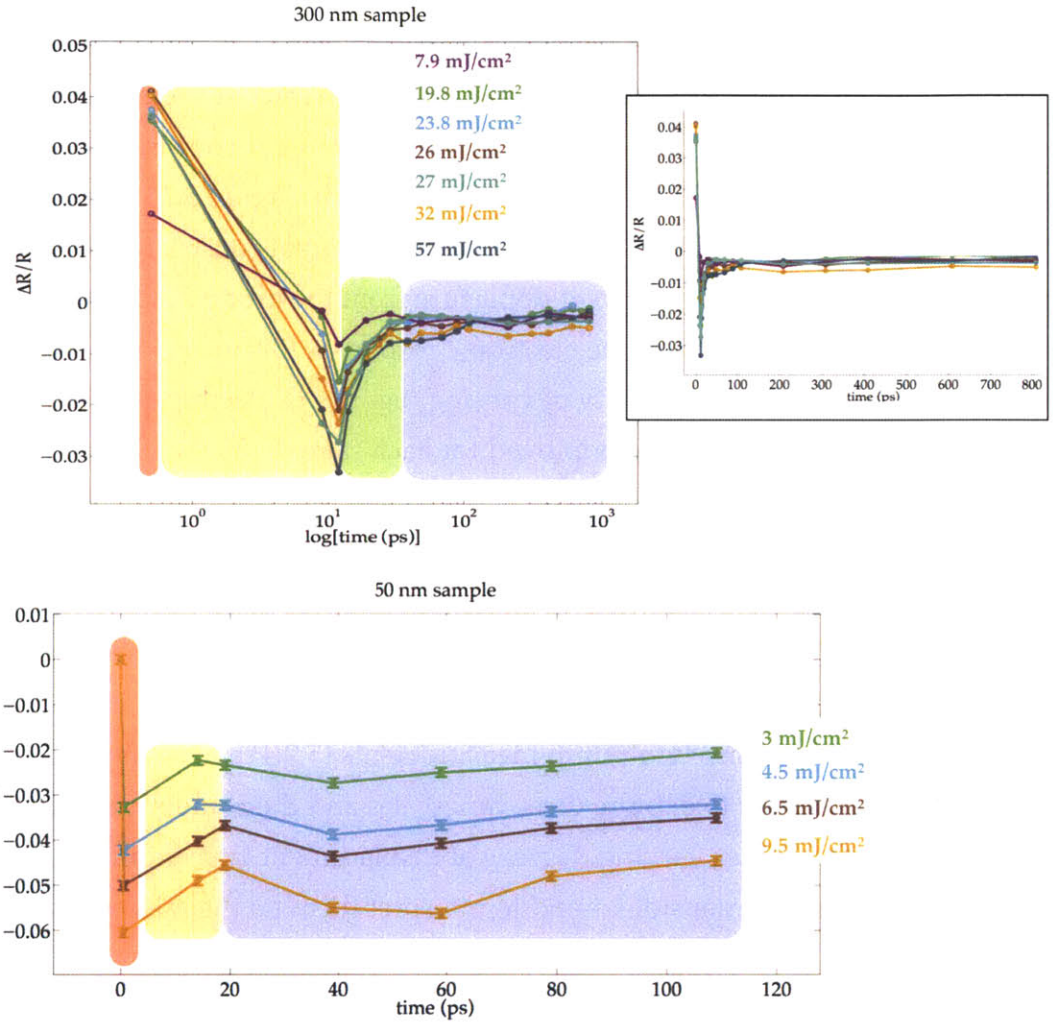

Figure 5-23: Summary of timescales of interest in bismuth single-shot measurements for two samples: a 300 nm film (top), which approximates a three-dimensional environment, and a 50 nm film (bottom), which approximates a two-dimensional environment. The 300 nm traces were collected out to 800 ps, and are displayed on a log time scale in the main figure (linear scale: inset). Both samples exhibit an instantaneous response on the order of 500 fs (red), an early-time recovery on the order of 10-15 ps (orange), and long-time dynamics past 20-50 ps (blue). We observe an intermediate relaxation stage in the 300 nm sample onset at 10 ps with a ~15 ps time constant (green).

When scaled by incident fluence, the 50 nm sample instantaneous response and the short-time post-pump relaxation component increase with fluence (Figure 5-18, and Figure 5-15), while the 300 nm instantaneous response and short-time post-pump

relaxation component decrease with fluence when scaled (Figure 5-18 and Figure 5-11). In both samples, the scaled responses corresponding to electronic relaxation over > 10 ps increase with fluence (Figure 5-12 and Figure 5-16).

For both samples at moderately low fluence, we observe lattice oscillations 500 fs after pump arrival that last for 1-5 ps, with a damping that decreases with fluence. The oscillation frequency red-shifts with increasing fluence, which is the expected mode-softening result. Strong departure from the ground-state frequency is onset at a much lower fluence for the 50 nm film than for the 300 nm film (Figure 5-13 and Figure 5-17), indicating a dependence of lattice dynamics on dimensional constraints. In both samples, the plateaus that mark strong departure from the ground-state frequency are similar to identifiable plateaus in the electronic responses (50 nm: 6.5 mJ/cm^2, 300 nm: 20 mJ/cm^2), indicating the possibility of varying regimes of electron-phonon coupling strengths. At the highest fluences employed for each sample (50 nm: 9.5 mJ/cm^2, 300 nm: 57 mJ/cm^2), oscillations can no longer be resolved. Because phonon amplitude increases with fluence, we expect that this result reflects material dynamics even though noise increases at high fluence. The effect may be induced by either very fast dephasing (< 1 cycle renders fitting to Eq. 5-2 inconclusive) or to the absence of the Raman-active mode in the highly photoexcited state.

Our goal in obtaining two-pump measurements (5.2.4) and in modeling the material dynamics (5.3) is to explore these timescales and their underlying dynamics as they evolve in time—under varying degrees of displacement from equilibrium and constrained in varying dimensions—and to interpret them on the microscopic level.

5.2.4 Spectroscopy of Photoexcited Bismuth: Two-pump Measurements

In the previous section, results were presented on photoexcited bismuth films from moderate to very high excitation densities. The results suggest key differences between a quasi-two-dimensional environment (the 50 nm film) and a quasi-three-dimensional environment (the 300 nm film), such as their instantaneous responses and recovery mechanisms. They also suggest striking parallels, such as analogous thresholding effects between lattice and electronic parameters despite the different fluence regimes used for each sample's photoexcitation measurements. In this section we present two-pump measurements on bismuth while varying both the film depth and

initial excitation strength. As described in Chapter 2 and demonstrated in our results on PtI(en) (Chapter 4), overlapping the probe array with a second pump at a specified time following photoexcitation enables a measurement of the photoexcited lattice as it evolves. For the 300 nm measurements, the second pump fluence was 8-9 mJ/cm^2. For the 50 nm measurements, the second pump fluence was 3 mJ/cm^2.

Two-pump measurements on 300 nm bismuth

Figure 5-24 shows select two-pump data on the 300 nm bismuth film. At left is a comparison of the photoexcited state after 3 ps, varying the level of initial excitation fluence from 9.5 to 57 mJ/cm^2. Above 50 mJ/cm^2, there is a small electronic response but no resolvable phonon oscillation, suggesting the strong possibility of photo-induced structural change. At right, measurements at varying time delays following 57 mJ/cm^2 excitation are shown. Lattice oscillations grow in following the 3 ps delay, and by 400 ps the lattice response resembles the expected ground-state response (e.g., as compared with the 11.2 mJ/cm2 one-pump trace in Figure 5-9).

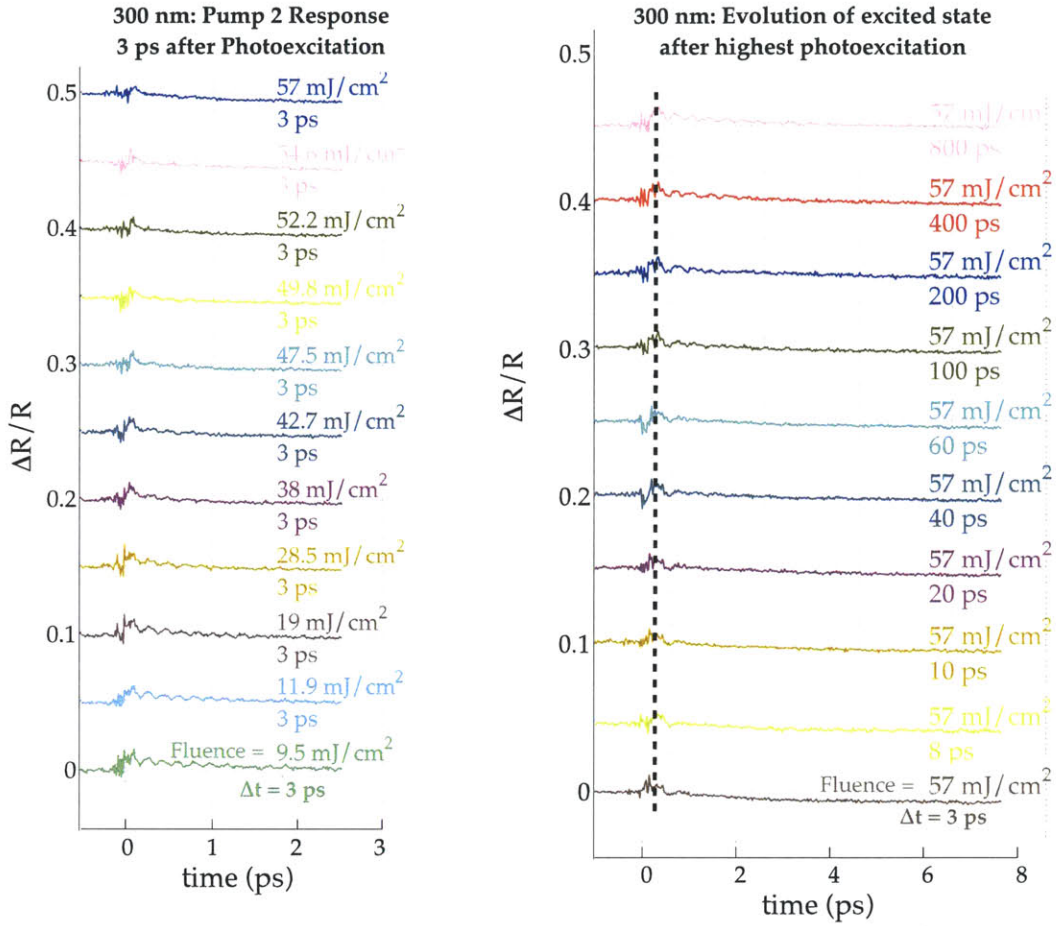

Figure 5-24: Representative two-pump measurements on 300 nm bismuth film across different excitation fluences and measurement time delays. Left: the photoexcited state is probed 3 ps after excitation by the fluence indicated. Qualitatively, we observe the familiar lattice response below 20 mJ/cm² excitation. Above this excitation, the measurement does not identify lattice vibrations 3 ps after photoexcitation. Right: the highly photoexcited state is probed at varying time delays. We see oscillations after 3 ps, and the response resembles the ground-state excitation response after ~400 ps.

Several measurements across multiple excitation densities and time delays were obtained on the 300 nm film. In order to compress these data for visualization in the following figures, parameters of interest are displayed versus measurement delay time with a continuous excitation fluence color-map. Figure 5-25 and Figure 5-26 show the electronic amplitude for each measurement—defined as the peak height following the second pump arrival—for various excitation levels for the first 100 ps and the full 800 ps, respectively. Figure 5-27 and Figure 5-28 show the frequency measured (fit to Eq. 5-2) as a function of time delay and excitation fluence, also for the first 100 ps and the

full 800 ps, respectively. These measurements were obtained under varying conditions, which yields more variation than a single set of measurements obtained over a few hours. Still, trends from low to high excitations regimes are identifiable and reasonably consistent. For clarity in visualizing trends, dashed lines illustrate the trajectory of a single photoexcited state (i.e., response to a single fluence as a function of time). For the electronic amplitudes, values are not scaled by pump fluence, as they were in the previous section, since the second pump intensity was kept constant.

For the lowest fluence range (dark blue), we observe a low instantaneous electronic amplitude that increases over ~30 ps and continues to increase slowly over the 800 ps measurement span. Similar trends are observed for the moderate fluence range (light blue). In the highest fluence range, the instantaneous electron amplitude is lower still. The recovery dynamics on the sub-20 ps timescale are not resolvable above the noise, but a slow increase is apparent starting from ~50 ps throughout the 800 ps measurement span. These results confirm the slow recovery over 800 ps (or longer) suggested by the one-pump long-timescale measurements (Figure 5-21). The recovery in the ~30 ps timeframe visible for low and moderate fluence regimes also suggests a relation to the intermediate recovery from those measurements (green shaded region in Figure 5-23).

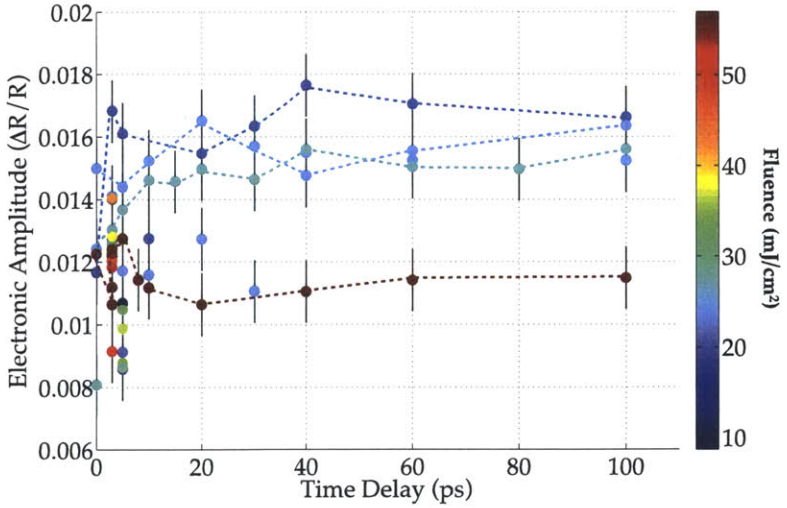

Figure 5-25: Electronic amplitudes extracted from two-pump measurements on 300 nm bismuth at varying time delays and degrees of photoexcitation. The first 100 ps are shown.

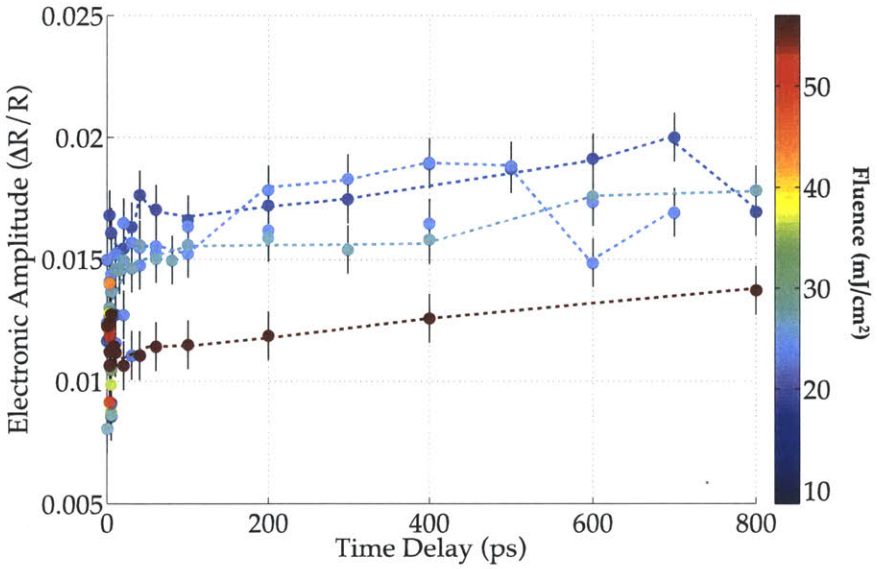

Figure 5-26:Electronic amplitudes extracted from two-pump measurements on 300 nm bismuth at varying time delays and degrees of photoexcitation. The full 800 ps are shown.

We monitor the lattice response of the photoexcited state via the oscillation frequency launched by the second pump pulse. For the lowest fluence range, we observe that even immediately after photoexcitation, the ground state frequency near 3 THz is reproduced, indicating that the photoexcited state has quickly relaxed to near the ground state. Still, there is a slight increase over 800 ps. We note that this fluence—9.5 mJ/cm^2, the lowest in our two-pump measurements on the 300 nm sample—is still significantly higher than that employed by most prior work on bismuth. In the moderate fluence range, we observe a lower frequency (2.3-2.7 THz) immediately following the initial photoexcitation. There is an increase in measured frequency as the photoexcited state relaxes over ~20 ps, and continued slow recovery over 800 ps. At the highest fluence, the earliest time points exhibit significantly reduced frequency (below 2 THz). We note that below 2 THz, there is a very large error in the fitting. After ~10 ps, the frequency rises above 2 THz (or alternatively, the frequencies become resolvable above the noise). The frequency in the highest fluence case continues to rise over the 800 ps span. We note that the highest excitation measurements do not result in the ground state frequency by 800 ps.

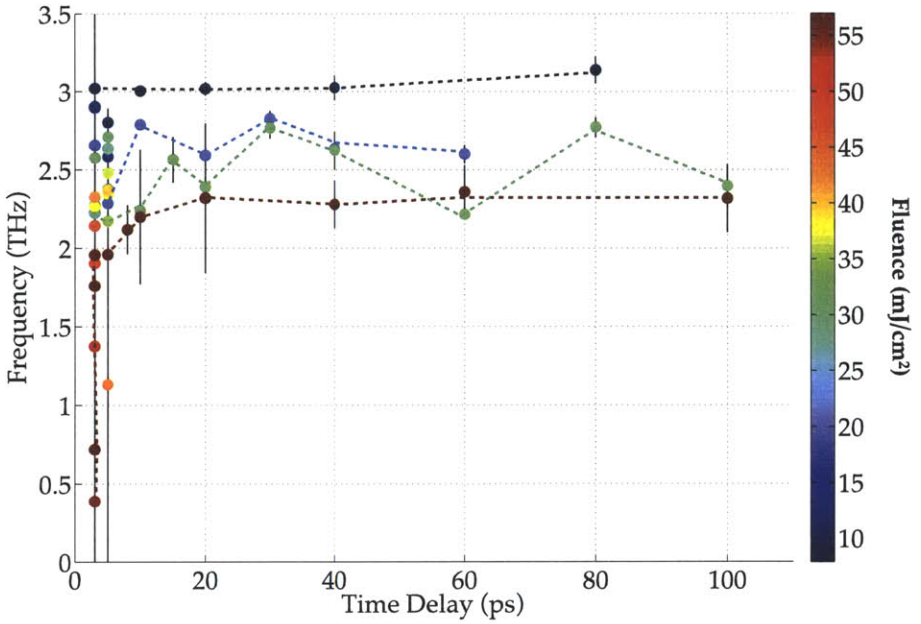

Figure 5-27: Phonon frequency extracted from two-pump measurements on 300 nm bismuth at varying time delays and after varying degrees of photoexcitation. The first 100 ps are shown.

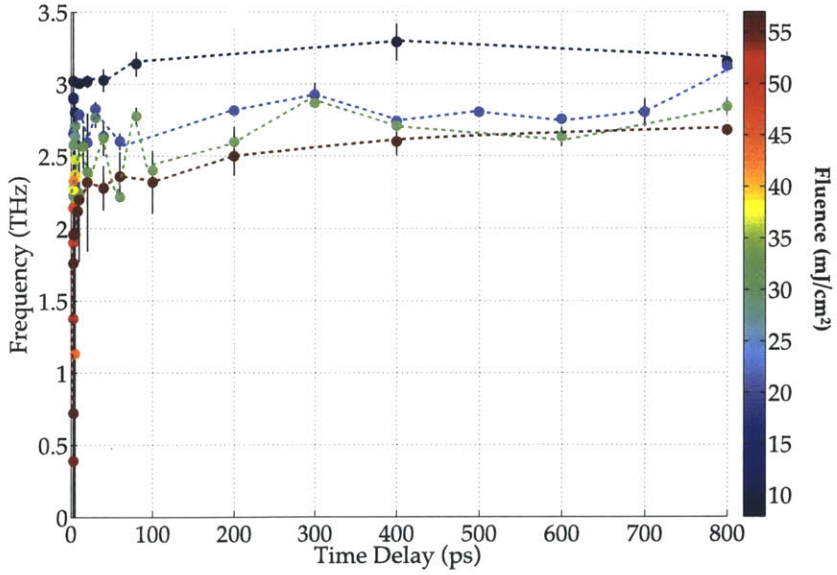

Figure 5-28: Phonon frequency extracted from two-pump measurements on 300 nm bismuth at varying time delays and after varying degrees of photoexcitation. The full 800 ps are shown.

Two-pump measurements on 50 nm bismuth

Figure 5-29 displays data from two-pump measurements on 50 nm bismuth up to 100 ps after two representative photoexcitation levels. At moderate excitation (left), the lattice response is visibly reduced below 10 ps, but is present at all time delays. The electronic amplitude increases slightly as a function of time. At high excitation (right), no lattice response is visible until ~30 ps following excitation, which is suggestive of structural change. Relative to the moderate excitation case, the electronic amplitude response is reduced for all time delays.

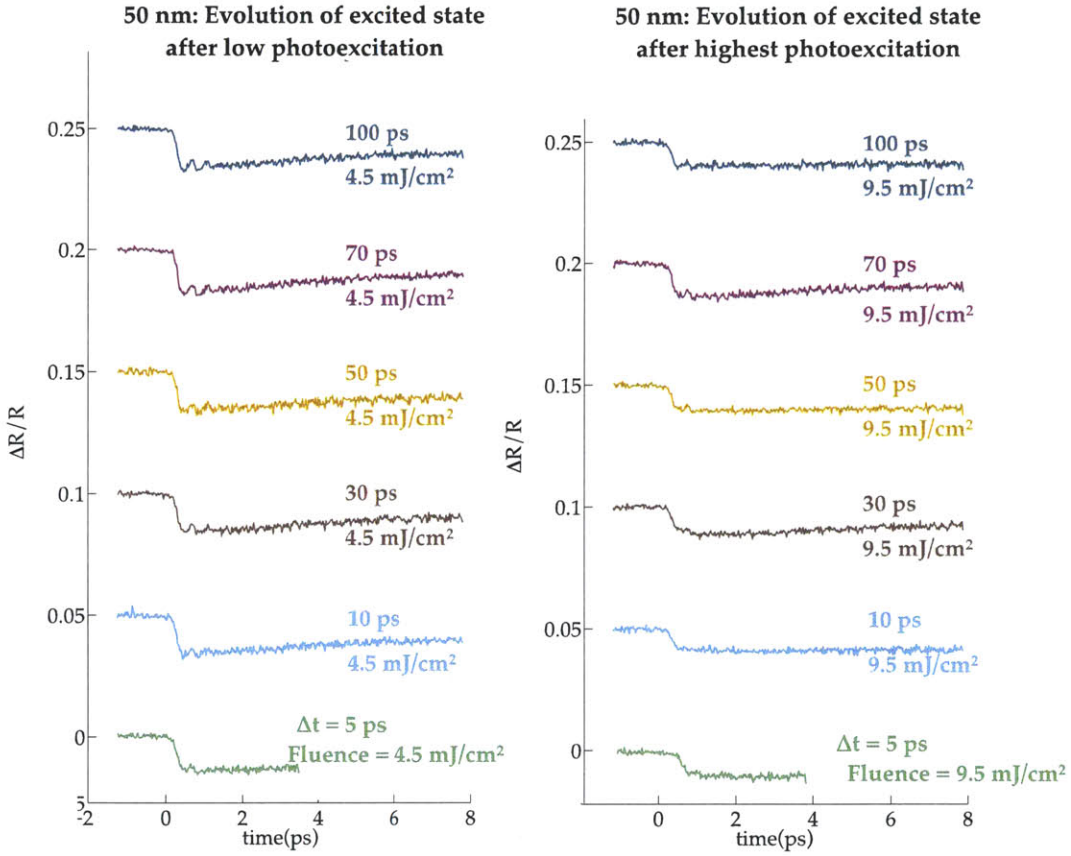

Figure 5-29: Representative two-pump measurements on 50 nm bismuth film across different excitation fluences and measurement time delays. Left: the photoexcited state is probed from 3 to 100 ps after excitation by a moderate fluence, 4.5 mJ/cm². Right: the photoexcited state is probed from 3 to 100 ps following excitation at a high fluence, 9.5 mJ/cm².

Electronic amplitudes from the 50 nm bismuth film response to four different initial excitation levels at multiple time delays are shown in Figure 5-30, and the frequencies measured in each case are displayed in Figure 5-31. For all initial excitation levels, we

observe an increase in the electronic amplitude over 100 ps; however, the amplitudes do not converge near the same level by 100 ps (as they did in the 300 nm case, for all but the highest fluence). This is in keeping with the indication from the composite time traces (

Figure 5-22) that suggest only an initial recovery has occurred by 100 ps. For all but the highest fluence, the measured lattice frequency at early times decreases slightly with fluence, and all measurements converge to nearly the same value after 100 ps. At the highest fluence, no oscillations are resolved until 30 ps after excitation. Afterwards, the lattice response increases in frequency throughout the 100 ps delay but does not converge to the same value as the lower fluence measurements. In all cases, the frequency at 100 ps remains relatively low (2.5 THz), which is similar to the 300 nm case over this timescale.

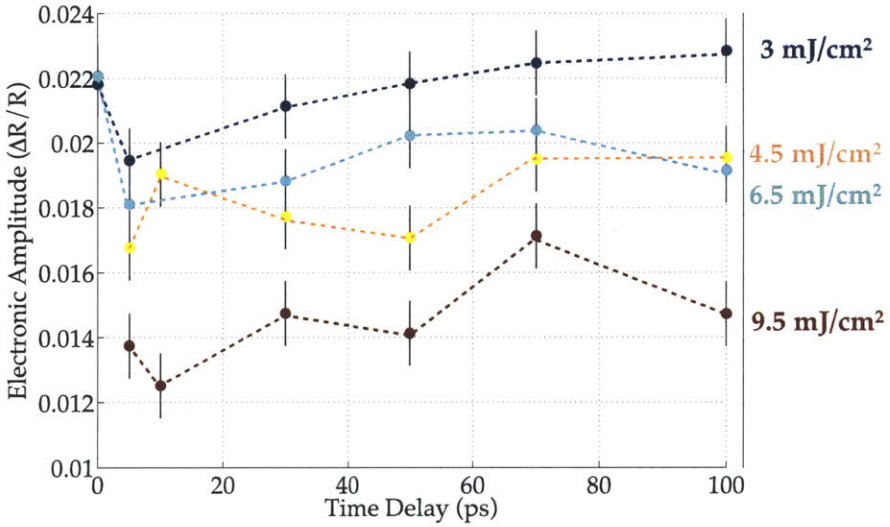

Figure 5-30: Electronic amplitudes extracted from two-pump measurements on 50 nm bismuth at varying time delays (0-100 ps) and after varying degrees of photoexcitation.

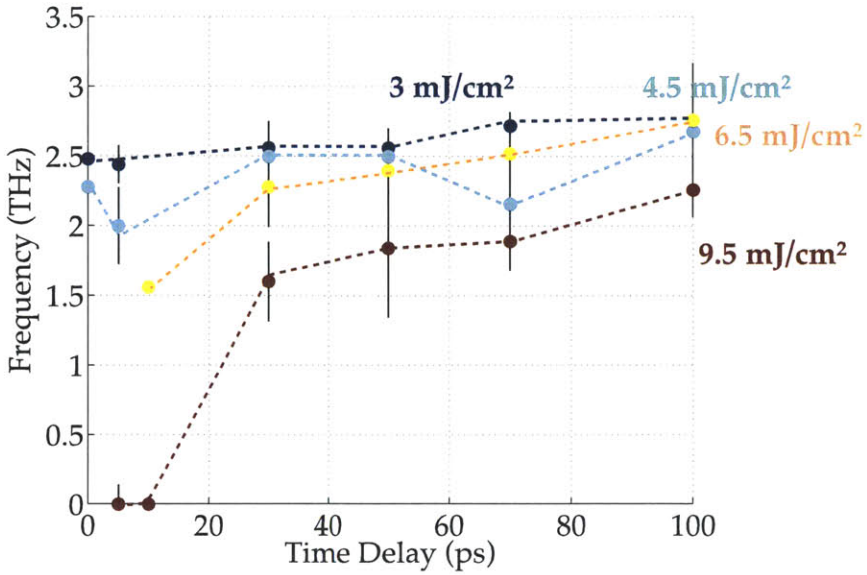

Figure 5-31: Phonon frequency extracted from two-pump measurements on 50 nm bismuth at varying time delays (0-100 ps) and after varying degrees of photoexcitation.

From the one-pump measurements, we observed a lower threshold for significant frequency down-shifting and for the plateau of electronic signal for the thinner sample. Figure 5-32 compares the frequency value measured as a function of time delay for the two samples upon similar incident fluence excitation. Being partially transparent, the thinner sample is likely to absorb a smaller fraction of incident light than the thicker sample. Still, the 50 nm film exhibits a more dramatic response and recovers more slowly, while the 300 nm film response to a similar incidence fluence nearly returns to the ground state frequency in under 20 ps.

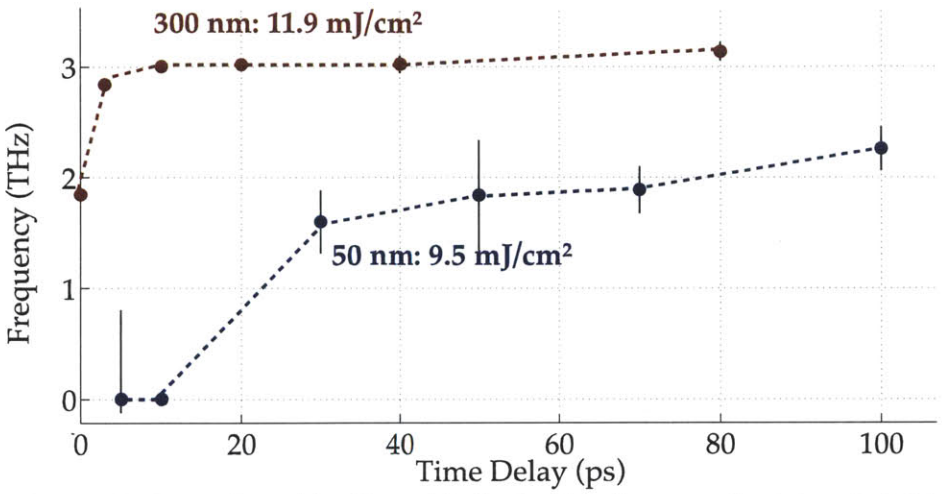

Figure 5-32: Comparison of the effects of similar incident fluence on the photoexcited state lattice response in 300 nm and 50 nm bismuth films. The thinner film exhibits a more dramatic frequency reduction, and recovers more slowly, than does the thicker film for comparable incident pulse fluences.

For both samples, the highest fluence employed for two-pump measurements was chosen to be above the threshold that led to the disappearance of phonon oscillations following one-pump excitation (Figure 5-9 and Figure 5-14). Figure 5-33 shows the evolution of lattice frequency upon excitation above this threshold for each sample. Fewer time points were obtained for the 50 nm sample, so the frequency recovery time cannot be determined precisely. However, it is apparent that the 300 nm film frequency response begins recovering from its lowest measured value in under 10 ps, while the 50 nm film does not. Notably, the two sample frequencies converge to nearly the same value at 100 ps. Furthermore, by comparison to the long-time reflectivity response (inset for both samples at the indicated fluence in Figure 5-33), we see that the 300 nm lattice frequency appears to recover on roughly the same timescale as does the reflectivity response, although not to the ground state frequency. In contrast, the 50 nm lattice frequency appears to recover on a longer timescale than the initial electronic relaxation.

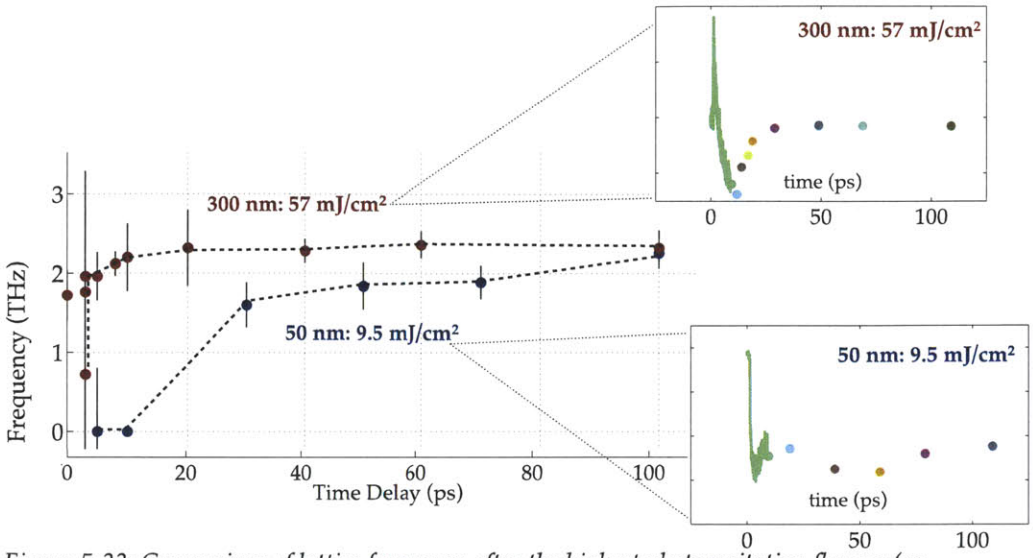

Figure 5-33: Comparison of lattice frequency after the highest photoexcitation fluence (as determined by the disappearance of phonon oscillations in one-pump measurements). The initial 300 nm film lattice recovery time appears to be less then 20 ps, while that of the 50 nm film appears to be ~20 ps. The long-time reflectivity responses are inset for each sample-fluence pair for comparison of timescales.

5.3 Modeling of Nonequilibrium and Equilibrium Dynamics

We seek to evaluate our measurements in the context of photoinduced structural change to determine the mechanisms at work. Some theoretical efforts have predicted a symmetric state that can only be reached nonthermally.[40,159,183] Meanwhile, other works have illustrated the ongoing interplay between thermal and nonthermal processes in semimetals and other materials, highlighting their complexity.[62,68,184-186] Questions regarding the potential in controlling material dynamics on the ultrafast timescale remain open. As presented in this chapter, we have measured electronic and lattice dynamics under intense photoexcitation far from equilibrium, under conditions theoretically sufficient to induce structural change with a laser pulse. Further, we have observed strong indications of structural change via two-pump measurements, and observed alternative dynamics following this apparent change when the system is in two versus three dimensions. Finally, our measurements suggest specific timescales and responses that are due to dimensionality of the electron-phonon coupled system, which may improve our understanding of the processes at work on a fundamental level.

5.3.1 Carrier Population Estimates

To proceed in placing our measurements in the context of prior work by Murray, et al[159] and Fritz, et al,[40] we estimate the photoinduced carrier density.

Assuming linear absorption, the density of promoted carriers in the excited region at $t = 0$, n_l, may be calculated as the ratio of absorbed photons to the number of valence electrons in the photoexcited area:

$$n_l = \frac{(1-R)F}{\delta E_p} \frac{a^3}{10\,v.e.} \qquad \textit{Eq. 5-3}$$

where a is the bismuth unit cell length (0.453 nm), a reflectivity of 70% at 800 nm is assumed, and we consider 5 valence electrons per bismuth atom (10 per unit cell). Below, n_l is multiplied by 100 to be expressed as a percentage in keeping with the standard convention. For an excitation fluence of 1.15 mJ/cm^2, which we use as a point of comparison to other estimates below, n_l is calculated to be 0.87%.

It is also instructive to relate the measured phonon frequency to the theoretically predicted corresponding carrier density presented by Murray, et al.[159] We employ the calculated relationship between frequency and carrier density. In that work, the phonon frequency was calculated as a function of carrier density via frozen phonon calculations. In a later work, the same authors presented x-ray diffraction measurements that verified the validity of these calculations up to a carrier density of ~1.3%.[40] In those measurements, frequency was measured alongside the inter-nuclear distance (via simultaneous measurements of optical coherent phonon detection and x-ray diffraction efficiency), and the inter-nuclear distance was related to carrier density by DFT calculations (Figure 5-3, left). Indirectly, a relation between phonon frequency and carrier density was also established (Figure 5-3, right), which confirmed the prediction of a harmonic frequency up to a carrier density of 1.3%. Higher carrier densities could not be induced due to laser-induced damage at the surface.

Using the calculation from Murray, et al[159] shown in Figure 5-2, we extract an estimated carrier density for each measurement via spline interpolation from the phonon frequency measured. Figure 5-34 shows the result of interpolating carrier density values from the measured frequencies in 300 nm one-pump measurements (*i.e.*, the frequencies displayed in Figure 5-13). The highest fluence measurement for which a

phonon frequency could be extracted (top curve in Figure 5-9) is estimated to reflect a carrier density of 2.24% (via a measured frequency of 1.8 THz, obtained from 48.6 mJ/cm^2 photoexcitation). The point representing the theoretically predicted symmetric state is also shown, corresponding to 3% carrier density. Measurements conducted at 57 mJ/cm^2 excitation did not yield resolvable lattice oscillations; however, the induced carrier density at this fluence is assumed to be larger than 2.24%.

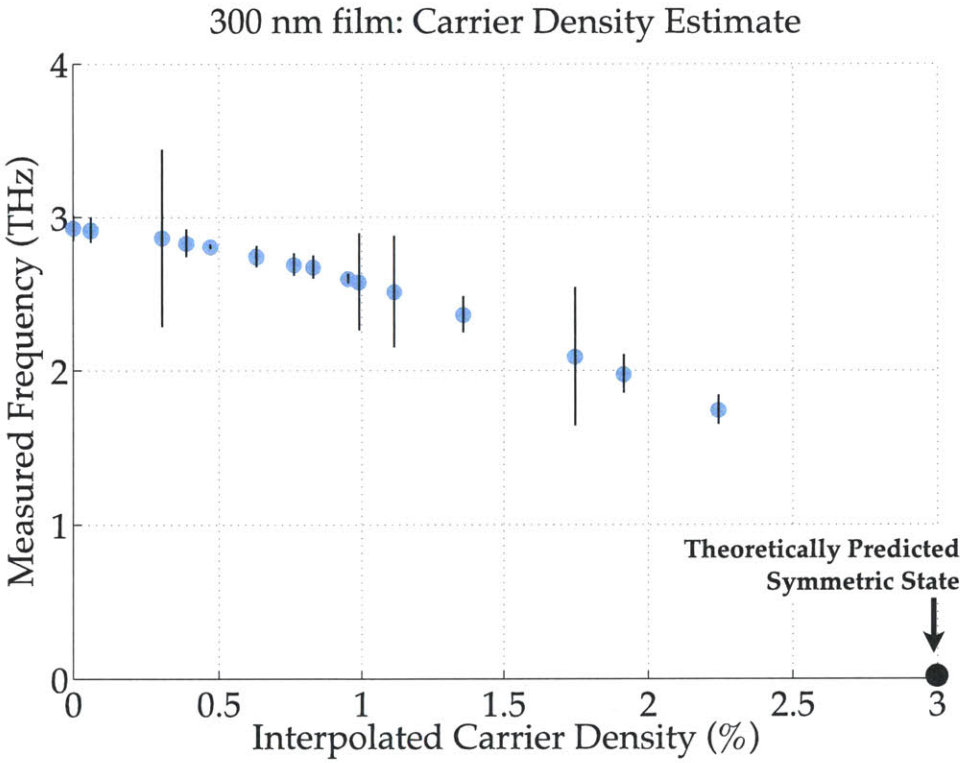

Figure 5-34: Carrier densities are interpolated based on the frequency of each measurement. The dashed curved line is the calculated frequency as a function of carrier density from Figure 5-2. Horizontal lines among the low-frequency data connect the two resulting estimates from one single-shot measurement.

At a low fluence for which measurements were taken, 1.15 mJ/cm^2, interpolation yields an estimated carrier density of 0.06%, significantly lower than the estimate from linear absorption. Calculation of the carrier density n_l based on the number of absorbed photons and linear absorption yielded 0.87% for a fluence of 1.15 mJ/cm^2 as described above, an order of magnitude larger than the interpolated value. We propose that an initial high density of carriers created by absorption of photons in an ultrafast pulse is drastically reduced on the femtosecond timescale by fast transport (diffusive or

otherwise). Transport dynamics may vary drastically based on the sample geometry and the carrier density. Given an electron mean free path of 250 nm and electron-electron scattering times of 100 fs in bismuth,[187] it is reasonable to expect a substantial transport effect out of the sample penetration depth within the first 500 fs of our measurement post-pulse. Such an effect could account for the drastic reduction in carrier density from e.g. 0.28% to 0.06% within the first 0.5 – 1 ps of the measurement, the time at which coherent phonon oscillations are observed. This effect is explored more fully below in the context of modifications to the two-temperature model for electron-phonon coupled heat transfer.

5.3.2 The Two-temperature Model

The two-temperature model has been frequently used to describe the transfer of energy from a heat source to the electrons and interatomic bonds of metallic materials. It has been especially useful for visualizing energy transfer in ultrafast experiments where the heat source is a laser pulse and where a femtosecond time resolution is of interest, despite its inability to correctly characterize nonequilibrium populations. Because the lattice heat capacity is typically two orders of magnitude larger than the electronic heat capacity in metals, electrons are assumed to thermalize significantly faster (femtoseconds) than the lattice (picoseconds).[188] The expressions in this and the following sections are derived from the fundamental relation:

$$\frac{\partial Q}{\partial t} = \frac{\partial}{\partial t}(nCT) \qquad \textit{Eq. 5-4}$$

In the simplest two-temperature model, the electron temperature $T_e(t,z)$ is described in one dimension by the partial differential equation:

$$C_e n_e(t,z)\frac{\partial T_e(t,z)}{\partial t} = C_e D_e \nabla_z n_e(t,z) \nabla_z T_e(t,z) - g[T_e(t,z) - T_l(t,z)] \qquad \textit{Eq. 5-5}$$

The first term on the right-hand side of Eq. 5-5 is a result of Fick's first law for an electric current $j = -D_e \frac{\partial n_e}{\partial z}$ and the diffusion equation $\frac{\partial n}{\partial t} = D_e \nabla^2 n_e$. In these expressions, n_e is the density of valence electrons promoted to the conduction band, and D_e is the electronic diffusivity. The resulting term is a heat source for the electron temperature, dictated by the population of photoexcited carriers present in space and time. The second term on the right-hand side governs energy transfer between the lattice and

electron populations, and is present in Eq. 5-5 as a heat sink for the electronic temperature. Here, the heat capacity per electron C_e has been treated as constant with respect to temperature to be $2.07 \times 10^{-23} J/K$.

Because in our measurements the laser spot size (~500 μm) is several orders of magnitude larger than the laser pulse penetration depth (~15 nm at 800 nm wavelength), the temperature and population gradients into the depth of the sample are of primary importance, rendering the one-dimensional approximation indicated in Eq. 5-5 adequate. For the same reason, photoexcited electrons are expected to diffuse out of the probed area into the sample depth. Treating the dependence of photoexcited carrier density in time and space with the diffusion relation, we obtain:

$$\frac{\partial n_e}{\partial t} = D_e \nabla^2 n_e \qquad \textit{Eq. 5-6}$$

The lattice temperature is described using the conventional heat equation $\frac{\partial u}{\partial t} = \alpha \nabla^2 u$ and includes the electronic heat sink term from Eq. 5-5 as a heat source:

$$C_l \frac{\partial T_l}{\partial t} = \kappa_l \nabla^2 T_l + g(T_e - T_l) \qquad \textit{Eq. 5-7}$$

where C_l is the material's volumetric heat capacity ($1.18 \times 10^{-21} J/K nm^3$). κ_l is the material-specific thermal conductivity equal to $C_l D_l$, with D_l as the lattice diffusivity ($6.7\,\mathrm{nm}^2/\mathrm{ps}$). Dependencies of T_e, T_l, and n_e on z and t are henceforth implied. The coupled differential relations in Eq. 5-5, Eq. 5-6, and Eq. 5-7 can be solved to yield space- and time-dependent pictures of electronic temperature, excited electron density, and lattice temperatures. Boundary conditions are set such that the electron density at equilibrium n_g is 0.001%, the measured value in the ground state.[189] All temperatures calculated are temperature differences in Kelvin relative to 293 K, corresponding to our room temperature measurements. The initial condition for the lattice temperature is $\Delta T = 0$.

We refer to the creation of an excited carrier population as instantaneous, though in reality it occurs over pulse duration. The initial condition for electron density n_e is therefore given by the spatial profile of the absorbed laser pulse assuming linear absorption. For these calculations, the initial time (t=0) is formally after pump absorption, both because we do not have expressions to describe the creation of the

electron population in time, and because our measurement is not capable of distinguishing variation on the 100 fs timescale. Since the laser pulse penetrates into the material with an exponential profile determined by the penetration depth δ (15 nm for bismuth at 800 nm laser wavelength), the initial distribution is given in space by:

$$n(z) = n_l e^{-z/\delta} + n_g \qquad \textit{Eq. 5-8}$$

Electron heating also takes place on the sub-picosecond timescale; therefore, we set the initial condition for electron temperature to be the maximum calculated temperature following pump absorption. In interpreting this parameter, it is acknowledged that the electron temperature is undefined at the earliest times, so the calculated initial condition for change in electron temperature T_e, as well as its earliest-time evolution, should not be interpreted strictly physically. As carriers are promoted into the conduction band with excess kinetic energy, the change in electron temperature T_e may be regarded as the maximum available energy contained within the excited electron population when multiplied by C_e. We expect this energy to be transferred out of the population through various pathways, only one of which is thermal. Still, capturing the available electronic energy in one term is convenient, and likely to be well-defined ~1 ps into the measurement. The maximum change in electron temperature T_e (relative to room temperature) is given by:

$$T_e|_{t=0} = \frac{E_p - E_{gap}}{E_p} \frac{F(1-R)}{\delta C_e^v} \qquad \textit{Eq. 5-9}$$

where C_e^v is volumetric electron heat capacity, E_p is the photon energy (1.55 eV), E_{gap} is the narrowest bismuth band gap in k-space (0.2 eV), F is the incident fluence, and R the reflectivity (0.7). The initial electron temperature distribution in space relative to room temperature is given by:

$$T_e(z) = T_e|_{t=0}(e^{-z/\delta}) \qquad \textit{Eq. 5-10}$$

Figure 5-35 shows an example solution to the above differential equations and conditions, solved for the case of a 300-nm bismuth film. The film thickness provides the z value at which far-edge boundary conditions are enforced.

The electron density is calculated to rapidly decrease as a function of space and time. The calculated electron temperature change increases appreciably through the

first 100 nm of the material from a maximum of 10^4 K above room temperature, and is seen to decrease appreciably after about 25 ps, with a finite temperature change above 293 K 100 ps post-pulse. The lattice temperature change also extends significantly into the first 100 nm of material, and the lattice temperature change at ~100 ps post-pulse is 600 K.

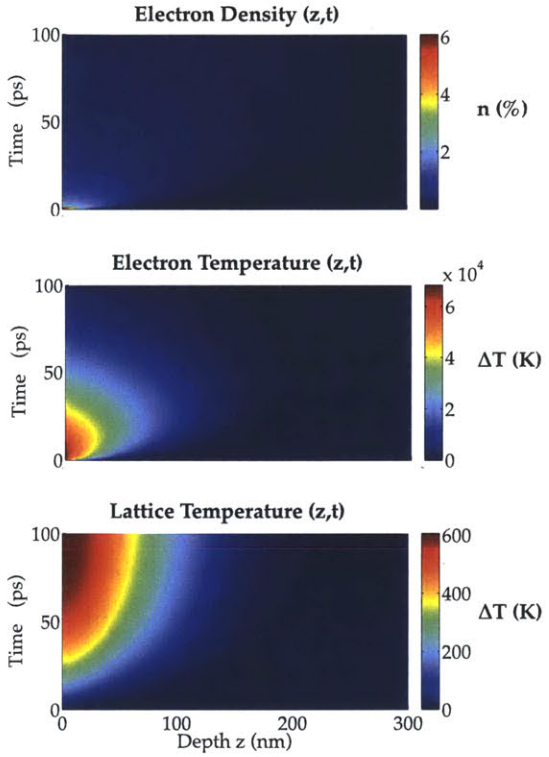

Figure 5-35: The solutions to coupled differential equations of the two-temperature model with diffusion and electron-phonon coupling for the first 100 picoseconds (y-axis) in a 300 nm (x-axis) bismuth film under 8 mJ/cm² excitation. Initial electron density is given by the laser source with temporal and spatial profiles determined experimentally. The color indicates the value of the relevant property as a function of time and depth: electron density (top), electron temperature (middle), and lattice temperature (bottom).

Four primary results are suggested by this calculation. First, the electron temperature peaks near 5 ps, indicating the point at which significant energy is transferred from the electron population to the lattice. Second, the photoinduced instantaneous carrier density exceeds 6% at 8 mJ/cm² photoexcitation, far greater than the 3% figure theoretically predicted to correspond to the symmetric state. This high density is transient, remaining above 3% for only 1-2 ps under these calculation

conditions. Third, the temperature of the lattice nearly reaches the bismuth melting temperature of 543 K ($\Delta T = 250K$) after 100 ps. The latent heat of melting for bismuth is $5.3 \times 10^{-19} J/nm^3$, which corresponds to an effective decrease of 440 K to the lattice temperature reached relative to the calculated temperature change. Thus, a *calculated* lattice temperature change of $\Delta T_e = 690K$ (543 + 440 - 298) would indicate conditions necessary for a melted lattice at the material surface. The calculation was repeated for increasing incident fluence, and it was determined that the melting threshold is ~9 mJ/cm^2, resulting in a calculated temperature change of 740 K. Fourth, the lattice temperature remains very high through at least 200 ps post-pulse, as shown in Figure 5-36. Under these conditions, the lattice was calculated to return to room temperature over 20 nanoseconds post-pulse by solving the differential equations for extended times.

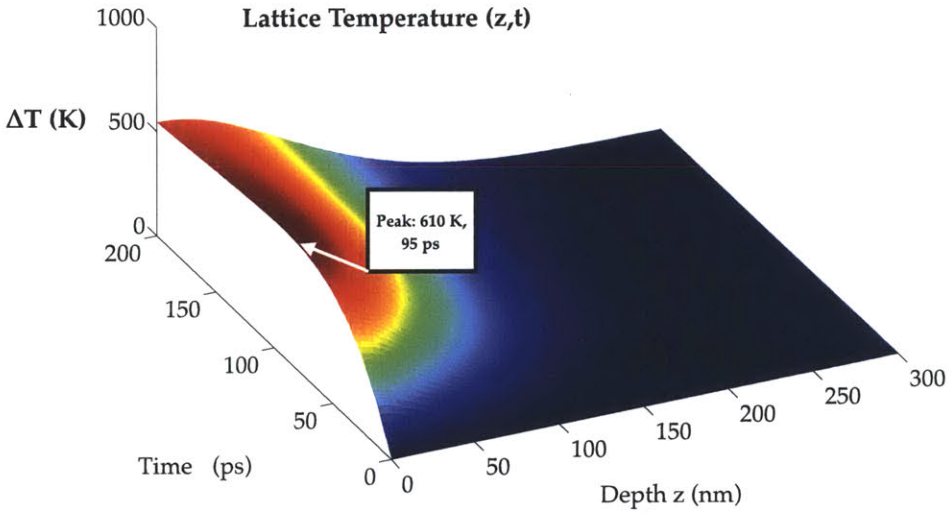

Figure 5-36: The solution to the simple two temperature model for the lattice temperature in a 300 nm bismuth film under 8 mJ/cm^2 excitation is shown out to 200 ps. The solution calculates an extended heating time that is not consistent with our experimental data.

We compare the result of this calculation to the measured dynamics of a 300 nm bismuth photoexcited with a 7.9 mJ/cm^2 pump pulse. Referring to the results of two-pump measurements for 300 nm (Figure 5-28), we note that the lattice remains intact (with observable phonon oscillations) for all time delays following excitations far exceeding 9 mJ/cm^2. (Frequencies became ill-defined or are reported with large errors above 40 mJ/cm^2). Figure 5-37 shows the composite time trace measured following 7.9

mJ/cm^2 photoexcitation (bottom: log scale). We observe minimum change, up to the highest measured time delay of 800 ps, after the measured reflectivity recovers close to the pre-pump level 50-100 ps post-pump. Recalling that the induced change in reflectivity is the sum of contributions from electron density, lattice motion, and lattice temperature, we also note that of these, lattice temperature is expected to evolve along the slowest timescale, as it is governed by thermal diffusion. Therefore, the calculations shown in Figure 5-35 appear to overestimate both the temperature reached and the onset time of lattice cooling.

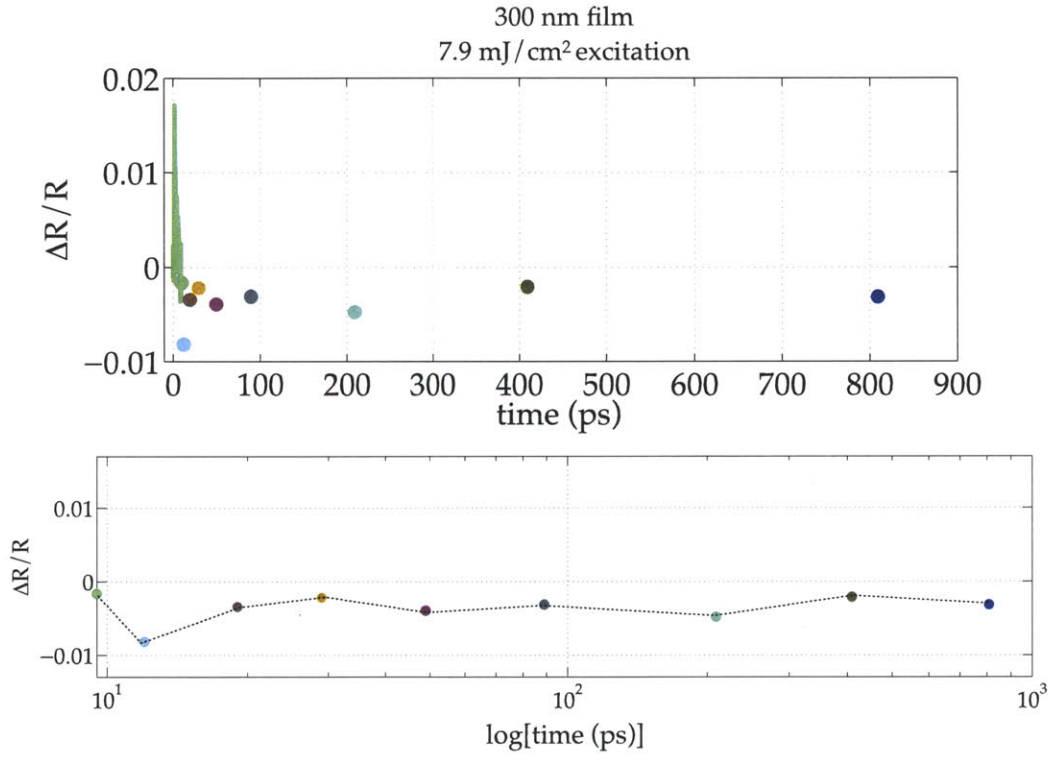

Figure 5-37: Composite long-time traces of 300 nm film under 7.9 mJ/cm^2 excitation suggest that the calculation shown in Figure 5-36 overestimates the lattice heating time. Near full recovery is observed by 100 ps, with very slowly varying reflecitivity modulation past 100 ps.

Our measurements of background reflectivity changing in time reflect the dynamics of carrier density, electron, and lattice temperature throughout the depth of the sample. The physical depth of the sample is expected to matter for heat diffusion, and possibly carrier transport, but our measurement with the probe laser pulse only monitors the evolving dynamics in the first several nanometers. To account for this, we examine time-dependent traces of electron density and temperatures that are integrated

through the sample depth. The calculated surfaces (such as those shown in Figure 5-35) are weighted in the depth dimension by Beer's Law up to the maximum depth reported on by the probe pulse (defined here as the depth at which the pulse intensity fall to 95% of the maximum, or 26 nm). The result for lattice temperature is illustrated in Figure 5-38. Subsequently, displayed traces are the result of integrating the calculated surfaces through the sample depth measured by the optical probe pulse.

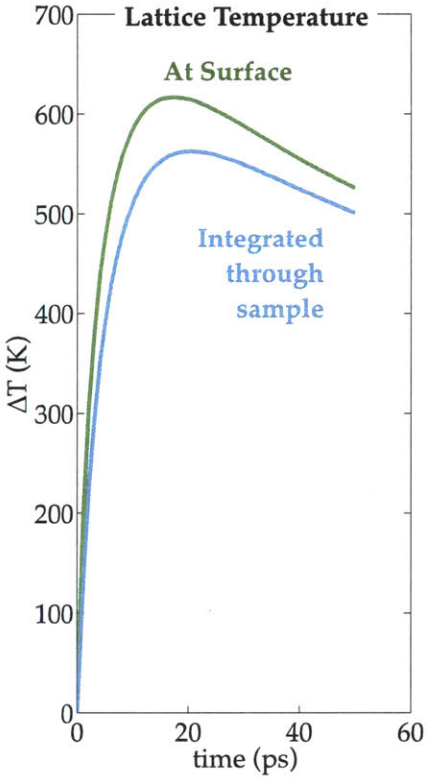

Figure 5-38: Demonstration of integrating calculated surfaces for lattice temperature into the sample depth to simulate the effect of an optical probe pulse reporting on material dynamics. Here, the difference in reported lattice temperature using the two methods is about 400 K.

5.3.3 Modifications to the two-temperature model

The two-temperature model is a helpful tool to aid understanding of fast-timescale energy transfer in materials, but the simple case described above must be modified to provide accurate insight into increasingly complex dynamical questions. With reference to the solution in Figure 5-35 and other works, we add features to the coupled equations that are of particular relevance to understanding energy transfer in bismuth on femtosecond and picosecond timescales under high-density laser excitation.

Electron-hole Recombination

Carriers recombine through multiple pathways, affecting the temporal electron density and therefore the electron and lattice temperatures. We modify Eq. 5-6 to reflect a loss in carrier population determined by the recombination rate $\kappa_r = 1/\tau_r$.

$$\frac{\partial n_e}{\partial t} = D_e \nabla^2 n_e - \kappa_r (n_e - n_g) \qquad \textit{Eq. 5-11}$$

Recalling Eq. 5-4, we note that the differential expressions for electron and lattice temperatures depend on the time derivative of n_e. The expression for the electron temperature is unchanged from Eq. 5-5 due to canceling terms, while the expression for lattice temperature is modified from Eq. 5-7 to be:

$$C_l \frac{\partial T_l}{\partial t} = \kappa_l \nabla^2 T_l + g(T_e - T_l) + \kappa_r n_e C_e T_e \qquad \textit{Eq. 5-12}$$

The solutions to the modified coupled differential equations for a 300 nm film up to 100 ps post-pulse (8 mJ/cm^2 excitation) are shown in Figure 5-39. Relative to the solutions displayed in Figure 5-35, the calculated maximum lattice temperature change is significantly higher (1450-2450 K for increasing values of τ_r, relative to 600 K for no recombination effect), and the time corresponding to the maximum is shorter (12-35 ps for increasing values of τ_r, relative to 95 ps for no recombination effect). Subsequently, we employ $\tau_r = 26ps$ for the 300 nm film in accordance with recent measurements in bismuth thin films by Sheu, et al.[190] (By rough extrapolation of thickness-dependent measurements in that work, a value of $\tau_r = 10ps$ was used for the 50 nm film).

We see that the introduction of carrier recombination yields a more realistic heating time for the lattice, given our observations that recovery after 50-100 ps is gradual (Figure 5-37). The introduction of a recombination term provides an additional heat source to the lattice, since it dictates that some carrier population will recombine and release thermal energy instead of diffusing out of the measured region.

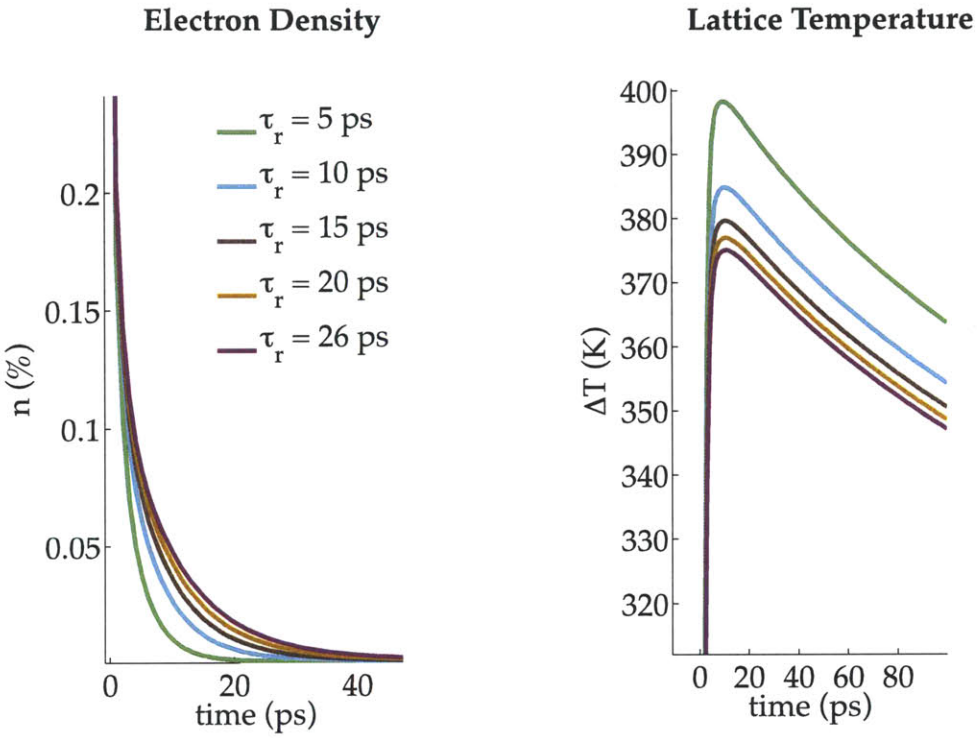

Figure 5-39: Solutions to the coupled differential equations modified to include electron-hole recombination, with multiple recombination times displayed. The input parameters were for a 300 nm bismuth film under 8 mJ/cm^2 excitation.

Electron-phonon coupling: temperature dependence

We introduce into the differential equations an electron temperature-dependent electron-phonon coupling constant $g(T_e)$. It has recently been shown by Arnaud, et al. that the electron-phonon coupling constant, which governs electron cooling to the lattice, increases drastically with the electron temperature (e.g., by four orders of magnitude as T is increased from 100 K to 4000 K).[191] This effect can be ascribed to the increasingly metallic nature of bismuth under high carrier density. Due to nonequilibrium conditions immediately post-pulse, this factor is unnecessary for describing the first ~1 ps of evolution following excitation. However, it is expected to contribute significantly on longer timescales. The calculated relation is shown for $g(T_e)$ in Figure 5-40.

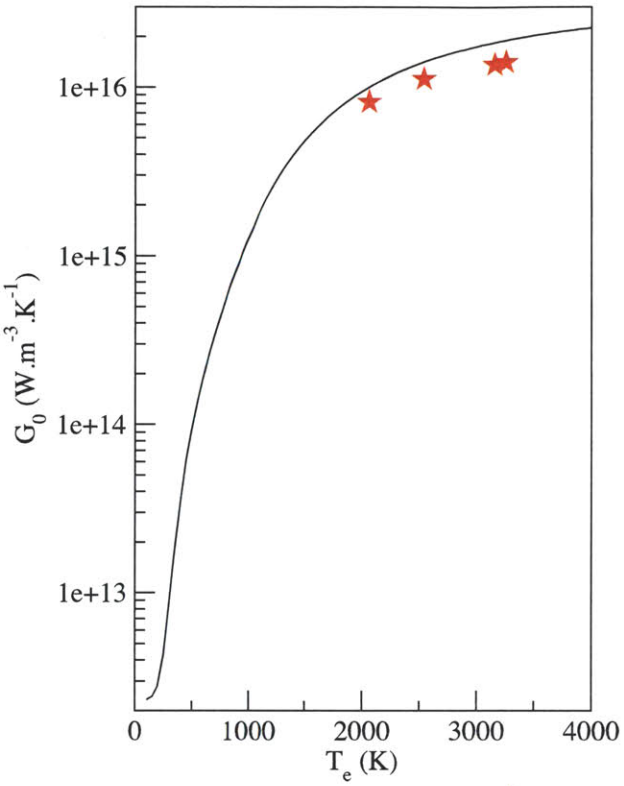

Figure 5-40: Calculated relation from Arnaud, et al.[191] giving the electron-phonon coupling constant as a function of electron temperature. The quantity is predicted to rise significantly with electron temperature. Red markers indicate correspondence to the electron diffraction results that reported sub-picosecond melting in bismuth.[62] The correspondence was established numerically by relating the electron-phonon coupling constant in the calculation to Debye-Waller factors extracted from the diffraction peaks in the experiment.

Figure 5-41 and Figure 5-42 demonstrate the effect of varying the electron-phonon coupling constant on the electronic and lattice temperatures at low and high fluence in the 300 nm film. When values close to room temperature are used, we calculate an unrealistically long lattice heating time at low fluence. Subsequently, the temperature-dependent factor is used.

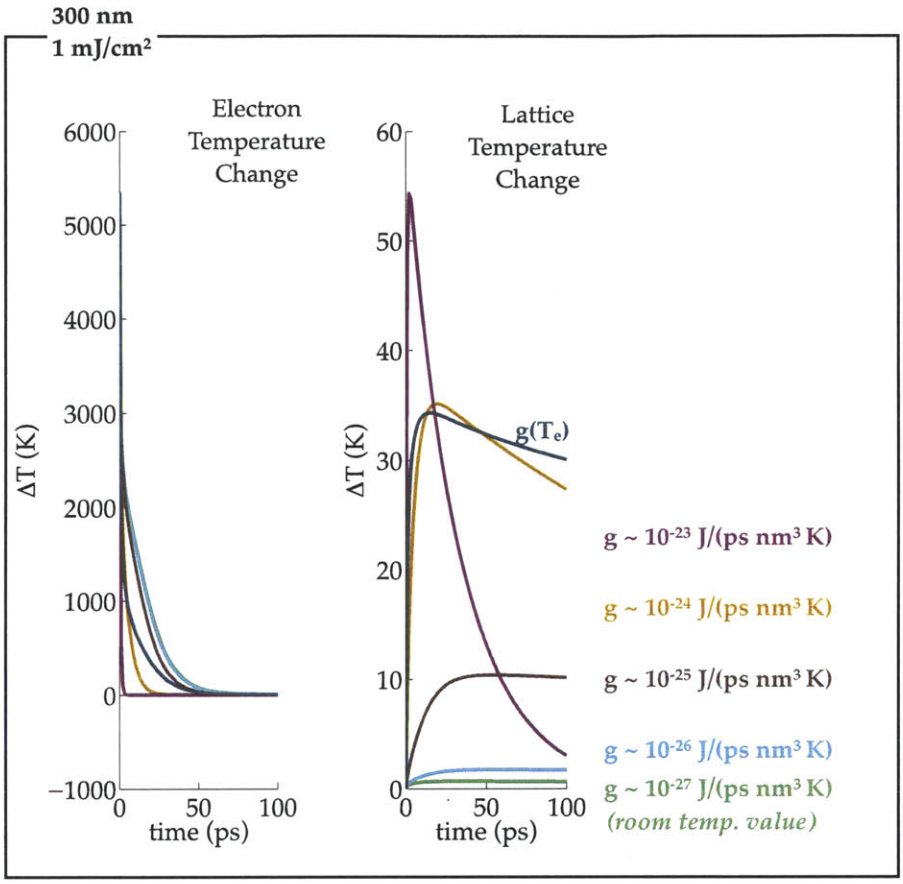

Figure 5-41: Demonstration of the effect of varying the electron phonon coupling constant g in the 300 nm film calculations at low fluence. The lattice heating time, the maximum temperature reached, and the rate of electronic relaxation are all dependent on the order of magnitude of g. In the calculations presented below, we use the temperature-dependent $g(T_e)$ presented by Arnaud, et al.[191] The room temperature value is ~10^{-27} J/(ps nm^3 K) (yielding the green curve).

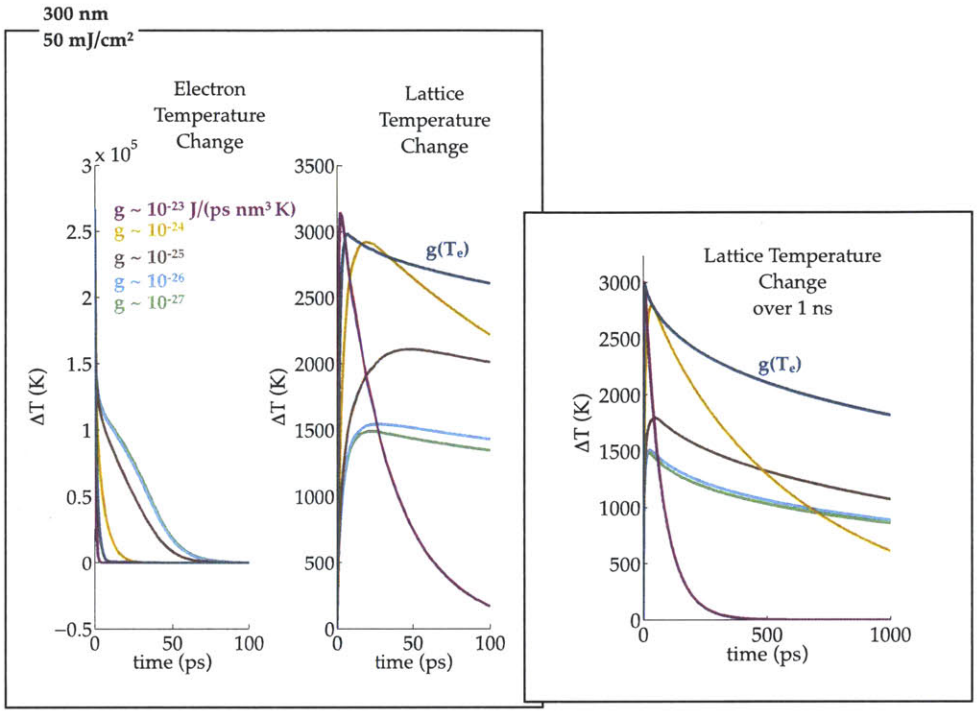

Figure 5-42: Demonstration of the effect of varying the electron phonon coupling constant g in the 300 nm film calculations at high fluence. The lattice heating time, the maximum temperature reached, and the rate of electronic relaxation are all dependent on the order of magnitude of g. In the calculations presented below, we use the temperature-dependent $g(T_e)$ presented by Arnaud, et al.[191] The room temperature value is ~10^{-27} J/(ps nm³ K) (yielding the green curve).

Diffusion and Transport

Recent measurements have reported diffusion constants for bismuth films based on counter-propagating pump-probe measurements.[190] Ambipolar diffusivities ranging from 20-30 cm^2/s in films between 200 and 400 nm thick were measured. For the low fluence measurement (1.15 mJ/cm^2), the two-temperature calculation was performed using the linear absorption estimate from Eq. 5-3. At ~0.5 ps, where phonon oscillations begin in the measured signal, we calculate an electron density of 0.29%, which is significantly higher than the interpolated value of 0.06%. In 5.3.1, it was proposed that the discrepancy between the carrier density calculated via linear absorption and the carrier density estimated by the measured phonon frequency may be due to fast transport out of the photoexcited region at times faster than the electron-phonon coupling time. Figure 5-43 compares, the 50 nm thin film sample, the results from both carrier density estimates across fluence measurements. In green is the interpolated

carrier density, obtained via the frequency observed in a given measurement. In blue is the result at t = 0.5 ps (where we observe phonon signal) of the coupled equations Eq. 5-11, Eq. 5-4, and Eq. 5-12. Carrier density n_l from Eq. 5-3 is used as the initial condition for Eq. 5-8, and the film thickness is employed as a boundary condition in the equation set.

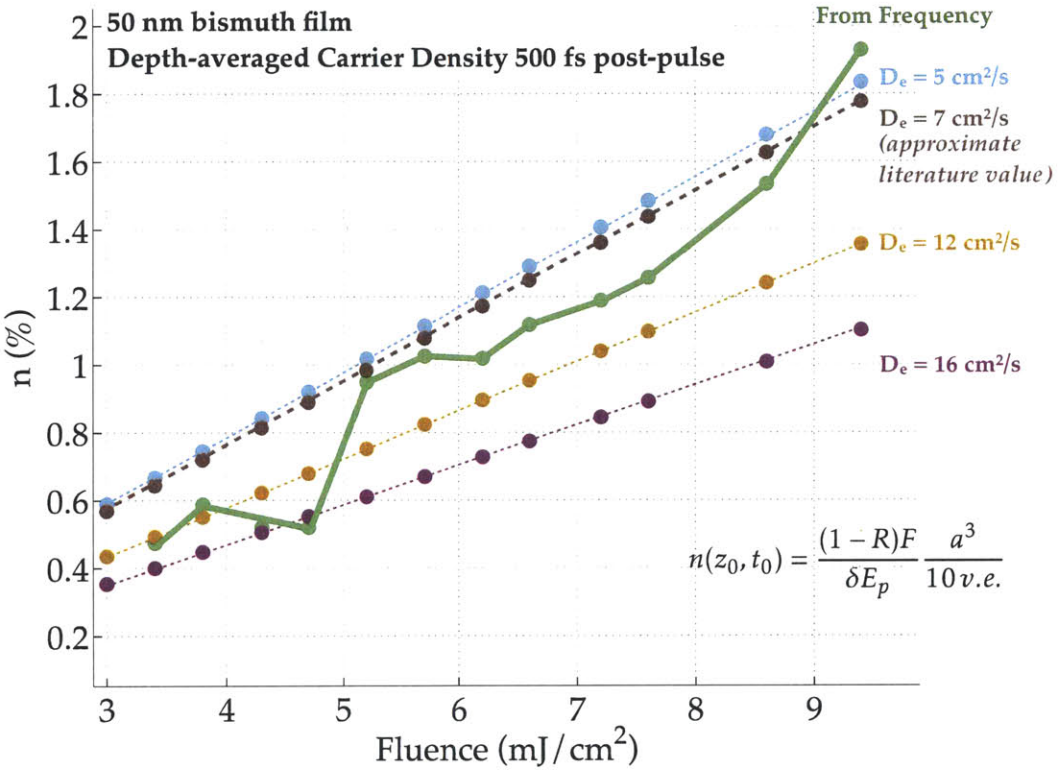

Figure 5-43: The interpolated carrier density from measured frequency (green) in 50 nm film measurements is compared to expected carrier densities resulting from varying carrier diffusivities. A value of ~7-8 cm²/s is expected by extrapolation of the results by Sheu, et al. A diffusitivity of 7 cm²/s is chosen by comparison of its slope with the measured quantity.

The results of several diffusion constants are shown. The slope of fluence versus carrier density for $D_e = 7cm^2/s$ most closely approximates the interpolated carrier density. We observe very close agreement for most of the measured fluence range for the 50 nm film, indicating that linear absorption and a diffusion constant of $D_e = 7cm^2/s$ predict with good accuracy the measured phonon frequency 0.5 ps after photoexcitation. By rough extrapolation of the thickness-dependent measurements of diffusivity by Sheu, et al,[190], the diffusivity value of 7 cm²/s is reasonable.

For the 300 nm film, we begin with the diffusivity value measured for that thickness. This figure, however, significantly overestimates the carrier density at 0.5 ps, as judged by comparison to the measured phonon frequency (Figure 5-44). Increasing the diffusivity value even by an order of magnitude does not closely approximate the interpolated carrier density. A value of more than 200 cm^2/s would be necessary to describe the observed fluence dependence, which is physically unlikely based on literature values. Diffusion is sufficient to describe early-time transport in the 50 nm film, and insufficient to describe early-time transport in the 300 nm film. This suggests that ballistic transport plays a role in determining the early-time electron distribution. The mean free path of electrons in bismuth films is 250 nm,[187] suggesting that ballistic transport is significant in the 300 nm film but not in the 50 nm film, where carriers that transport ballistically out of the region are reflected back by the interface 50 nm away from the surface.

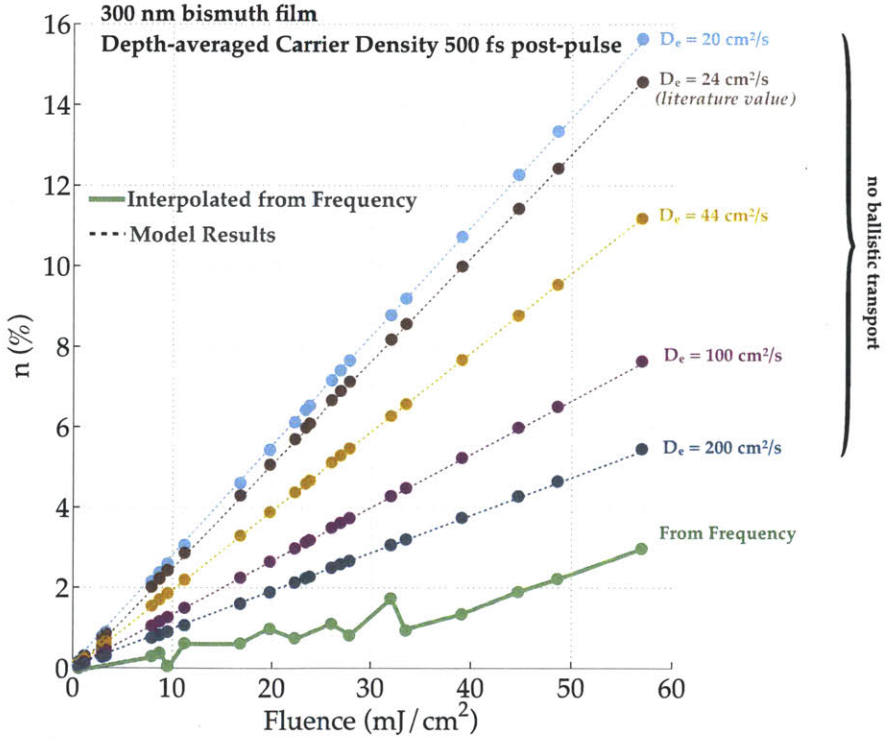

Figure 5-44: The interpolated carrier density from measured frequency (green) in 300 nm film measurements is compared to expected carrier densities resulting from varying carrier diffusivities. Diffusivities up to ten times the literature value fail to describe the measured phonon frequency 500 fs post-pulse, suggesting the contribution of ballistic transport to the carrier density at 500 fs.

To estimate the effect of ballistic transport, we can consider the ballistic and diffusive electronic populations separately, as has been described by Hopkins, et al:[192]

$$\frac{\partial n_e}{\partial t} = \frac{\partial}{\partial t}(n_b + n_d) \qquad \textit{Eq. 5-13}$$

We can approximate the carrier dynamics by requiring that the ballistic system relaxes to the diffusive system on a timescale determined by the electron-electron scattering time:

$$n_d(t) = n_b e^{-t/\tau_{ee}} \qquad \textit{Eq. 5-14}$$

where $\tau_{ee} = 0.1\,\mathrm{ps}$.[187] Eq. 5-14 was employed for different values of t to serve as the initial condition for the thermal model (n_l in Eq. 5-8), such that t in Eq. 5-14 is regarded as t_0 in calculating the solutions. The solution to the electron density was then evaluated at $0.5\ \mathrm{ps} - t$ and compared to the carrier density interpolated from the measured frequency. It was found that employing Eq. 5-14 evaluated at 200 fs as the initial condition predicts the measured frequency very accurately, as demonstrated in Figure 5-45 by comparison with the interpolated carrier density.

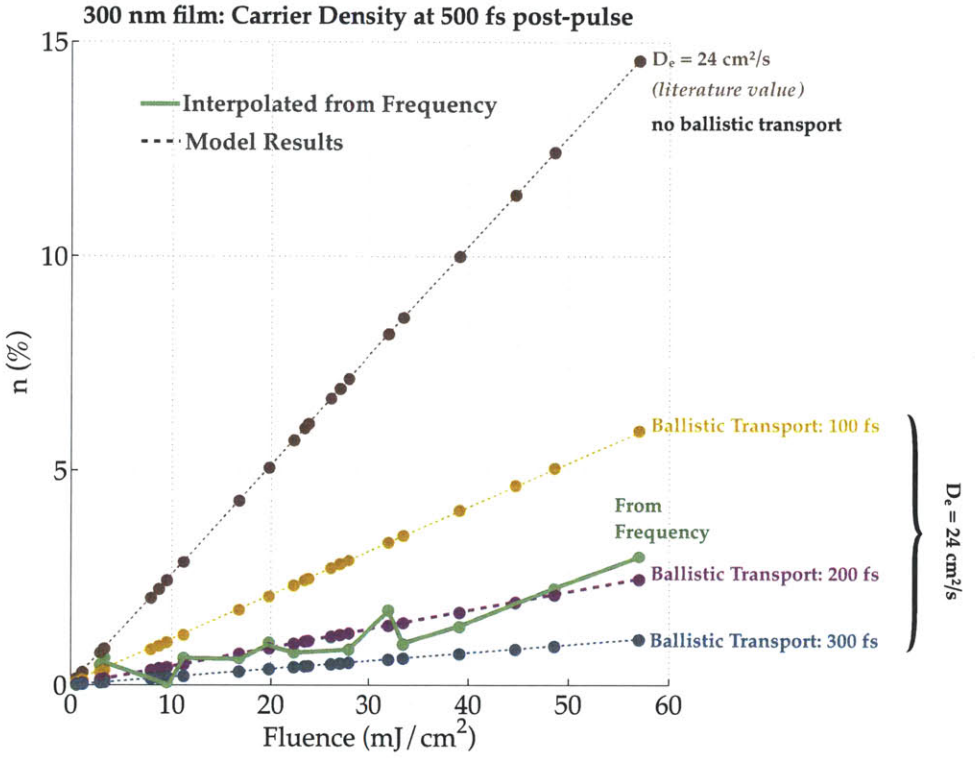

Figure 5-45: The interpolated carrier density from measured frequency (green) in 300 nm film measurements is compared to expected carrier densities resulting from sub-picosecond ballistic transport. The ballistic population is allowed to propagate for 100, 200, and 300 fs before diffusion is onset. The result with no ballistic transport and a diffusivity value of 24 cm/² is also shown.

Calculation Results

Figure 5-46, Figure 5-47, and Figure 5-48 show the calculated solutions to the model described above for the 300 nm and 50 nm bismuth film. In both cases, electron-hole recombination was included (with a characteristic recombination time of 26 ps for the 300 nm film and 10 ps for the 50 nm film). The electron temperature dependent electron-phonon coupling factor was used (Figure 5-40). For the 50 nm film, a percent absorption of 25% was used to determine the initial carrier density, and a diffusion constant of 7 cm^2/s (700 nm^2/ps) was used to describe transport. For the 300 nm film, a percent absorption of 25% was also used to determine pre-ballistic carrier density, and a ballistic electron population propagating for 200 fs on the electron-electron scattering time of 100 fs was used to generate the initial diffusive carrier population. Subsequently, a diffusion constant of 24 cm^2/s (2400 nm^2/ps) was used for calculations

on that sample. Electronic and lattice heat capacities, as well as diffusivities, were assumed to be independent of temperature.

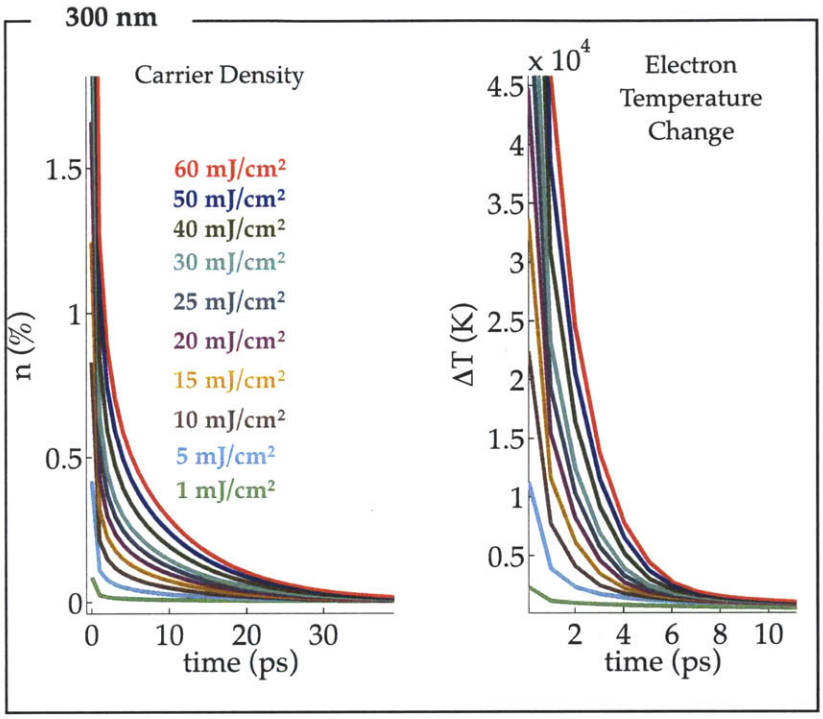

Figure 5-46: The solutions to the coupled differential equations for a 300 nm bismuth film under varying degrees of excitation, with all modifications proposed in this section, for carrier density (left), and electron temperature change (right).

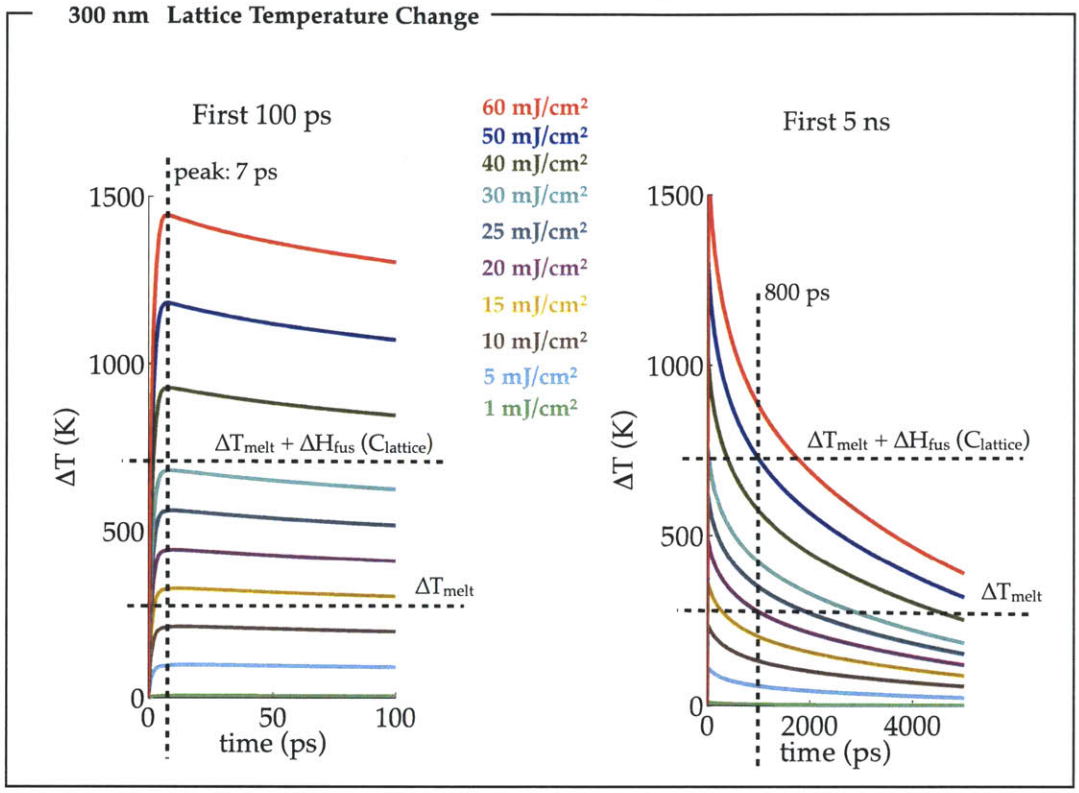

Figure 5-47: The lattice temperature solution to the coupled differential equations for a 300 nm bismuth film under varying degrees of excitation, with all modifications proposed in this section. Left: first 100 ps of evolution. Right: first 5 ns of evolution.

For the 300 nm film, we observe decay in the carrier density that is determined chiefly by the electron-hole recombination time. There is also a short-time component that reflects diffusion out of the region before any recombination, discussed in the next section (Figure 5-49). This is distinct from ballistic transport, which yields the initial carrier density shown in Figure 5-46. The electron temperature decays on a faster timescale (sub-10 ps), which is governed by the temperature-dependent electron-phonon coupling constant. As shown in Figure 5-47, we calculate that the lattice temperature reaches the melting point for all fluences above ~10 mJ/cm^2, and fluences above 30 mJ/cm^2 are sufficient to provide the enthalpy of melting. At these high calculated temperatures, the lattice is predicted to take many nanoseconds to recrystallize. Our measurements extend to 0.8 ns. In our measurements, fluences between 15 and 30 mJ/cm^2 are calculated to be high enough to induce melting, but low enough to yield a recrystallized structure within the 800 ps time span. However, at all

fluence levels, we observe the recovery of lattice oscillations in well under 10 ps, indicating that the lattice does not melt at any fluence. As discussed below, the modeling in the three-dimensional environment is likely to overestimate the lattice temperature reached, due to an incomplete treatment of ballistic transport in the material.

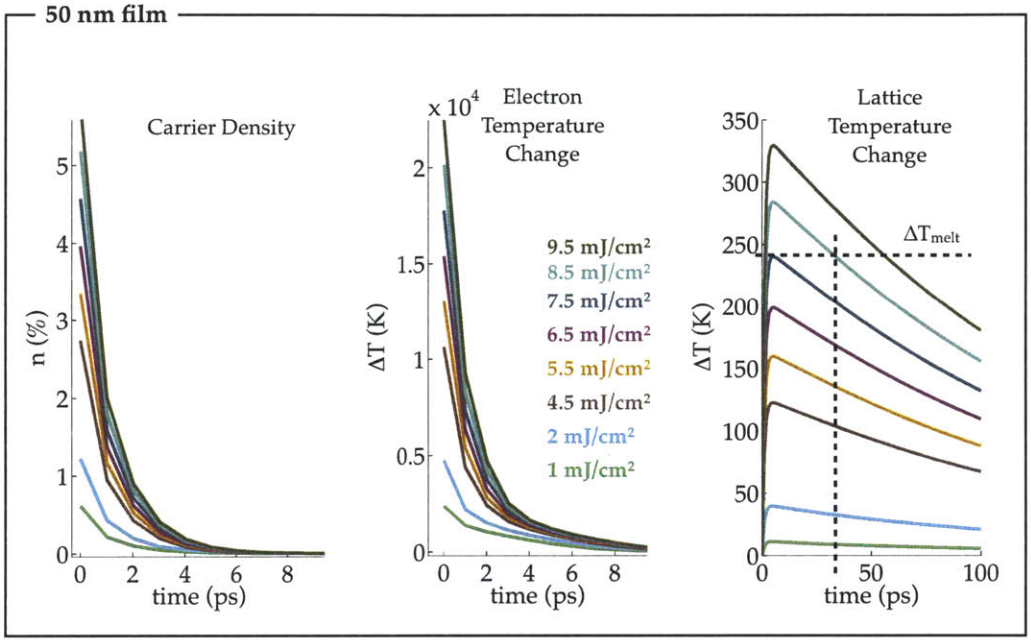

Figure 5-48: The solutions to the coupled differential equations for a 50 nm bismuth film under varying degrees of excitation, with all modifications proposed in this section, for carrier density (left), electron temperature change (middle), and lattice temperature change (right).

For the 50 nm film, we observe carrier density relaxation over the 10 ps recombination time that was input, and electron temperature decay over a similar timescale. The lattice melting temperature is calculated to be achieved under fluences exceeding ~7.5 mJ/cm^2. Because of the input energy required for the phase transition, the higher fluences employed in this measurement (up to 9.5 mJ/cm^2) are assumed to heat the lattice only to the melting temperature (245 K on the ΔT above room temperature scale shown in Figure 5-48). For a lattice heating to slightly above the melting temperature, the model predicts cooling below the melting temperature on the timescale of 30 ps.

5.4 Discussion: Relating Measurements and Modeling

Carrier absorption and sub-picosecond transport

One-pump measurements on bismuth samples of varying thickness across increasing excitation fluence led to observation of distinctly different temporal behavior, as well as observation of similar electron-lattice coupling dynamics. In the instantaneous response, we observed that the thinnest sample (50 nm film) scales super-linearly with fluence over most of the excitation region employed, while the thicker sample response and the bulk decrease with fluence. The bulk sample responses decreases continuously, while the 300 nm sample response decreases and plateaus above 10 mJ/cm^2. We conclude that the strong positively scaling response in the 50 nm sample is due to hot carrier absorption. Initially excited carriers are constrained to the probed region during the pulse duration and afterwards by the lack of a depth dimension, and absorb additional pulse energy. The percent reflectivity of bismuth was confirmed to change by less than 1% over a large fluence range (5-50 mJ/cm^2), over multiple samples. We therefore ascribe the changes in instantaneous response to the material response itself rather than a change in the number of photons absorbed, except for the highest fluence case in bulk bismuth, where we approximate that created carriers leave the region without constraint on any timescale. This interpretation is confirmed by the comparison with 300 nm and the bulk. Both instantaneous responses decrease with fluence. We interpret the threshold in the 300 nm sample, where the response stops decreasing with fluence, to be indicative of valence carrier saturation, leading to hot carrier absorption. In this sample, carriers are also constrained, but in a less dramatic fashion than in the 50 nm sample. The bulk sample exhibits continuously decreasing absorption with fluence, indicating no constraints to the hot carriers within this interpretation.

By comparing the result of calculations 500 fs post-pulse with the interpolated carrier density based on frequency measurements, we have shown that diffusion is sufficient to describe sub-picosecond carrier transport in the 50 nm film, yet insufficient to describe sub-picosecond carrier transport in the 300 nm film. We ascribe this difference to ballistic transport in the 300 nm film, which enables a rapid decrease of carriers in the probed region on the electron-electron scattering timescale of 100 fs. The

length scale for ballistic transport is estimated from mean free path literature values to be 250 nm, which supports the conclusion that ballistic transport is precluded in the 50 nm case.

Picosecond relaxation processes

Post-pulse, the sample response can be fit to a biexponential with a <10 picosecond time component and a >10 ps time component. In the 300 nm sample, the <10 ps time component decreases when scaled by fluence, while it increases in the 50 nm and bulk samples. This is consistent with the observed pattern of instantaneous response, and we conclude that the amplitude of the short-time relaxation response is dominated in large part by the same factor as the instantaneous responses, i.e., carrier absorption. Because diffusion out of the region is a gradient-dependent process, it is reasonable to expect the diffusion response to correlate with the size of the carrier population. Lattice heating and electron cooling are also calculated occur on the sub-picosecond timescale. Because exponential temporal decay patterns could not be distinguished among our data above the noise, we cannot determine which of these effects might be primarily responsible based on the modeling. Additionally, no mechanism to describe additional absorption by pulse-created carriers is present in our model. Figure 5-49 shows the fluence-scaled calculated carrier density short-time decay component for both film samples. In both cases, the short-time component exhibits a decay time of ~0.5 ps for both samples. (A second calculated decay time corresponded directly to the input electron-hole recombination time of 26 ps for the 300 nm film, and 10 ps for the 50 nm film). We observe a significant increase of the scaled amplitude in the 50 nm case relative to the 300 nm case. This suggests that initial relaxation in the carrier population may indeed be responsible for the observed difference in the measured amplitudes, also shown in Figure 5-49.

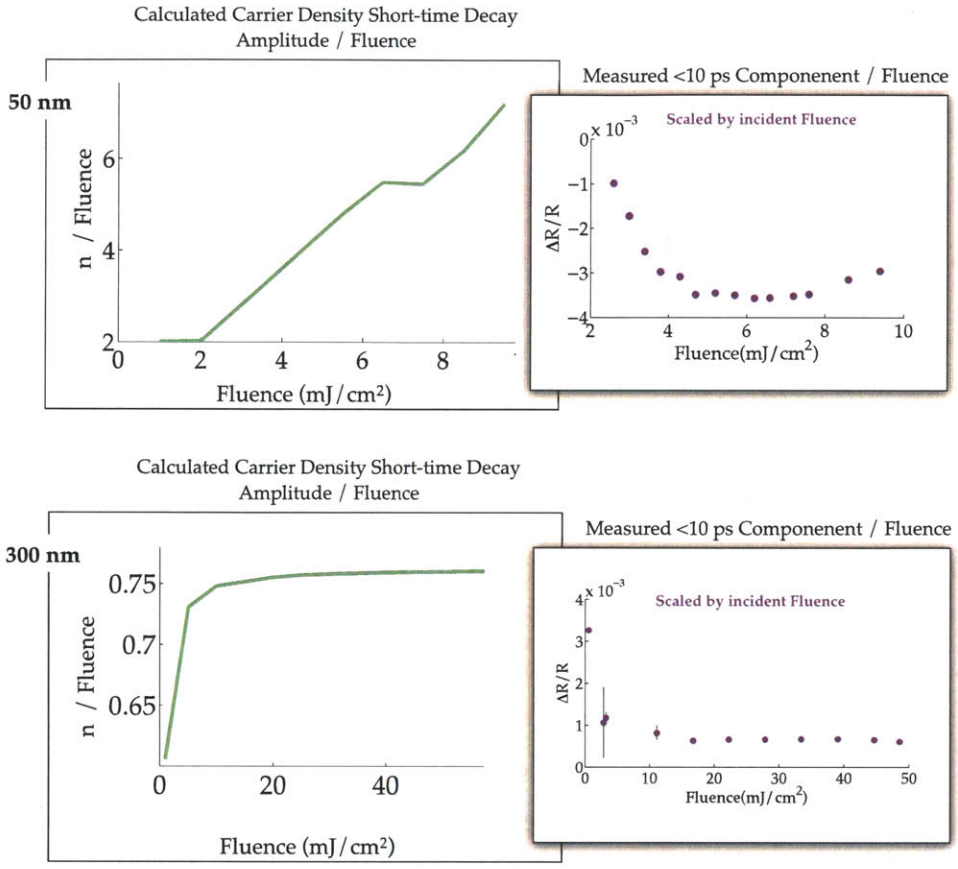

Figure 5-49: Left: Calculated short-time decay component amplitude (corresponding to <10 ps) of the carrier density for the 50 nm film (top) and the 300 nm film (bottom). Right: The measured short-time decay component amplitude of the reflectivity for both samples. The displayed calculated quantity may be a dominant contributor to the measured quantity.

In all samples, the longer time (>10 ps) component increases when scaled by fluence, and plateaus in the thin film cases. We suggest that one primary contributor to this component amplitude is the extent of lattice heating. Figure 5-50 shows the maximum calculated lattice temperature reached, scaled by fluence, as a function of fluence for both film samples. Also shown are the measured scaled parameters from the data, which increase for both samples until a fluence threshold is reached. Lattice heating is calculated to occur on a ~7 ps timescale, which agrees with prior work.[178] The time component related to cooling from this maximum temperature is expected to be related in magnitude to the maximum temperature reached.

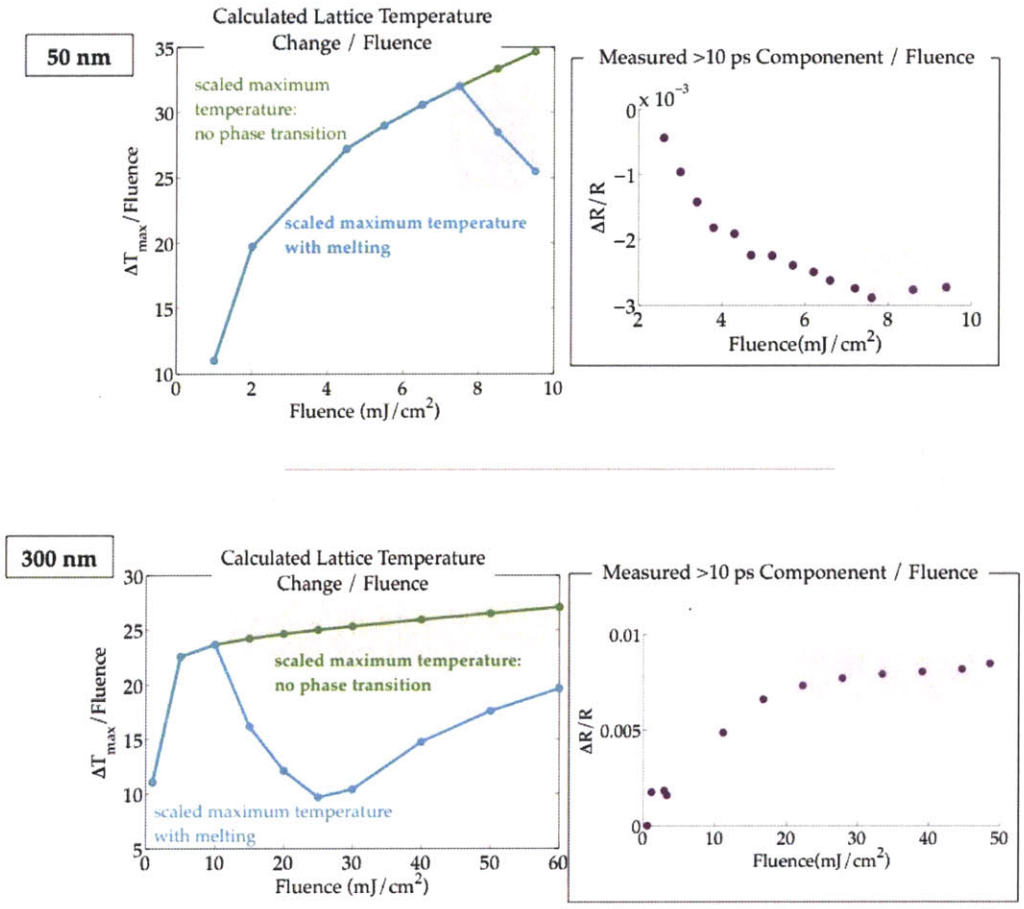

Figure 5-50: Calculated maximum lattice temperature change scaled by fluence (left) for the 50 nm film (top) and the 300 nm film (bottom) as calculated from Figure 5-47 Figure 5-48 (green) and with consideration of the enthalpy of melting on the temperature change (blue). At right is the measured >10 ps electronic component amplitude scaled by fluence for each sample. This comparison suggests melting in the 50 nm case, but not in the 300 nm case.

The melting temperature of 242 K (on the ΔT scale relative to room temperature) is noted in Figure 5-47 and Figure 5-48. Above this point, until the lattice melts, the true lattice temperature is not expected to change. The calculated maximum temperature per fluence, corrected to account for the enthalpy of melting, is also plotted in Figure 5-50. The results closely predict the measured component amplitude trends in both cases when we consider melting in the thinner sample, and no melting effect in the thicker sample.

We observed frequency red-shifting with fluence for both film samples, in accordance with the expected mode-softening result under increased carrier density. We noted stronger dependence of the frequency shift with carrier density above 5.5

mJ/cm^2 in the 50 nm film case, and above 20 mJ/cm^2 in the 300 nm film case. In both cases, these thresholds correspond to measured electronic signals observed in the data. These electronic signals were suggested by our modeling to result from a combination of carrier absorption saturation and lattice heating. The frequency down-shifting cannot result from an increase in lattice temperature at these early times (500 fs), but may be due to a significantly more energetic electron distribution which couples more strongly to the relevant lattice mode. This interpretation is indeed suggested by the instantaneous amplitudes shown in Figure 5-18. If the saturation of this signal, above 5 mJ/cm^2 in the 50 nm sample and above 15 mJ/cm^2 in the 300 nm sample, indicates additional absorption by hot carriers, we expect higher electron temperatures to result, even if the carrier density does not change. Since absorption by conduction band electrons results in carriers in high-lying regions of the conduction band, it is conceivable that these carriers scatter toward broader distributions in k-space. In the interpretation of Melnikov et al—who reported varying relaxation rates across the Bruillion zone—absorption by hot carriers could lead to an electronic distribution that more strongly couples to lattice modes.[30] Wavelength-dependent single-shot measurements are planned, which would be sensitive to this result.

It is typically assumed that the frequency chiefly reflects carrier density, as we have done here by interpolation of the carrier frequency. This remains an appropriate estimation on the short timescale, prior to lattice temperature equilibration. Two-pump results, discussed below, indicate that there may be slight dependence of frequency on lattice temperature; however, this relation is not likely to dictate the early-time measured frequency.

Dynamics of the photoexcited state

Two-pump measurements on the photoexcited state induced by varying degrees of excitation in both samples provide further insight to the dynamics discussed thus far. In the 300 nm sample, we observe two electronic recovery periods: over 30 ps and over the 800 ps timescale—and likely beyond (Figure 5-25 and Figure 5-26). The ~30 ps time component was also apparent from the composite time traces presented from multiple single shot measurements (Figure 5-23). We ascribe this component primarily to electron-hole recombination based on a literature value of 26 ps, which is also reflected by design in the solution to electron density for the 300 nm sample shown in Figure

5-46. An equivalent component was seemingly absent in the 50 nm time traces, as the initial recovery on the 10-15 ps timescale gave way to no apparent further recovery on the 100 ps timescale of those measurements (Figure 5-23). We suggest that a shorter electron-hole recombination time yields the single observable sub-100 ps relaxation, on the same timescale as lattice heating and electron cooling. This corresponds to the estimate of a 10 ps recombination time, estimated by extrapolation from the work of Sheu, et al.[190], and reflected by design in the carrier density solution shown in Figure 5-48. The long-time (>100 ps) relaxation component is ascribed to the slow process of lattice cooling (estimated to occur on the 10 ns timescale via diffusion). Measurements on the 50 nm film are planned on the longer timescale to observe lattice cooling in that sample.

In both samples, the highest fluence employed led to the absence of observable lattice vibrations, suggesting the possibility of structural change. In our two-pump measurements on both samples, structural change was confirmed by the absence of oscillations immediately after initial photoexcitation. In contrast at lower fluence in both samples, interrogating the lattice response immediately following initial photoexcitation confirmed that no structural change occurred. In the 300 nm case, no oscillations were resolved above the noise level until after 3 ps. The two-pump measurements indicate initial recovery of the lattice on the ~20 ps timescale, and a more gradual continuous recovery on the >100 ps timescale. While oscillations at the highest fluence are difficult to resolve, measurements from the moderate fluence regime confirm the separate recovery timescales. We attribute the faster recovery timescale, over which significant frequency blue-shifting is observed, to electron-hole recombination. This is in keeping with the suggestion that electronic recovery over this timescale corresponds to recombination dynamics. We also suggest that the slow recovery over many hundred picoseconds is due to the slow cooling of the lattice, although dependence on slowly relaxing carriers cannot be ruled out by these measurements. Importantly, we conclude that despite a high predicted temperature from the model employed, the lattice does not appear to have melted even at the highest fluence. This result is suggested by the reappearance of oscillations in response to a second pump almost immediately after photoexcitation. Oscillations may be present at $t = 0$, and they are clearly resolved above the noise by ~10 ps. As the calculation in Figure 5-47 makes clear, a bismuth

lattice heated to the maximum calculated temperature, 1500 K (or ~1000 K when enthalpy is accounted for), would not recover to below the melting temperature until after more than 5 ns. Our measurements, which extend to 0.8 ns, report that the lattice is intact well before this time. Figure 5-51 summarizes the early-time results under highest fluence, and links measured frequency with carrier density. We conclude that the carrier population is induced to a high enough initial density to induce the phase change to the symmetric structure, and indications are strong that the lattice does not melt. However, the likely reason that the lattice remains intact—the fast transport of out carriers out of the region on a sub-picosecond timescale, before electron-lattice equilibration—also likely precludes the visualization of the symmetric solid state, which we estimate from these measurements to last less than 100 fs. Given the initial carrier density, it is likely that the instantaneous photoinduced state is the symmetric lattice, but it is not resolvable with our ~100 femtosecond pulse given the very rapid cooling by ballistic transport.

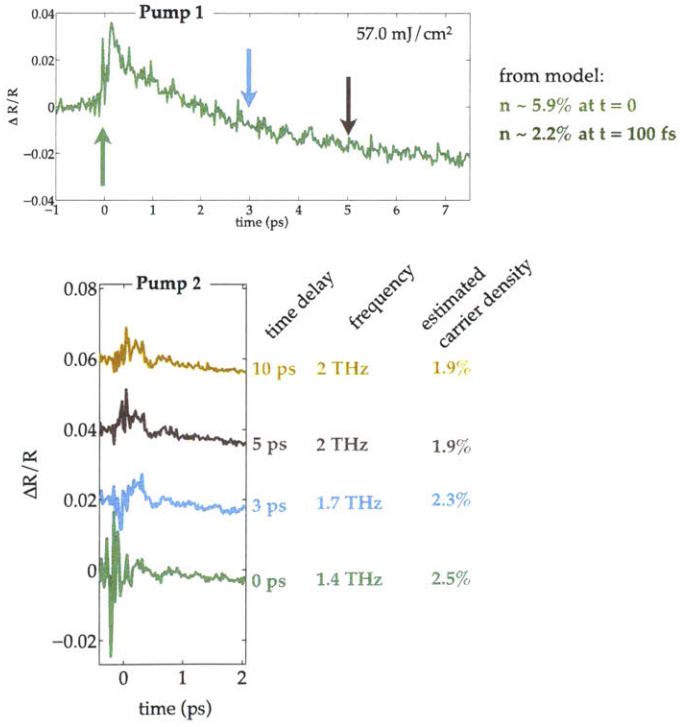

Figure 5-51: Response of 300 nm bismuth film to strong initial excitation (top) and subsequent weak perturbation (bottom) at 0, 3, 5, and 10 ps. Blue-shifting of the measured frequency is observable within the first few picoseconds, indicating a rapid reduction in the carrier density that may prevent measurement of a transient symmetric crystalline phase. With ballistic transport, the carrier population is estimated to be reduced from 5.9% to 2.2% within 100 fs.

In the 50 nm film, two-pump measurements do not resolve phonon dynamics until 30 ps. Our measurements suggests that melting has occurred in the 50 nm case for three reasons. First, the lattice is predicted to be in the melting regime in the highest fluence case (Figure 5-48). Since the evaluation of early-time transport suggests that the model is well-suited to describe transport in the 50 nm film, we conclude that the calculated temperature is close to the true one. Second, at all fluences employed for this sample above 7.5 mJ/cm^2, the lattice temperature is expected to remain at the melting temperature as a phase transition is induced. Figure 5-48 demonstrates that a lattice heated slightly above this temperature will cross the melting point and recrystallize at approximately 30 ps, corresponding closely to the time delay that lattice vibrations are seen by the two-pump measurement. Third, in the 300 nm case we observed lattice frequency recovery on the order of the electron-hole recombination time, which suggests that the carrier population dictates lattice relaxation in that case. In the thinnest sample, we observe no lattice recovery on the order of the estimated lattice-hole recombination time (10 ps), suggesting that an alternate process governs lattice relaxation under high fluence excitation in a quasi-two-dimensional environment.

Figure 5-52 provides a visual comparison of each sample's two-pump response at comparable time delays. While lattice responses at low frequency are difficult to resolve with numeric precision, a comparison by eye is sufficient to verify the absence of oscillations in the 50 nm sample at 5 ps relative to the 300 nm sample. The data are shown immediately following the electronic response to the second pump. The data are the same as those shown in Figure 5-24 and Figure 5-29, and are not rescaled.

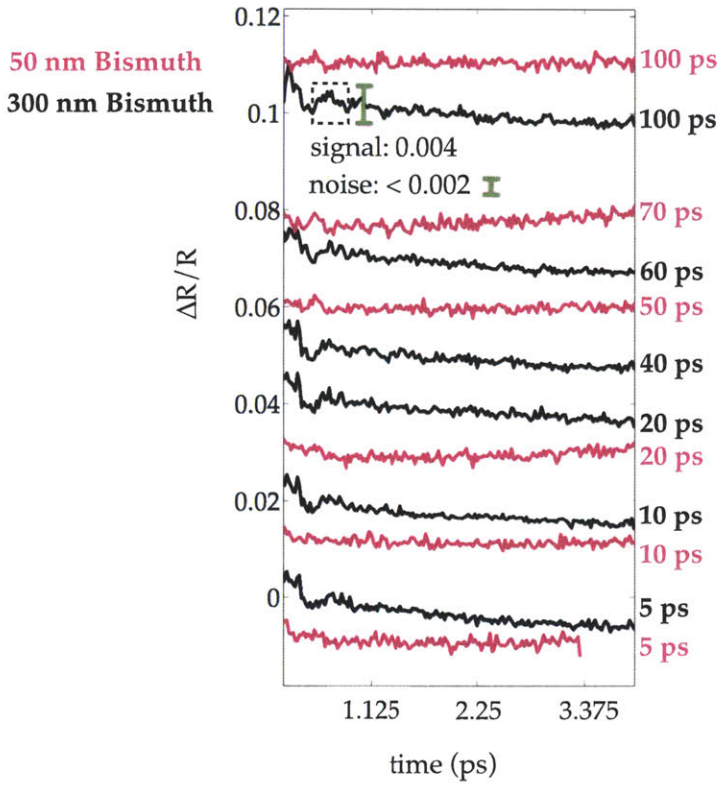

Figure 5-52: Early-time response to a second pump pulse after strong excitation in 50 nm (magenta) and 300 nm (black) bismuth thin films. A conservative indication of the instrumental noise, 0.002, is shown relative to the height of one oscillation. Oscillations in the 300 nm film are visible at all delays; oscillations in the 50 nm film are not visible until after 20 ps.

Comparing to the results of modeling in Figure 5-47 and Figure 5-48, we conclude that the lattice temperatures predicted by the model are more accurate in the case of the 50 nm film than in the case of the 300 nm film. This is consistent with the understanding that transport dynamics in part govern the carrier distribution in the 300 nm film, since our model only employed a modified initial condition based on the electron-electron scattering time. A modification to the model that includes a time-dependent ballistic component within the coupled equations is expected to significantly reduce the calculated temperature and better describe our experimental results.

Finally, the interpretation of the 50 nm film dynamics as a melting process presents the intriguing possibility that the frequency down-shifting observed in the one-pump measurement may be a demonstration of the lattice breakdown as it melts,

launched by a nonthermal process to a greater degree at higher fluence (observed in our one-pump measurement) and completed by a thermal process.

At the highest fluence employed on this sample, the instantaneous carrier density created by the pulse (before any diffusion) is calculated to be 4.2%. In the DECP picture presented in Chapter 1, we expect the instantaneous lattice potential shift to induce large excursions of the lattice atoms along the lattice mode coordinate. From the calculation by Fritz, et al. reproduced in Figure 5-3, we can estimate the extent of nuclear motion in a lattice vibration at a carrier densities in the calculated region. A carrier density of 2% will launch the atoms from a fractional lattice spacing of 0.468 to one of 0.48, or 2.5%. A density of 2.5% will induce a lattice shift of 4.7%, and a 3% photoinduced density will induce a lattice shift of 6.9%. Extrapolating, a 4% photoinduced density will induce a lattice shift of ~9.5%, which is in the regime characterized as the Lindemann criterion for melting as described in Chapter 1 (typically 10-15% of the lattice equilibrium distance). The approximate lattice displacement as a function of fluence is shown in along with the percent of latent heat per cubic nanometer provided by the laser pulse above the melting temperature. The possibility of real-time melting observed in our experiment is also corroborated by the work of Sciani et al., wherein the authors reported the melting of 30 nm bismuth films on the timescale of less than a single lattice vibration.[62]

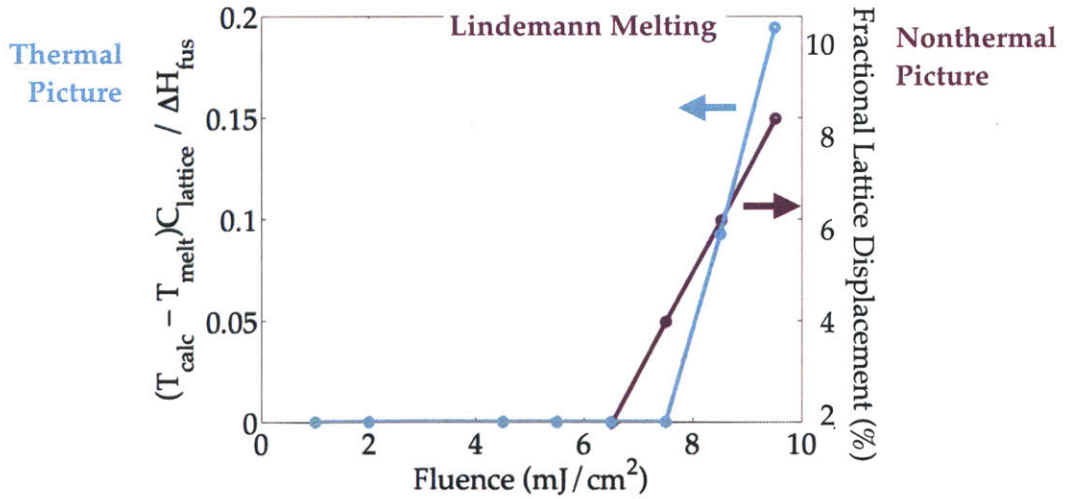

Figure 5-53: For the 50 nm film, the percent latent heat per volume element provided by the laser pulse (past the melting temperature) is shown (blue, left axis). The approximate lattice displacement for the upper fluence range is also shown, and nears the 10% Lindemann melting criterion at the highest employed fluence (purple, right axis).

5.5 Conclusions and Future Work

In conclusion, we have demonstrated that the laser-induced structural response of the semimetal bismuth can be varied by changing the sample thickness. We attribute this variability—melting in the quasi-two-dimensional case but not in the quasi-three dimensional case—to cooling by ballistic transport of photoexcited carriers when the sample is thicker than the electron mean free path in bismuth (~250 nm). While the conditions are sufficient in the quasi-three-dimensional case to induce a solid-solid phase change to the symmetric structure, our measurements suggest that, due to fast transport which relaxes the lattice potential on a 100 ps timescale, this state cannot be resolved by our current experimental apparatus on the >500 fs timescale, where our primary sensitivity to structural state derives from lattice oscillations. We have presented a modified two-temperature model with a simple inclusion of pre-diffusion ballistic transport in the three-dimensional case. While the model accurately predicts the measured phonon frequency at earliest times, adaptation to include time-varying ballistic transport is likely to better predict the lattice temperature reached when both ballistic and diffusive electron populations are present. Two-pump measurements, sensitive to rapid changes in the lattice frequency over multiple measurements, can provide a platform for experimental verification of carrier density as a function of time upon further modifications to the model. We propose that melting in the quasi-two-dimensional (50 nm) case is launched by a nonthermal process as the induced carrier population generates large instantaneous shifts in the potential energy surface, and is completed by a thermal process on the order of the electron-phonon coupling time. Since morphological change was not observed (which is expected upon melting), the additional measurements are needed to confirm the melting effect. We observe the solid state to reappear on the timescale of ~30 ps, which is consistent with the timescale predicted by our model. We observe striking similarities in key electronic and lattice behaviors across samples. We propose two possibilities for this phenomenon, which may both contribute. First, when hot carriers exceed a key temperature, the temperature-dependent electron-phonon coupling rapidly transfers energy to the lattice, inducing larger amplitude, lower frequency vibrations. Second, high-fluence excitation may lead to hot carrier absorption, which has the effect of scattering carriers

more broadly in the Bruillon zone and creating populations that couple especially strongly to lattice modes due to symmetry.

As described in the previous section, wavelength-dependent measurements are sensitive to electron populations that absorb according to their transition dipoles across the Bruillion zone. By varying the probe wavelength across one-pump and two-pump measurements, we can monitor the electron populations at varying points in momentum space as a function of fluence. We wish to know if creating more hot carriers, which we have suggested is accomplished in constrained two-dimensional environments, leads to broader momentum scattering? If so, our measurement may be sensitive to evidence that certain electron populations in k-space couple more strongly to the lattice vibration of interest.

The conclusions presented here beg one experiment in particular: the low-temperature measurement of a two-dimensionally constrained bismuth film. While we have concluded that our single-shot measurements can induce carrier populations high enough to yield the symmetric state nonthermally, and that a two-dimensional environment constrains carriers in the probed region, performing the measurement at room temperature melts the sample due to the 544 K melting temperature of bismuth. We estimate that performing the 50 nm measurement at liquid Helium temperatures will constrain the sample below the melting point up to a fluence of ~8.5 mJ/cm^2. Samples thinner than 50 nm are preferable for this measurement, as a slightly higher carrier density will be constrained within the probed region at the same fluence. Additionally, measurements of the type presented here on the structurally similar semimetal Antimony can more easily be constrained below its melting temperature of 904 K, 360 K higher than that of bismuth. This and related experiments can continue and expand efforts to understand the intricate interplay among energetic modes of solid-state materials, from the near equilibrium regime extending into far from equilibrium conditions.

References

1. Barber, J. Photosynthetic energy conversion: natural and artificial. *Phys. Rev. B* **38,** 185 (2008).
2. Blankenship, R. E. *et al.* Comparing Photosynthetic and Photovoltaic Efficiencies and Recognizing the Potential for Improvement. *Science* **332,** 805–809 (2011).
3. Russell, P. Photonic Crystal Fibers. *Science* **299,** 358–362 (2003).
4. Krames, M. R. *et al.* Status and Future of High-Power Light-Emitting Diodes for Solid-State Lighting. *Phys. Rev. B* **3,** 160–175 (2007).
5. Kukura, P., McCamant, D. W. & Mathies, R. A. Femtosecond Stimulated Raman Spectroscopy. *Annu Rev Phys Chem* **58,** 461–488 (2007).
6. Cass, S. The 50 Most Innovative Companies 2012. *Technology Review* **115,** 36–39 (2012).
7. Fleming, G. & Ratner, M. Grand challenges in basic energy sciences. *Physics Today* **61,** 28–33 (2008).
8. Minnich, A. J., Dresselhaus, M. S., Ren, Z. F. & Chen, G. Bulk nanostructured thermoelectric materials: current research and future prospects. *Science* **2,** 466 (2009).
9. Meral, M. E. & Dinçer, F. A review of the factors affecting operation and efficiency of photovoltaic based electricity generation systems. *Renewable and Sustainable Energy Reviews* **15,** 2176–2184 (2011).
10. Aliberti, P. *et al.* Investigation of theoretical efficiency limit of hot carriers solar cells with a bulk indium nitride absorber. *Science* **108,** 094507 (2010).
11. BCST. *Materials Science and Technology. The National Academies Press* (The National Academies Press, 2003).
12. Jimenez, R., Fleming, G. R., Kumar, P. V. & Maroncelli, M. Femtosecond solvation dynamics of water. *Nature* **369,** 471–473 (1994).
13. Rabitz, H. Shaped Laser Pulses as Reagents. *Science* **299,** 525–527 (2003).
14. Rosker, M. J., Dantus, M. & Zewail, A. H. Femtosecond real-time probing of reactions. I. The technique. *The Journal of Chemical Physics* **89,** 6113 (1988).
15. Vos, M. H. & Martin, J. L. Femtosecond processes in proteins. *Biochim Biophys Acta* (1999).
16. Miao, J., Sandberg, R. L. & Song, C. Coherent X-Ray Diffraction Imaging. *Quantum Electronics, IEEE Journal of* **18,** 399–410 (2012).
17. Hebling, J., Yeh, K.-L., Hoffmann, M. C. & Nelson, K. A. High-Power THz Generation, THz Nonlinear Optics, and THz Nonlinear Spectroscopy. *IEEE Journal of Selected Topics in Quantum Electronics* **14,** 345–353 (2008).
18. Jackson, J. D. *Classical electrodynamics.* (Wiley, 1999).
19. Kuzmany, H. *Solid-state spectroscopy: an introduction.* (Springer, 1998).
20. Klingshirn, C. F. *Semiconductor Optics.* (Springer, 2006).
21. Yu, P. & Cardona, M. *Fundamentals of semiconductors: physics and materials properties.* (Springer, 2010).
22. Dressel, M. & Scheffler, M. Verifying the Drude response. *Ann. Phys.* **15,** 535–544 (2006).
23. Demtroder, W. *Laser Spectroscopy: Volume 1.* **1: Basic Principles,** (Springer Berlin Heidelberg, 2008).
24. Rethfeld, B., Sokolowski-Tinten, K., Linde, Von der, D. & Anisimov, S. I. Timescales in the

response of materials to femtosecond laser excitation. *Applied Physics A* **79,** 767–769 (2004).
25. Linde, Von der, D., Sokolowski-Tinten, K. & Bialkowski, J. Laser–solid interaction in the femtosecond time regime. *Appl Surf Sci* **109-110,** 1–10 (1997).
26. Lundstrom, M. *Fundamentals of Carrier Transport - Mark Lundstrom - Google Books*. (Cambridge University Press, 2000).
27. Mero, M., Zeller, J. & Rudolph, W. in *Femtosecond Laser Spectroscopy* 1–25 (2005).
28. Zeller, J. *et al.* Femtosecond dynamics of highly excited dielectric thin films. in *XXXV Annual Symposium on Optical Materials for High Power Lasers: Boulder Damage Symposium* (Exarhos, G. J. et al.) **5273,** 515–526 (SPIE, 2004).
29. Keldysh, L. V. Ionization in Field of a Strong Electromagnetic Wave. *Soviet Physics JETP-USSR* **20,** 1307–&
30. Melnikov, A., Misochko, O. & Chekalin, S. Ultrafast dynamics of photoexcited bismuth films.
31. Weiner, A. M., Leaird, D. E., Wiederrecht, G. P. & Nelson, K. A. Femtosecond pulse sequences used for optical manipulation of molecular motion. *Science* **247,** 1317–1319 (1990).
32. Wefers, M. W., Kawashima, H. & Nelson, K. A. Optical control over femtosecond polarization dynamics. *Journal of Physics and Chemistry of Solids* **57,** 1425–1432 (1996).
33. Yan, Y.-X., Gamble, E. B. & Nelson, K. A. Impulsive stimulated scattering: General importance in femtosecond laser pulse interactions with matter, and spectroscopic applications. *The Journal of Chemical Physics* **83,** 5391–5399 (1985).
34. Zeiger, H. *et al.* Theory for displacive excitation of coherent phonons. *Phys. Rev., B Condens. Matter* **45,** 768–778 (1992).
35. Ishioka, K. & Misochko, O. in *Coherent Lattice Oscillations in Solids and Their Optical Control* 1–25 (2012).
36. Dhar, L., Rogers, J. A. & Nelson, K. A. Time-resolved vibrational spectroscopy in the impulsive limit. *Chem. Rev.* **94,** 157–193 (1994).
37. Kutt, W. A., Albrecht, W. & Kurz, H. Generation of coherent phonons in condensed media. *Quantum Electronics, IEEE Journal of* **28,** 2434–2444 (1992).
38. Cheng, T. K. *et al.* Impulsive excitation of coherent phonons observed in reflection in bismuth and antimony. *Applied Physics Letters* **57,** 1004–1006 (1990).
39. Zijlstra, E. S., Tatarinova, L. L. & Garcia, M. E. Laser-induced phonon-phonon interactions in bismuth. *Phys. Rev. B* **74,** 1–4 (2006).
40. Fritz, D. M. *et al.* Ultrafast bond softening in bismuth: mapping a solid's interatomic potential with X-rays. *Science* **315,** 633–636 (2007).
41. Garrett, G., Albrecht, T., Whitaker, J. & Merlin, R. Coherent THz Phonons Driven by Light Pulses and the Sb Problem: What is the Mechanism? *Phys. Rev. Lett.* **77,** 3661–3664 (1996).
42. Stevens, T. E., Kuhl, J. & Merlin, R. Coherent phonon generation and the two stimulated Raman tensors. *Physical Review B* **65,** 144304 (2002).
43. Bucksbaum, P. H. The Future of Attosecond Spectroscopy. *Science* **317,** 766–769 (2007).
44. Byskov-Nielsen, J., Savolainen, J.-M., Christensen, M. S. & Balling, P. Ultra-short pulse laser ablation of copper, silver and tungsten: experimental data and two-temperature model simulations. *Applied Physics A: Materials Science & Processing* **103,** 447–453 (2011).
45. Bulgakova, N. M., Stoian, R., Rosenfeld, A., Hertel, I. V. & Campbell, E. Electronic transport and consequences for material removal in ultrafast pulsed laser ablation of materials. *Physical Review B* **69,** 054102 (2004).
46. Poulin, P. R. & Nelson, K. A. Irreversible organic crystalline chemistry monitored in real time. *Science* **313,** 1756–1760 (2006).
47. Nasu, K. *Photoinduced Phase Transitions*. (World Scientific Publishing Company Incorporated, 2004).
48. Prasad, S. K., Nair, G. G., Sandhya, K. L. & Rao, D. Photoinduced phase transitions in liquid crystalline systems. *Current Science* **86,** 815–823
49. Wuttig, M. & Yamada, N. Phase-change materials for rewriteable data storage. *Nature materials* (2007).
50. Fiebig, M. Revival of the magnetoelectric effect. *J. Phys. D: Appl. Phys.* **38,** R123–R152 (2005).
51. Fidler, J. & Schrefl, T. Micromagnetic modelling - the current state of the art. *J. Phys. D: Appl. Phys.* **33,** R135–R156 (2000).
52. Basov, D., Averitt, R., van der Marel, D., Dressel, M. & Haule, K. Electrodynamics of correlated

electron materials. *Rev. Mod. Phys.* **83,** 471–542 (2011).
53. Dagotto, E. Complexity in Strongly Correlated Electronic Systems. *Science* **309,** 257–262 (2005).
54. Nasu, K., Ping, H. & Mizouchi, H. Photoinduced structural phase transitions and their dynamics. *J. Phys.: Condens. Matter* **13,** R693–R721 (2001).
55. Malvezzi, A. M. Laser heating and surface optical monitoring techniques: A survey. *Int J Thermophys* **14,** 347–359 (1993).
56. Huang, C. Y., Malvezzi, A. M. & Bloembergen, N. Analysis of picosecond pulsed laser melted graphite. *MRS ...* (1986).
57. Shank, C., Yen, R. & Hirlimann, C. Femtosecond-Time-Resolved Surface Structural Dynamics of Optically Excited Silicon. *Phys. Rev. Lett.* **51,** 900–902 (1983).
58. Hubbard, J. Electron Correlations in Narrow Energy Bands. III. An Improved Solution. *Proceedings of the Royal Society A: Mathematical, Physical and Engineering Sciences* **281,** 401–419 (1964).
59. Rini, M. *et al.* Control of the electronic phase of a manganite by mode-selective vibrational excitation. *Nature* **449,** 72–74 (2007).
60. Kristoffel, N. & Konsin, P. Vibronic Theory of Structural Phase Transitions and Displacive Ferroelectrics. *physica status solidi (b)* **149,** 11–40 (1988).
61. Stampfli, P. & Bennemann, K. Dynamical theory of the laser-induced lattice instability of silicon. *Phys. Rev. B* **46,** 10686–10692 (1992).
62. Sciaini, G. *et al.* Electronic acceleration of atomic motions and disordering in bismuth. *Nature* **458,** 56–59 (2009).
63. Graves, J. & Allen, R. Response of GaAs to fast intense laser pulses. *Phys. Rev. B* **58,** 13627–13633 (1998).
64. Varma, C. M. & Simons, A. L. Strong-coupling theory of charge-density-wave transitions. *Phys. Rev. Lett.* **51,** 138–141 (1983).
65. Hellmann, S. *et al.* Ultrafast melting of a charge-density wave in the Mott insulator 1T-TaS2. *Phys. Rev. Lett.* **105,** 187401 (2010).
66. Koshihara, S.-Y., Takahashi, Y., Sakai, H., Tokura, Y. & Luty, T. Photoinduced Cooperative Charge Transfer in Low-Dimensional Organic Crystals. *J. Phys. Chem. B* **103,** 2592–2600 (1999).
67. Wall, S., Rini, M., Dhesi, S. S., Schoenlein, R. W. & Cavalleri, A. Advances in Ultrafast Control and Probing of Correlated-Electron Materials. *IEEE Journal of Selected Topics in Quantum Electronics* **18,** 81–91 (2012).
68. Wall, S. *et al.* Ultrafast changes in lattice symmetry probed by coherent phonons. *Nat Comms* **3,** 721 (2012).
69. Hellmann, S. *et al.* Time-domain classification of charge-density-wave insulators. *Nat Comms* **3,** 1069 (2012).
70. Cowley, R. A. Structural phase transitions I. Landau theory. *Advances in Physics* **29,** 1–110 (1980).
71. Ross, M. Generalized Lindemann Melting Law. *Physical Review* **184,** 233–242 (1969).
72. Lindemann, F. A. *Phys. Z.* **11,** 609 (1910).
73. Chakravarty, C. Path integral simulations of quantum Lennard-Jones solids. *The Journal of Chemical Physics* **116,** 8938–8947 (2002).
74. Luo, S. N., Strachan, A. & Swift, D. C. Vibrational density of states and Lindemann melting law | Browse - Journal of Chemical Physics. *The Journal of Chemical Physics* (2005).
75. Chakravarty, C., Debenedetti, P. G. & Stillinger, F. H. Lindemann measures for the solid-liquid phase transition. *The Journal of Chemical Physics* **126,** 204508–204508–10 (2007).
76. Bennemann, K. H. Photoinduced phase transitions. *J. Phys.: Condens. Matter* **23,** 073202 (2011).
77. Hanamura, E. & Nagaosa, N. Theory of photo-induced structure changes. *Solid State Communications* **62,** 5–9 (1987).
78. Nagaosa, N. & Ogawa, T. Theory of photoinduced structure changes. *Phys. Rev. B* **39,** 4472–4483 (1989).
79. Yonemitsu, K. & Nasu, K. Theory of Photoinduced Phase Transitions. *Journal of the Physical Society of Japan* **75,** (2006).
80. Koechner, W. & Bass, M. *Solid-State Lasers: A Graduate Text.* (Springer-Verlag, 2003).
81. Trebino, R. *et al.* Measuring ultrashort laser pulses in the time-frequency domain using frequency-resolved optical gating. *Rev. Sci. Instrum.* **68,** 3277 (1997).
82. Trebino, R. Measuring the seemingly immeasurable. *Nature Photonics* (2011).
83. Boyd, R. W. *Nonlinear Optics.* (Academic Press, 2002).

84. Brodeur, A. & Chin, S. L. Ultrafast white-light continuum generation and self-focusing in transparent condensed media. *Journal of the Optical Society of America B-Optical Physics* **16,** 637–650
85. Gaeta, A. in *Self-focusing: Past and Present* (Boyd, R. W., Lukishova, S. G. & Shen, Y. R.) 399–411 (Springer, 2009).
86. Poulin, P. Coherent Lattice and Molecular Dynamics in Ultrafast Single-Shot Spectroscopy. 1–413 (2005).
87. Gale, G. M., Hache, F. & Cavallari, M. Broad-bandwidth parametric amplification in the visible: femtosecond experiments and simulations. *IEEE Journal of Selected Topics in Quantum Electronics* **4,** 224–229 (1998).
88. Harris, S. E., Oshman, M. K. & Byer, R. L. Observation of tunable optical parametric fluorescence. *Phys. Rev. Lett.* **18,** 732–734 (1967).
89. Shin, T. Photoinduced Phase Transitions Studied by
Femtosecond Single-shot Spectroscopy. 1–228 (2010).
90. Hecht, E. Optics. *San Francisco: Addison-Wesley* (2002).
91. Bennett, B. R., Soref, R. A. & Del Alamo, J. A. Carrier-induced change in refractive index of InP, GaAs and InGaAsP. *IEEE J. Quantum Electron.* **26,** 113–122 (1990).
92. Yamada, K., Watanabe, W., Toma, T., Itoh, K. & Nishii, J. In situ observation of photoinduced refractive-index changes in filaments formed in glasses by femtosecond laser pulses. *Optics Letters* **26,** 19–21
93. Clark, R., Kurmoo, M. & Mountney, D. Electronic and resonance Raman spectra of mixed-valence, linear-chain complexes of platinum and palladium with 1, 2-diaminocycloalkanes (N–N),[MII (N–N) 2][MIV .... *J. Chem. Soc.* (1982).
94. Tomimoto, S. *et al.* Femtosecond Dynamics of the Exciton Self-Trapping Process in a Quasi-One-Dimensional Halogen-Bridged Platinum Complex. *Phys. Rev. Lett.* **81,** 417–420 (1998).
95. Dexheimer, S., Van Pelt, A. & Brozik, J. Dynamics of the formation of the self-trapped exciton in the MX complex PtBr (en). *Synthetic Metals* (2001).
96. Kitagawa, T. S. H. N. M. N. A. H. Time-resolved luminescence spectroscopy of self-trapped excitons in ladder type Br-bridged Pt complexes. *The Journal of Chemical Physics* 1–6 (2011).
97. Kida, S. A New Red Platinum(II)-Platinum(IV) Compound. 1–1 (1965).
98. Clark, R. Electronic and resonance Raman spectra of one-dimensional mixed-valence platinum-ethylamine complexes at ca. 80 K. *Inorg. Chem.* (1978).
99. Albin, M. & Patterson, H. H. Optical-Properties of Mixed-Valence Platinum Halides. *Chemical physics letters* **73,** 451–455 (1980).
100. Conradson, S. D. *et al.* Charge density waves and local states in quasi-one-dimensional mixed valence inorganic complexes. *Solid State Communications* **65,** 723–729 (1988).
101. Degiorgi, L., Wachter, P., Haruki, M. & Kurita, S. Far-infrared optical investigations on quasi-one-dimensional halogen-bridged mixed-valence compounds. *Phys. Rev., B Condens. Matter* **40,** 3285–3293 (1989).
102. Donohoe, R. J., Worl, L. A., Swanson, B. I. & Bulou, A. Polarons and bipolarons in weak 1-D CDW solids: Spectral studies of local states in [PtII(en)2][PtIV(en)2Br2](CIO4)4 and [PtIV(en)2I2](CIO4)4. *Synthetic Metals* **42,** 2749–2752 (1991).
103. Robin, M. B. & Day, P. Mixed Valence Chemistry-A Survey and Classification. *Advances in Inorganic Chemistry and Radiochemistry* **10,** 247–422 (1968).
104. Matsumoto, N., Yamashita, M. & Kida, S. Studies on Mixed Valence Complexes of Platinum and Palladium. *Bulletin of the Chemical Society of Japan* **51,** 2334–2337 (1978).
105. Wada, Y., Mitani, T., Toriumi, K. & Yamashita, M. Optical Properties of Halogen-Bridged Mixed-Valence Complexes,[M (en) 2][PtX2 (en) 2](C104) 4,(M= Pt, Pd and Ni; X= C1, Br and I): Effects of Metal-Alternation. *Journal of the Physical Society of Japan* **58,** 3013–3021 (1989).
106. Okamoto, H., Mitani, T., Toriumi, K. & Yamashita, M. Photogeneration of solitons and polarons in 1-D halogen-bridged metal complexes. *Phys. Rev. Lett.* **69,** 2248–2251 (1992).
107. Huckett, S. C. *et al.* Effects of temperature on the crystal and molecular structure of the mixed-valence linear chain bis (ethylenediamine) platinum bis (ethylenediamine) dihaloplatinum tetraperchlorate (halo= chloro, bromo). *Inorg. Chem.* **32,** 2137–2144 (1993).
108. Wada, Y., Mitani, T., Yamashita, M. & Koda, T. Charge Transfer Exciton in Halogen-Bridged Mixed-Valent Pt and Pd Complexes: Analysis Based on the Peierls-Hubbard Model. *J. Phys. Soc. Jpn.* **54,** 3143–3153 (1985).

109. Landau, L. D. On the motion of electrons in a crystal lattice. *Physikalische Zeitschrift der Sowjetunion* (1933).
110. Stoneham, A. M. *et al.* Trapping, self-trapping and the polaron family. *J. Phys.: Condens. Matter* **19,** 255208 (2007).
111. Williams, R. T. & Song, K. S. The self-trapped exciton. *Journal of Physics and Chemistry of Solids* **51,** 679–716 (1990).
112. Mott, N. F. & Stoneham, A. M. The lifetime of electrons, holes and excitons before self-trapping. *J. Phys. C: Solid State Phys.* **10,** 3391 (1977).
113. Brazovskii, S. A. Self-localized excitations in the Peierls-Fröhlich state. *Soviet Journal of Experimental and Theoretical Physics* **51,** 342 (1980).
114. Donohoe, R. & Swanson, B. Phenomenological description of the longitudinal vibrations of the quasi-one-dimensional solid PtCl: calculation of the valence defect frequencies. ... *Physics: Condensed Matter* (1991).
115. Bulou, A., Donohoe, R. J. & Swanson, B. I. Lattice dynamics in MX chains; localized modes associated with polaronic and bipolaronic defects in PtX CDW systems. *Synthetic Metals* **43,** 3663–3666 (1991).
116. Yamamoto, S. & Ohara, J. Photoproduction of spin and charge carriers in halogen-bridged binuclear platinum chain complexes. *J. Phys.: Condens. Matter* **20,** 415215 (2008).
117. Gammel, J., Saxena, A., Batistic, I., Bishop, A. & Phillpot, S. Two-band model for halogen-bridged mixed-valence transition-metal complexes. I. Ground state and excitation spectrum. *Phys. Rev., B Condens. Matter* **45,** 6408–6434 (1992).
118. Takaishi, S. & Yamashita, M. Solitons, polarons and their dynamics in mixed-valence halogen-bridged MX-chains. *Solitons, polarons and their dynamics in mixed-valence halogen-bridged MX-chains* 1–9 (2008). doi:10.1098/rsta.2007.2142
119. Dexheimer, S. & Morrissey, F. X. Ultrafast lattice dynamics in excitonic self-trapping. in *Conference on Lasers and Electro-Optics/International Quantum Electronics Conference and Photonic Applications Systems Technologies (2004), paper IMJ1* (Optical Society of America, 2004).
120. Clark, R. Electronic, infrared, and resonance-Raman spectra of mixed-valence iodide-bridged linear-chain complexes of platinum. *J. Chem. Soc.* (1981).
121. Suemoto, T. Femtosecond dynamics of self-trapped excitons in quasi-one-dimensional halogen-bridged Pt complexes. *Journal of Luminescence* (1999).
122. Tomimoto, S., Saito, S., Suemoto, T., Takeda, J. & Kurita, S. Ultrafast dynamics of lattice relaxation of excitons in quasi-one-dimensional halogen-bridged platinum complexes. *Phys. Rev. B* **66,** (2002).
123. Sugita, A., Saito, T., Kano, H. & Yamashita, M. Wave Packet Dynamics in a Quasi-One-Dimensional Metal-Halogen Complex Studied by Ultrafast Time-Resolved Spectroscopy. *Phys. Rev. Lett.* (2001).
124. Tanino, H., Rühle, W. & Takahashi, K. Time-resolved photoluminescence study of excitonic relaxation in one-dimensional systems. *Phys. Rev. B* **38,** 12716–12719 (1988).
125. Tomimoto, S. *et al.* Observation of the wave-packet oscillation during the exciton self-trapping process in a quasi-one-dimensional halogen-bridged Pt complex. *Phys. Rev. B* **60,** 7961–7965 (1999).
126. Dexheimer, S., Van Pelt AD, Brozik, J. & Swanson, B. Femtosecond vibrational dynamics of self-trapping in a quasi-one-dimensional system. *Phys. Rev. Lett.* **84,** 4425–4428 (2000).
127. Bardeau, J. F. *et al.* Neutron diffraction study of [Pt (en) 2][Pt (en) 2I2](ClO4) 4 at 20 K: structure and evidence of a new phase transition. *Acta Crystallographica Section B: Structural Science* **52,** 854–864 (1996).
128. Huckett, S. C. *et al.* Mixed-halide MX chain solids: effect of chloride doping on the crystal structure and resonance Raman spectra of [Pt(en)2Br2][Pt(en)2](ClO4)4. *Chem. Mater.* **3,** 123–127 (1991).
129. Bulou, A. *et al.* Structural phase transition in the quasi-one-dimensional PtCl. *Ferroelectrics* **125,** 45–50 (1992).
130. Toriumi, K., Yamashita, M., Kurita, S., Murase, I. & Ito, T. Phase transitions of the halogen-bridged MII-X-MIV mixed-valence complexes [M (en) 2][MX2 (en) 2](ClO4) 4 (M= Pt, Pd; X= Cl, Br). Structural studies of the high-and low-temperature phases of [Pt (en) 2][PtBr2 (en) 2](ClO4) 4. *Acta Crystallographica Section B: Structural Science* **49,** 497–506 (1993).
131. Scott, B., Berkey, M. & Swanson, B. I. Synthesis and characterization of [Pt(chxn)2][Pt(chxn)2I2)I4. A quasi-one-dimensional material at the CDW/SDW phase boundary. *Chemical physics letters* **226,** 537–542 (1994).

132. Yamashita, M., Takaishi, S. & Kobayashi, A. Tuning of electronic structures of quasi one-dimensional iodide-bridged dinuclear platinum mixed-valence complexes. *Coordination chemistry ...* (2006).
133. Kurita, S., Haruki, M. & Miyagawa, K. Photo-Induced Defect States in a Quasi One-Dimensional Mixed-Valence Platinum Complex. *J. Phys. Soc. Jpn.* **57,** 1789–1796 (1988).
134. Iwano, K. Theory for photoinduced phase transition from a charge-density-wave state to a Mott-Hubbard insulator in a quasi-one-dimensional Br-bridged Pd compound. *Physical Review B* **70,** 241102 (2004).
135. Iwano, K. Mechanism for photoinduced structural phase transitions in low-dimensional electron-lattice systems: Nonlinearity with respect to excitation density and aggregation of excited domains. *Phys. Rev. B* **61,** 279–289 (2000).
136. Kimura, K., Matsuzaki, H., Takaishi, S., Yamashita, M. & Okamoto, H. Ultrafast photoinduced transitions in charge density wave, Mott insulator, and metallic phases of an iodine-bridged platinum compound. *Physical Review B* **79,** 1–5 (2009).
137. Peierls, R. E. *Quantum theory of solids*. (Clarendon Press, 1964).
138. Fogle, W. & Perlstein, J. Semiconductor-to-Metal Transition in the Blue Potassium Molybdenum Bronze, K_{0.30} MoO_{3}; Example of a Possible Excitonic Insulator. *Phys. Rev. B* **6,** 1402–1412 (1972).
139. Wilson, J. A., Di Salvo, F. J. & Mahajan, S. Charge-density waves in metallic, layered, transition-metal dichalcogenides. *Phys. Rev. Lett.* **32,** 882–885 (1974).
140. Nasu, K. Extended Peierls-Hubbard model for one-dimensional N-sites N-electrons system. III. Lattice relaxation after optical excitation in CDW. *J. PHYS. SOC. JAPAN.* (1984).
141. Frohlich, H. On the Theory of Superconductivity: The One-Dimensional Case. *Proceedings of the Royal Society A: Mathematical, Physical and Engineering Sciences* **223,** 296–305 (1954).
142. Berlinsky, A. J. One-dimensional metals and charge density wave effects in these materials. *Rep. Prog. Phys.* **42,** 1243–1283 (2001).
143. Clark, R. J. H. & Kurmoo, M. Excitation wavenumber dependence of the symmetric chain-stretching mode of linear-chain mixed-valence platinum complexes. *J. Chem. Soc., Faraday Trans. 2* **79,** 519–527 (1983).
144. Tranquada, J. M., Sternlieb, B. J., Axe, J. D., Nakamura, Y. & Uchida, S. Evidence for stripe correlations of spins and holes in copper oxide superconductors. *Nature* **375,** 561–563 (1995).
145. Demler, E., Sachdev, S. & Zhang, Y. Spin-Ordering Quantum Transitions of Superconductors in a Magnetic Field. *Phys. Rev. Lett.* **87,** 067202 (2001).
146. Chang, J. *et al.* Direct observation of competition between superconductivity and charge density wave order in YBa2Cu3O6.67. *Nat Phys* **8,** 871–876 (2012).
147. Ghiringhelli, G. *et al.* Long-Range Incommensurate Charge Fluctuations in (Y,Nd)Ba2Cu3O6+x. *Science* **337,** 821–825 (2012).
148. Takahashi, K. *et al.* Unusually long-lived light-induced metastable state in a thermochromic copper(II) complex. *Chem. Commun. (Camb.)* 1578–1579 (2002).
149. Iwano, K. Nonlinearity in the domain growth and macroscopic oscillations in photoinduced structural phase transitions. *Journal of Luminescence* **94,** 513–517 (2001).
150. Iwano, K. Precursor of photoinduced structural phase transitions in a coupled-chain system with an electron-lattice interaction. *Phys. Rev., B Condens. Matter* **65,** 024302 (2001).
151. Allen, J. Short term spectral analysis, synthesis, and modification by discrete Fourier transform. *Acoustics, Speech and Signal Processing, IEEE Transactions on* **25,** 235–238 (2002).
152. Stuller, J. *Introduction to Signals and Systems*. (Thomson-Engineering, 2007).
153. Gabor, D. Acoustical Quanta and the Theory of Hearing. *Nature* **159,** 591–594 (1947).
154. Araoka, F. *et al.* Time resolution of chirped lattice vibrations in a mixed-valence metal-halogen complex system. *Phys. Rev. B* **75,** 224304 (2007).
155. Mishima, A. & Nasu, K. Nonlinear lattice relaxation of photogenerated charge-transfer excitation in halogen-bridged mixed-valence metal complexes. I. Soliton and self-trapped exciton. *Phys. Rev. B* **39,** 5758–5762 (1989).
156. Suzuki, M. & Nasu, K. Nonlinear lattice-relaxation process of excitons in quasi-one-dimensional halogen-bridged mixed-valence metal complexes: Self-trapping, solitons, and polarons. *Phys. Rev., B Condens. Matter* **45,** 1605–1611 (1992).
157. Suzuki, M. & Nasu, K. Nonlinear lattice relaxations and proliferation of excitons in one- and two-

dimensional charge density waves. *Synthetic Metals* **64,** 247–253 (1994).
158. Yamamoto, S. Possible nonlinear excitations in quasi-one-dimensional halogen-bridged binuclear metal complexes. *Phys. Rev., B Condens. Matter* **66,** 165113 (2002).
159. Murray, É. D., Fritz, D. M., Wahlstrand, J. K., Fahy, S. & Reis, D. A. Effect of lattice anharmonicity on high-amplitude phonon dynamics in photoexcited bismuth. *Physical Review B* **72,** (2005).
160. Yonemitsu, K. & Nasu, K. Theory of photoinduced phase transitions in itinerant electron systems. *Physics Reports* **465,** 1–60 (2008).
161. Dexheimer, S. L. in *Coherent Vibrational Dynamics* (De Silvestri, S., Cerullo, G. & Lanzani, G.) **36,** 223–254 (CRC Press, 2008).
162. Baeriswyl, D. & Bishop, A. R. Halogen-Bridged Metal Complexes: Model Compounds for High-TcSuperconductors? *Phys. Scr.* **T19A,** 239–245 (2007).
163. Sun, C. K., Vallee, F., Acioli, L. H., Ippen, E. P. & Fujimoto, J. G. Femtosecond-tunable measurement of electron thermalization in gold. *Physical Review B* **50,** 15337 (1994).
164. Goldsmid, H. J. Bismuth--The Thermoelectric Material of the Future? 5–10 (2006).
165. Tang, S. & Dresselhaus, M. S. Constructing Anisotropic Single-Dirac-Cones in Bi1-xSbx Thin Films. *Nano Letters* **12,** 2021–2026
166. Peierls, R. *Quantum Theory of Solids (Clarendon, Oxford, 1955).* (Proc. Roy. Soc. A, 1976).
167. DeCamp, M., Reis, D., Bucksbaum, P. & Merlin, R. Dynamics and coherent control of high-amplitude optical phonons in bismuth. *Solid State Commun Phys Rev B* (1997).
168. Wu, A. & Xu, X. Coupling of ultrafast laser energy to coherent phonons in bismuth. *Applied Physics Letters* (2007).
169. Ishioka, K., Kitajima, M. & Misochko, O. Temperature dependence of coherent A and E phonons of bismuth. *Journal of Applied Physics* (2006).
170. Hase, M., Kitajima, M., Nakashima, S. & Mizoguchi, K. Dynamics of coherent anharmonic phonons in bismuth using high density photoexcitation. *Phys. Rev. Lett.* (2002).
171. Lobad, A. & Taylor, A. Coherent phonon generation mechanism in solids. *Phys. Rev. B* **64,** 180301 (2001).
172. Fahy, S. & Reis, D. Coherent Phonons: Electronic Softening or Anharmonicity? *Phys. Rev. Lett.* (2004).
173. Kandyla, M. Ultrafast dynamics of the laser-induced solid-to-liquid phase transition in aluminum.
174. Siders, C. W. *et al.* Detection of nonthermal melting by ultrafast X-ray diffraction. *Science* **286,** 1340–1342
175. Lindenberg, A. M. Atomic-Scale Visualization of Inertial Dynamics. *Science* **308,** 392–395 (2005).
176. Gamaly, E. G. & Rode, A. V. Ultrafast electronic relaxation in superheated bismuth. *Phys. Scr.* **15,**
177. Misochko, O., Hase, M., Ishioka, K. & Kitajima, M. Observation of an Amplitude Collapse and Revival of Chirped Coherent Phonons in Bismuth. *Phys. Rev. Lett.* **92,** 197401 (2004).
178. Melnikov, A., Misochko, O. & Chekalin, S. Ultrafast lattice dynamics of bismuth studied by femtosecond pulses in visible and near-infrared range. 1–1 (2011).
179. Vecchi, M. & Dresselhaus, M. Temperature dependence of the band parameters of bismuth. *Phys. Rev. B* **10,** 771–774 (1974).
180. Mikhail, I. F. I. & Ismail, I. M. M. The dielectric function of bismuth and the temperature dependence of the band structure parameters. *J. Phys. C: Solid State Phys.* **19,** 5393–5404 (1986).
181. Heremans, J. & Hansen, O. P. Influence of non-parabolicity on intravalley electron-phonon scattering; the case of bismuth. *J. Phys. C: Solid State Phys.* **12,** 3483–3496 (2001).
182. De Sande, J., Missana, T. & Afonso, C. Optical properties of pulsed laser deposited bismuth films. *Journal of Applied Physics* (1996).
183. Murray, É. D. *et al.* Phonon dispersion relations and softening in photoexcited bismuth from first principles. *Phys. Rev. B* **75,** 1–6 (2007).
184. Sokolowski-Tinten, K., Bialkowski, J., Boing, M., Cavalleri, A. & Linde, Von der, D. Thermal and nonthermal melting of gallium arsenide after femtosecond laser excitation. *Phys. Rev. B* **58,** R11805–R11808 (1998).
185. Sokolowski-Tinten, K., Schulz, H., Bialkowski, J. & Linde, D. Two distinct transitions in ultrafast solid-liquid phase transformations of GaAs. *Applied Physics A: Materials Science & Processing* **53,** 227–234 (1991).
186. Reis, D. A., Gaffney, K. J., Gilmer, G. H. & Torralva, B. Ultrafast dynamics of laser-excited solids. *MRS Bulletin-Materials Research Society* **31,** 601 (2006).

187. Landolt-Bornstein. The Landolt-Börnstein Database: Bismuth. *springermaterials.com* at <http://www.springermaterials.com/docs/pdf/10681727_1165.html>
188. Singh, N. Two-temperature model of nonequilibrium electron relaxation: A review. *International Journal of Modern Physics B* **24,** 1141–1158 (2010).
189. Jain, A. L., Suri, S. K. & Tanaka, K. Charge carrier densities and mobilities in bismuth. *Physics Letters A* **28,** 435–436 (1968).
190. Sheu, Y. M., Chien, Y. J., Uher, C., Fahy, S. & Reis, D. A. Free-carrier relaxation and lattice heating in photoexcited bismuth. *Phys. Rev. B* **87,** 075429 (2013).
191. Arnaud, B. & Giret, Y. Electron Cooling and Debye-Waller Effect in Photoexcited Bismuth. *Phys. Rev. Lett.* **110,**
192. Hopkins, P. E. & Norris, P. M. Contribution of Ballistic Electron Transport to Energy Transfer During Electron-Phonon Nonequilibrium in Thin Metal Films. *J. Heat Transfer* **131,** (2009).